

University of Southampton Research Repository

Copyright © and Moral Rights for this thesis and, where applicable, any accompanying data are retained by the author and/or other copyright owners. A copy can be downloaded for personal non-commercial research or study, without prior permission or charge. This thesis and the accompanying data cannot be reproduced or quoted extensively from without first obtaining permission in writing from the copyright holder/s. The content of the thesis and accompanying research data (where applicable) must not be changed in any way or sold commercially in any format or medium without the formal permission of the copyright holder/s.

When referring to this thesis and any accompanying data, full bibliographic details must be given, e.g.

Thesis: Author (Year of Submission) "Full thesis title", University of Southampton, name of the University Faculty or School or Department, PhD Thesis, pagination.

Data: Author (Year) Title. URI [dataset]

UNIVERSITY OF SOUTHAMPTON

FACULTY OF ENGINEERING AND PHYSICAL SCIENCES

School of Chemistry

**Precursor Synthesis, Chemical Vapour Deposition and
Thermoelectric Measurements of Group (14) and (15)
Chalcogenide Thin Films**

by

Fred Robinson

Thesis

August 2021

UNIVERSITY OF SOUTHAMPTON**ABSTRACT****FACULTY OF NATURAL AND ENVIRONMENTAL SCIENCES****School of Chemistry**

Thesis for the degree of Doctor of Philosophy

**Precursor Synthesis, Chemical Vapour Deposition and
Thermoelectric Measurements of Group (14) and (15)
Chalcogenide Thin Films**

Fred Robinson

The overarching aims of the project were to use a single source precursor (SSP) approach to the chemical vapour deposition (CVD) of thin films of materials of interest for thermoelectrics and to develop this further to enhance the performance of these deposits. This approach would allow for exploration of the materials and the potential for optimisation whilst considering sustainability and enhancements possible through nanostructuring, charge carrier concentration, crystal structure modulation, morphology and composition. In this work these factors have been controlled through adjustments to deposition temperature, precursor load, precursor design and mixture.

With a focus on materials that are of interest for their thermoelectric properties, SnSe was selected as the initial target due to its exciting reported potential for thermoelectric applications.¹ Previous single source precursors developed within the group had been utilised to deposit SnSe,² however, these depositions produced only a small amount of discontinuous SnSe, the depositions occurred at very high temperatures and produced other phases. Thus, an alternative single source precursor capable of producing phase pure, continuous SnSe thin films, preferably at lower temperatures, was investigated initially.

Once a feasible SSP had been identified for SnSe depositions, this type of precursor was extended to explore the deposition of other group 14 chalcogenide materials and then adapted for the deposition of Bi and Sb chalcogenide thin films. This thesis will cover the low pressure chemical vapour deposition of tin and germanium chalcogenides, silicon telluride, bismuth and antimony chalcogenides as well as a number of ternary solid solution systems, the selective deposition of SnTe³ and the wafer scale CVD of SnSe using a commercial rig. The importance of these materials for thermoelectric applications or other semiconductor functionalities will also be discussed along with measured electrical and thermoelectric properties and potential avenues for their optimisation.

Table of Contents

Table of Contents	ii
Table of Tables	ix
Table of Figures	xiii
Research Thesis: Declaration of Authorship	xxv
Acknowledgements	xxvii
Definitions and Abbreviations.....	xxix
Chapter 1 Introduction.....	33
1.1 Semiconducting materials	34
1.1.1 Semiconductor Junctions.....	38
1.2 Introduction to Thermoelectric Materials	39
1.2.1 Applications	41
1.2.1.1 Temperature regimes and applications.....	42
1.2.2 Challenges.....	44
1.2.2.1 Electrical conductivity, σ , and thermal conductivity, κ	44
1.2.2.2 The Seebeck coefficient, S , the electrical conductivity, σ and the charge carrier concentration, n	46
1.2.2.3 Deconvoluting thermoelectric parameters	47
1.2.3 Chemical properties and their relationship to thermoelectric properties.....	47
1.2.3.1 Bond Strength	48
1.2.3.2 Energy gap.....	48
1.2.3.3 Bonding ionicity and effective mass	49
1.2.3.4 Anharmonicity.....	49
1.2.3.5 Lone pair effect	50
1.2.4 Thermoelectric Materials.....	51
1.3 Optimisation of thermoelectric properties	52
1.3.1 Doping.....	53
1.3.2 Nanostructuring	53

1.3.3	Superlattices.....	54
1.3.4	Solid solutions	55
1.3.5	Crystal structure modification.....	55
1.4	Thermoelectric devices	55
1.5	Thin film deposition techniques.....	58
1.5.1	Atomic layer deposition vs chemical vapour deposition	58
1.5.2	Wafer scale commercial CVD process.....	60
1.6	CVD Precursors.....	61
1.7	Bulk versus thin film properties	61
1.8	Growth mechanisms and control.....	62
1.8.1	Layers/ thickness control	63
1.8.2	Phase control.....	63
1.8.3	Morphological control.....	63
1.8.4	Orientational control.....	64
1.8.5	Quality, dopants and defects	64
1.9	Characterisation techniques	64
1.9.1	Precursor characterisation	64
1.9.1.1	Nuclear Magnetic Resonance (NMR) Spectroscopy.....	65
1.9.1.2	Microanalysis.....	66
1.9.1.3	Thermogravimetric analysis (TGA)	67
1.9.2	Thin film characterisation	67
1.9.2.1	Grazing Incidence X-Ray Diffraction (GIXRD)	67
1.9.2.2	Raman spectroscopy	70
1.9.2.3	Scanning Electron Microscopy (SEM) with Energy Dispersive X-ray Spectroscopy (EDX)	71
1.9.2.4	Ellipsometry.....	73
1.9.3	Thermoelectric and Electrical Property Measurements.....	74
1.9.3.1	Hall effect and Van der Pauw Measurements	74
1.9.3.2	Variable temperature Seebeck coefficient measurements	76
1.10	References.....	77

Chapter 2 Group 14 Metal Chalcogenide Single Source Precursor Synthesis and Characterisation	88
2.1 Introduction	88
2.1.1 Precursor systems.....	89
2.1.2 Film growth.....	94
2.1.3 Material deposition.....	94
2.2 Experimental.....	96
2.2.1 Precursor preparation and characterisation	96
2.2.2 Precursor synthesis.....	97
2.3 Results and Discussion	103
2.3.1 Group 14 chalcogenide single source precursor preparation	103
2.3.2 Single source precursor evaluation	108
2.4 Conclusions	117
2.5 References	117
Chapter 3 CVD and Thermoelectric Properties of Tin Chalcogenide Thin Films	121
3.1 Single source precursors used	121
3.2 Introduction	121
3.2.1 Structure	122
3.2.2 Applications of SnE based materials.....	124
3.2.3 Deposition of SnE.....	126
3.2.3.1 Comparison of previously reported single source SnE precursors.....	126
3.2.4 Optimisation	128
3.2.4.1 Nanostructuring	129
3.2.4.2 Solid solutions	130
3.2.4.3 Superlattice	130
3.2.4.4 Mesostructure.....	131
3.2.4.5 Panoscopic approach	131
3.2.4.6 Anharmonicity.....	132
3.2.5 Aims	133

3.3	Experimental	133
3.3.1	Thin film growth by low pressure CVD onto fused silica substrates.....	133
3.3.2	Thin film growth by low pressure CVD onto patterned SiO ₂ /TiN substrates	134
3.4	Results and Discussion	134
3.4.1	Synthesis and Characterisation of SSPs for LPCVD	134
3.4.2	Low Pressure Chemical Vapour Deposition Experiments	136
3.4.3	Tin sulfide (SnS) thin films	138
3.4.4	Tin mono-selenide (SnSe) thin films	144
3.4.5	Tin mono-telluride (SnTe) thin films	147
3.4.6	Thermoelectric performance	149
3.4.6.1	Tin Sulfide	149
3.4.6.2	Tin Selenide	151
3.4.6.3	Tin Telluride	151
3.4.7	Selective deposition of tin telluride	153
3.5	Conclusions.....	155
3.6	References.....	155
Chapter 4 CVD of Germanium (II) Chalcogenide Thin Films and Thermoelectric		
	Properties of GeTe	161
4.1	Precursors used	161
4.2	Introduction.....	161
4.2.1	Crystal structures	162
4.2.2	Germanium chalcogenide deposition techniques and single source precursors	163
4.2.3	Temperature regime and applications.....	164
4.2.4	Property comparison.....	165
4.2.5	Electrical band structure and engineering.....	167
4.3	Experimental	171
4.3.1	Precursor Preparation and Characterisation	171
4.3.2	LPCVD onto fused quartz substrates.....	171
4.3.3	Thermoelectric and electrical property measurements	172

Table of Contents

4.4	Results and Discussion	172
4.4.1	Evaluation of SSPs for LPCVD procedure	172
4.4.2	Low Pressure Chemical Vapour Deposition Experiments.....	173
4.4.3	Germanium sulfide sample	174
4.4.4	Germanium selenide thin films.....	177
4.4.5	Germanium telluride thin films	181
4.4.6	Thermoelectric measurements of GeTe	186
4.5	Conclusions	190
4.6	References	190
Chapter 5 Application of $[\text{Si}^n\text{Bu}_3(\text{E}^n\text{Bu})]$ as Single Source Precursors for the Deposition of Silicon Chalcogenide Thin Films		
194		
5.1	Single source precursors used	194
5.2	Introduction	194
5.3	Experimental.....	197
5.3.1	LPCVD onto fused quartz substrates	197
5.4	Results and discussion	198
5.4.1	Synthesis and Characterisation of SSPs for LPCVD	198
5.4.2	Low Pressure Chemical Vapour Deposition Experiments using $[\text{Si}^n\text{Bu}_3(\text{Te}^n\text{Bu})]$ 200	
5.5	Conclusions	208
5.6	References	208
Chapter 6 Deposition of SnSe Thin Films Using a Commercial Picosun Instrument and LPCVD of Ternary Solid Solutions of the Form ME (M = Ge or Sn and E = S, Se or Te).....		
211		
6.1	Precursors used.....	211
6.2	Introduction	212
6.2.1	Thermoelectric performance enhancement using solid solutions.....	212
6.2.1.1	Techniques for identifying of solid solutions.....	213
6.2.2	Enhanced parameter control and growth	213

6.3	Experimental	213
6.3.1	Wafer scale CVD and PECVD of SnSe using a commercial Picosun R-200 Advanced ALD reactor	213
6.3.2	LPCVD growth of ternary solid solutions using combined precursors.....	214
6.4	Results and discussion.....	214
6.4.1	Wafer scale chemical vapour deposition using a Picosun R-200 Advanced ALD system	215
6.4.2	Towards the deposition of ternary group 14 chalcogenide thin films using mixed precursor systems	222
6.4.2.1	Attempted growth of a germanium selenide telluride ternary thin film using LPCVD	223
6.4.2.2	Attempted deposition of a germanium tin telluride ternary thin film using LPCVD	227
6.4.2.3	Attempted growth of a tin selenide telluride ternary thin film using LPCVD	230
6.5	Conclusions.....	233
6.6	References.....	234
Chapter 7 Evaluation of Single Source Precursors for the Deposition of Bi₂E₃ and Sb₂E₃ (E = S, Se or Te) Thin Films		237
7.1	Single source precursors used in this work.....	237
7.2	Introduction.....	237
7.2.1	The crystal structure of Sb ₂ E ₃ and Bi ₂ E ₃ (E = S, Se or Te).....	238
7.2.2	Thermoelectric properties of Sb ₂ E ₃ and Bi ₂ E ₃	238
7.2.3	Optimised properties	239
7.2.4	Applications near room temperature	239
7.2.5	Previous single source precursors and deposition	240
7.3	Experimental	241
7.3.1	Precursor preparation and characterisation.....	241
7.3.2	Precursor synthesis	242
7.3.3	Thin film growth by low pressure CVD onto fused silica substrates.....	243

Table of Contents

7.4	Results and discussion	245
7.4.1	Single source precursor preparation and evaluation	245
7.4.2	Low pressure chemical vapour deposition experiments.....	251
7.4.3	Sb ₂ S ₃ depositions.....	252
7.4.4	Bi ₂ S ₃ depositions	255
7.5	Conclusions	257
7.6	References	257
Chapter 8	Summary and outlook.....	262
Appendix A – General Experimental Techniques	263
A.1	Precursor Preparation and Characterisation	263
A.2	Thin film characterisation	263
A.3	Thermoelectric and electrical property measurements.....	263
A.4	Evaluation of LPCVD setup.....	264
A.5	References	264

Table of Tables

Table 1-1- Magnetic properties and natural abundances of specific nuclei relevant to NMR spectroscopy used in this work. ¹⁷⁵	65
Table 2-1: Precursors used for the deposition of tin chalcogenide thin films a)-j) or tin chalcogenide powders k) and l) and the deposition technique used. Precursors used for the deposition of germanium chalcogenide thin films m) or germanium chalcogenide powders or crystals n) and o) and the deposition technique used. p) Large scale CVD process described for the production of Si ₂ Te ₃ thin films and q) CVD of Si ₂ Te ₃ nanoplates and nanoribbons.	89
Table 2-2: Heteronuclear NMR data and, when applicable, coupling constants for starting reagents and single source precursors prepared in this work.	112
Table 2-3: Displays the boiling points, determined from TGA experiments, and the vapour pressures obtained from calculations and experimental data, where tetrabutyltin was used as a reference. *Vapour pressure values stated for Sn ⁿ Bu ₄ acquired from literature. ³⁰ No vapour pressure experiments conducted on [SiⁿBu₃(SⁿBu)] as this was not isolated pure.....	113
Table 2-4: Boiling point, T _{vap} , from Sigma Aldrich safety data sheet (SDS) and estimated from TGA data, a enthalpy of vaporisation calculated using the Clausius–Clapeyron equation and reference values given for ⁿ Bu ₄ Sn, as well as the entropy of vaporisation calculated using ΔH _{vap} /T _{vap} along with reference values for ⁿ Bu ₄ Sn.	114
Table 3-1: Data pertaining to tin chalcogenide materials for the crystal structure in the form of the unit cell lattice parameters, the unitless Grüneisen parameter, which provides information about the volume expansion with temperature, the electronic band gap and the Seebeck coefficient maxima.	124
Table 3-2: Energy dispersive X-ray analysis results for some SnS depositions.	137
Table 3-3: Energy dispersive X-ray analysis results for SnSe depositions.....	138
Table 3-4: Energy dispersive X-ray analysis results for SnTe depositions. The large values observed for the O% is likely in part due to the overlap of characteristic X-rays of oxygen with minor lines from Sn and Te.....	138

Table of Tables

Table 4-1: Lattice parameters, band gaps, thermal and electronic conductivities and maximum Seebeck coefficients for the germanium monochalcogenides at ambient temperature and pressure.	167
Table 4-2: Room temperature Van der Pauw electrical measurements for a film of GeSe and the deposition temperature. Note that the measurements inside the brackets have been calculated using an assumed thickness of 1 μm	180
Table 4-3: Table of EDX analysis results for GeTe films deposited using [GeⁿBu₃(TeⁿBu)] , (1) , and [GeⁿBu₂(TeⁿBu)₂] (2)	184
Table 5-1: Bond enthalpies for diatomic ME units, where M is C, Si, Ge or Sn and E is C, S, Se or Te. All values are stated for room temperature. ²⁸ Data labelled ^a was obtained from separate literature sources. ^{29,30}	200
Table 5-2: Electrical measurements obtained at room temperature using a 750 nA current for van der Pauw and 0.5 Tesla magnet for Hall effect measurements, describing sheet values as a thickness is yet to be obtained by cross sectional SEM. The resistivity values stated in parenthesis are obtained using an assumed thickness of 2 μm	208
Table 6-1: Atom percent measured using EDX for the deposited SnSe onto silicon wafer.	221
Table 6-2: EDX analysis of a sample determined to be a solid solution of GeSe _{1-x} Te _x by GIXRD.	224
Table 6-3: Comparison of the lattice parameters and cell volumes for both the binary materials, GeSe and GeTe, and the ternary deposition comprised of GeSe _{1-x} Te _x formed using a 9:1 ratio of [GeⁿBu₃(SeⁿBu)] and [GeⁿBu₃(TeⁿBu)]	226
Table 6-4: Comparison of the lattice parameters and cell volumes for both the binary materials, GeTe and SnTe, and the ternary deposition comprised of GeSnTe.	229
Table 6-5: EDX analysis results for a solid solution thin film containing Ge, Sn and Te (on SiO ₂).	230
Table 6-6: EDX analysis results showing the atom percentages for all the elements present..	231
Table 6-7: Comparison of the lattice parameters and cell volumes for both the binary materials, SnSe and SnTe, and the ternary deposition comprised of SnSeTe.	232
Table 7-1: Collection of some room temperature thermoelectric and electrical parameters for Bi ₂ E ₃ and Sb ₂ E ₃ including the electrical conductivity, Seebeck coefficient, thermal conductivity and the electronic bandgap. *Predicted value, no experimental	

value available due to the low electrical conductivity leading to instrumental
difficulties.239

Table of Figures

Figure 1-1- The DOS for a metal, semiconductor and an insulator. ⁵ Here the grey shaded areas represent filled energy levels and the white represents unoccupied energy levels.	35
Figure 1-2- Relative energy of the DOS and the carrier distributions for (a) n, (b) p and (c) intrinsic semiconducting materials.	36
Figure 1-3- Electronic band structures of Si and GaAs showing an indirect and direct band gap, respectively. ^{6,7}	37
Figure 1-4- Brillouin zones for primitive orthorhombic and face centred cubic crystal structures, respectively. ⁸ Reproduced with permission from Elsevier.	38
<i>Figure 1-5- The energy band diagram for a p-n junction. Where E_F is the Fermi level, E_g^p is the energy gap of the p-type semiconductor and E_g^n is the energy gap of the n type material.⁶</i>	38
Figure 1-6- The Seebeck (power generation) and Peltier (active refrigeration) effects in a thermoelectric module.	39
Figure 1-7- Energy band diagram showing the excitation and relaxation of electrons moving through a thermoelectric module containing both n and p type thermoelectric materials in a) the Seebeck effect and b) the Peltier effect. ¹⁴	40
Figure 1-8- Graph showing the power efficiency of some different processes, the theoretical power efficiencies offered by some different values for ZT as well as the Carnot Cycle, which shows the theoretical maximum efficiency for a heat engine operating between two temperatures. ^{37,42-44}	43
Figure 1-9- Change of the Seebeck coefficient (blue), electrical conductivity (green), power factor (black) and total thermal conductivity (red), both the electronic and lattice contributions indicated, relative to the free carrier concentration. ⁴⁴	45
Figure 1-10- The relationship between lattice thermal conductivity and bond strength by consideration of the lattice thermal conductivity versus a) the mean speed of sound and b) the average bond length. ^{49,50,59-62,51-58}	48
Figure 1-11- The influence of the Grüneisen parameter, and therefore anharmonicity, on the lattice thermal conductivity, κ_L . The correlation shown is drawn between	

Table of Figures

compounds with zincblende (T_d) and rock salt (O_h) structure ^{49,50,59–62,72,51–58} as well as values of single crystal layered orthorhombic (D_{2h}) SnS and SnSe. ^{38,73–76} The black line is to guide the eye.	50
Figure 1-12- Crystal structures of some different thermoelectric materials from different material classes. a) Inorganic clathrates e.g. $\text{Eu}_8\text{Ga}_{16}\text{Ge}_{30}$ ⁸¹ b) metal chalcogenide materials Pb/ SnTe ⁹⁰ c) skutterudites e.g. CoSb_3 ⁸¹ d) half-Heusler intermetallic compounds e.g. TiNiSn ⁸¹ e) silicides e.g. SrAl_2Si_2 ⁸² f) metal oxides e.g. NaCo_2O_4 ⁸¹ and g) SnSe. ^{1,38}	51
Figure 1-13- Phonon scattering rate versus phonon frequency highlighting the degree to which different scattering mechanisms reduce phonon transport and the frequency of the phonons that they interact with represented graphically. Diagram of some phonon scattering structures included for a multiscale optimised material. ^{111,112}	54
Figure 1-14- A schematic diagram showing n-type and p-type legs in a thermoelectric module indicating leg length L and contact length l_c	56
Figure 1-15- Illustration of the type of photolithographically patterned SiO_2 / TiN substrates which have been used to demonstrate selective deposition. ^{125–128}	57
Figure 1-16: SEM images showing a section of a patterned SiO_2 substrate with differently sized TiN wells (circles and squares) and a higher magnification image showing deposition of Bi_2Te_3 inside a well and not outside of the well. ¹²⁷ Reproduced from Ref. 127.	57
Figure 1-17: Precursor adsorption and surface reaction in the CVD or ALD of thin film materials producing volatile by-products that are removed using an exhaust system..	59
Figure 1-18- The steps involved in material growth by ALD. (a) Functional groups exposed on the substrate surface. (b) Pulse of precursor 1 and its reaction with the functional groups on the surface. (c) Reaction by products and excess precursor 1 is purged from the reactor by the flow of inert gas and vacuum evacuation. (d) Pulse of precursor 2 and its reaction with the new surface functional groups. (e) Reaction by products and excess precursor 2 is purged from the reactor by the flow of inert gas and vacuum evacuation. (f) Steps (a) to (e) are repeated until the desired thickness is achieved. ¹⁴³	60

Figure 1-19- X-ray diffraction geometry for an asymmetric scan like that of grazing incidence XRD. ¹⁸⁴	68
Figure 1-20- A simplified Jablonski diagram showing the energy level transitions observed in Raman spectroscopy from the vibration states, $v = 0$ and $v = 1$, to the virtual excited state and back to the vibrational states. ¹⁹²	71
Figure 1-21- Diagram outlining the effect an electron beam has when it interacts with a material. Including all of the different electrons and photons emitted and their relative penetration depths into the material. ¹⁹⁴	72
Figure 1-22: Diagram of the setup of an ellipsometer.....	73
Figure 1-23- The probe set up for the Hall effect and Van der Pauw system.....	74
Figure 1-24- The probe set up for the variable temperature Seebeck coefficient and resistivity measurement equipment. The outer probes control the temperature gradient across the film and the two central smaller probes measure voltage for the resistivity measurement.	76
Figure 2-1: Schematic of the LPCVD set up with a portion of an SEM image of a sample of a tin selenide thin film deposited using this equipment.	95
Figure 2-2: ^1H NMR spectrum for [SnⁿBu₃(SⁿBu)] , showing the clean SSP with no impurities..	105
Figure 2-3: $^{13}\text{C}\{^1\text{H}\}$ NMR spectrum for [GeⁿBu₃(SeⁿBu)] , showing the clean SSP with 8 well defined ^{13}C environments with no impurities.....	106
Figure 2-4: $^{77}\text{Se}\{^1\text{H}\}$ NMR spectrum for [SnⁿBu₃(SeⁿBu)] , showing the clean SSP. The inset image is of a zoomed in section of the spectrum showing well-defined satellites from the adjacent ^{119}Sn and ^{117}Sn	107
Figure 2-5: $^{119}\text{Sn}\{^1\text{H}\}$ NMR spectrum for [SnⁿBu₃(SeⁿBu)] , showing the clean SSP. The inset image is of a zoomed in section of the spectrum showing well-defined satellites from the adjacent ^{77}Se	107
Figure 2-6: TGA results compiled for all group 14 chalcogenide SSPs showing the boiling point range and clean volatilisation.....	110
Figure 2-7: Electronegativity values for group 14 and the chalcogens period 2 to 5. The values stated use the Pauling scale. ³⁵	111

Table of Figures

Figure 2-8: A graphical representation of the values obtained for vapour pressure at 125 °C against molecular weight for all the group 14 chalcogenide single source precursors developed in this work.	115
Figure 2-9: Raoult's law and a representation of positive and negative deviations from ideal behaviour. ³⁸	116
Figure 3-1- Molecular orbital diagram for an octahedral (O_h) ML_6 fragment and a distorted (C_{3v}). The orbitals of the ligands adjust to allow for the expression of the s^2 lone pair and the energy of the s^2 lone pair is reduced meaning the L orbitals become the HOMO. The degree to which the s^2 orbital is stabilised is proportional to the degree of distortion of the fragment. ¹³	123
Figure 3-2: Crystal structures of a) SnS^{28} or $SnSe^7$ and b) $SnTe.^3$	124
Figure 3-3- Compilation of the ZT values for polycrystalline pristine SnS , the b axis of single crystal $SnSe$ and pristine $SnTe$, recreated using literature sources. ^{7,27,47}	125
Figure 3-4: Examples of some of the single source precursors available in the literature. ^{54,56,69,57,62-68}	128
Figure 3-5: Low magnification TEM image of Hg doped $SnTe$ showing the individual grains and thus the mesostructure of the material. ⁸⁸ The colours added to the image are to aid in the visualisation of individual grains. Reproduced with permission from	131
Figure 3-6: Multiscale phonon scattering displayed in a) showing the different scale features that can be used for phonon scattering. Examples of these features in b) nanoprecipitates of $MnTe$ in $SnTe$, c) dislocations in the form of stacking faults and strain clusters in a $MnTe-SnTe$ alloy and d) heterostructure of SnS_2 nanoplates deposited onto SnS flakes providing further grain boundaries. ^{87,91-93} Images b), c) and d) reproduced with permissions from the Royal Society of Chemistry, John Wiley and Sons and Elsevier.	132
Figure 3-7: Examples of deposits on silica substrates of SnS from $[Sn^nBu_3(S^nBu)]$, SnS from $[Sn^nBu_2(S^nBu)_2]$, $SnSe$ and $SnTe$ (top left to bottom right).	134
Figure 3-8: TGA results, for all the precursors used in this chapter, showing suitable volatility in the range of 30- 600 °C with no, or less than 5%, residual mass left in the crucible after the experiment.	136

Figure 3-9: Top down SEM images a) and b) of two thin films of sulfur deficient SnS deposited using [SnⁿBu₃(SⁿBu)] and c) a GIXRD pattern (black) for the film seen in b) matched to a bulk literature pattern (red). ¹⁵	139
Figure 3-10: Top down SEM image (a), cross sectional SEM image (b) and grazing incidence XRD pattern for SnS thin film obtained by low pressure CVD using [SnⁿBu(SⁿBu)₂] (red = XRD pattern for bulk SnS ¹⁵) with a thickness of around 6 μm.....	141
Figure 3-11: EDX spectrum obtained for a stoichiometric deposition of SnS, signal from the Si is from the underlying substrate material and is indicative of a thin film.....	142
Figure 3-12: Top down SEM image (a), cross sectional SEM image (b) and grazing incidence XRD pattern for SnS thin film obtained by low pressure CVD using [SnⁿBu(SⁿBu)₂] (red = XRD pattern for bulk SnS ¹⁵) with a thickness of ca. 700 nm.....	143
Figure 3-13: Raman spectrum with the data highlighting the A _g and B _{2g} modes.	144
Figure 3-14: EDX Spectrum collected for a stoichiometric sample of SnSe.....	145
Figure 3-15: Grazing incidence XRD pattern for SnSe thin film (black) and the pattern for bulk Pnma SnSe (red). ¹⁹	146
Figure 3-16: Raman spectra of an SnSe thin film with the peaks at 152, 130, 72 and 110 cm ⁻¹ , corresponding to the A _g , A _g , A _g and B _{3g} modes highlighted. Also highlighted is the small feature at 186 cm ⁻¹ which is likely SnSe ₂ . ³⁷	147
Figure 3-17: (a) grazing incidence XRD pattern for SnTe thin film (thickness ca. 1 μm) with XRD pattern for bulk cubic SnTe (Fm-3m) (red), ³ (b)Top down and (c) cross sectional SEM images.....	148
Figure 3-18: (a) EDX spectrum highlighting the elements present within the SnTe film, the silicon present is attributed to the substrate. (b) Raman spectrum with the data highlighting the A ₁ and E modes at 124 and 143 cm ⁻¹ , respectively. ^{29,100}	149
Figure 3-19: Comparison of stoichiometric SnS, filled circles, and SnS _{0.9} , empty circles, for a) conductivity, b) carrier concentration, red, and mobility, blue, c) Seebeck coefficient and d) power factor.....	150
Figure 3-20: a) Electrical conductivity, b) the carrier concentration in red and the mobility in blue, c) the Seebeck coefficient and d) the power factor for the SnSe deposited using [SnBu₃(SeBu)]	151

Table of Figures

Figure 3-21: Temperature dependence of (a) the electrical conductivity, (b) carrier concentration and mobility. The lines connecting the electrical conductivity and the dotted trendlines of the carrier concentration and mobility are to guide the eyes.	152
Figure 3-22: Temperature dependence of the Seebeck coefficient and power factor with connective lines to guide the eyes.	153
Figure 3-23: (a) Top-view SEM image of a TiN/SiO ₂ patterned substrate with SnTe selectively deposited on the TiN surface (right). (b) EDX spectra taken from the rectangular areas indicated in (a). EDX element mapping of (c) Sn, (d) Te, (e) Ti and (f) O.	154
Figure 4-1: The view looking down the axis of GeS, ²⁶ GeSe ²⁷ and black phosphorus ²⁸ to highlight the similarities in their structure and the structure of rhombohedral GeTe. ²⁹	163
Figure 4-2: Examples of single source precursors reported for the deposition of germanium selenide and germanium telluride thin films. ^{17,22,31,32}	164
Figure 4-3: Collation of germanium monochalcogenide based thermoelectric materials with promising ZT values, plotted against both temperature at which ZT is maximised and the year or their publication. ¹ This highlights the mid temperature regime and the recent surge of interest in germanium chalcogenide-based thermoelectric materials. Reproduced with permission from ACS publications.	165
Figure 4-4: a) Electronic band structure of GeS, b) electronic band structure GeSe, c) the first Brillouin zone of orthorhombic structure adopted by GeS and GeSe and d) the electronic band structure of GeTe and e) the first Brillouin zone of rhombohedral GeTe. ⁵⁵⁻⁵⁷ Reproduced with permissions from the Royal Society of Chemistry and John Wiley and Sons.	168
Figure 4-5: The increase in band gap and band coalescence observed when alloying GeTe with MnTe or doping with antimony. ¹	169
Figure 4-6: The percentage of mass lost during heating from 30- 600 °C at a fixed heating rate for [Ge ⁿ Bu ₃ (S ⁿ Bu)], [Ge ⁿ Bu ₃ (Se ⁿ Bu)], [Ge ⁿ Bu ₃ (Te ⁿ Bu)], [Ge ⁿ Bu ₂ (Te ⁿ Bu) ₂] and [Ge ⁿ Bu ₂ (S ⁿ Bu) ₂], all showing complete volatilisation.	173
Figure 4-7: Image of the small amount of deposited GeS (grey material at left hand side of tile).	174

Figure 4-8: Grazing incidence XRD pattern measured for the deposited germanium sulfide (black) and the matched literature pattern (red). ²⁶	175
Figure 4-9: SEM image of germanium sulfide deposited from [GeⁿBu₃(SⁿBu)]	176
Figure 4-10: EDX spectrum collected for the GeS deposition produced using [GeⁿBu₃(SⁿBu)] with region between 9-10 keV inset to highlight the Ge K _{α1} peak.....	176
Figure 4-11: Raman spectrum of germanium sulfide, with A _g ³ , B _{3g} , A _g ¹ and A _g ² stretches at 112, 211, 239 and 267 cm ⁻¹ , respectively. ⁷²	177
Figure 4-12: Image of a tile containing highly orientated GeSe. The red cross indicates the region investigated for characterisation.....	177
Figure 4-13: Grazing incidence XRD pattern measured for germanium selenide deposited from [GeⁿBu₃(SeⁿBu)] (black) and the matched literature bulk pattern (red). ²⁷ The broad feature observed around 21° is attributed to the SiO ₂ substrate and it indicates that the film is relatively thin.	178
Figure 4-14: EDX spectrum collected for the GeSe deposition produced using [GeⁿBu₃(SeⁿBu)] .179	
Figure 4-15: SEM images of germanium selenide, deposited from [GeⁿBu₃(SeⁿBu)]	179
Figure 4-16: Raman spectrum of germanium selenide with B _{3g} , A _{g(1)} and A _{g(2)} stretches at 151, 175 and 188 cm ⁻¹ , respectively. ⁷⁷	180
Figure 4-17: Image of a tile containing GeTe. (Note: the scratch marks occurred during the electrical and thermoelectrical measurements).	181
Figure 4-18: Grazing incidence XRD pattern measured for a deposit of GeTe (black) and the matched literature pattern (red). ²⁹ The broad artifact around 22 ° corresponds to the underlying fused quartz substrate.	182
Figure 4-19: Top down SEM images of germanium telluride, deposited from [GeⁿBu₃(TeⁿBu)] , at 2,000 (top left) and 5,000 × magnification (top right) and a cross sectional SEM image showing the film thickness to be <i>ca.</i> 3 μm.	183
Figure 4-20: EDX spectrum collected for the GeTe deposition produced using [GeⁿBu₃(TeⁿBu)] .184	
Figure 4-21: Raman spectrum for germanium telluride, deposited using [GeⁿBu₃(TeⁿBu)] , with E and A _{1g} stretches at 86 and 123 cm ⁻¹ , respectively. ⁸⁰	185

Table of Figures

- Figure 4-22: Comparison of the A_{1g} Raman stretching modes for 4 separate GeTe films deposited at different deposition temperature using $[\text{Ge}^n\text{Bu}_3(\text{Te}^n\text{Bu})]$ 186
- Figure 4-23: **a)** Electrical conductivity, **b)** Seebeck coefficient and **c)** power factor for four samples of GeTe deposited at different temperature, measured between ~ 300 - 625 K samples deposited using $[\text{Ge}^n\text{Bu}_3(\text{Te}^n\text{Bu})]$ 187
- Figure 4-24: **a)** Charge carrier concentration and **b)** the charge carrier mobility versus temperature and **c)** the mobility at 300 °C versus grain size for GeTe measured between ~ 125 - 450 K samples deposited using $[\text{Ge}^n\text{Bu}_3(\text{Te}^n\text{Bu})]$ 188
- Figure 4-25: **a)** The Lorentz number and **b)** the calculated electronic contribution to the thermal conductivity factor for four samples of GeTe deposited at different temperature, between ~ 300 - 625 K samples deposited using $[\text{Ge}^n\text{Bu}_3(\text{Te}^n\text{Bu})]$ 189
- Figure 4-26: ZT values acquired using the calculated electronic contribution to the thermal conductivities shown in Figure 4-25b and the measured power factors displayed in Figure 4-23c. 189
- Figure 5-1: Crystal structure of Si_2Te_3 looking down the a axes to visualise the layers and down the c axis to emphasise the hexagonal structure of the Te slabs and the Si dumb-bells in the octahedral sites.¹³ 195
- Figure 5-2: SEM images of; a) nanoribbons,⁵ b) nanoplates,⁸ c) nanotapers¹⁷ and d) nanowires,¹⁸ of Si_2Te_3 . Figures reproduced with permission from the American Chemical Society, AIP Publishing, Springer Nature and AIP publishing, respectively. 196
- Figure 5-3: Crystal structure of SiS_2 and SiSe_2 .²¹ 196
- Figure 5-4: Example of Si_2Te_3 deposited onto a silica substrate. 198
- Figure 5-5: TGA of $[\text{Si}^n\text{Bu}_3(\text{S}^n\text{Bu})]$, $[\text{Si}^n\text{Bu}_3(\text{Se}^n\text{Bu})]$ and $[\text{Si}^n\text{Bu}_3(\text{Te}^n\text{Bu})]$ showing clean evaporation with no residue remaining. 199
- Figure 5-6: Typical appearance of the CVD tube after a LPCVD experiment using $[\text{Si}^n\text{Bu}_3(\text{Te}^n\text{Bu})]$ at a furnace temperature of 700 °C. Left to right (area of tube in the hottest region of the tube furnace to the bulb, which is external to the furnace during depositions) the deposited material highlighted by the coloured squares are elemental Te, Si_2Te_3 , mixed Si and Si_2Te_3 and Si. Note the colour change observed from black/ brown to red on cooling. 201

- Figure 5-7: Raman spectra for different tiles in a single LPCVD experiment from **[SiⁿBu₃(TeⁿBu)]**. Peak from silicon³¹ indicated with * and the stretching modes from Si₂Te₃ are highlighted also.¹⁹ Spectrum **a)** is that of the tile at the lowest deposition temperature and shows elemental Te.³² **b), c), d) and e)** all show some Si₂Te₃. **d), e) and f)** have a stretching mode from Si.202
- Figure 5-8: GIXRD patterns collected for individual substrates positioned at different deposition temperatures in the CVD tube shown in Figure 5-4. Literature bulk pattern of Si₂Te₃,¹³ bottom, and Te,³³ top, are displayed in red. Peaks highlighted with * indicate peaks from Si.³⁴ The collected GIXRD patterns, **a), b), c), d), e) and f)**, are in deposition temperature order with the coolest temperature at the top, **a)**, and the hottest at the bottom, **f)**.203
- Figure 5-9: GIXRD pattern of Si₂Te₃ deposited from **[SiⁿBu₃(TeⁿBu)]** (black) and a literature bulk pattern (red).¹³204
- Figure 5-10: Top down SEM image of a Si₂Te₃ film deposited (374 °C/ 0.01 mmHg) using **[SiⁿBu₃(TeⁿBu)]** onto a fused quartz substrate.205
- Figure 5-11: EDX spectrum for a deposition of Si₂Te₃ onto SiO₂ using **[SiⁿBu₃(TeⁿBu)]**.205
- Figure 5-12: Raman spectrum of a film of Si₂Te₃ with the E_g modes, at 103 and 279 cm⁻¹, and A_{1g} modes, at 128 and 145 cm⁻¹.^{5,19,35} Note that care was taken to collect the Raman spectrum immediately after the depositions.207
- Figure 6-1: a) Image of a Picosun R-200 Advanced ALD system. Included is a separate vacuum wafer loading chamber adjacent to the control screen.¹¹ b) Illustration showing a Picohot 200 bubbler with a 40 mL capacity and c) a Picohot 300 bubbler with a 400 mL capacity.215
- Figure 6-2: Ellipsometry of the silicon wafer after 100 cycles (left) and 2000 cycles (right) and a photograph of the wafer after the 2000 cycle experiment with deposition of material visible on the top left of the wafer. Both depositions used **[SnⁿBu₃(SeⁿBu)]** with a reaction chamber temperature of 300 °C, precursor bubbler temperature of 200 °C and hydrogen plasma to assist in the decomposition of **[SnⁿBu₃(SeⁿBu)]**.217
- Figure 6-3: Top down and cross-sectional SEM images of a SnSe deposit grown from **[SnⁿBu₃(SeⁿBu)]** using the wafer scale CVD procedure and showing the film to be

Table of Figures

ca. 200 nm thick. GIXRD pattern for the same deposition, in black, and an XRD pattern from bulk SnSe. ¹²	218
Figure 6-4: Ellipsometry thickness map showing a thicker region on the right hand side of the wafer and a photograph showing the wafer with some thicker deposit along the same edge. Note the ellipsometry measurement does not analyse within 1 cm of the edge and so the thickest part of the deposition is missed. The red arrow indicates the region characterised.	219
Figure 6-5: a) Top down and b) cross-sectional SEM images of a thin film deposited from [SnEt₃(SeⁿBu)] using the enhanced CVD procedure showing the film to be around 5 μm thick, an area not observed by the ellipsometry measurement. c) GIXRD pattern for the same deposition, in black, and a literature bulk pattern of SnSe. ¹²	220
Figure 6-6: EDX spectra for SnSe depositions onto silicon wafer using the enhanced CVD approach, using a) [SnⁿBu₃(SeⁿBu)] with a hydrogen plasma and b) [SnEt₃(SeⁿBu)] , respectively.	221
Figure 6-7: Raman spectra for an enhanced CVD film deposited from a) [SnⁿBu₃(SeⁿBu)] and b) [SnEt₃(SeⁿBu)]	222
Figure 6-8: a) Top down SEM image of ternary GeSe _{1-x} Te _x deposition, b) the corresponding EDX spectrum and c) an image of the tile.	224
Figure 6-9: GIXRD pattern for GeSeTe ternary film in black as well as patterns for GeSe in green and GeTe in red.	225
Figure 6-10: Raman spectra for GeSe _{1-x} Te _x in black, GeSe in green and GeTe in red.....	227
Figure 6-11: GIXRD pattern for Ge _{1-x} Sn _x Te ternary film displayed in black as well as the patterns for GeTe in green and SnTe in red.	228
Figure 6-12: a) Top down SEM image of ternary GeSnTe thin film, b) the corresponding EDX spectrum and c) an image of the deposition tile in investigated.....	229
Figure 6-13: The Raman spectrum for the deposited solid solution containing Ge, Sn and Te.	230
Figure 6-14: a) Top down SEM image of a deposition obtained using a precursor mixture of [SnⁿBu₃(SeⁿBu)] and [SnⁿBu₃(TeⁿBu)] , b) the corresponding EDX spectrum	

collected for that same deposition and c) an image of the deposition tile investigated.	231
Figure 6-15: GIXRD pattern for the mixed precursor deposition from 9 parts [SnⁿBu₃(SeⁿBu)] to 1 part [SnⁿBu₃(TeⁿBu)] , in green, and literature profiles for bulk SnSe ¹² and SnTe, ²⁴ in black and red respectively.	232
Figure 6-16: Raman spectra for ternary SnSe _{1-x} Te _x in black, SnTe in green and SnSe in red.	233
Figure 7-1: Crystal structures of a) Sb ₂ S ₃ , ¹² Sb ₂ Se ₃ , ¹³ Bi ₂ S ₃ ¹⁴ and b) Sb ₂ Te ₃ , ¹⁵ Bi ₂ Se ₃ ¹⁶ and Bi ₂ Te ₃ . ¹⁷	238
Figure 7-2: Some examples of single source precursors reported in the literature for the deposition of Sb ₂ S ₃ and Bi ₂ S ₃ , namely: a) [Bi(SCOPh) ₃], ⁵¹ b) (M[S ₂ P(OC ₈ H ₁₇) ₂] ₃), ⁵² c) [M(S ₂ CNEt ₂) ₃] ⁵³ and d) [Sb(S ₂ CO ⁱ Pr) ₃]. ⁵⁴	240
Figure 7-3: Single source precursors described in the literature for the deposition or synthesis of Sb ₂ Te ₃ and Bi ₂ Te ₃ , namely: a) [MCl ₃ (E ⁿ Bu ₂) ₃], ^{1,2} b) [SbMe(Te ⁿ Bu) ₂], ^{3,9} c) [BiEt ₂ (TeEt)], ⁵⁵ d) Sb[(Te ⁱ Pr ₂) ₂ N] ₃ , ⁵⁶ e) (Et ₂ M) ₂ Te ^{55,57} and f) [SbPh ₂ (TeEt)]. ⁵⁸	241
Figure 7-4: Examples of deposited material on tiles for Bi ₂ S ₃ (left) and Sb ₂ S ₃ (right).	244
Figure 7-5: Sb ₂ Se ₃ deposited onto a silica tile.	244
Figure 7-6: TGA experiments showing the change in mass with increasing temperature for [Sb(SⁿBu)₃] , [Bi(SⁿBu)₃] and [Sb(SeⁿBu)₃]	247
Figure 7-7: Powder XRD pattern of the residue from the TGA of [Bi(SⁿBu)₃] , matched to a literature pattern for BiS, ⁶⁶ blue, and Bi ₂ S ₃ , ¹⁴ red.	249
Figure 7-8: Powder XRD pattern of the decomposition product formed in the TGA of [Sb(SⁿBu)₃] , matched to literature patterns for Sb ₂ O ₃ . ⁶⁷ The small peaks labelled with * correspond to elemental Sb. ⁶⁶	250
Figure 7-9: : Powder XRD pattern of the decomposition product formed in the TGA of [Sb(SeⁿBu)₃] , with some of the more intense peaks highlighted with the Miller index labels that coincide with literature bulk Sb ₂ Se ₃ . ⁶⁸	251
Figure 7-10: GIXRD pattern of an Sb ₂ S ₃ , deposited using [Sb(SⁿBu)₃] , in black matched to a literature pattern of Sb ₂ S ₃ . ⁶⁹	253

Table of Figures

- Figure 7-11: **a)** Top down SEM image of a deposit of Sb_2S_3 and **b)** the corresponding EDX spectrum for the same deposit. 254
- Figure 7-12: Raman spectrum collected from a sample of Sb_2S_3 deposited from **[Sb(SⁿBu)₃]**. The peaks indicated at 158, 191, and 282 cm^{-1} correspond to the A_g modes and the peaks indicated at 130, 239, and 312 cm^{-1} correspond to B_{1g} modes.⁷⁰ 255
- Figure 7-13: GIXRD pattern, in black, collected for a Bi_2S_3 thin film deposited using **[Bi(SⁿBu)₃]** matched to a literature pattern of Bi_2S_3 .¹⁴ The broad feature observed between *c.a* 15 and 30 ° is caused by the underlying fused quartz substrate. 256
- Figure 7-14: Raman spectrum of Bi_2Te_3 deposited using **[Bi(SⁿBu)₃]**. The peaks indicated correspond to A_g , B_{1g} , A_g , A_g and B_{1g} modes, respectively.⁷¹ 257

Research Thesis: Declaration of Authorship

Print name: Fred Robinson

Title of thesis: Precursor Synthesis, Chemical Vapour Deposition and Thermoelectric Measurements of Group (14) and (15) Chalcogenide Thin Films

I declare that this thesis and the work presented in it are my own and has been generated by me as the result of my own original research.

I confirm that:

1. This work was done wholly or mainly while in candidature for a research degree at this University;
2. Where any part of this thesis has previously been submitted for a degree or any other qualification at this University or any other institution, this has been clearly stated;
3. Where I have consulted the published work of others, this is always clearly attributed;
4. Where I have quoted from the work of others, the source is always given. With the exception of such quotations, this thesis is entirely my own work;
5. I have acknowledged all main sources of help;
6. Where the thesis is based on work done by myself jointly with others, I have made clear exactly what was done by others and what I have contributed myself;
7. Parts of this work have been published as:

“Low-Pressure CVD of GeE (E = Te, Se, S) Thin Films from Alkylgermanium Chalcogenolate Precursors and Effect of Deposition Temperature on the Thermoelectric Performance of GeTe”, F. Robinson, V. Sethi, C. H. K. de Groot, A. L. Hector, R. Huang and G. Reid, *ACS Appl. Mater. Interfaces*, 2021, **13**, 47773

“ $\text{Bu}_2\text{Sn}(\text{S}^n\text{Bu})_2$ and ${}^n\text{Bu}_3\text{SnE}^n\text{Bu}$ (E = S or Se) – effective single source precursors for the CVD of SnS and SnSe thermoelectric thin films”, F. Robinson, P. J. Curran, C. H. (Kees) de Groot, D. Hardie, A. L. Hector, K. Holloway, R. Huang, D. Newbrook and G. Reid, *Mater. Adv.*, 2021, **2**, 4814

“Low temperature CVD of thermoelectric SnTe thin films from the single source precursor, ${}^n\text{Bu}_3\text{Sn}(\text{Te}^n\text{Bu})$ ”, F. Robinson, D. W. Newbrook, P. Curran, C. H. (Kees) de Groot, D. Hardie, A. L. Hector, R. Huang and G. Reid, *Dalton Trans.*, 2021, **50**, 998

Research Thesis: Declaration of Authorship

“Thioether complexes of WCl_4 , $WOCl_4$ and WCl_3 and evaluation of thiochloride complexes as CVD precursors for WS_2 thin film”, D. E. Smith, V. K. Greenacre, A. L. Hector, R. Huang, W. Levason, G. Reid, F. Robinson and S. Thomas, *Dalton Trans.*, 2020, **49**, 2496

“Two-Dimensional SnSe Nanonetworks: Growth and Evaluation for Li-Ion Battery Applications”, F. Davitt, K. Stokes, T. W. Collins, M. Roldan-Gutierrez, F. Robinson, H. Geaney, S. Biswas, S. L. Y. Chang, K. M. Ryan, G. Reid and J. D. Holmes, *ACS Appl. Energy Mater.*, 2020, **3**, 6602.

" Crystallographically Controlled Synthesis of SnSe Nanowires: Potential in Resistive Memory Devices", F. Davitt, H. G. Manning, F. Robinson, S. L. Hawken, S. Biswas, N. Petkov, M. van Druenen, J. J. Boland, G. Reid and J. D. Holmes, *Adv. Mater. Interfaces*, 2020, 2000474.

" Synthesis, properties and structures of gallium(III) and indium(III) halide complexes with neutral pnictine coordination", K. R. Cairns, V. K. Greenacre, L. A. Grose, W. Levason, G. Reid and F. Robinson, *J. Organomet. Chem.*, 2020, **912**, 121176.

" Chalcogenoether complexes of tantalum(V) sulfide trichloride – Synthesis, properties and structures", R. D. Bannister, W. Levason, G. Reid and F. Robinson, *Polyhedron*, 2019, **169**, 129.

Signature:Date: 08/08/2021

Acknowledgements

I have been extraordinarily fortunate over the course of my PhD. Firstly, I could not have done any of the work without the constant guidance, patience and conversation with my supervisor Gill and co-supervisor Andrew. The help and support offered was invaluable and even when things leaned towards the stressful a chat with Gill would always leave me feeling revitalised!

Additionally, the conversations and assistance from the group, past and present, allowed me to both develop my understanding of difficult concepts and enjoy every moment of lab work. Particular thanks to Stephen Richards, whose advice and guidance in material growth and inorganic synthesis were vital to my development and conversations were appreciated in making time in the lab worthwhile, Victoria Greenacre, whose inorganic synthetic knowledge was constantly of help and Francesco Monzittu (Franci), who helped tremendously with my communication of scientific ideas through extensive conversations (*grazie per tutto e in particolare il ride*). Similar thanks to Rhys, Daniie, Robert, Kelsey, Maddie and Charley.

Thanks to the three project students I had the pleasure of supervising: Katherine Halloway, Haamidah Sana and Hannah Watson. Your work has been very useful and forms contributions to this thesis. Katie compared several single source precursors for the deposition of SnS, Sana undertook work that was vital to the comparison of $[\text{BiCl}_3(\text{E}^n\text{Bu})_3]$ and $[\text{Bi}(\text{E}^n\text{Bu})_3]$ for LPCVD and Hannah did extensive work into $[\text{MCl}_3(\text{E}^n\text{Bu})_3]$ and $[\text{M}(\text{E}^n\text{Bu})_3]$ precursors which was essential for Chapter 7.

The collaborate work with members of the ECS department including Daniel Newbrook, Ruomeng Huang, Vikesh Sethi and Kees de Groot was of high importance for the work in this thesis. In particular training received from Ruomeng and Daniel on the use of the Hall effect and variable temperature Seebeck tools and thermoelectric measurement performed by Daniel on the SnS and SnSe samples and Vikesh on the GeTe samples. This work was vital to chapters 3 and 4.

A huge thank you to the whole team at Deregallera for guidance and help with understanding and taking my research to the next level. In particular Duncan and Pete for their input in projects and Chris for his patience and assistance with getting up to speed with the ALD reactor.

Finally, I could not have done the work without the support of my friends and family. To Giulia (and also Mike), thanks for your constant support and superior understanding of grammar in my language. Without you this would have been much less enjoyable. Sorry for explaining thermoelectric materials to you a hundred times.

Definitions and Abbreviations

δ	Chemical shift (ppm)
Å	10^{-10} m (Ångström)
ALD	Atomic layer deposition
CVD.....	Chemical vapour deposition
PVD.....	Physical vapour deposition
AACVD	Aerosol assisted chemical vapour deposition
LPCVD.....	Low pressure chemical vapour deposition
MBE.....	Molecular beam epitaxy
SSP.....	Single source precursor
XRD.....	X-ray diffraction
SEM	Scanning electron microscopy
EDX.....	Energy dispersive X-ray spectroscopy
TGA.....	Thermogravimetric analysis
DOS.....	Density of states
IoT	Internet of things
μ - TEGs	Micro thermoelectric generator
GIXRD	Grazing incident X-ray diffraction
NMR	Nuclear magnetic resonance
ppm	Parts per million
PXRD.....	Powder X-ray diffraction
THF	Tetrahydrofuran
WDX	Wavelength Dispersive X-ray Spectroscopy
sccm	Standard cubic centimetres per minute
HPa	Hectopascal
mmHg.....	Millimetres of mercury
IR	Infrared

Definitions and Abbreviations

J.....	Coupling constant
Hz.....	Hertz (s^{-1})
Bu.....	Butyl
Et.....	Ethyl
Bz.....	Benzyl
ZT.....	Unitless figure of merit
S.....	Seebeck coefficient
σ	Electrical conductivity
κ	Thermal conductivity
β	Thermoelectric quality factor
μ	Charge carrier mobility
n.....	Charge carrier concentration
L.....	Lorenz number
N_V	Band degeneracy
e.....	Elementary charge
τ	Charge carrier lifetime
K^*	Charge carrier pocket anisotropy
m_c^*	Effective mass for conductivity
m_s^*	Density of states effective mass
γ	Grüneisen parameter
E_g	Energy gap
E_F	Fermi level
R.....	Ideal gas constant ($8.3145 \text{ J mol}^{-1} \text{ K}^{-1}$)
p	Vapour pressure
α	The vapour coefficient
M.....	Molecular mass (kg mol^{-1})
Pa.....	Pascal ($\text{kg m}^{-1} \text{ s}^{-2}$)
T_{vap}	Boiling point (K)

ΔH_{vap} Enthalpy of vaporisation

ΔS_{vap} Entropy of vaporisation

Chapter 1 Introduction

The initial chapter sets out the background information that is essential to an understanding of the later chapters. It includes the basics of semiconductors, thermoelectric materials and thermoelectric modules, optimisation of thermoelectric materials, deposition methods, the reasoning behind the choice of group 14 and 15 chalcogenides, why single source precursors are used and an overview of the characterisation techniques employed.

Chapter 2 relates to the design, characterisation and vapour pressure approximation of the single source precursors used in this work. This contains a comparison with other precursors in the literature and the rationale behind any iterations made. A comparison of the vapour pressure is also made between the precursors and precursor mixtures. With an aim to explore the physical properties of the single source precursors used to deposit group 14 chalcogenide materials.

Chapter 3 sets out to explore the data relating to the CVD of tin (II) chalcogenides and their thermoelectric measurements. This includes the precursor synthesis and characterisation, thin film characterisation, discussion of their measured thermoelectric properties and the area selective deposition of SnTe. With the hope of determining the thermoelectric properties of the films produced, exploring the potential for control over the properties and potential for selective deposition.

Chapter 4 contains the data relating to the CVD of germanium (II) chalcogenides and their thermoelectric measurements. This includes the thin film characterisation and discussion of their measured thermoelectric properties. The aim of this chapter was to explore the family of single source precursors further and to determine if there were any factors of the deposition process that could lead to control over the thermoelectric properties of GeTe.

Chapter 5 is concerned with the extension of the single source precursor family to include the CVD of silicon chalcogenide materials. The chapter sets out to discuss the characterisation of the single source precursors used and the films produced along with measurements of many of the materials properties. This includes a description of the precursor synthesis and complications in the use of these precursors for the establishment of single source precursors for silicon chalcogenide materials.

Chapter 6 describes the use of a Picosun R-200 Advanced ALD reactor for an upscaled CVD process to explore its suitability to allow scale-up of the SnSe deposition onto full wafers. This chapter aims to discuss the characterisation of the films produced in this method and a discussion

Chapter 1

of optimisation potential afforded by this process. Also discussed is the deployment of mixed precursor systems using LPCVD to produce solid solutions.

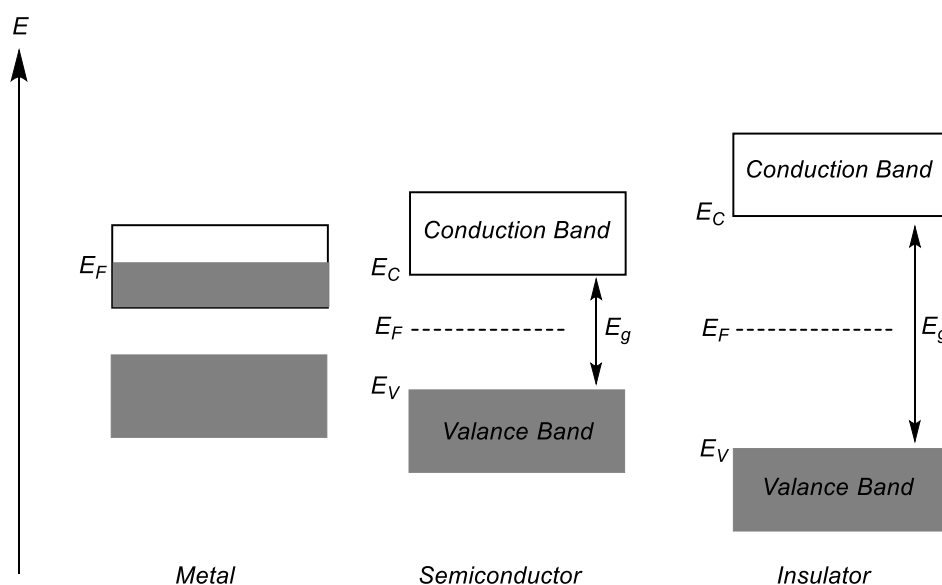
Chapter 7 is composed of the data relating to the development of single source precursors for the CVD of Sb_2E_3 and Bi_2E_3 , where E is S, Se or Te. With an aim of exploring a uniform series of precursors that would enable the easy investigation of ternary systems. This includes the precursor synthesis and characterisation, thin film characterisation and a comparison of the precursor family design used in these depositions.

Chapter 8 contains final conclusions, summary and the outlook of the field. This includes a review of the more novel and impactful achievements of this work.

1.1 Semiconducting materials

A typical semiconducting material has a small bandgap, the energy difference between their valence and conduction bands, of less than 4 eV.⁴ This absolute gap between the upper edge of the valence and lower edge of the conduction band is caused by forbidden energy levels within the bandgap. This is unlike the energy states in metals, which have no bandgap between their valence and conduction bands and an insulator which has a larger bandgap of around 10 eV. The conductivity of a semiconducting material increases with temperature as more charge carriers are promoted to energy levels where they can then be transported. Conversely, in a metal the electrical conductivity is reduced with temperature as the higher temperatures increase the occurrence of scattering incidences, both phonon-electron and electron-electron.

The filling of the energy states within a material is dictated by the Pauli Exclusion Principle, which follows that no two identical elementary particles with spin of $\frac{1}{2}$ can occupy the same quantum state within a quantum system simultaneously. This means that no two electrons can have identical values in their quantum numbers; the principle quantum number n , the azimuthal quantum number l , the magnetic quantum number m_l , and the spin quantum number m_s . Therefore, if two electrons occupy the same energy state then they must have opposing, $+\frac{1}{2}$ and $-\frac{1}{2}$, spins. This principle explains how the energy states within a material are populated by electrons. For an electron within a semiconducting material to become excited from the valence band into the conduction band, some specific minimum energy, equal to the bandgap, must be provided. The size of this bandgap, therefore, dictates the energy that will be absorbed by the material and thus the functionality of the material. For example, a light emitting diode (LED) emits photons with an energy equal to the bandgap of the semiconducting material they are comprised of. This can be visualised in the density of states (DOS) diagrams shown in Figure 1-1.



E_F - Fermi level
 E_C - Conduction band minimum
 E_V - Valance band maximum
 E_g - Bandgap

Figure 1-1- The DOS for a metal, semiconductor and an insulator.⁵ Here the grey shaded areas represent filled energy levels and the white represents unoccupied energy levels.

Semiconductors are either intrinsic or extrinsic. In an intrinsic semiconductor the number of holes, positive charge carriers, must always be equal to the number of excited electrons, negative charge carriers. Electrical conductivity within such materials is caused by defects or excited electrons and thus is highly temperature dependent. Extrinsic semiconductors are semiconductors which have a foreign element or chemical incorporated into the host system, known as a doping agent. This doping agent must be selected carefully so that it changes the electrical properties of the material. A doping agent that supplies filled energy levels above the Fermi level of the host material, and thus supplies negative charge carriers, form n-type semiconductors and doping agents that supply empty energy levels below the Fermi level of the host material, and thus provide sources for further holes within the system, form p-type semiconductors. The type signifies that the material, n or p, is either mostly comprised of negative charge carriers or positive charge carriers, respectively.

Chapter 1

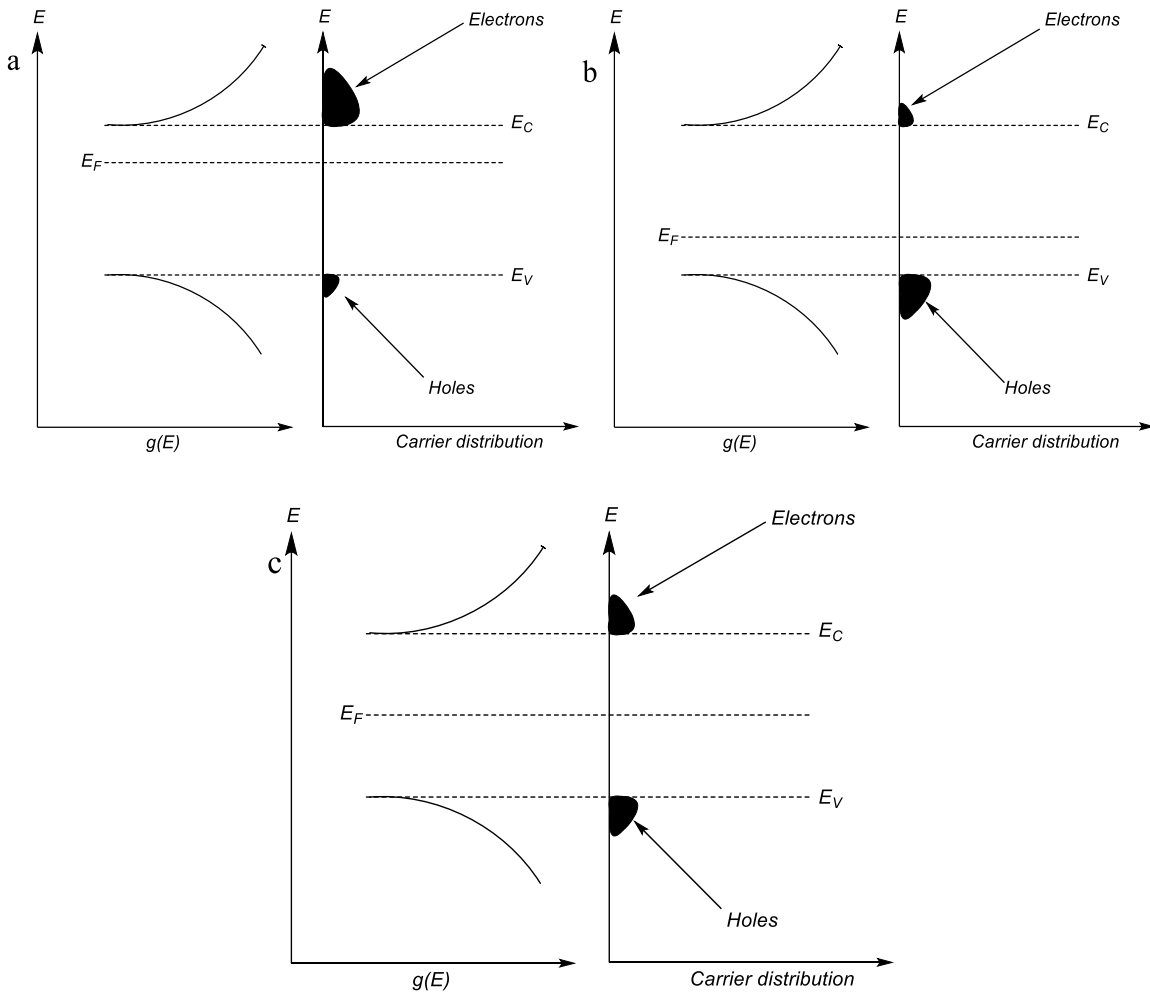


Figure 1-2- Relative energy of the DOS, $g(E)$, and the carrier distributions for (a) n, (b) p and (c) intrinsic semiconducting materials.

One way that this information can be summarised for a material is by using an electrical band diagram and a density of states (DOS) diagram. These diagrams are derived from a combination of theoretical calculations and experimental observations. The purpose of electrical band diagrams is to show the relative energy levels at a given wave vector, which are points of symmetry in k space, and the DOS displays the relative population of these energy levels. A number of physical properties can also be ascertained from an understanding of a material's detailed band structure. This includes, of course, the band gap of the material, along with information about carrier mobility and band degeneracy. These are all important properties for thermoelectric performance.

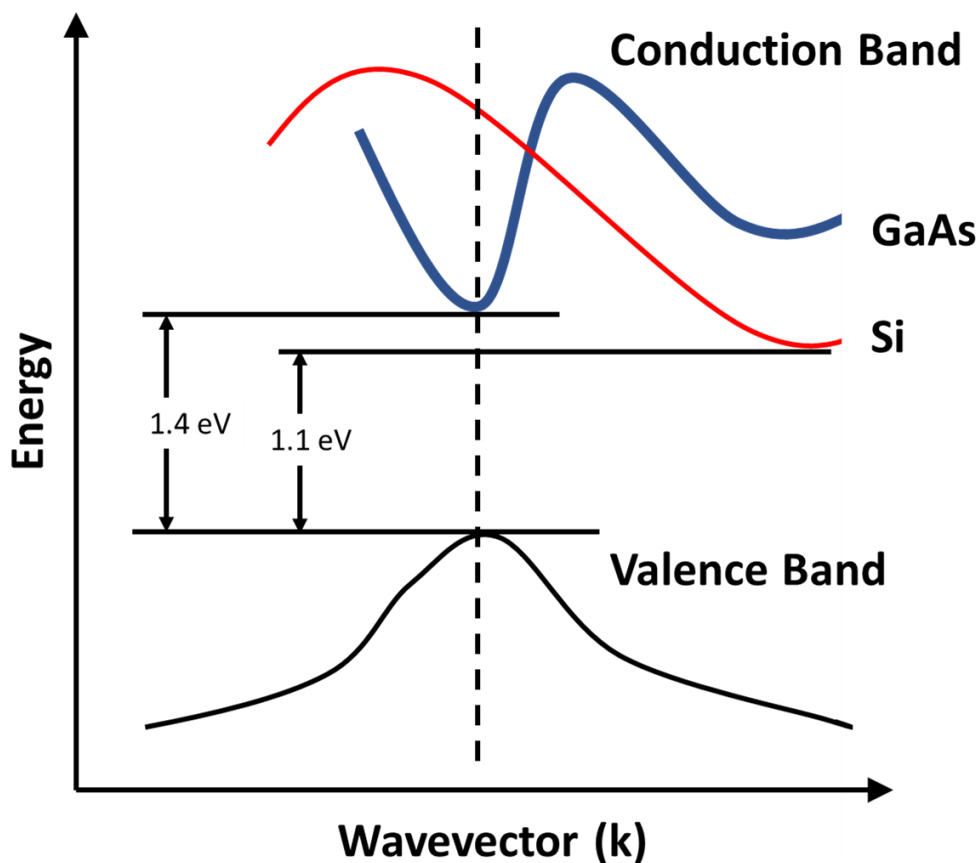


Figure 1-3- Electronic band structures of Si and GaAs showing an indirect and direct band gap, respectively.^{6,7}

Semiconducting materials can be divided into two classes. Those with direct band gaps and those with indirect band gaps, meaning the highest point on the valence band and the lowest point on the conduction band are at the same wave vector and thus above one another in the band structure diagram or, like silicon in Figure 1-3, offset by some amount in terms of wavevector. The Greek letters shown in the band diagrams indicate points of symmetry in the Brillouin zone. The Brillouin zone is a 3D representation centred in k space, which relates to the crystal structure of the material, but unlike the unit cell, which exists in real space, exists in reciprocal space (Figure 1-4). The surface of the Brillouin zone is known as the Fermi surface, its shape depends on the crystal structure of the material and the size depends on the lattice parameters.

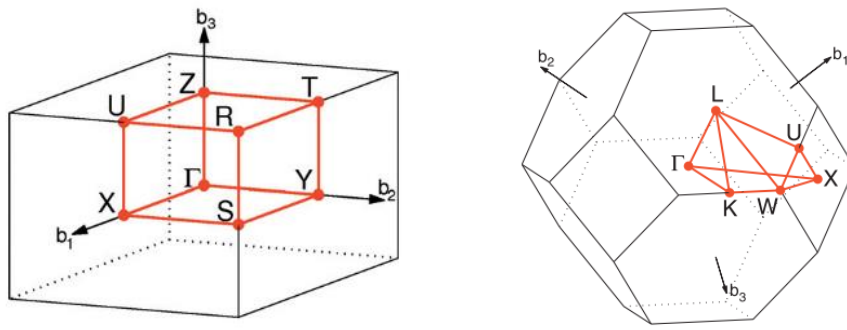


Figure 1-4- Brillouin zones for primitive orthorhombic and face centred cubic crystal structures, respectively.⁸ Reproduced with permission from Elsevier.

1.1.1 Semiconductor Junctions

Where two different semiconducting materials are connected, charge carriers are able to transfer between the two materials and an interface occurs. This interface is known as a heterojunction. One type of heterojunction is a p-n junction, as shown in Figure 1-5. These junctions restrict the flow of current, movement of electrons, to one direction meaning that a current can only flow from the n-type semiconducting material to the p-type semiconducting material. If the current is applied in the opposite direction then the electrons from the p-type material need a large amount of energy to be promoted for electrical conduction, thus the flow current is halted. This type of heterojunction is common as they are the foundation of important semiconductor electrical devices such as diodes and transistors.

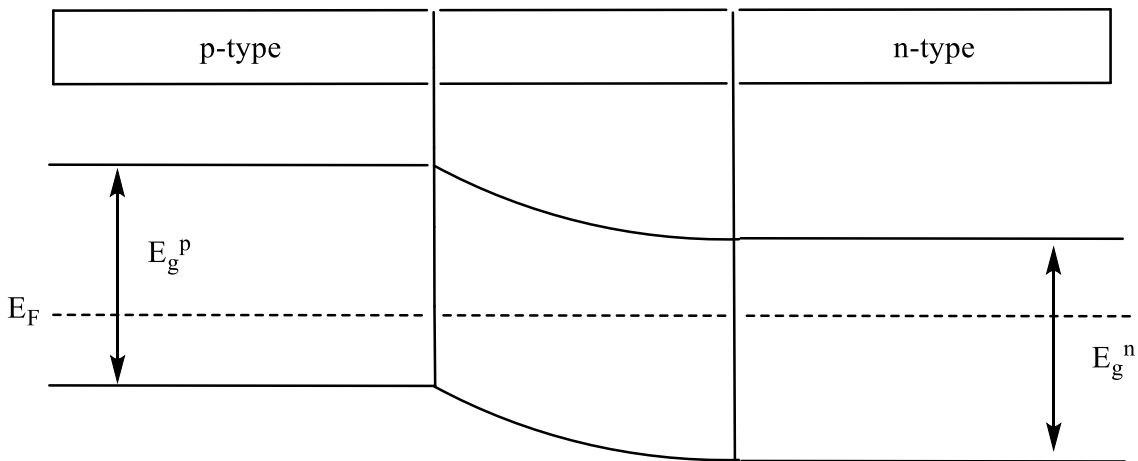


Figure 1-5- The energy band diagram for a p-n junction. Where E_F is the Fermi level, E_g^p is the energy gap of the p-type semiconductor and E_g^n is the energy gap of the n type material.⁶

When fabricating a device containing semiconducting materials, it is inevitable that it will contain semiconducting materials connected by some electrically conductive contact material, typically a

metal. For this reason, it is important to understand how this will affect the material properties. In the interface between the metal and semiconductor a heterojunction is formed, widely referred to as a Schottky junction, which consists of a region of varying free charge carrier concentration.⁹ Another consideration at these Schottky junctions is that some diffusion of the contact material into the semiconducting material and vice versa is possible.^{10,11} This will obviously affect the properties and can hinder efficiency. This effect can be mitigated by the application of a diffusion barrier, for example Ni, Mo or $\text{Cr}_{80}\text{Si}_{20}$.¹²

1.2 Introduction to Thermoelectric Materials

The conversion of thermal energy to electrical energy is known as the Seebeck effect, as discovered by J. T Seebeck in 1822, and the conversion of electrical energy to active cooling is known as the Peltier effect, discovered by J. C. A Peltier in 1834.¹³ In an n-type thermoelectric material, when a heat gradient is applied, negative charge carriers diffuse from the hot region towards the cold region, as in Figure 1-6. In a p-type material holes diffuse from the hot zone to the cold zone. Both scenarios result in a chemical potential being induced across the material from hot to cold and thus, when connected in series, this effect can be used to induce a current.

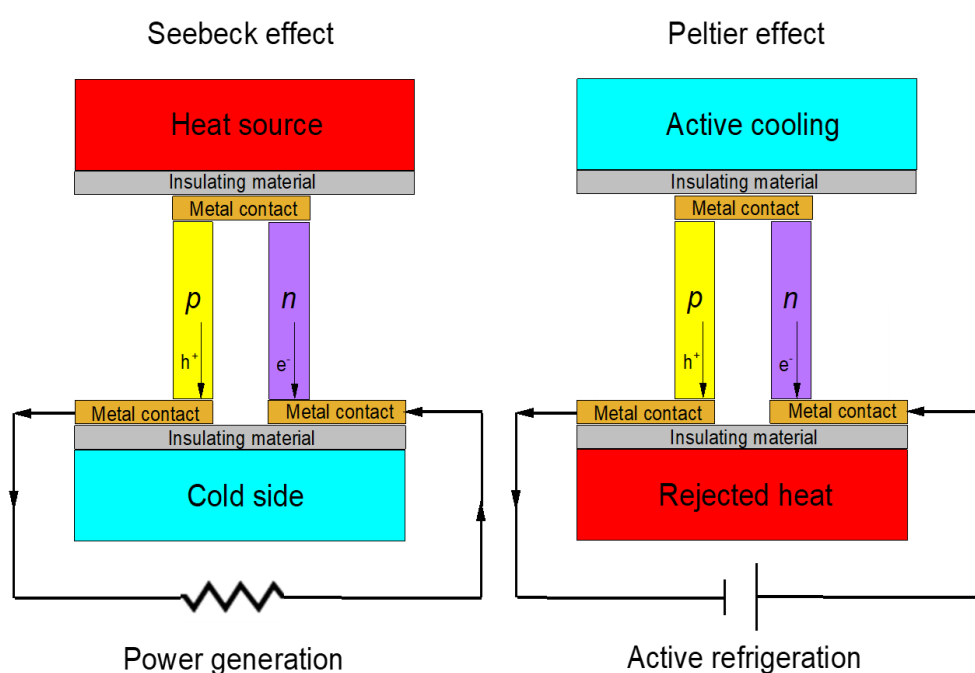


Figure 1-6- The Seebeck (power generation) and Peltier (active refrigeration) effects in a thermoelectric module.

The origin of the Seebeck effect is the higher population of excited states at the hot zone. These excited electrons can diffuse into the colder regions in n type materials or electrons from the cold zone are able to fill holes in the hot zone for p type materials. These two methods for electron

and hole transport across a material can, therefore, allow for the flow of current when an n and p type material are connected in series, as in Figure 1-7.

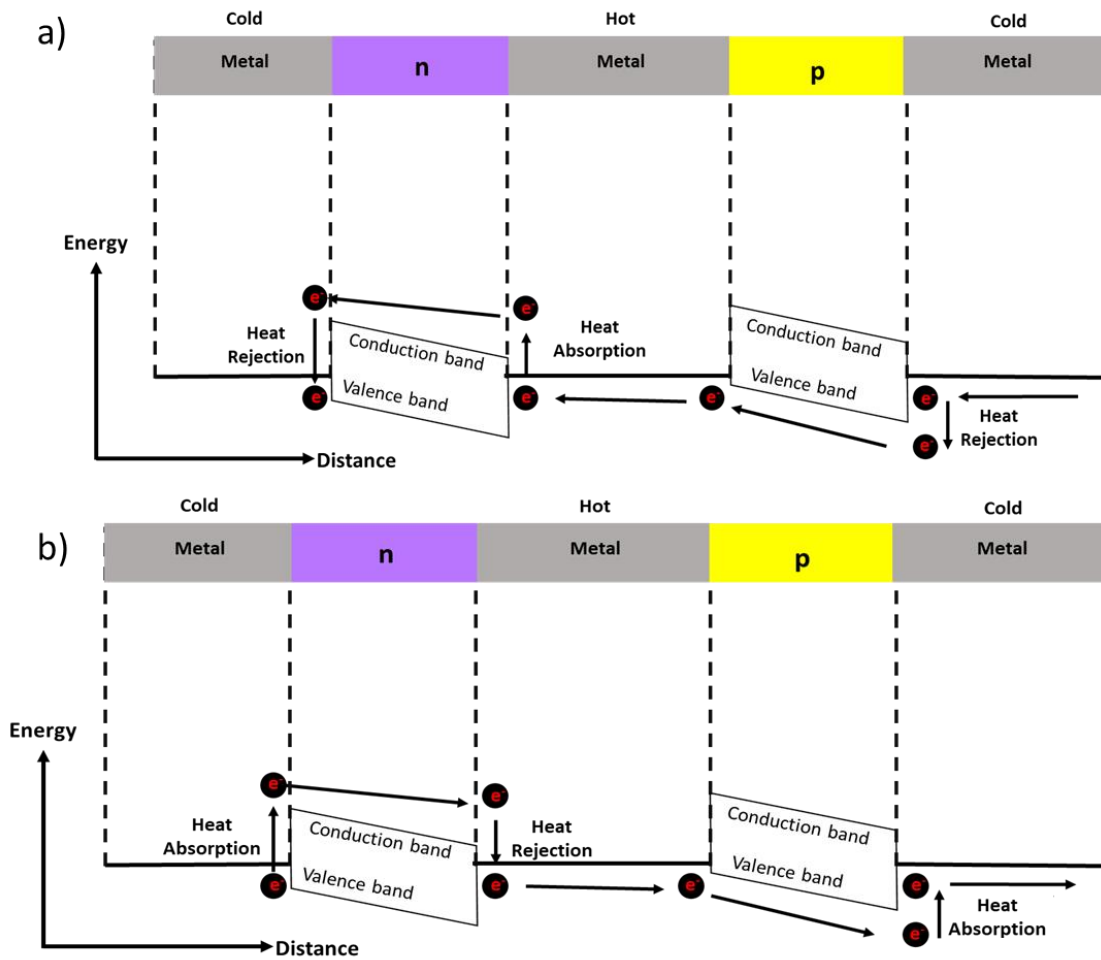


Figure 1-7- Energy band diagram showing the excitation and relaxation of electrons moving through a thermoelectric module containing both n and p type thermoelectric materials in a) the Seebeck effect and b) the Peltier effect.¹⁴

The coefficient describing the measure of charge carrier entropy in the solid state, the Seebeck coefficient, was first described by Kelvin in 1850.¹⁵ The equation that combines the fundamental parameters of a thermoelectric material together to give an easy comparison value is that of the unitless figure of merit. This equation was first established in 1911 by Altenkirch, as shown in equation (1). Although it gives no grasp over the ideal temperature range or versatility of a material, it is a good indicator of potentially high performing materials.¹⁶

$$ZT = \frac{S^2 \sigma T}{\kappa} \quad (1)$$

Where the ZT value is the unitless figure of merit, which combines thermal conductivity, κ , which describes the conduction of phonons through a material, electrical conductivity, σ , which

describes the conduction of charge carriers within a material and the Seebeck coefficient, S , which describes a materials ability to produce a potential difference in response to a temperature gradient. These are combined to give a number which relates to the usefulness of a material for thermoelectric applications. As described in the above equation, a good thermoelectric material has a combination of good electrical conductivity, low thermal conductivity and a high Seebeck coefficient.

1.2.1 Applications

Some of the first examples of thermoelectric devices were used in space projects for reliable power generation without the presence of moving mechanical parts. Notably, NASA utilised radioisotope thermoelectric generators in the Voyager space probes, which have been operating for over 43 years and have now left the solar system.¹⁷ Other applications of thermoelectric materials include not only energy generation in satellites for space projects,¹⁸ but active refrigeration systems using Peltier coolers and for the generation of electricity in sensors in predominantly industrial environments using thermoelectric generators.¹⁷ Although there is still much advancement required within the thermoelectric field, there are many promising applications which suit many of the properties either being developed or currently achievable for thermoelectric materials. One such prospect is the potential for integrating thermoelectric materials into windows generating electricity from the temperature difference inside and outside of a building.¹⁹ Also currently in the early stages of development is the incorporation of thermoelectric devices into computer systems for energy production and more efficient internal cooling.²⁰ Perhaps most exciting of all is the incorporation of thermoelectric devices into appliances for the internet of things (IoT) and into clothing for applications in wearable electronics,²¹ considered as one of the fundamental advancements of the fourth industrial revolution.²²

Thermoelectric devices are suited to the development of the IoT, which relies on an increase of appliances that contain sensors for a variety of stimuli. Applications of the IoT are very widespread, from temperature regulation of a building to medical monitoring systems to parking space sensors and beyond. All of these sensors require power to function. The reliability, lack of moving parts or noise produced from thermoelectric devices along with the constant heat source available, in the form of the person in possession of the device or other temperature gradients found in urban settings, means that these are promising tools for the IoT.²³ The use of thermoelectric devices for the IoT would undoubtedly require micro-thermoelectric devices as bulk systems would be expensive and cumbersome.

Chapter 1

Traditionally thermoelectric applications have been confined to low power applications where reliability outweighed power output in importance. As discussed by L. Bell, an average ZT of 1.5 or greater would be required for adequate efficiencies for a thermoelectric device to be competitive as a primary power generator.²⁴ However, the benefits of solid state energy conversion are substantial and so in some niche applications low efficiency thermoelectric devices can be more cost effective and preferential to other methods of power generation. With increased material performances, sustainability and reduction of material fabrication costs along with advances in the intelligent design of thermoelectric devices, their economic viability moves closer to being realised. The key benefit is likely to come in the reduction of cost, both in resources, due to the smaller quantities of expensive semiconducting materials, and in labour costs, due to the long lifetime of the generators afforded by their lack of moving parts. The need for low cost, renewable, reliable and specialised materials is one of the main challenges for technological advancement. As the world becomes more and more technologically driven, interconnectivity of conventionally separate fields will be the largest leap forwards of the 21st century. Thermoelectric technologies have the potential to play a large role in this development.

1.2.1.1 Temperature regimes and applications

Thermoelectric materials and their applications are separated into three categories based on the temperature regime they fit into. Firstly, low temperature or near room temperature applications, which consists of operation below 450 K. The main applications for this temperature profile consist of sensors for medical applications (pulse monitors for example), wearable electronics, microelectronics and micro-generators for sensors in homes or workplaces. The classical materials that operate within this window are Bi_2Te_3 and Sb_2Te_3 .^{25,26} However, new materials have shown some promising properties for low temperature applications, for example organic thermoelectric materials.^{27,28} Although these organic systems often generate low figures of merit, when combined with inorganic materials in composites or as layers the thermoelectric performance can be greatly enhanced.^{29,30} The next temperature regime is mid-temperature, it corresponds to those applications that operate between 450 K and 850K. These applications consist of energy harvesting from exhaust systems for gas turbines, combustion engines and steam boilers. The material which has been used most widely for this temperature range is PbTe .^{31–33} However, due to the comparatively high toxicity of lead, materials containing this element are becoming less attractive for applications and alternative materials are the focus of research. The final group of materials and their applications consists of those that operate at temperatures above 850 K, known as the high temperature regime. This regime is optimal for applications including heat scavenging from iron smelting, chemical processing and nuclear reactors³⁴ or from magma in volcanos or fractures in the Earth's crust.³⁵

Current state of the art thermoelectric materials can achieve ZT values of around 3,^{36–38} as achieved for Bi-doped n-type $\text{PbSe}_x\text{Te}_{1-x}/\text{PbTe}$ quantum-dot superlattice (QDSL),³⁹ and current power efficiencies achieved by thermoelectric generators are around 5%.⁴⁰ A comparison of a number of processes for energy generation are displayed in Figure 1-8, where a power efficiency of 5% can be seen to correlate with a ZT of around 0.5, thus the ZT values realised within devices are markedly lower. Therefore, the actual application of thermoelectric materials is likely to consist of more niche applications, where low currents are sufficient and the reliability and low manual labour costs are the primary concern. An example of an application that fits this description is a sensor in a difficult to access or dangerous location, such as in a setting that is radioactive, at high temperature or perhaps in space. The main sector currently for commercial use of thermoelectric materials is military and aerospace, however, the large emerging markets in low power generation for sensors for IoT will likely alter this landscape.⁴¹

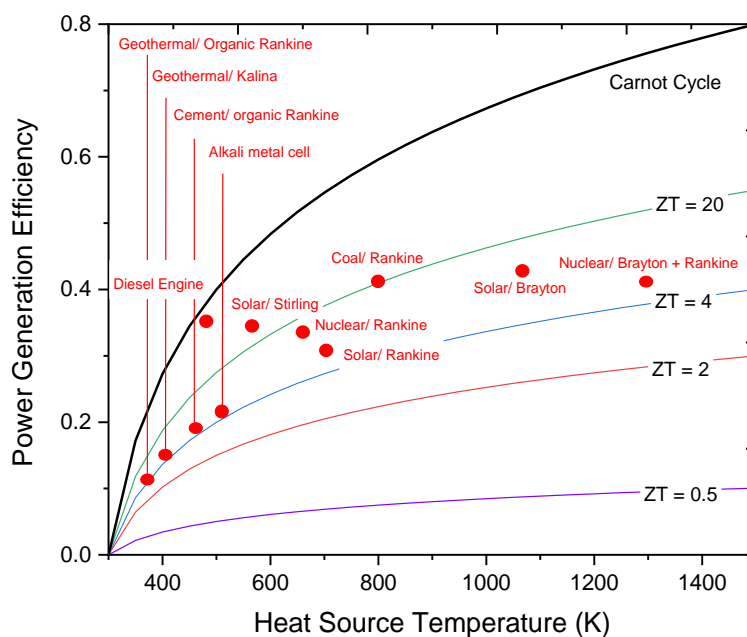


Figure 1-8- Graph showing the power efficiency of some different processes, the theoretical power efficiencies offered by some different values for ZT as well as the Carnot Cycle, which shows the theoretical maximum efficiency for a heat engine operating between two temperatures.^{37,42–44}

Initial measurements for the ZT of Bi_2Te_3 and PbTe were around 0.5. Since then, huge improvements have been made and considering the increase in interest and the huge advancements in the understanding of how to improve thermoelectric performances,³⁷ a ZT larger than 4 is not outside the realms of possibility in the near future. This means thermoelectric

materials will likely play a larger role in the future of power generation and efficient cooling systems.

1.2.2 Challenges

There are many challenges related to thermoelectric materials and thermoelectric energy harvesting in general. With respect to the materials, the main issues revolve around the interdependency of many of the parameters involved.

1.2.2.1 Electrical conductivity, σ , and thermal conductivity, κ

Electrical conductivity is related to the thermal conductivity through the Wiedemann-Franz law, which states that:

$$\kappa_e = L\sigma T$$

Where the electrical contribution to the thermal conductivity, κ_e , is equal to the product of the Lorenz number, L , the electrical conduction, σ , and the temperature of the measurement, T . This of course complicates the enhancement of thermoelectric materials as both a high electrical conductivity and a low thermal conductivity are required. As the total thermal conductivity is comprised of both an electrical and lattice part, the best way to decouple these two vital parameters is by reduction of the lattice thermal conductivity, κ_L . The relationships of some key thermoelectric parameters are displayed graphically in Figure 1-9.

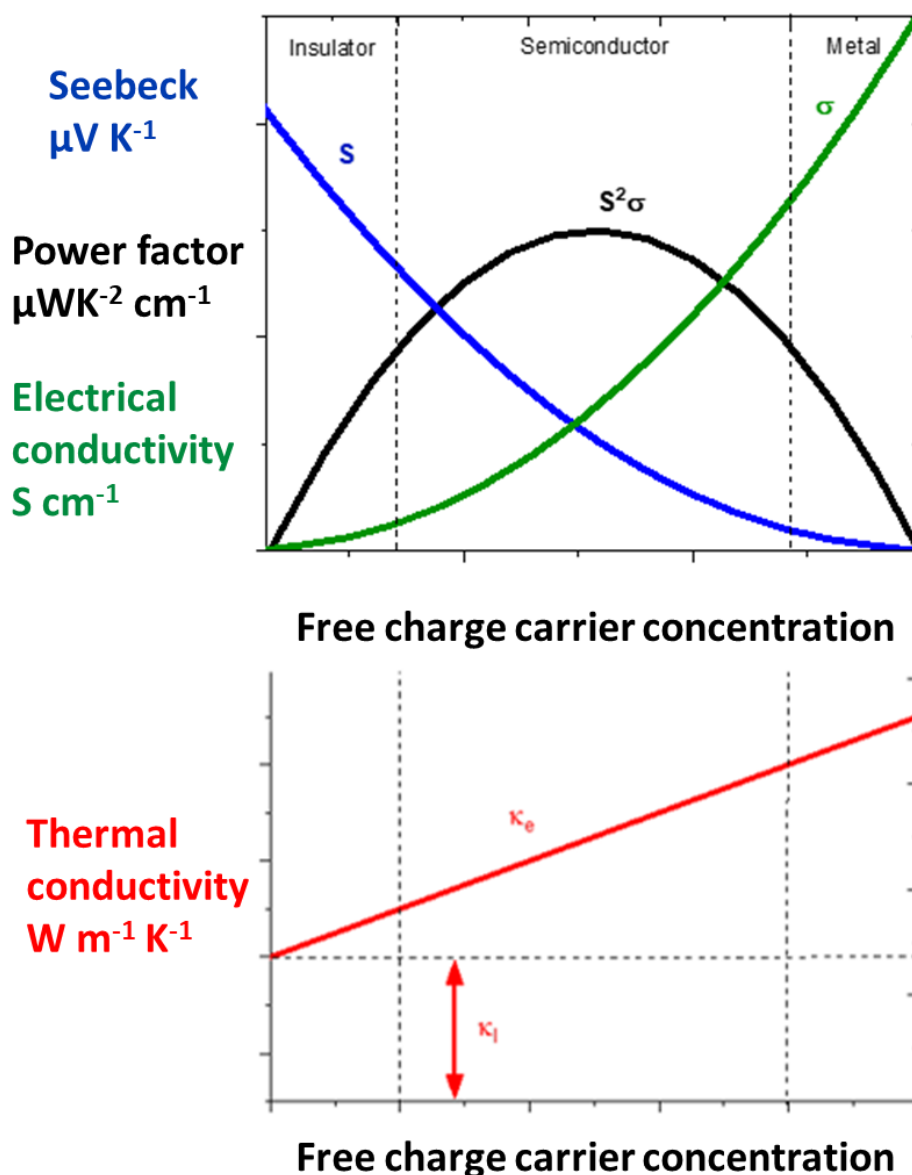


Figure 1-9- Change of the Seebeck coefficient (blue), electrical conductivity (green), power factor (black) and total thermal conductivity (red), both the electronic and lattice contributions indicated, relative to the free carrier concentration.⁴⁴

One method for overcoming the problematic relationship between the electrical and thermal conductivity is by utilising low dimensionality systems. This allows for a reduction in the thermal conductivity while not affecting the electrical conductivity and thus decoupling these factors. This and a discussion of other methods for optimization of thermoelectric properties is collated in section 1.4.

Furthermore, as it can be very challenging to measure the thermal conductivity of polycrystalline films and so it is convenient to give an assumed value of κ_L , based on those determined for the material in the literature, and calculated value for κ_e .⁴⁵ This can be performed using the Lorentz number, which is related to the electronic contribution to the thermal conductivity through the

Wiedemann-Franz Law, as discussed. Evaluation of the Lorenz number can be used to evaluate an approximation for the electronic contribution to the thermal conductivity, and therefore a ZT_{calc} value. The Lorenz number can be calculated using the Seebeck coefficient through the equation:

$$L = 1.5 + e^{-\frac{|S|}{116}}$$

This can then be used to give an approximate value for ZT , when a value for κ_L is assumed.

1.2.2.2 The Seebeck coefficient, S , the electrical conductivity, σ and the charge carrier concentration, n

Another important consideration when unpicking the entangled physical parameters of thermoelectric materials is the relationship between Seebeck coefficient, electrical conductivity and charge carrier concentration. The complication arises due to the opposing relationship of the Seebeck coefficient and the electrical conductivity with charge carrier concentration. The electrical conductivity is related to the charge carrier concentration through the equation:

$$\sigma = ne\mu = \frac{ne^2\tau}{m_C^*}$$

Where σ is electrical conductivity, n is the charge carrier concentration, e is the elementary charge, μ is charge carrier mobility, τ is the average time taken for charge carriers to be scattered and m_C^* is the inertial effective mass, sometimes called the band effective mass. Thus, it follows that a larger charge carrier concentration will result in a larger electrical conductivity. However, the relationship between charge carrier concentration and Seebeck coefficient causes further complications in the optimisation of thermoelectric properties, as highlighted in Mott's formula as described below:

$$S = \frac{8\pi^2 K_B^2}{3eh^2} m_S^* T \left(\frac{\pi}{3n} \right)^{\frac{2}{3}}$$

Where K_B is the Boltzmann constant, h is Planck's constant and m_S^* is the effective mass concerned with the Seebeck coefficient, sometimes referred to as the DOS effective mass.⁴⁶ Here the charge carrier concentration must be reduced in order to increase the Seebeck coefficient.

Therefore, a compromise must be found to optimise the charge carrier concentration for both the electrical conductivity and the Seebeck coefficient. Another parameter that emerges, upon inspection of Mott's formula and the Drude model equation for electrical conductivity, is that of effective mass, m_i^* , denoted as m_S^* and m_C^* in the above equations. These parameters are, however, not equivalent but are related through the equation below:

$$m_S^* = (N_V^* K^*)^{\frac{2}{3}} m_C^*$$

Where N_V^* is the effective valley degeneracy, K^* is the carrier pocket anisotropy and the product of N_V^*, K^* is referred to as the Fermi surface complexity factor.⁴⁷ Here, in principle, m_S^* can be increased by increasing the Fermi surface complexity factor while simultaneously decreasing m_C^* somewhat. This would allow for the increase of both the Seebeck coefficient and the electrical conductivity. The effective mass correlated with electrical conductivity, m_C^* , is a tensor value and is a good measure of the average inertial effective mass of a charge carrier within a system but it does not inform much about the density of electronic states in a system with multiple bands, in other words a system with a N_V^* value larger than 1.⁴⁷ To describe this the Density of States (DOS) must be investigated and the effective mass that describes its relation to the Seebeck coefficient is where m_S^* originates.^{47,48}

1.2.2.3 Deconvoluting thermoelectric parameters

One helpful way to declutter these parameters is to use a holistic approach. That is to consider the optimisation of the performance using the thermoelectric quality factor, β . The use of this value, β , condenses the parameters down to just the total valley degeneracy, N_V , the inertial effective mass, m_C^* and the lattice thermal conductivity, κ_L .^{47,49}

$$\beta \propto \frac{N_V}{m_C^* \cdot \kappa_L}$$

The electronic band structure provides information on more than just the energy gap between the valance and conduction bands. Information about the charge carrier mobility can be gained from inspection of the broadness or sharpness of the peaks of the valance and conduction maxima and minima as well as the band degeneracy, which is equal to the number of band extrema at the same energy near the Fermi level.⁴⁹ An important contributor to the Seebeck coefficient and the electrical conductivity is the DOS effective mass, m_S^* . This coefficient is a useful descriptor of the electronic band structure used to describe not only the DOS but also the electron transport.⁴⁷ This is why an understanding of the electronic structure is so critical to thermoelectric optimisation, although this is outside the scope of the present study.

1.2.3 Chemical properties and their relationship to thermoelectric properties

It is important to consider the relationship between chemical properties of a material and its thermoelectric properties to intelligently design and optimise thermoelectric materials. As a chemist some of the intuitive chemical properties that are the most attractive to consider are

bond strengths, energy gaps, bond ionicity and crystal structure. All of these chemical properties are correlated to the thermoelectric properties discussed so far as outlined below.

1.2.3.1 Bond Strength

The strength associated to the bonds between atoms within a thermoelectric material has been shown to correlate strongly with the mean free path otherwise referred to as the mean speed of sound, l . This means that the average distance travelled by a phonon or other moving particle will be larger in a material with stronger bonds. Since l is proportional to the lattice contribution of the thermal conductivity, the strength of the bonds within the material can be shown to be a good indicator of the thermal conductivity of the material, as shown in the Figure 1-10.⁴⁹

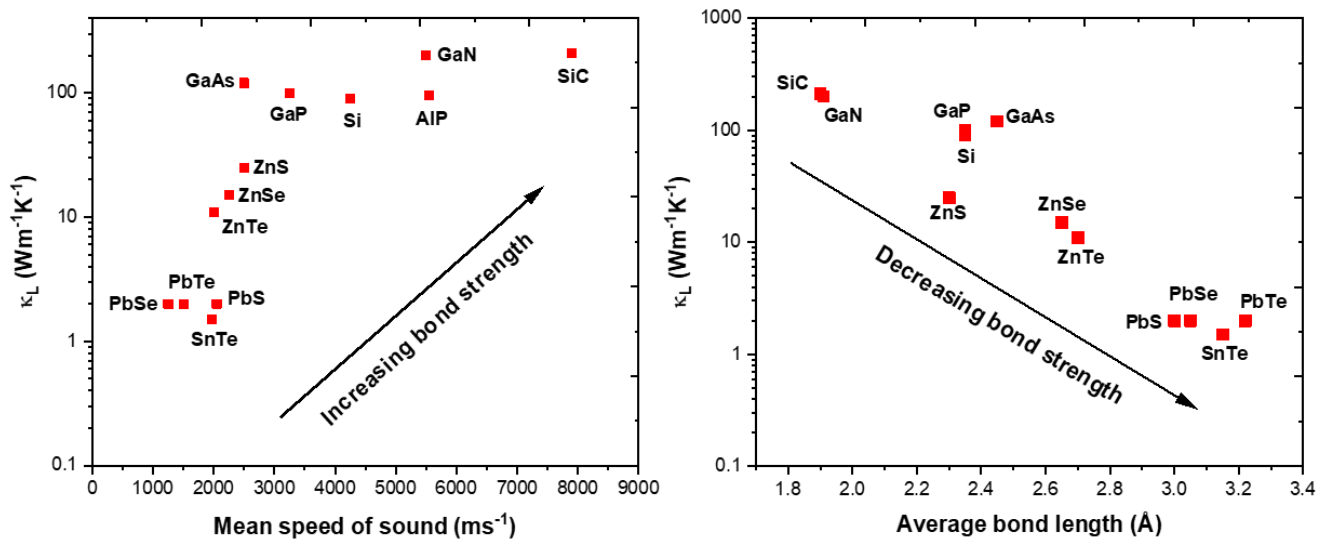


Figure 1-10- The relationship between lattice thermal conductivity and bond strength by consideration of the lattice thermal conductivity versus a) the mean speed of sound and b) the average bond length.^{49,50,59–62,51–58}

Higher coordination numbers in a crystal system also correlate to a decreased thermal conductivity, as observed by Ioffe *et al.*^{49,63} Usually a higher coordination number is also accompanied by a larger bond length. Typically, more weakly bonded ionic structures also contain higher coordination numbers and lower thermal conductivity. Thus, to reduce the thermal conductivity the best place to start is with weakly bonded materials with high coordination numbers.

1.2.3.2 Energy gap

Although not shown in the equation for the thermoelectric quality factor or the equation for ZT, the energy gap, E_g , holds great importance for thermoelectric performance. The energy gap shown in the band structure defines the temperatures at which the thermoelectric material can

operate, as it determines the energy required to excite electrons. This is important because a larger band gap will reduce the promotion of minor charge carriers of an opposing sign which counteract the majority carriers, reducing the thermopower. The promotion of minor charge carriers also increases bipolar conduction which increases the thermal conductivity thus reducing the ZT value of the material further.⁶⁴ Bipolar conduction is particularly a problem for narrow band semiconducting materials, as the narrow band allows for thermal excitation of minority charge carriers allowing for the conduction of both electrons and holes simultaneously. This reduces the Seebeck coefficient as there are both positive and negative contributions and the recombination of the holes and electrons produces heat and thus increases the thermal conductivity.⁴² The band gap, E_g , has also been shown to have a strong relationship to the peak Seebeck coefficient.^{65,66} This connection arises as the larger the band gap is, the easier it is for a material to maintain a potential across it due to less movement of minor charge carriers. Therefore, to improve the Seebeck coefficient and to enable further working temperature ranges a large energy gap is beneficial.

1.2.3.3 Bonding ionicity and effective mass

The difference in electronegativity between elements within a material, or its ionicity, have a direct influence on the inertial effective mass, m_C^* , of the system. This effect is caused by increasing electronegativity leading to more electron charge transfer.⁴⁹ In a binary material with high ionicity the valence bands are dominated by the electronic states of the more anionic species within the system. Thus, substituting the negatively charged element for one that forms a more covalent bond with the positively charged elements will affect the band effective mass of the material, m_C^* . This means that the m_C^* can be altered by means of incorporating other elements into the material, for example using solid solutions.⁴⁹ Incorporating more covalent anions has been shown to cause better overlap in the valence band, higher mobility and altered band gaps for $\text{PbSe}_{1-x}\text{S}_x$, $(\text{PbTe})_{1-x-y}(\text{PbSe})_x(\text{PbS})_y$ and $\text{Cu}_2\text{ZnGeSe}_{4-x}\text{S}_x$.⁶⁷⁻⁶⁹ However, even small quantities of dopants can have profound effects on the m_C^* of the material, as observed by Wang *et al.* for doped PbSe.⁷⁰

1.2.3.4 Anharmonicity

One feature that can drastically reduce the lattice thermal conductivity of a material is the anharmonicity of its lattice vibrations. The measure of this anharmonicity is given by the Grüneisen parameter, γ , which is a measure of an atoms ability to vibrate harmonically around its position. It is precisely this feature of SnSe which leads to its very low lattice thermal conductivity.^{38,71}

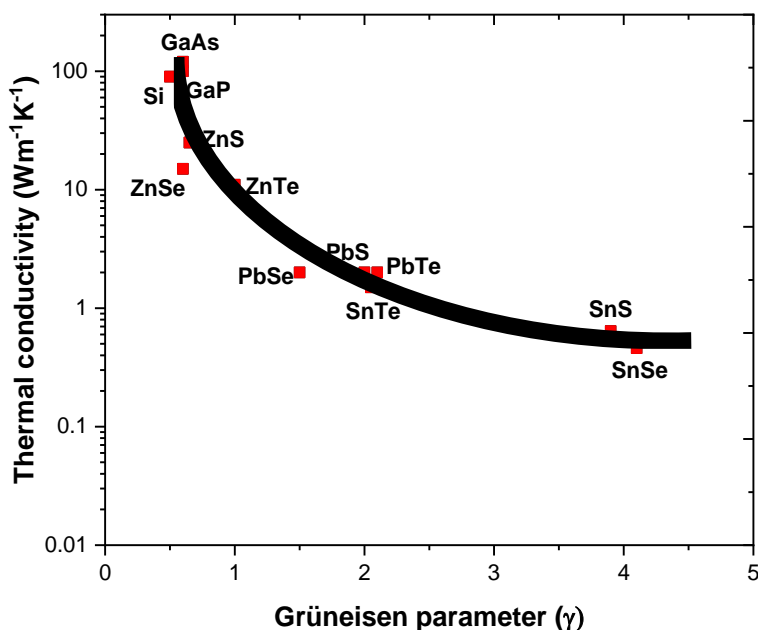


Figure 1-11- The influence of the Grüneisen parameter, and therefore anharmonicity, on the lattice thermal conductivity, κ_L . The correlation shown is drawn between compounds with zincblende (T_d) and rock salt (O_h) structure^{49,50,59–62,72,51–58} as well as values of single crystal layered orthorhombic (D_{2h}) SnS and SnSe.^{38,73–76} The black line is to guide the eye.

1.2.3.5 Lone pair effect

Inspection of the group 14 metal monochalcogenide materials, where the chalcogens are S, Se and Te, shows that there is a transition from an s^2 pair on the metal atom involved either being quenched, and thus having no impact on the structure of the material, or expressed, and thus having an important role in the structure of the material. This can be observed when considering the change in crystal structure from orthorhombic SnSe to cubic SnTe, orthorhombic GeSe to rhombohedral GeTe and rhombohedral GeTe to cubic SnTe. In the first two of these examples we see the heavier chalcogen is more likely to quench the s^2 pair on the metal and thus the overall symmetry is increased. This feature is reflected in the different structure of SnTe compared to that of SnSe and SnS. The cubic structure adopted by SnTe is consistent with an inactive lone pair on the tin centre, which is in contrast to the distorted SnE_7 polyhedra seen in SnSe and SnS, caused by the lone pair on the Sn^{2+} cation.⁷⁷ The change in crystal structure in GeTe versus SnTe emerges from the higher stability of the lone pair on tin meaning that the electrons in SnTe are less available for bonding than in GeTe. Semiconducting materials that contain these elements therefore have profound effects on their stereochemistry and electrical band structure. The expression of the lone pair on the metal means that the orbital containing the electrons is

stabilised in energy meaning that the energy gap is enlarged.⁴⁹ This is a contributing factor in the difference in energy gap moving from 0.829 eV for SnSe and 0.19 eV for SnTe.^{78–80} Therefore, the selection of a material with a larger Grüneisen parameter, caused by distortion in structure from an expressed s^2 lone pair, would likely lead to a smaller lattice thermal conductivity and a larger bandgap and, thus, a larger Seebeck coefficient.

1.2.4 Thermoelectric Materials

There are a large number of materials which exhibit promising thermoelectric properties. These are all semiconductors and have much higher electrical conductivity than their thermal conductivity. They can be separated into a number of groups, namely, inorganic clathrates, perovskites, skutterudites, half-Heusler intermetallic compounds, metal oxides,⁸¹ silicides,⁸² electrically conducting organic materials,⁸³ alloys^{84,85} and metal chalcogenides.^{38,76,79,86–89}

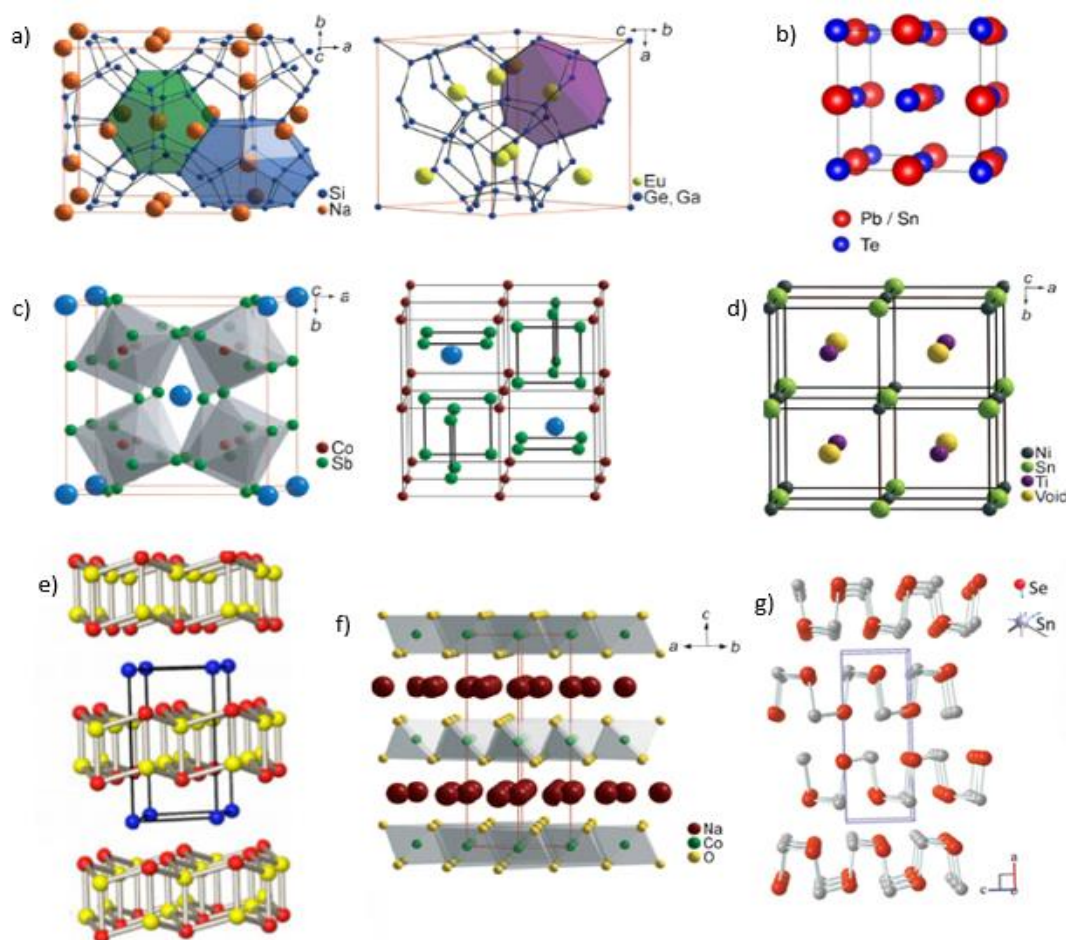


Figure 1-12- Crystal structures of some different thermoelectric materials from different material classes. a) Inorganic clathrates e.g. $\text{Eu}_8\text{Ga}_{16}\text{Ge}_{30}$ ⁸¹ b) metal chalcogenide materials Pb/ SnTe⁹⁰ c) skutterudites e.g. CoSb_3 ⁸¹ d) half-Heusler intermetallic compounds e.g. TiNiSn ⁸¹ e) silicides e.g. SrAl_2Si_2 ⁸² f) metal oxides e.g. NaCo_2O_4 ⁸¹ and g) SnSe .^{1,38}

Chapter 1

One common feature of many of these classes of thermoelectric materials is systematic voids within the crystal structures, Figure 1-12. These voids are either in the form of large Van der Waals interactions seen in the layered orthorhombic metal chalcogenides or systematic ion containing voids in the inorganic clathrates, perovskites, skutterudites and half-Heusler intermetallic compounds. These voids decrease the thermal conductivity of the materials by allowing for more anharmonic vibrations, increasing the Grüneisen parameter and lowering the lattice thermal conductivity.

Metal chalcogenides are an important group of semiconducting materials. The applications of which span a vast array of different technological realms, for instance sensor and memory systems as well as thermoelectric. With respect to the group 14 metal chalcogenides the materials adopt several compositions, ME , M_2E_3 and ME_2 , depending on the formal oxidation state of the metal. The different compositions have vastly different properties and thus, selection of the correct composition for the desired function is important. For example, the electrical conductivity of $SnSe$ and $SnSe_2$ differ greatly and while single crystal $SnSe$ has a reported high ZT of around 2.6, whereas $SnSe_2$ has a reported ZT of around 0.2.^{38,91} This is not to say that there is no scope for $SnSe_2$ as a thermoelectric material, but that $SnSe$ has the larger intrinsic ZT and thus is the more attractive starting material for thermoelectric applications. The materials selected for discussion in the following chapters were chosen based upon values reported within the literature for their thermoelectric performance and the similar chemistry required for their precursor synthesis. With respect to the tin and germanium materials explored, SnE and GeE ($E = S, Se$ and Te), this phase has been selected rather than the other phases due to the interest surrounding the monochalcogenides, $SnSe$ and $GeTe$, in particular. This interest has been sparked by the large ZT value reported for $SnSe$ and the large number of high performing materials based around $GeTe$.^{38,71,92–96} Although other phases of tin and germanium chalcogenide are of interest for various applications, the focus of this thesis was to explore the thermoelectric performances of the materials and so these other phases were not investigated. The lighter, lead free, group 14 chalcogenides contain several state of the art, low toxicity,^{95,97–100} alternatives to the currently adopted material for thermoelectric applications.^{101,102}

1.3 Optimisation of thermoelectric properties

Once the material has been selected, as outlined in the section: **1.2.3**, there are further techniques which can be implemented to enhance the thermoelectric performance.^{81,103–107} Optimisation usually focuses on either the alteration of the electrical band structure of the material, improving the electrical conductivity, or on the maximisation of phonon scattering effects by providing scattering sites at the atomic, nano, micro or mesoscale in order to reduce

thermal conductivity. Ideally these techniques can be used in tandem to simultaneously improve different thermoelectric, thermal and electronic parameters.

1.3.1 Doping

Firstly, the materials can be doped to improve charge carrier concentration and mobility, therefore improving the materials electrical conductivity while simultaneously creating point defects in the material which cause phonon scattering, reducing the thermal conductivity. Secondly, the materials can also be optimised further by careful consideration and engineering of the band structure. This can be achieved by measuring the energies of the conduction and valence bands of the material and tuning them to make them more favourable for thermoelectric applications. This tuning of the band structure, or band structure engineering, can be performed by alloying one material with another different material to change the electronic structure, by introducing impurities with energy levels that resonate with the host material, known as resonant doping, or a combination of these two approaches.¹⁰⁷ This approach of resonant doping has been shown to dramatically improve thermoelectric performance in indium doped SnTe, for example, where this doping occurs with an increase in band valley degeneracy greatly improving the thermoelectric properties.¹⁰⁸ It is also important to note that the large Seebeck coefficient observed for tin selenide is maintained with the activation of multiple valence bands. Thus, the manipulation of a material's band structure to increase the mobility and band valency is a powerful tool in thermoelectric optimisation.

1.3.2 Nanostructuring

Another method for the improvement of a thermoelectric material is nanostructuring. Here by reducing one or more of the dimensions of the material, typically to a few nanometres or less, quantum confinement effects lead to an increase in phonon scattering events reducing the lattice thermal conductivity without affecting the electrical transport properties of the material, thus improving the ZT value. This has also been shown to improve the Seebeck coefficient of the material as low energy charge carriers are filtered meaning a larger potential difference can be maintained and thus a larger Seebeck coefficient is observed.¹⁰⁹ Another strategy for nanostructuring is to incorporate nanostructures into the parent bulk material. This creates grain boundaries which cause phonon-scattering events, thus, reducing the lattice thermal conductivity. The best way to improve the thermoelectric properties of a material by adapting its architecture is to consider an array of different techniques considering the material at an atomic level, with point defects, at the nano-scale, for example with the inclusion of nano-precipitates, on the sub-micron

scale using structural modulations and then between the micro and macro-scale with mesostructures, as described in Figure 1-13.^{86,103,105,110}

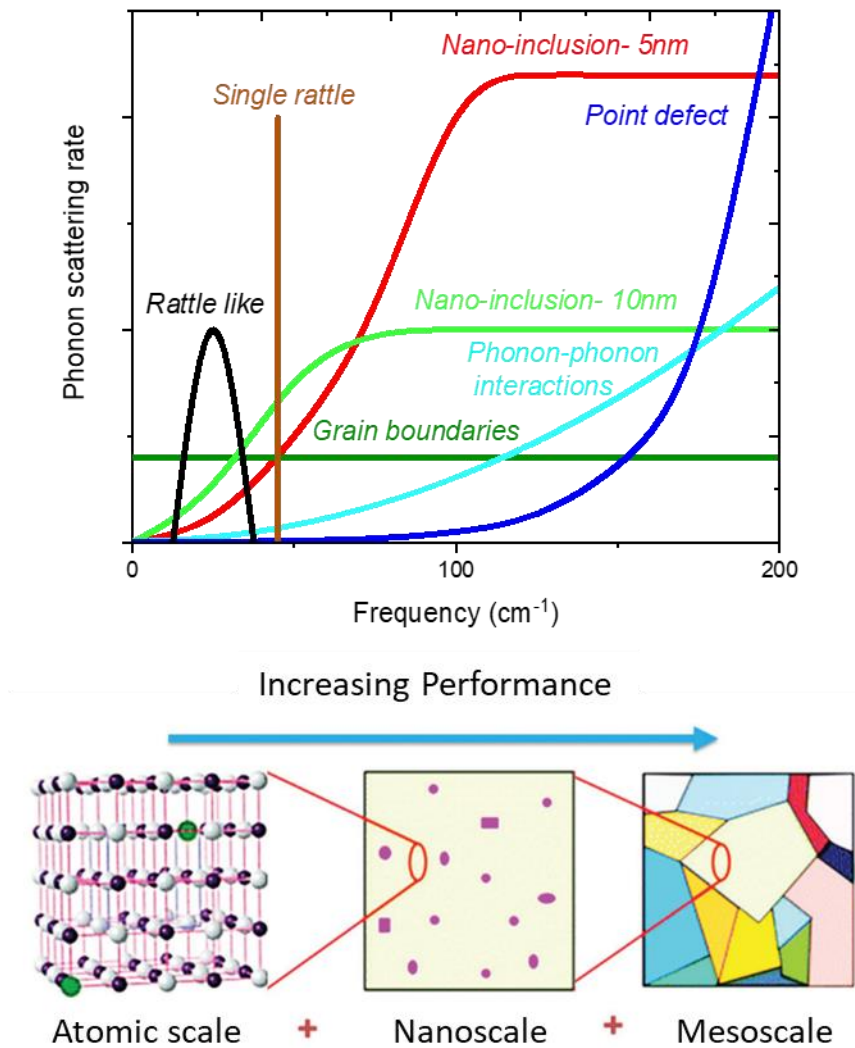


Figure 1-13- Phonon scattering rate versus phonon frequency highlighting the degree to which different scattering mechanisms reduce phonon transport and the frequency of the phonons that they interact with represented graphically. Diagram of some phonon scattering structures included for a multiscale optimised material.^{111,112}

1.3.3 Superlattices

Another method of improving the thermoelectric performance through the adaptation of a material’s architecture is to incorporate other materials in alternating layers referred to as a superlattice.^{113–115} This can affect both the electronic structure as well as introduce an interface which acts as a site for phonon scattering, which lower the thermal conductivity of the system.¹¹⁶ A good example of this technique is in p-type Bi₂Te₃/Sb₂Te₃ superlattices.¹¹⁵

1.3.4 Solid solutions

In solid solutions a minor component is evenly distributed throughout the major material crystal structure. The distinction between a solid solution and a doped material is in the concentration of the minor element or material involved. These material systems both affect the electronic structure of the host material, as previously mentioned, and will also cause a reduction in the thermal conductivity of the system. The reduction in the thermal conductivity occurs due to the different masses of the atoms substituted scattering short-wavelength phonons.¹¹⁷ A good example of this being utilised to improve a materials thermoelectric properties is in $\text{Ge}_{0.9}\text{Sb}_{0.1}\text{Te}_{0.9}\text{Se}_{0.05}\text{S}_{0.05}$, for which a remarkable ZT of 2.1 at 630 K has been reported.⁹⁴ This introduction of a second material throughout the host material can have a large impact on the electronic structure of the material if the minor material added has resonant energy levels, as in indium doped GeTe, or can be a non-resonant dopant and primarily reduce the lattice thermal conductivity through point defect scattering sites, for example in sodium doped PbTe.^{118,119}

1.3.5 Crystal structure modification

Another method for the enhancement of thermoelectric properties is by crystal structure modification. As discussed in Section 1.2.3.4, the Grüneisen parameter has a strong connection with the lattice contribution to the thermal conductivity. More anharmonicity means a larger Grüneisen parameter and thus lower lattice thermal conductivity. Alternatively, in some cases it may be beneficial to increase the crystal symmetry to increase the carrier mobility. This has been reported to be very beneficial for tellurium doped tin selenide. In this case, increasing the crystal symmetry results in the bond lengths becoming more roughly equal in length which increases the carrier mobility. There is also no increase in the thermal conductivity due to the extra phonon scattering caused by the tellurium and the increased displacement of tin within the structure.¹²⁰

1.4 Thermoelectric devices

Another consideration is the pairing of the n and p-type materials within a thermoelectric device. By, for example, considering the temperature range of the application and the material's compatibility. Alternatively to considering just the ZT values, a more useful equation concerning the energy output of a device simply considers the heat energy put in versus the electrical energy produced to give the overall efficiency, as in equation (2).¹²¹

$$\eta = \frac{\text{Net Power Out}}{\text{Heat Input}} \quad (2)$$

As well as careful consideration of how to optimise the thermoelectric materials themselves, the design of the device can also be altered to improve its efficiency. One way this is achieved is by using a large number of thermoelectric legs in series (Figure 1-14). For most applications the most important thing to consider is the actual power output of the thermoelectric device, and since this is directly proportional to the number of legs, and maximising the number of thermoelectric legs present in the device is a great way to achieve this.¹⁷ However, there is of course a limitation to this, in the form of the resistance added by the conducting material connecting the semiconducting materials together.

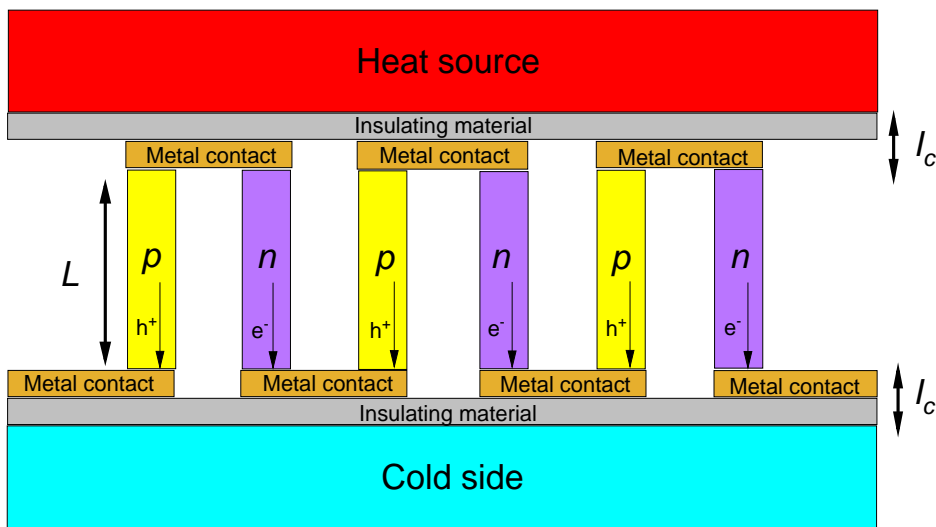


Figure 1-14- A schematic diagram showing n-type and p-type legs in a thermoelectric module indicating leg length L and contact length l_c .

As discussed in section 1.2.1, the applications compatible with thermoelectric devices are those which require small but reliable power outputs. Bulk scale thermoelectric generators typically involve powder processing and sintering to produce ingots or pellets which can then be further processed for the fabrication of individual n and p-type legs. The processes used for the manufacturing of the thermoelectric legs typically require subtractive techniques such as sawing and grinding which wastes semiconducting material.¹²² To reduce the amount of material required, and improve the performance of the device by increasing phonon scattering effects, micro-thermoelectric generators (μ -TEGs) are an exciting and relatively new approach.^{123,124} The use of μ -TEGs reduces the amount of thermoelectric material required for the device, therefore vastly reducing the production costs. The fabrication of these μ -TEGs containing a large number of n and p-type legs can in some cases be complex, due to the difficulties in resolution. In some cases it is possible to etch an original layer of a p-type thermoelectric material leaving the pattern required and produce a separate n-type material into a corresponding pattern so that the two can be bonded together and be connected electrically in series.^{123,125} In other cases this is impractical and other approaches are required for the fabrication, such as selective deposition. Using

selective deposition of a material onto a substrate that has previously been patterned with the desired design is achievable for some materials using chemical vapour deposition (CVD) and may present a more efficient processing method for micro thermoelectric generator fabrication. These patterned substrates are produced using photolithography as indicated in Figure 1-15.

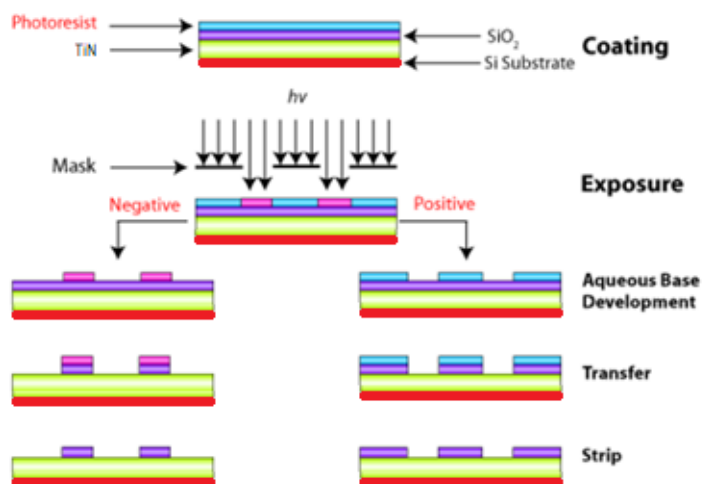


Figure 1-15- Illustration of the type of photolithographically patterned SiO_2/TiN substrates which have been used to demonstrate selective deposition.^{125–128}

The limit to how small the wells or other features, known as the critical dimension, is related to the wavelength of the light source used and inversely proportional to the size of the numerical aperture.¹²⁹ Selective deposition can only be performed when the precursor for this process has a preference to deposit onto one substrate material more than another substrate material, for example deposition into TiN wells etched into a silica coated substrate (Figure 1-16).^{127,130} This has been demonstrated in dual source CVD^{131,132} and also using single source CVD,^{125–127} which is a strong motivating factor for the exploration of single source precursors in this work.

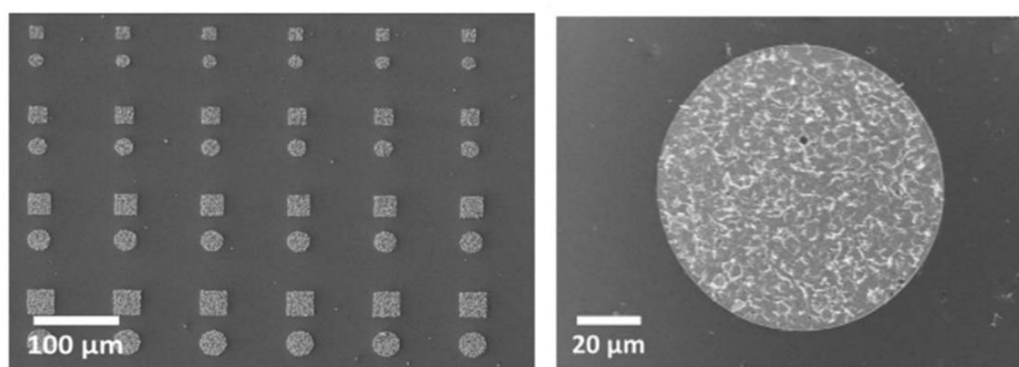


Figure 1-16: SEM images showing a section of a patterned SiO_2 substrate with differently sized TiN wells (circles and squares) and a higher magnification image showing deposition of Bi_2Te_3 inside a well and not outside of the well.¹²⁷ Reproduced from Ref. 127.

Chapter 1

The fabrication of thermoelectric generators has been demonstrated using several fabrication techniques. These consist of: ink processed printing,^{133,134} ALD,¹³⁵ selective deposition,¹³⁶ screen printing¹³⁷ or pulsed laser deposition,¹³⁸ thermal evaporation¹³⁹ and electrochemical deposition¹⁴⁰ using back etching, the use of a shadow mask or lithography.¹⁴¹ Of these methods, the non-destructive techniques are favourable as they do not waste semiconducting material, which is often made of expensive and rare elements. Thus, printed devices, ALD fabricated devices and selectively deposited CVD based devices hold the most promise for wider application. Of these the technique with the least demands, in terms of both equipment sophistication and precursor specifications, is those selectively deposited by CVD. These are of high quality and, due to the single source precursor design, have no unintended impurities.

1.5 Thin film deposition techniques

Thin films can be produced using a number of different deposition techniques. These techniques differ greatly in the delivery of material to a substrate. Some techniques, like: physical vapour deposition (PVD), molecular beam epitaxy and sputtering, evaporate or eject atoms from the pure elements and transport them to a substrate using either gas flow, pressure differences, convection or electrostatic interactions in low vacuum. Other methods require precursors, either individual species containing all the elements required (single source precursors) or multiple precursors each containing one of the required elements, that can be delivered to the substrate in either the gas phase (CVD), direct liquid injection, solvated and nebulised to be delivered as a mist (AACVD), solvated and printed, solvated and coated by electrolysis (electrodeposition).

Each deposition method has its own unique set of requirements, benefits and drawbacks. These can be specific precursor requirements, high energy demands or the requirement for highly specialised equipment. The deposition techniques focused on in this work are low pressure CVD and the commercial scale CVD technique described below in section **1.5.1**.

1.5.1 Atomic layer deposition vs chemical vapour deposition

The primary deposition method that this work is concerned with is low pressure CVD (LPCVD). This technique requires the precursor to evaporate at low pressure and moderate temperature so that it can be transported to a position above or on the substrate, where deposition can then take place. This can be visualised in Figure 1-17 which shows the reaction process in CVD and ALD type systems.

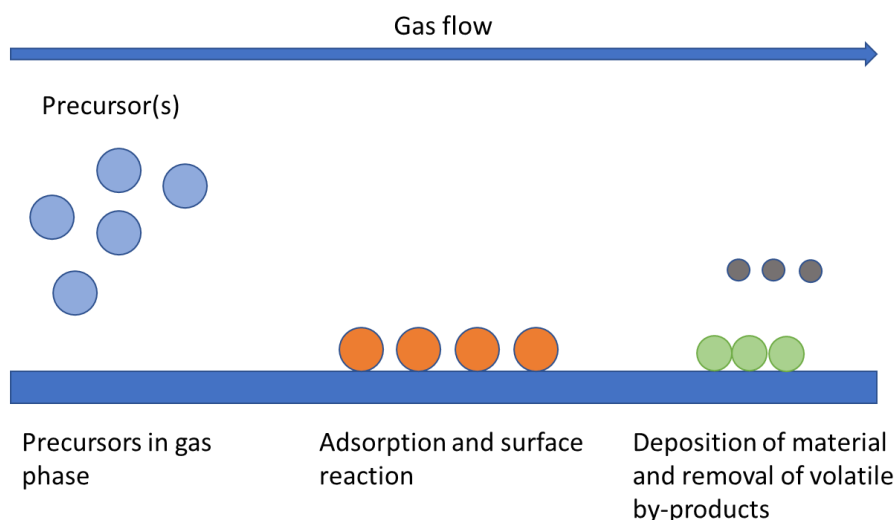


Figure 1-17: Precursor adsorption and surface reaction in the CVD or ALD of thin film materials producing volatile by-products that are removed using an exhaust system.

The broad range of temperatures along the CVD tube and viable precursor volatilities, in a LPCVD experiment, allow for the upper and lower range of deposition temperature to be explored in a single experiment. This means that it is a very rapid method of screening for useful precursors and determining the optimum conditions for the material deposition. The parameters that can be controlled using LPCVD allow for the determination of whether a precursor could be adapted for another deposition process. The use of SSPs allows for much greater balance of the stoichiometry, when compared to dual source precursor systems, and reduces the requirement for multiple vessels for highly volatile, and often hazardous, reactants. The use of SSPs can also be implemented to selectively deposit predetermined patterns, when combined with patterned substrates,^{3,125-127,130,136,142} as mentioned in section 1.4.

The commercial scale CVD process that is discussed in Chapter 6 allows for far greater control over a wider range of the deposition parameters. Not only does it allow for fine control over the temperature across the substrate, the concentration of the precursor delivered into the system, and therefore the rate of growth, but also allows for the introduction of other precursors in quick succession. This makes producing multi-layered systems and solid solutions much easier while allowing for fine control over the amount of each element within the final deposited material. Another exciting feature in an improved system, like the commercial scale CVD herein, is for selectively deposited films for device fabrication, which require fine control over temperature, precursor type and delivery, all desirable possibilities for the exploration of high-performance thermoelectric materials and devices.

Although it may be possible to perform both processes using the same instrument in some cases, ALD and CVD differ in a few important ways. A typical ALD process consists of the build-up of

Chapter 1

atomic layer by atomic layer to give fine control over thickness and a full substrate surface coverage, as shown in Figure 1-18. As each precursor pulse is followed by a full purge of the reactor, all waste and excess precursor is removed. It is precisely this step and the chemisorption of the precursor to the substrate which allows for the step by step atomic growth of the films deposited using this method.

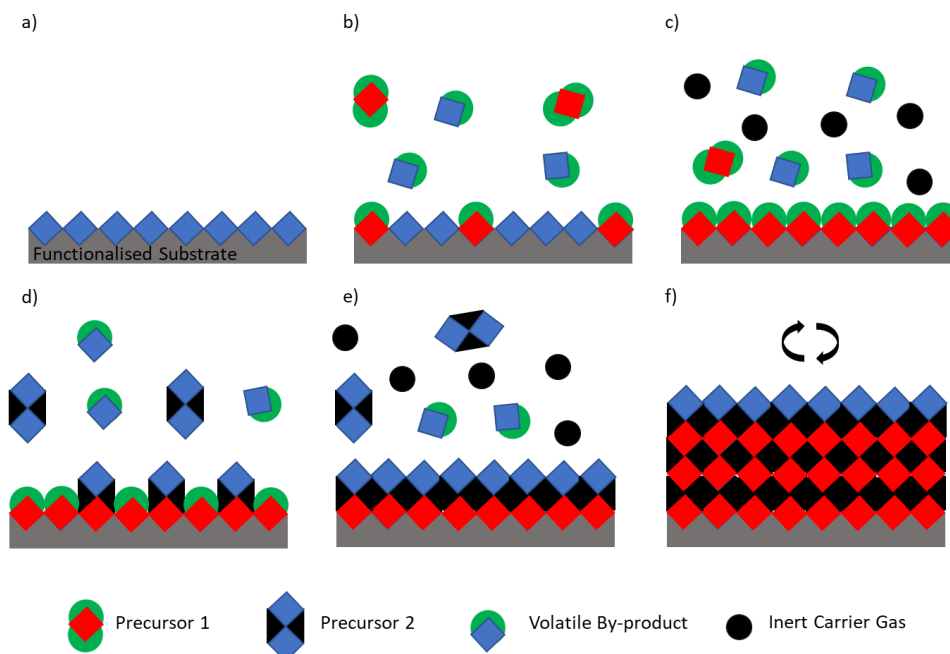


Figure 1-18- The steps involved in material growth by ALD. (a) Functional groups exposed on the substrate surface. (b) Pulse of precursor 1 and its reaction with the functional groups on the surface. (c) Reaction by products and excess precursor 1 is purged from the reactor by the flow of inert gas and vacuum evacuation. (d) Pulse of precursor 2 and its reaction with the new surface functional groups. (e) Reaction by products and excess precursor 2 is purged from the reactor by the flow of inert gas and vacuum evacuation. (f) Steps (a) to (e) are repeated until the desired thickness is achieved.¹⁴³

1.5.2 Wafer scale commercial CVD process

In some cases, different precursors can also be translated to the same deposition rig used for an ALD process but, unless the growth is via the chemisorption of one atomic layer followed by the next, the process is not ALD. Otherwise, the deposition occurs by the thermal decomposition of the precursor used and not by its chemical reaction with a functional group on the surface of the substrate. This is beneficial for the CVD style process as it allows for the higher degree of control offered by the more readily controlled instrument. Not only does the adaptation of CVD precursors to a commercial scale CVD process allow for improved parameter control, but also the ability to incorporate other precursors for more complex (ternary or layered) materials becomes

much simpler. These material layers can consist of an initial seeding layer of an ALD grown material such as alumina or alternatively the build-up of several materials to form a superlattice or solid solution.^{132,144,145} The potential for this is allowed because of the multiple precursor inlets offered by the deposition rig. Further details regarding the set-up of this deposition rig and a figure detailing the instrument and the precursor source bubblers can be found in Chapter 6.

1.6 CVD Precursors

For a precursor to be appropriate for a CVD procedure it must be stable enough not to decompose prematurely, but not so stable that it does not fully decompose to deposit the desired material. Another parameter that is of high concern is the volatility of the precursor, especially for LPCVD, as insufficient volatility will lead to the deposition occurring not on the substrate. This can be remedied by solvating the precursor and deploying aerosol assisted CVD or direct liquid injection CVD. A more thorough discussion of these factors along with other considerations and comparisons of literature precursors for CVD can be found in Chapter 2.

1.7 Bulk versus thin film properties

All the optimisation techniques discussed can be utilised for both bulk and thin film systems. One of the key benefits of thin films is the reduction in the amount of often expensive and sparse semiconducting material that is required. This not only makes thin films more sustainable but also far more economical. However, polycrystalline thin film systems do tend to perform less favourably than their bulk counterparts. One contribution to this observed effect is crystallite orientation, as the optimum thermoelectric performance will be in a certain crystallographic plane which will not be maintained in randomly orientated polycrystalline samples. Another feature that can reduce the performance of the thin films is undesired surface chemistry of the sample, for example oxidation,¹⁴⁶ which plays a larger role in the overall performance for a thin film when compared to a bulk material. The charge carrier mobility of polycrystalline samples is reduced, compared to single crystal samples, due to the accumulation of charge carriers at grain boundaries which leads to scattering effects.¹⁴⁷⁻¹⁴⁹ Additionally, as different crystal axes can have different transport properties, an average of the crystal axes is seen for randomly orientated polycrystalline samples. Thus the electronic properties in randomly orientated samples are an average of the electronic properties of all the crystal axes of the material.¹⁵⁰ This results in a reduction to the electrical conductivity and the Seebeck coefficient and thus comparatively worse thermoelectric performance. It has been predicted that despite thermoelectric devices being unlikely to threaten the power efficiencies of solar panel systems, the large reduction in

semiconducting materials required comparatively, means that thermoelectric power generation may well become more viable.^{151,152}

1.8 Growth mechanisms and control

In order to control the deposition of materials as well as their optimisation, it is important to understand the growth mechanism and the factors that affect the growth of materials. The growth of the material is what determines the number of layers, morphology, orientation, phase, dopants, defects and quality. The factors which affect growth consist of the precursor(s), temperature, substrate, pressure and the number of nucleation sites.

This is of particular concern for CVD processes as the continuity of the films produced is defined by the growth mechanism and thus may not yield continuous films in some instances. This can also help to produce very thin continuous films by CVD if the growth mechanism is epitaxial, where the crystallite growth occurs with a strong preferred orientation with respect to a crystalline substrate. The three main growth mechanisms for thin films are Volmer-Weber (island growth), Frank- Van der Merwe (layer by layer) and Straski-Kranstanov (layer plus island growth).¹⁵³ The growth mechanism is determined by the deposition technique utilised, the chemistry of the precursor, the temperature of the deposition, the rate of precursor delivery to the substrate, the strain caused by the mismatch in crystal lattices between the deposit and the substrate and, in industrial settings with suitable equipment, centrifugal forces.^{154–156} An important feature that determines the growth mechanism is the wetting angle that forms between the surface the material is depositing onto with the deposited material. If this wetting angle is low, near 0° , then the growth mechanism will be Frank-Van der Merwe (layer by layer) growth.¹⁵⁷ This growth mechanism means that the interactions between the substrate and the deposited material are stronger than those between the deposited material with itself. These growth mechanisms, however, are based on surface tension comparisons between the film and the substrate and the assumption that the in-plane interaction is similar to that of the two out-of-plane interactions during growth. These assumptions do not apply to the growth of layered van der Waals material systems, where the in-plane interaction is dominant.^{158,159} In the growth of layered materials, kinetic factors such as on-substrate diffusion, adsorption, desorption and edge diffusion play a large role. Thus, the mechanism that is more appropriate when considering 2D materials growth is that of adsorption-diffusion-attachment mechanism proposed by Yue et. al.¹⁵⁹ Other mechanisms exist for the deposition of nanowires, including vapour-liquid-solid (VLS), vapour-solid (VS) and vapour-solid-solid (VSS). These have been used to deposit nanostructures of SnSe¹⁶⁰ and SnTe,^{161–166} but are of less interest for the scope of this work.

Precursor chemistry can greatly influence growth. Whether the decomposition of the precursor occurs at the substrate or above depends on the stability of the precursor and the energy barrier to adsorption to the substrate. In reality, for most cases the actual situation is a balance between both of these, but the ratio can be controlled by consideration of the precursor, the substrate material, temperature, pressure and the method of decomposition (e.g. thermal, plasma, etc.).

1.8.1 Layers/ thickness control

The number of layers, and the deposition thickness, can be controlled to a fine detail by means of growth manipulation. It has been shown that by careful consideration of temperature, substrate material and nucleation sites it is possible to deposit MoSe₂ monolayers with coverages of up to 2.5 nm by depositing onto molten glass.¹⁶⁷ In particular with respect to thermoelectric applications, monolayers hold the greatest potential, with their larger band gaps, unique conductive properties and phonon confinement effects. The degree to which the electronic structure can be tuned or engineered is most apparent in materials of only a few layers and thus exploration of these is highly attractive.

1.8.2 Phase control

The ability to select the phase is of the utmost importance for almost all applications as different phases of the same material can have vastly different properties. An example of the phase being selected by means of the manipulation of growth is in the temperature dependent deposition of either orthorhombic-SnS (α -SnS) or zinc blende-SnS (ZB-SnS) polymorphs. In this case, detailed by Ahmet et. al., it was shown to be temperature that could be used to select between the two polymorphs for the single source precursor used.^{2,168} Another means of selecting between phases is through consideration of the substrate material and in particular the use of single crystal substrates, matching the desired deposit phase with a substrate with similar lattice parameters. Examples of this is the deposition of metastable cubic-SnSe onto cubic-SnS by Nair et. al.¹⁶⁹ or onto Bi₂Se₃ substrates as shown by Wang et. al.¹⁷⁰

1.8.3 Morphological control

The morphology of a polycrystalline material describes the topology of its surface. Different morphologies suit different applications. For example, a higher surface area might be ideal for one use whereas a smooth surface will be preferable for another. Control over the morphology can be achieved by manipulation of the substrate material and the use of so-called catalysts, as shown for Si₂Te₃ and SnTe,^{166,171} and temperature, as shown in the deposition of SnSe films.¹⁷² These

catalysts are comprised of different compositions of metals within a substrate, as described by Zou et. al.¹⁶⁶

1.8.4 Orientational control

The orientation of the crystallite in a thin film describes the crystallographic lattice planes in relation to one another and that of the substrate. A strong preferred orientation can greatly reduce the number of grain boundaries and increase the uniformity, which can improve the electrical performance of materials. This can be achieved through the selection of the substrate material as well as precursor flow direction and deposition temperature. The selection of particular substrates has been shown to cause lattice-guided seed formation in MoS₂.¹⁷³ The choice of substrate was also shown to significantly affect the orientation of Sb₂Te₃ crystallites.¹⁴²

1.8.5 Quality, dopants and defects

Minuscule quantities of impurities can have large impacts on the properties and performances of semiconducting materials, as discussed in section 1.4.1. These can be in the form of carefully selected dopants or engineered defects. Control over the quality of the material is important particularly in the tuning of charge carrier concentration and mobility, and in turn the Seebeck coefficient and electrical conductivity. The defects can either be encouraged, by means of heat treatments or exposure to an electron beam, or be repaired by chemical treatments.¹⁷⁴

Controlling the electronic structure of semiconducting materials by means of doping is a well-known method. Growth can have a profound effect on the quality of a material. This is due to stacking faults and mismatching causing defects. One method of controlling defects with a film is by means of substrate temperature, as shown by Hema et. al.¹⁷² Since the growth method will determine the crystallite size, orientation and defect concentration, an understanding of how to influence growth is important in controlling the properties of the deposited material and its final application potential.¹⁵⁷

1.9 Characterisation techniques

1.9.1 Precursor characterisation

Discussed below are the characterisation techniques used to characterise and ensure the purity of the single source precursors used in this work.

1.9.1.1 Nuclear Magnetic Resonance (NMR) Spectroscopy

A well established and useful method of characterising molecules is using NMR spectroscopy. This typically involves the determination of a solvated molecules structure, and composition, although for insoluble molecules and materials solid state NMR spectroscopy is also possible. NMR spectroscopy relies on the spin of one or more isotopes present within a molecule with a spin quantum number (I) of $n/2$ where n is an odd integer.

Isotope	Spin	Natural Abundance (%)	Gyromagnetic Ratio ($10^7 \text{radT}^{-1}\text{s}^{-1}$)	NMR Frequency (MHz)	Relative Receptivity
^1H	$\frac{1}{2}$	99.98	26.7510	100	1
^{13}C	$\frac{1}{2}$	1.11	6.7263	25.144	1.76×10^{-4}
^{29}Si	$\frac{1}{2}$	4.70	- 5.3141	19.865	3.69×10^{-4}
^{77}Se	$\frac{1}{2}$	7.60	5.1008	19.068	5.29×10^{-4}
^{119}Sn	$\frac{1}{2}$	8.60	-9.9707	37.272	4.44×10^{-3}
^{125}Te	$\frac{1}{2}$	7.00	-8.4525	31.597	2.21×10^{-3}

Table 1-1- Magnetic properties and natural abundances of specific nuclei relevant to NMR spectroscopy used in this work.¹⁷⁵

The receptivity of an NMR active nucleus relates to its natural abundance, and its sensitivity, which is related to the gyromagnetic ratio. The gyromagnetic ratio relates to the magnetic and angular momentum of a nucleus. In a molecule, asymmetry in the local charge distribution caused by the electrons and other nuclei results in an electric field gradient. The nucleus will orientate itself so that it is at the lowest energy, with the nuclear spin aligned with the electric field gradient. While this is possible for nuclei with a spin equal to $\frac{1}{2}$, nuclei with a spin greater than $\frac{1}{2}$, quadrupolar nuclei, are constantly reorientating themselves to the lowest energy level. A quadrupolar nucleus is one with a spin quantum number of greater than $\frac{1}{2}$ and this causes a lower symmetry of the nuclei compared to spin $\frac{1}{2}$ nuclei. A quadrupolar moment is a measure of this asymmetry. Nuclei with a quadrupolar moment have a short T_2 relaxation time which leads to very broad and difficult to interpret NMR spectra or no signal measured.¹⁷⁶ Of the elements used in this work, S, Ge, Sb and Bi have isotopes with quadrupolar moments due to having spins of: $3/2$, $9/2$, $7/2$ and $5/2$, respectively.^{175,177} For this reason, particularly in low symmetry environments, these nuclei will display very short relaxation times, and hence these nuclei are typically unsuitable for NMR characterisation.

Chapter 1

NMR spectroscopy was utilised to determine the success of precursor synthesis and to confirm the purity of the single source precursors. In some of the precursors used, the presence of two adjacent heteroatoms, for example Sn-Te, leads to satellites being observed in the respective NMR spectra with equivalent coupling constants.

1.9.1.1.1 Silicon NMR spectroscopy

The NMR active isotope is ^{29}Si , which has a typical chemical shift range of between +50 and -200 ppm, relative to tetramethylsilane (TMS).¹⁷⁸ As shown in Table 1, the natural abundance of ^{29}Si is low. This leads to some difficulty in detecting satellites of silicon. The use of glass and quartz for the NMR tubes causes a broad feature within all ^{29}Si NMR spectra, around -110 ppm.

1.9.1.1.2 Selenium NMR spectroscopy

The only NMR active isotope of selenium is ^{77}Se , which has a nuclear spin of $\frac{1}{2}$, as displayed in Table 1-1. The chemical shift range of ^{77}Se NMR, relative to dimethylselenide (Me_2Se), is typically between 2000 and -1000 ppm.¹⁷⁹ In the NMR spectra of nuclei bonded to a selenium atom the ^{77}Se satellites are easy to resolve and show a simple coupling pattern.

1.9.1.1.3 Tin NMR spectroscopy

There are 3 NMR active isotopes of tin, ^{115}Sn , ^{117}Sn and ^{119}Sn , both with nuclear spins of $\frac{1}{2}$. As ^{119}Sn has the higher abundance and receptivity it is the isotope of choice for NMR studies. The chemical shift range, relative to tetramethyltin (Me_4Sn), is typically between 700 and -1900 ppm.¹⁷⁹ In the NMR spectra of nuclei bond to tin atoms satellites can be observed for both ^{119}Sn and ^{117}Sn leading to 4 lines in total, when the satellites are fully resolved. The outer pair of satellites correspond to ^{119}Sn as it is the heavier isotope and so has a larger energy separation between its states.

1.9.1.1.4 Tellurium NMR spectroscopy

There are 2 NMR active isotopes of tellurium, ^{123}Te and ^{125}Te , both with spin of $\frac{1}{2}$. Due to its much higher sensitivity and abundance, ^{125}Te is the isotope of choice for NMR studies. The chemical shift for tellurium ranges from 3400 to -1400, relative to dimethyltelluride (Me_2Te). Satellites observed in the NMR of other nuclei bonded to tellurium atoms for simple coupling patterns that are easy to resolve.

1.9.1.2 Microanalysis

Microanalysis experiments measuring H, C and N composition were undertaken by MEDAC Ltd. The experiment consists of the sample material being combusted in a pure oxygen atmosphere

and the corresponding CO₂, H₂O and N₂ are separated using gas chromatography, allowing for accurate quantification.¹⁸⁰ Microanalysis allows for the confirmation of the purity of the bulk compounds and that other structural assignments were correct and there is only a small degree of error ($\sim\pm 0.5\%$) associated with the measurement, hence this is a useful means of establishing sample purity, particularly for the precursors developed in this work. In this work microanalysis were outsourced to MEDAC Ltd.

1.9.1.3 Thermogravimetric analysis (TGA)

The boiling point and purity of a sample can be evaluated by means of TGA. This involves the precise heating of a sample in an alumina crucible under the constant flow of inert gas whilst accurately determining the mass. As the temperature rises, at a steady predetermined rate, the sample will begin to volatilise or decompose reducing the mass. If impurities are present or the sample compound decomposes prior to volatilisation, artefacts will be observed within the thermogravimetric analysis graph showing the rapid loss of mass before stabilisation and or later mass loss revealing either no residual mass or some residual mass corresponding to material or materials with very low volatility within the temperature window of the experiment. This technique is useful to determine if a compound is suitable for low pressure chemical vapour deposition and help to determine likely temperature regimes for deposition.

Another useful way that thermogravimetric analysis can be used is to determine the vapour pressure of a sample at different temperatures. This is performed using an isothermal step experiment. This means heating the sample to a desired temperature and holding it at this temperature, under a flow of inert gas, and observing any changes in the mass of the sample. There are instrumental and sample dependent factors which can be used to measure the vapour pressure.¹⁸¹ Therefore in order to accurately evaluate the vapour pressure of a unknown compound a reference sample must be used to determine the instrument dependent factor. This reference sample must have known literature vapour pressures within the desired temperature range for the experiment.

1.9.2 Thin film characterisation

Discussed below are the characterisation techniques used to determine the composition, phase, quality, thickness and morphology of the thin films produced in this work.

1.9.2.1 Grazing Incidence X-Ray Diffraction (GIXRD)

A highly powerful and non-destructive technique for phase determination of a crystalline material is XRD. The best XRD technique for thin films is GIXRD. This involves firing a beam of X-rays at a 1°

Chapter 1

incident angle (ω) to the sample (typically), where the X-rays are diffracted by any crystalline material present and thus can be detected at different angles, relating to the position of atoms within the lattice of the crystalline material(s) present and their size. A diffraction pattern can then be produced which contains the peaks diffracted at specific angles (2θ) and their intensities. GIXRD is an out of plane asymmetric scan which enhances the quantity of the thin film material that the X-ray beam encounters.¹⁸² Each phase of each material has a unique diffraction pattern corresponding to its unique composition and structure. Thus, the identity of a material can be confirmed by comparison to published patterns from the database.¹⁸³

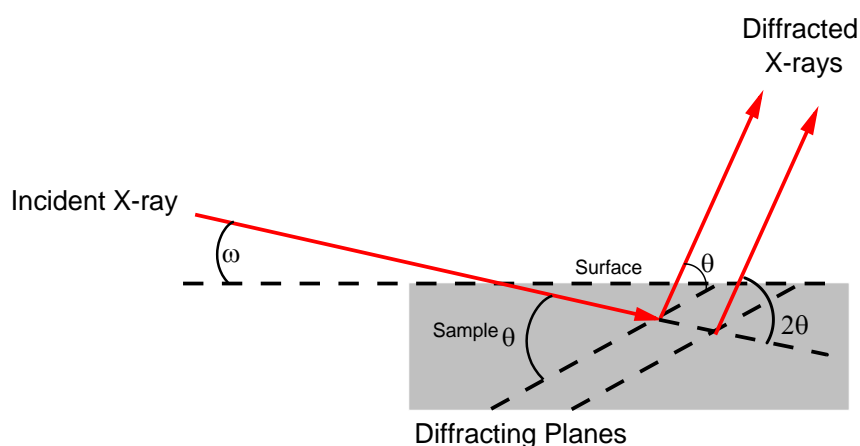


Figure 1-19- X-ray diffraction geometry for an asymmetric scan like that of grazing incidence XRD.¹⁸⁴

Other information that can be obtained for a thin film through evaluation of its diffraction pattern include: the refined lattice parameters, crystallite size and strain as well as any preferred crystallite orientation. These parameters were obtained using the integrated XRD software PDXL for all the samples in this work.¹⁸⁵ The crystallite size and strain of powders and polycrystalline materials are related to the peak widths. The widths of the peaks in the powder XRD pattern are related to instrumental factors, defects in the lattice, differences in strain between grains and the size of the crystallites. These contributions can be separated and the instrumental factor can be accounted for by means of collecting an instrument standard sample, such as LaB_6 . The methods used to determine the crystallite size and strain in PDXL are the Williamson-Hall and the Halder-Wagner methods. The derivation of the Williamson-Hall method consists of a combination of the Scherrer equation,¹⁸⁶ which relates to crystallite size, and the microstrain effect on broadening can be found by consideration of the differential of Bragg's law.¹⁸⁷

The Scherrer equation,

$$\beta_D = \frac{K\lambda}{D\cos\theta}$$

Where the integral breadth is β_D in radians, D is the average crystallite size, K is the dimensionless shape factor, λ is the wavelength of the X-ray radiation used and θ is the Bragg angle in radians.

$$\lambda = 2d \sin \theta$$

$$\Delta\theta = \frac{\Delta d}{d} \tan \theta = -\varepsilon \tan \theta$$

Where d is the lattice plane spacing and the profile broadening due to microstrain is ε . Meaning peak broadening due to microstrain is proportional to $\tan \theta$.¹⁸⁷ Stokes and Wilson showed that the integral breadth, β_ε , from isotropic microstrain is related to the integral breadth of the strain distribution, ξ , through:¹⁸⁸

$$\beta_\varepsilon = 2\xi \tan \theta$$

As β_D and β_ε relate to θ in vastly different ways, Williamson and Hall combined the integral breadths β_D and β_ε into the approximation:

$$\beta = \beta_\varepsilon + \beta_D$$

Combining the equations and multiplying both sides by $\cos \theta$ gives:

$$\beta \cos \theta = C\varepsilon \sin \theta + \frac{K\lambda}{D}$$

Where C is the proportional constant that converts ξ to ε . The above equation can be considered as a straight line of the form $y = mx + c$ with $y = \beta \cos \theta$ and $x = \sin \theta$. This means that, as all other terms are known constants, the values of ε and D can be found. This straight line graph is known as a Williamson-Hall plot.¹⁸⁸

Halder and Wagner provide an alternative method for determining ε and D by considering the reciprocal integral breadth, β^* and reciprocal lattice plane spacing, d^* .^{189,190}

$$\beta^* = \frac{\beta \cos \theta}{\lambda}$$

$$d^* = \frac{2 \sin \theta}{\lambda}$$

For the reciprocal cell:

$$\left(\frac{\beta^*}{d^*}\right)^2 = \frac{K}{D} \cdot \frac{\beta^*}{(d^*)} + (2\varepsilon)^2$$

Which when assuming that the Lorentzian and Gaussian components of β^* are entirely due to the size and strain effects, respectively, can be rewritten as:

$$\left(\frac{\beta \cos \theta}{\sin \theta}\right)^2 = \frac{K\lambda}{D} \cdot \frac{\beta \cos \theta}{\sin^2 \theta} + 16\varepsilon^2$$

The straight line of the $y = mx + c$ can be drawn with $y = (\beta / \tan \theta)^2$ and $x = \beta / (\tan \theta \sin \theta)$ is known as a Halder-Wagner plot. The slope, m , and y intercept, c , of the resulting straight line gives $\frac{K\lambda}{D}$ and $16\varepsilon^2$. The Halder-Wagner method is advantageous when compared to the Williamson-Hall method as it puts more emphasis on the peaks at low and intermediate angles, which are often more reliable than those at high angles.¹⁸⁷

A property of some powder samples and thin films is their ability to display preferred orientations. This effect is identifiable by observation of unusual peak intensities when compared to the diffraction pattern of the bulk and will appear at different intensities, comparatively with other peaks in the pattern, when other incident angles are used. A preferred orientation is characterised by an alignment of the crystal lattice of the polycrystalline material. This is an important feature to explore as single crystal orientation and degree of preferred orientation can have a profound effect on its properties. A good method for investigating the average texture of a powdered sample or thin film material is pole figure measurements. The measurement gives the average texture within the irradiated area, typically between 10 μm to 50 mm, by maintaining a fixed diffraction (2θ) angle whilst varying two geometric parameters α , the tilt of the stage and β , the rotation of the stage.¹⁹¹

1.9.2.2 Raman spectroscopy

When a sample is irradiated with a light source that has energy less than that required to promote an electron to an excited state, a virtual excited state is created. This virtual excited state has a very short lifetime and most of the light reemitted is at the same energy as the incoming light beam, this is called Rayleigh scattering. However, some small portions of the light reemitted differs from the incident light by energy gaps that correspond to some of the vibrational modes. The peaks with reduced energy compared to the Rayleigh scattering photons are known as Stokes lines and the peaks with an increased energy are the anti-Stokes lines, see Figure 1-20. Signals that are strongest in Raman spectra correspond to a vibrational mode that results in a large change of polarizability, and not a change in electric dipole which is the basis of IR spectroscopy.¹⁹²

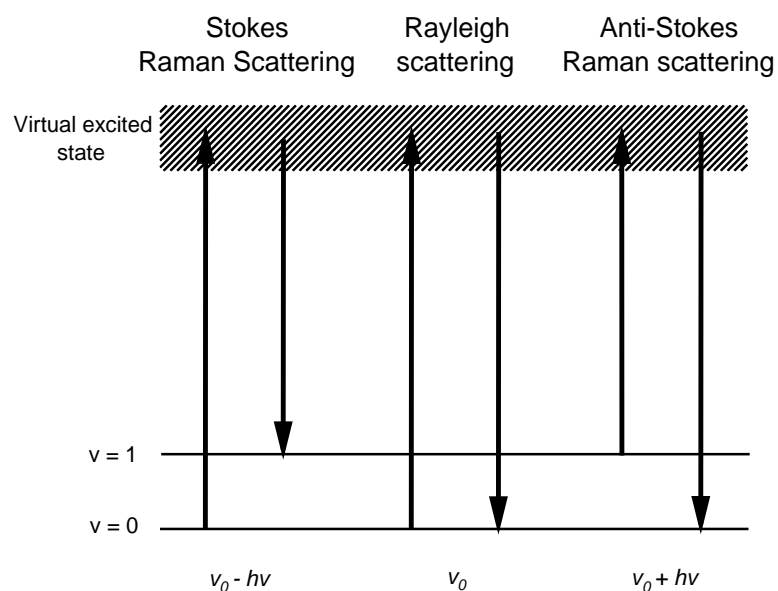


Figure 1-20- A simplified Jablonski diagram showing the energy level transitions observed in Raman spectroscopy from the vibration states, $v = 0$ and $v = 1$, to the virtual excited state and back to the vibrational states.¹⁹²

Raman is a non-destructive surface technique. This makes it ideal for the investigation of surface contamination, such as oxidation. Each Raman active material has its own unique fingerprint pattern that it can be identified by. For a vibration to be Raman active it must cause a change in polarizability, counter to IR which requires a change in permanent dipole moment for a vibration to be active. Raman spectroscopy is of particular use in the characterisation of thin films. This is due to the high sensitivity, often down to a few layers,¹⁹³ and the low penetration depth making Raman spectroscopy perfect for probing the surface chemistry of thin films.

1.9.2.3 Scanning Electron Microscopy (SEM) with Energy Dispersive X-ray Spectroscopy (EDX)

SEM is a surface technique which involves a focused beam of electrons in a raster scan pattern to analyse the surface topology of a sample. When the beam of electrons interacts with the surface of a sample, electrons and characteristic energy waves are emitted, as in Figure 1-21. The emitted electrons that are important for SEM are known as secondary electrons. These secondary electrons are best for investigation of the surface topology as these are of low energy and have a short mean free path through solids meaning only those close to the surface can be detected. With respect to thin film samples, SEM allows for the determination of whether the material deposition was continuous, the size of the grains imaged and the general topology of the surface.

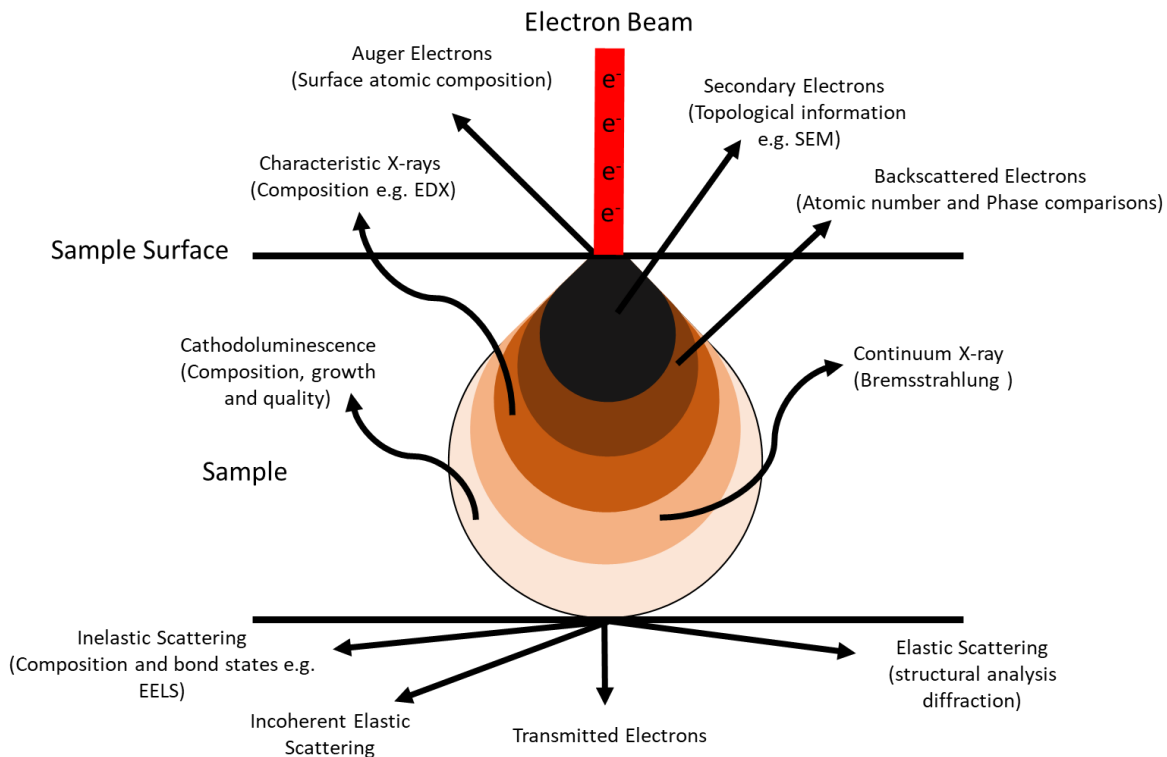


Figure 1-21- Diagram outlining the effect an electron beam has when it interacts with a material. Including all of the different electrons and photons emitted and their relative penetration depths into the material.¹⁹⁴

Another type of electron emitted when a focused beam of electrons interacts with a sample is termed a backscattered electron. These backscattered electrons are slightly higher in energy and come closely in contact with the nucleus of atoms in the material. This means that backscattered electrons are less sensitive for surface topologic investigations but are related to the atomic number of the atoms in the material and thus are useful for determining the phase of a material and identifying other materials present. For this reason the backscatter detector is often the best choice for film thickness determination using cross sectional SEM, as the substrate material and the film will have different brightness's due to the contrasts caused by the atomic sizes in the two materials (heavier atoms appear brighter) not being identical.

EDX detectors can be paired with SEM instruments. When a focused beam of electrons comes into contact with a sample an electron from the core of an atom can be knocked out of orbit leaving a hole which can then be filled by an electron in a higher energy shell. When the hole becomes filled a characteristic X-ray is emitted and can be used to identify the atom. EDX can therefore be used to analyse the composition of a material, the elements present and their concentrations in different regions of the sample.¹⁹⁵ Electron penetration via EDX is on the micrometre scale meaning that EDX is a bulk technique. This allows for an average sample composition to be collected and means that any surface contamination is minimised. This is in

contrast to X-ray photoelectron spectroscopy (XPS), which only penetrates a few nanometres into the sample and is therefore ideal for surface composition investigation.¹⁹⁶ The larger depth penetration in EDX (sampling volume $\sim 1 \mu\text{m}^3$) does lead to observation of substrate material when analysing thinner films, leading to a larger experimental error, typically $\pm 5\%$ or more, hence care is required when interpreting the data obtained from films with thicknesses of ca. $1 \mu\text{m}$ or below.¹⁹⁷

1.9.2.4 Ellipsometry

One method of approximating film thickness in a non-destructive manner is by means of ellipsometry, Figure 1-22. This technique utilises a beam of linearly polarised light which makes contact with a sample and is reflected, absorbed, scattered or transmitted onto a detector. The beam of light makes contact with the sample and the refractive index as well as the extinction coefficient of the sample material leads to changes in the polarisation of the light, leading to it becoming elliptically polarised. Ellipsometry determines the change in polarisation and compares this to a model to determine optical properties as well as the film thickness. The accuracy of the technique is very high as layers down to a few angstroms thick can be detected, if a suitable model is available.¹⁹⁸

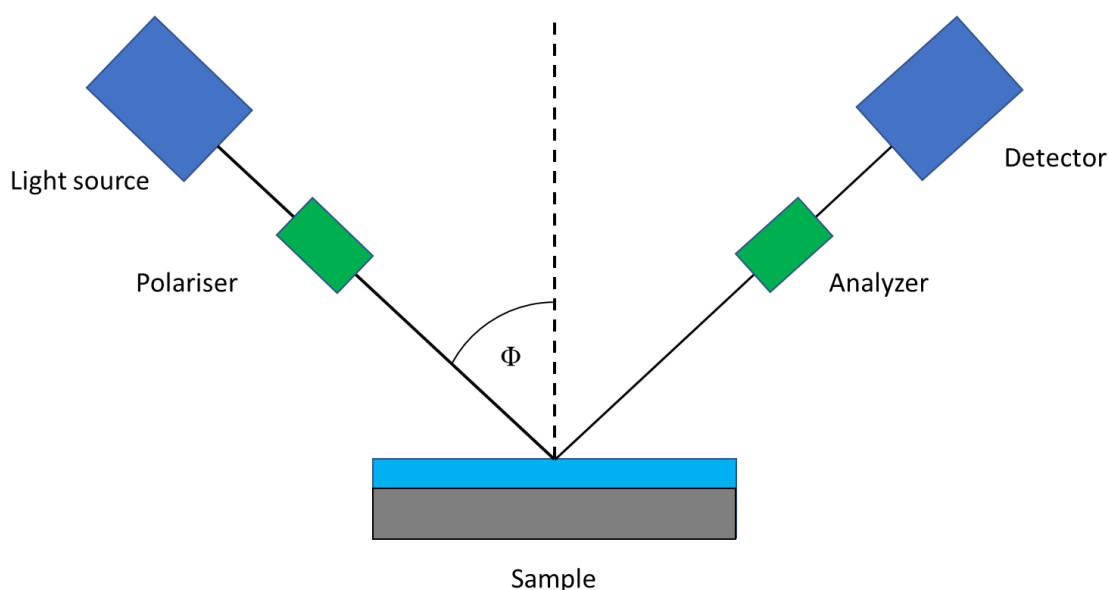


Figure 1-22: Diagram of the setup of an ellipsometer.

Ellipsometry can also be used in situ to monitor deposition processes as they occur. This typically involves a window into and out of the reaction chamber with the light source secured to one and the detector to another. This allows elliptically polarised light to contact the sample within the reaction chamber before reaching the detector where measurements can be carried out tracking the thickness throughout the deposition process.

1.9.3 Thermoelectric and Electrical Property Measurements

Discussed below are the methods used to determine the thermoelectric and electrical properties of the thin films deposited, namely, the resistivity, Hall coefficient, charge carrier concentration and mobility, the Seebeck coefficient, electrical conductivity and the power factor.

1.9.3.1 Hall effect and Van der Pauw Measurements

The Van der Pauw measurements involves a four point probe, Figure 1-23, with each probe being numbered 1 to 4 in a counter clockwise order, starting with 1 in the top left corner. The resistivity can then be measured by injecting a current through probe 1 and measuring it using probe 2, giving I_{12} in amperes, and measuring the voltage between probes 3 and 4, giving V_{34} in volts.

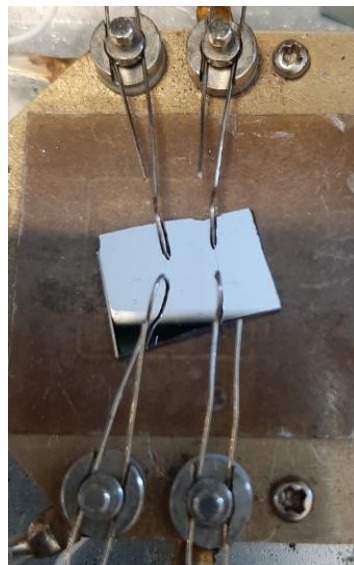


Figure 1-23- The probe set up for the Hall effect and Van der Pauw system.

These can then be used to find the vertical edge resistivity, $R_{12,34}$, using the below equation:

$$R_{12,34} = \frac{V_{34}}{I_{12}}$$

Once I_{23} and V_{14} have been measured, so that the horizontal resistivity $R_{23,41}$ can be calculated, the sheet resistivity can be calculated using the below equation:

$$R_{23,41} = \frac{V_{14}}{I_{23}}$$

Horizontal and vertical resistivity are then taken as averages using the below equations:

$$R_{vertical} = \frac{R_{12,34} + R_{34,12} + R_{21,43} + R_{43,21}}{4}$$

$$R_{horizontal} = \frac{R_{23,41} + R_{41,23} + R_{32,14} + R_{14,32}}{4}$$

The sheet resistivity, R_s , can then be found using the equation proposed by van der Pauw:¹⁹⁹

$$e^{\frac{-\pi R_{\text{vertical}}}{R_s}} + e^{\frac{-\pi R_{\text{horizontal}}}{R_s}} = 1$$

This equation cannot be simplified to give the sheet resistivity in terms of any known constants. However, a Newton-Raphson method can be used to approximate a value. The Newton-Raphson method is described by the below equation:

$$f(x) = 0$$

$$x_{n+1} = x_n - \frac{f(x_n)}{f'(x_n)}$$

Thus

$$R_s^+ = R_s - R_s^2 \frac{1 - e^{\frac{-\pi R_v}{R_s}} - e^{\frac{-\pi R_h}{R_s}}}{\pi \left(R_v \cdot e^{\frac{-\pi R_v}{R_s}} + R_h \cdot e^{\frac{-\pi R_h}{R_s}} \right)}$$

The value for the sheet resistivity is given in ohms per square (Ω/\square). Once a value for the film thickness has been measured, using cross sectional SEM, the resistivity of the film can be measured by dividing the sheet resistivity by the thickness.

When a magnetic field is applied perpendicular to the flow of charged particles in a film, a force is applied known as the Lorentz force, F_L . This effect is known as the Hall effect. The strength of F_L is proportional to the velocity of the charged particles, v , the particle charge, q , and the strength of the magnetic field, B .

$$F_L = qvB$$

This force causes charged particles to predominately reside on one side of the sample. This accumulation of charged particles causes a measurable potential difference, known as the Hall voltage, V_H . This can then be used to calculate the sheet charge carrier concentration, using the following calculation:

$$n_s = \frac{IB}{q|V_H|}$$

The majority charge carrier mobility is then calculated using the equation:

$$\mu = \frac{1}{qn_s R_s}$$

Thus, the resistivity, charge carrier mobility, charge carrier concentration and Hall voltage can be found using this method.²⁰⁰ All of these measurements and calculations can be performed at a range of temperatures to show how this affects the electrical properties of the film.

1.9.3.2 Variable temperature Seebeck coefficient measurements

A very important value, when considering thermoelectric materials, is the Seebeck coefficient, as discussed in previous sections. It quantifies the difference in electrochemical potential across a material per degree kelvin difference. Its measurement involves heating the sample to a temperature and then inducing a small temperature difference across the sample and measuring the voltage induced. When the temperature difference is small the Seebeck coefficient can be defined as:

$$S = -\frac{\Delta V}{\Delta T}$$

At each temperature selected as a data point, once the temperature has stabilised, a sweep of temperature difference from +5 K to -5 K is measured against voltage induced. This then allows for an average voltage per degree kelvin, thus, the Seebeck coefficient for one temperature is measured. This method for determining the Seebeck coefficient is known as the differential method.



Figure 1-24- The probe set up for the variable temperature Seebeck coefficient and resistivity measurement equipment. The outer probes control the temperature gradient across the film and the two central smaller probes measure voltage for the resistivity measurement.

The resistivity measurement is found in a different fashion to the method used for the Hall effect and Van der Pauw Measurements, discussed earlier. The Seebeck tool uses a four point probe method for resistivity determination, Figure 1-24. This method uses the outer probes to flow a current across the film while the two inner probes measure the voltage and these two values can then be used to gather the sheet resistivity (Ω/\square). Similar to the other resistivity measurement described, the value for the deposited material can then be calculated once the film thickness has

been determined. The instrument used has a measuring range of 0.1 $\mu\Omega\text{m}$ to 1000 $\text{k}\mu\Omega\text{m}$. This can lead to issues when measuring materials with high resistivities.

1.10 References

- 1 L. D. Zhao, C. Chang, G. Tan and M. G. Kanatzidis, *Energy Environ. Sci.*, 2016, **9**, 3044.
- 2 C. Gurnani, S. L. Hawken, A. L. Hector, R. Huang, M. Jura, W. Levason, J. Perkins, G. Reid and G. B. G. Stenning, *Dalton Trans*, 2018, **47**, 2628.
- 3 F. Robinson, D. W. Newbrook, P. Curran, C. H. (Kees) de Groot, D. Hardie, A. L. Hector, R. Huang and G. Reid, *Dalton Trans.*, 2021, **50**, 998.
- 4 B. V Suresh, *Solid State Devices and Technology*, Pearson, New Delhi, First edit., 2010.
- 5 B. G. Yacobi, *Semiconductor Materials An Introduction to Basic Principles*, Kluwer Academic Publishers, 2002.
- 6 J. P. Walter and M. L. Cohen, *Phys. Rev.*, 1969, **183**, 763.
- 7 J. S. Blakemore, *J. Appl. Phys.*, 1982, **53**, R123.
- 8 W. Setyawan and S. Curtarolo, *Comput. Mater. Sci.*, 2010, **49**, 299.
- 9 T. Wijesinghe and M. Premaratne, *Opt. Express*, 2012, **20**, 7151.
- 10 R. A. Kishore and S. Priya, *Materials (Basel)*, 2018, **11**, 1433.
- 11 B. Song, S. Lee, S. Cho, M. J. Song, S. M. Choi, W. S. Seo, Y. Yoon and W. Lee, *J. Alloys Compd.*, 2014, **617**, 160.
- 12 K. T. Wojciechowski, R. Zybala and R. Mania, *Microelectron. Reliab.*, 2011, **51**, 1198.
- 13 C. Wood, *Reports Prog. Phys.*, 1988, **51**, 459.
- 14 R. Tamer F, L. William S, D. Russell J, T. F. Refaat, W. S. Luck Jr and R. J. DeYoung, *NASA/TM*, 1999, 209689.
- 15 W. Thomson, *R. Soc. Edinburgh Earth Sci.*, 1851, **3**, 91.
- 16 E. Altenkirch, *Phys. Zeitschrift.*, 1909, **10**, 560.
- 17 P. Douglas, in *ICT - Energy - Concepts Towards Zero - Power Information and Communication Technology*, 2014, p. 49.

Chapter 1

- 18 R.D Abelson, *Thermoelectric Handbook: Macro to Nano*, CRC Press, 2006.
- 19 S. B. Inayat, K. R. Rader and M. M. Hussain, *Sci. Rep.*, 2012, **2**, 841.
- 20 J. P. Rojas, D. Singh, S. B. Inayat, G. A. T. Sevilla, H. M. Fahad and M. M. Hussain, *ECS J. Solid State Sci. Technol.*, 2017, **6**, N3036.
- 21 J. H. Bahk, H. Fang, K. Yazawa and A. Shakouri, *J. Mater. Chem. C*, 2015, **3**, 10362.
- 22 M. Xu, J. M. David and S. H. Kim, *Int. J. Financ. Res.*, 2018, **9**, 90.
- 23 M. Haras and T. Skotnicki, *Nano Energy*, 2018, **54**, 461.
- 24 L. E. Bell, *Science*, 2014, **321**, 1457.
- 25 D. A. Wright, *Nature*, 1958, **181**, 834.
- 26 S. Shen, W. Zhu, Y. Deng, H. Zhao, Y. Peng and C. Wang, *Appl. Surf. Sci.*, 2017, **414**, 197.
- 27 S. Peng, D. Wang, J. Lu, M. He, C. Xu, Y. Li and S. Zhu, *J. Polym. Environ.*, 2017, **25**, 1208.
- 28 G. H. Kim, L. Shao, K. Zhang and K. P. Pipe, *Nat. Mater.*, 2013, **12**, 719.
- 29 T. Zhang, K. Li, C. Li, S. Ma, H. H. Hng and L. Wei, *Adv. Electron. Mater.*, 2017, **3**, 1600554.
- 30 H. Ju, D. Park and J. Kim, *Nanoscale*, 2019, **11**, 16114.
- 31 J. J. Pulikkotil and S. Auluck, *AIP Adv.*, 2015, **5**, 037145.
- 32 Y. Pei, J. Lensch-Falk, E. S. Toberer, D. L. Medlin and G. J. Snyder, *Adv. Funct. Mater.*, 2011, **21**, 241.
- 33 Q. Zhang, F. Cao, W. Liu, K. Lukas, B. Yu, S. Chen, C. Opeil, D. Broido, G. Chen and Z. Ren, *J. Am. Chem. Soc.*, 2012, **134**, 10031.
- 34 Y. Kato, D. Saku, N. Harada and Y. Yoshizawa, *Prog. Nucl. Energy*, 1998, **32**, 563.
- 35 I. Sonder, B. Zimanowski and R. Büttner, *Geophys. Res. Lett.*, 2006, **33**, L02303.
- 36 C. Gayner and K. K. Kar, *Prog. Mater. Sci.*, 2016, **83**, 330.
- 37 J. He and T. M. Tritt, *Science*, 2017, **357**, 1369.
- 38 L.-D. Zhao, S.-H. Lo, Y. Zhang, H. Sun, G. Tan, C. Uher, C. Wolverton, V. P. Dravid and M. G. Kanatzidis, *Nature*, 2014, **508**, 373.
- 39 T. C. Harman, M. P. Walsh, B. E. Laforge and G. W. Turner, *J. Electron. Mater.*, 2005, **34**,

- L19.
- 40 D. M. Rowe and G. Min, *J. Power Sources*, 1998, **73**, 193.
- 41 A. Polozine, S. Sirovinskaya and L. Schaeffer, *Mater. Res.*, 2014, **17**, 1260.
- 42 L. Zhang, P. Xiao, L. Shi, G. Henkelman and J. B. Goodenough, *J. Appl. Phys.*, 2015, **117**, 155103.
- 43 C. B. Vining, *Nat. Mater.*, 2009, **8**, 83.
- 44 A. Shakouri, *Annu. Rev. Mater. Res.*, 2011, **41**, 399.
- 45 D. W. Newbrook, S. P. Richards, V. K. Greenacre, A. L. Hector, W. Levason, G. Reid, C. H. de Groot and R. Huang, *J. Alloys Compd.*, 2020, **848**, 156523.
- 46 A. Suwardi, D. Bash, H. K. Ng, J. R. Gomez, D. V. M. Repaka, P. Kumar and K. Hippalgaonkar, *J. Mater. Chem. A*, 2019, **7**, 23762.
- 47 Z. M. Gibbs, F. Ricci, G. Li, H. Zhu, K. Persson, G. Ceder, G. Hautier, A. Jain and G. J. Snyder, *Comput. Mater.*, 2017, **3**, 1.
- 48 D. S. Parker, A. F. May and D. J. Singh, *Phys. Rev. Appl.*, 2015, **3**, 064003.
- 49 W. G. Zeier, A. Zevalkink, Z. M. Gibbs, G. Hautier, M. G. Kanatzidis and G. J. Snyder, *Angew. Chem. Int. Ed.*, 2016, **55**, 6826.
- 50 D. H. Parkinson and J. E. Quarrington, *Proc. Phys. Soc. Sect. A*, 1954, **67**, 569.
- 51 N. Yacoubi, B. Girault and J. Fesquet, *Appl. Opt.*, 1986, **25**, 4622.
- 52 Y. Pei, A. Lalonde, S. Iwanaga and G. J. Snyder, *Energy Environ. Sci.*, 2011, **4**, 2085.
- 53 H. Wang, Y. Pei, A. D. Lalonde and G. J. Snyder, *Adv. Mater.*, 2011, **23**, 1366.
- 54 E. S. Toberer, A. Zevalkink and G. J. Snyder, *J. Mater. Chem.*, 2011, **21**, 15843.
- 55 M. G. Holland, *Phys. Rev.*, 1964, **134**, A471.
- 56 M. L. Cohen, *Phys. Rev. B*, 1985, **32**, 7988.
- 57 E. F. Steigmeier and I. Kudman, *Phys. Rev.*, 1966, **141**, 767.
- 58 R. J. Gummow and I. Sigalas, *Int. J. Thermophys.*, 1987, **8**, 607.
- 59 R. A. H. Hamilton and C. Park, *Phys. Lett. A*, 1969, **29**, 556.

Chapter 1

- 60 D. P. Spitzer, *J. Phys. Chem. Solids*, 1970, **31**, 19.
- 61 A. V. Ioffe, *Sov. Phys. Solid State*, 1963, **5**, 2446.
- 62 G. A. Slack, *J. Phys. Chem. Solids*, 1973, **34**, 321.
- 63 A. V. Ioffe, *Sov. Phys. Solid State*, 1963, **5**, 2446.
- 64 Z. M. Gibbs, H. Kim, H. Wang, R. L. White, F. Drymiotis, M. Kaviani and G. Jeffrey Snyder, *Appl. Phys. Lett.*, 2013, **103**, 262109.
- 65 H. J. Goldsmid and J. W. Sharp, *J. Electron. Mater.*, 1999, **28**, 869.
- 66 S. Yoshizawa and T. Uchihashi, *Appl. Phys. Lett.*, 2015, **106**, 022112.
- 67 H. Wang, J. Wang, X. Cao and G. J. Snyder, *J. Mater. Chem. A*, 2014, **2**, 3169.
- 68 R. J. Korkosz, T. C. Chasapis, S. H. Lo, J. W. Doak, Y. J. Kim, C. I. Wu, E. Hatzikraniotis, T. P. Hogan, D. N. Seidman, C. Wolverton, V. P. Dravid and M. G. Kanatzidis, *J. Am. Chem. Soc.*, 2014, **136**, 3225.
- 69 W. G. Zeier, C. P. Heinrich, T. Day, C. Panithipongwut, G. Kieslich, G. Brunklaus, G. J. Snyder and W. Tremel, *J. Mater. Chem. A*, 2014, **2**, 1790.
- 70 H. Wang, X. Cao, Y. Takagiwa and G. J. Snyder, *Mater. Horizons*, 2015, **2**, 323.
- 71 L.-D. Zhao, G. Tan, S. Hao, J. He, Y. Pei, H. Chi, H. Wang, S. Gong, H. Xu and V. P. Dravid, *Science*, 2016, **351**, 141.
- 72 M. D. Nielsen, V. Ozolins and J. P. Heremans, *Energy Environ. Sci.*, 2013, **6**, 570.
- 73 S. Hao, V. P. Dravid, M. G. Kanatzidis and C. Wolverton, *APL Mater.*, 2016, **4**, 104505.
- 74 Q. Tan and J.-F. Li, *J. Electron. Mater.*, 2014, **43**, 2435.
- 75 W. Shi, M. Gao, J. Wei, J. Gao, C. Fan, E. Ashalley, H. Li and Z. Wang, *Adv. Sci.*, 2018, **5**, 1700602.
- 76 S. Li, X. Li, Z. Ren and Q. Zhang, *J. Mater. Chem. A*, 2018, **6**, 2432.
- 77 G. Tan, L. D. Zhao and M. G. Kanatzidis, *Chem. Rev.*, 2016, **116**, 12123.
- 78 G. Shi and E. Kioupakis, *J. Appl. Phys.*, 2015, **117**, 065103.
- 79 J. Li, Z. Chen, X. Zhang, Y. Sun, J. Yang and Y. Pei, *NPG Asia Mater.*, 2017, **9**, e353.

- 80 D. J. Lewis, P. Kevin, O. Bakr, C. A. Muryn, M. A. Malik and P. O'Brien, *Inorg. Chem. Front.*, 2014, **1**, 577.
- 81 J. R. Sootsman, D. Y. Chung and M. G. Kanatzidis, *Angew. Chem. Int. Ed.*, 2009, **48**, 8616.
- 82 A. Nozariasbmarz, A. Agarwal, Z. A. Coutant, M. J. Hall, J. Liu, R. Liu, A. Malhotra, P. Norouzzadeh, M. C. Öztürk, V. P. Ramesh, Y. Sargolzaeiaval, F. Suarez and D. Vashaee, *Jpn. J Appl. Phys.*, 2017, **56**, 05DA04.
- 83 N. Toshima, *Macromol. Symp.*, 2002, **186**, 81.
- 84 B. Yu, M. Zebarjadi, H. Wang, K. Lukas, H. Wang, D. Wang, C. Opeil, M. Dresselhaus, G. Chen and Z. Ren, *Nano Lett.*, 2012, **12**, 2077.
- 85 V. P. Vedeneev, S. P. Krivoruchko and E. P. Sabo, *Semiconductors*, 1998, **32**, 241.
- 86 S. Roychowdhury, M. Samanta, S. Perumal and K. Biswas, *Chem. Mater.*, 2018, **30**, 5799.
- 87 Q. Wang, R. Quhe, Z. Guan, L. Wu, J. Bi, P. Guan, M. Lei and P. Lu, *RSC Adv.*, 2018, **8**, 21280.
- 88 W. Li, L. Zheng, B. Ge, S. Lin, X. Zhang, Z. Chen, Y. Chang and Y. Pei, *Adv. Mater.*, 2017, **29**, 1605887.
- 89 B. Poudel, Q. Hao, Y. Ma, Y. Lan, A. Minnich, B. Yu, X. Yan, D. Wang, A. Muto, D. Vashaee, X. Chen, J. Liu, Dresselaus, G. Chen and Z. Ren, *Science*, 2008, **320**, 634.
- 90 P. Bauer Pereira, I. Sergueev, S. Gorsse, J. Dadda, E. Müller and R. P. Hermann, *Phys. status. Solidi B*, 2013, **250**, 1300.
- 91 S. Saha, A. Banik and K. Biswas, *Chem. - A Eur. J.*, 2016, **22**, 15634.
- 92 S. Perumal, S. Roychowdhury and K. Biswas, *J. Mater. Chem. C*, 2016, **4**, 7520.
- 93 J. Li, X. Zhang, S. Lin, Z. Chen and Y. Pei, *Chem. Mater.*, 2017, **29**, 605.
- 94 M. Samanta and K. Biswas, *J. Am. Chem. Soc.*, 2017, **139**, 9382.
- 95 D. Wu, L.-D. Zhao, S. Hao, Q. Jiang, F. Zheng, J. W. Doak, H. Wu, H. Chi, Y. Gelbstein, C. Uher, C. Wolverton, M. Kanatzidis and J. He, *J. Am. Chem. Soc.*, 2014, **136**, 11412.
- 96 Z. Zheng, X. Su, R. Deng, C. Stoumpos, H. Xie, W. Liu, Y. Yan, S. Hao, C. Uher, C. Wolverton, M. G. Kanatzidis and X. Tang, *J. Am. Chem. Soc.*, 2018, **140**, 2673.
- 97 L. Zhang and J. L. Wang, *J. Mater. Chem. A*, 2016, **4**, 7936.

Chapter 1

- 98 H. Wu, X. Lu, G. Wang, K. Peng, H. Chi, B. Zhang, Y. Chen, C. Li, Y. Yan, L. Guo, C. Uher, X. Zhou and X. Han, *Adv. Energy Mater.*, 2018, **8**, 1800087.
- 99 Y. Xiao, C. Chang, Y. Pei, D. Wu, K. Peng, X. Zhou, S. Gong, J. He, Y. Zhang, Z. Zeng and L. D. Zhao, *Phys. Rev. B*, 2016, **94**, 125203.
- 100 P. D. Antunez, J. J. Buckley and R. L. Brutchey, *Nanoscale*, 2011, **3**, 2399.
- 101 D. Beretta, N. Neophytou, J. M. Hodges, M. G. Kanatzidis, D. Narducci, M. Martin-Gonzalez, M. Beekman, B. Balke, G. Cerretti, W. Tremel, A. Zevalkink, A. I. Hofmann, C. Müller, B. Dörling, M. Campoy-Quiles and M. Caironi, *Mater. Sci. Eng. R Reports*, 2019, **138**, 210.
- 102 A. D. Lalonde, Y. Pei, H. Wang and G. J. Snyder, *Mater. Today*, 2011, **14**, 526.
- 103 L. D. Zhao, V. P. Dravid and M. G. Kanatzidis, *Energy Environ. Sci.*, 2014, **7**, 251.
- 104 M. G. Kanatzidis, *Chem. Mater.*, 2010, **22**, 648.
- 105 L. Hicks, T. Harman, X. Sun and M. S. Dresselhaus, *Phys. Rev. B*, 1996, **53**, R10493.
- 106 M. S. Dresselhaus, G. Chen, M. Y. Tang, R. Yang, H. Lee, D. Wang, Z. Ren, J. P. Fleurial and P. Gogna, *Adv. Mater.*, 2007, **19**, 1043.
- 107 Y. Pei, H. Wang and G. J. Snyder, *Adv. Mater.*, 2012, **24**, 6125.
- 108 Q. Zhang, B. Liao, Y. Lan, K. Lukas, W. Liu, K. Esfarjani, C. Opeil, D. Broido, G. Chen and Z. Ren, *Proc. Natl. Acad. Sci.*, 2013, **110**, 13261.
- 109 K. Berland, X. Song, P. A. Carvalho, C. Persson, T. G. Finstad and O. M. Løvvik, *J. Appl. Phys.*, 2016, **119**, 125103.
- 110 S. Perumal, S. Roychowdhury, D. S. Negi, R. Datta and K. Biswas, *Chem. Mater.*, 2015, **27**, 7171.
- 111 R. Moshwan, L. Yang, J. Zou and Z. G. Chen, *Adv. Funct. Mater.*, 2017, **27**, 1703278.
- 112 J. Yang, L. Xi, W. Qiu, L. Wu, X. Shi, L. Chen, J. Yang, W. Zhang, C. Uher and D. J. Singh, *Comput. Mater.*, 2016, **2**, 15015.
- 113 J.-P. Niemelä, A. J. Karttunen and M. Karppinen, *J. Mater. Chem. C*, 2015, **3**, 10349.
- 114 A. Ishida, T. Yamada, T. Tsuchiya, Y. Inoue, S. Takaoka and T. Kita, *Appl. Phys. Lett.*, 2009, **95**, 122106.

- 115 J. Gellman, J. M. Hare, C. J. Lowenstein, G. Gerstenblith, V. Coombs, P. Langenberg, J. A. Brinker and J. R. Resar, *Nature*, 2001, **413**, 597.
- 116 K. Kothari and M. Maldovan, *Sci. Rep.*, 2017, **7**, 5625.
- 117 M. G. Kanatzidis, T. P. Hogan, J. L. Short, H. Kong, R. Pcionek, C. Uher, A. Downey, P. F. P. Poudeu and J. D'Angelo, *J. Am. Chem. Soc.*, 2006, **128**, 14347.
- 118 L. Wu, X. Li, S. Wang, T. Zhang, J. Yang, W. Zhang, L. Chen and J. Yang, *NPG Asia Mater.*, 2017, **9**, e343.
- 119 X. Wang, I. Veremchuk, M. Bobnar, U. Burkhardt, J. T. Zhao and Y. Grin, *Chem. Mater.*, 2018, **30**, 1362.
- 120 B. Qin, D. Wang, W. He, Y. Zhang, H. Wu, S. J. Pennycook and L. D. Zhao, *J. Am. Chem. Soc.*, 2019, **141**, 1141.
- 121 K. Gaurav and S. K. Pandey, *Condens. Matter*, 2016, **9**, 014701.
- 122 R. He, G. Schierning and K. Nielsch, *Adv. Mater. Technol.*, 2018, **3**, 1700256.
- 123 J. Yan, X. Liao, D. Yan and Y. Chen, *J. Microelectromech. Syst.*, 2018, **27**, 1.
- 124 J. H. Kiely, D. V. Morgan and D. M. Rowe, *Meas. Sci. Technol.*, 1994, **5**, 182.
- 125 C. H. de Groot, C. Gurnani, A. L. Hector, R. Huang, M. Jura, W. Levason and G. Reid, *Chem. Mater.*, 2012, **24**, 4442.
- 126 S. L. Benjamin, C. H. de Groot, C. Gurnani, A. L. Hector, R. Huang, K. Ignatyev, W. Levason, S. J. Pearce, F. Thomas and G. Reid, *Chem. Mater.*, 2013, **25**, 4719.
- 127 S. L. Benjamin, C. H. de Groot, C. Gurnani, A. L. Hector, R. Huang, E. Koukharenko, W. Levason and G. Reid, *J. Mater. Chem. A*, 2014, **2**, 4865.
- 128 A. De Ninno, A. Gerardino, G. Birarda, G. Greci and L. Businaro, *Biophys. Bioeng. Lett.*, 2010, **3**, 230583356.
- 129 T. Ito and S. Okazaki, *Nature*, 2000, **406**, 1027.
- 130 R. Huang, S. L. Benjamin, C. Gurnani, Y. Wang, A. L. Hector, W. Levason, G. Reid and C. H. de Groot, *Sci. Rep.*, 2016, **6**, 27593.
- 131 D. Ahn, M. H. Son, C. M. Park, E. K. Kim, S.-H. Song, S. W. Hwang and B. H. Choi, *Appl. Phys. Lett.*, 2001, **78**, 1403.

Chapter 1

- 132 B. J. Choi, S. Choi, Y. C. Shin, K. M. Kim, C. S. Hwang, Y. J. Kim, Y. J. Son and S. K. Hong, *Chem. Mater.*, 2007, **19**, 4387.
- 133 M. R. Burton, S. Mehraban, D. Beynon, J. McGettrick, T. Watson, N. P. Lavery and M. J. Carnie, *Adv. Energy Mater.*, 2019, **9**, 1900201.
- 134 D. Madan, A. Chen, P. K. Wright and J. W. Evans, *J. Appl. Phys.*, 2011, **109**, 034904.
- 135 G. Marin, R. Funahashi and M. Karppinen, *Adv. Eng. Mater.*, 2020, 2000535.
- 136 D. W. Newbrook, S. P. Richards, V. K. Greenacre, A. L. Hector, W. Levason, G. Reid, C. H. K. de Groot and R. Huang, *Appl. Energy Mater.*, 2020, **3**, 5840.
- 137 J. Weber, K. Potje-Kamloth, F. Haase, P. Detemple, F. Völklein and T. Doll, *Sensors Actuators, A Phys.*, 2006, **132**, 325.
- 138 P. Fourmont, L. F. Gerlein, F. X. Fortier, S. G. Cloutier and R. Nechache, *ACS Appl. Mater. Interfaces*, 2018, **10**, 10194.
- 139 M. R. Burton, T. Liu, J. McGettrick, S. Mehraban, J. Baker, A. Pockett, T. Watson, O. Fenwick and M. J. Carnie, *Adv. Mater.*, 2018, **30**, 1801357.
- 140 G. J. Snyder, J. R. Lim, C. K. Huang and J. P. Fleurial, *Nat. Mater.*, 2003, **2**, 528.
- 141 J. De Boor, N. Geyer, J. V. Wittemann, U. Gösele and V. Schmidt, *Nanotechnology*, 2010, **21**, 095302.
- 142 S. L. Benjamin, C. H. de Groot, A. L. Hector, R. Huang, E. Koukharenko, W. Levason and G. Reid, *J. Mater. Chem. C*, 2015, **3**, 423.
- 143 R. W. Johnson, A. Hultqvist and S. F. Bent, *Mater. Today*, 2014, **17**, 236.
- 144 T. Bülow, H. Gargouri, M. Siebert, R. Rudolph, H. H. Johannes and W. Kowalsky, *Nanoscale Res. Lett.*, 2014, **9**, 223.
- 145 S. K. Selvaraj, G. Jursich and C. G. Takoudis, *Rev. Sci. Instrum.*, 2013, **84**, 095109.
- 146 Y. K. Lee, Z. Luo, S. P. Cho, M. G. Kanatzidis and I. Chung, *Joule*, 2019, **3**, 719.
- 147 T. R. Wei, G. Tan, X. Zhang, C. F. Wu, J. F. Li, V. P. Dravid, G. J. Snyder and M. G. Kanatzidis, *J. Am. Chem. Soc.*, 2016, **138**, 8875.
- 148 Y. X. Chen, Z. H. Ge, M. Yin, D. Feng, X. Q. Huang, W. Zhao and J. He, *Adv. Funct. Mater.*, 2016, **26**, 6836.

- 149 T. R. Wei, C. F. Wu, X. Zhang, Q. Tan, L. Sun, Y. Pan and J. F. Li, *Phys. Chem. Chem. Phys.*, 2015, **17**, 30102.
- 150 S. Wang, S. Hui, K. Peng, T. P. Bailey, X. Zhou, X. Tang and C. Uher, *J. Mater. Chem. C*, 2017, **5**, 10191.
- 151 D. Kraemer, Q. Jie, K. Mcenaney, F. Cao, W. Liu, L. A. Weinstein, J. Loomis, Z. Ren and C. Gang, *Nat. Energy*, 2016, **1**, 16153.
- 152 D. Kraemer, K. McEnaney, M. Chiesa and G. Chen, *Sol. Energy*, 2012, **86**, 1338.
- 153 K. Oura, V. Lifshits, A. Saranin, A. Zotov and M. Katayama, *Surface Science: An Introduction*, Springer, Berlin, 2003.
- 154 A. Baskaran and P. Smereka, *J. Appl. Phys.*, 2012, **111**, 044321.
- 155 H. Heo, J. H. Sung, J. H. Ahn, F. Ghahari, T. Taniguchi, K. Watanabe, P. Kim and M. H. Jo, *Adv. Electron. Mater.*, 2017, **3**, 1600375.
- 156 F. Terai, H. Kobayashi, S. Katsui, Y. Sato, T. Nagatomo and T. Homma, *Jpn. J. Appl. Phys.*, 2005, **44**, 125.
- 157 N. Kaiser, *Appl. Opt.*, 2002, **41**, 3053.
- 158 Michely, Thomas and J. Krug, *Islands, Mounds, and Atoms: Patterns and Processes in Crystal Growth Far from Equilibrium*, Springer, Berlin, 2004.
- 159 R. Yue, Y. Nie, L. A. Walsh, R. Addou, C. Liang, N. Lu, A. T. Barton, H. Zhu, Z. Che, D. Barrera, L. Cheng, P. R. Cha, Y. J. Chabal, J. W. P. Hsu, J. Kim, M. J. Kim, L. Colombo, R. M. Wallace, K. Cho and C. L. Hinkle, *2D Mater.*, 2017, **4**, 045019.
- 160 F. Davitt, H. G. Manning, F. Robinson, S. L. Hawken, S. Biswas, N. Petkov, M. van Druenen, J. J. Boland, G. Reid and J. D. Holmes, *Adv. Mater. Interfaces*, 2020, 2000474.
- 161 J. Shen, Y. Xie and J. J. Cha, *Nano Lett.*, 2015, **15**, 3827.
- 162 M. Safdar, Q. Wang, M. Mirza, Z. Wang, K. Xu and J. He, *Nano Lett.*, 2013, **13**, 5344.
- 163 M. Safdar, Q. Wang, M. Mirza, Z. Wang and J. He, *Cryst. Growth Des.*, 2014, **14**, 2502.
- 164 M. Saghir, M. R. Lees, S. J. York and G. Balakrishnan, *Cryst. Growth Des.*, 2014, **14**, 2009.
- 165 Z. Li, S. Shao, N. Li, K. McCall, J. Wang and S. X. Zhang, *Nano Lett.*, 2013, **13**, 5443.

Chapter 1

- 166 Y. Zou, Z. Chen, J. Lin, X. Zhou, W. Lu, J. Drennan and J. Zou, *Nano Res.*, 2015, **8**, 3011.
- 167 J. Chen, X. Zhao, S. J. R. Tan, H. Xu, B. Wu, B. Liu, D. Fu, W. Fu, D. Geng, Y. Liu, W. Liu, W. Tang, L. Li, W. Zhou, T. C. Sum and K. P. Loh, *J. Am. Chem. Soc.*, 2017, **139**, 1073.
- 168 I. Y. Ahmet, M. S. Hill, A. L. Johnson and L. M. Peter, *Chem. Mater.*, 2015, **27**, 7680.
- 169 P. K. Nair, E. Barrios-Salgado and M. T. S. Nair, *Phys. Status Solidi Appl. Mater. Sci.*, 2016, **213**, 2229.
- 170 Z. Wang, J. Wang, Y. Zang, Q. Zhang, J. A. Shi, T. Jiang, Y. Gong, C. L. Song, S. H. Ji, L. L. Wang, L. Gu, K. He, W. Duan, X. Ma, X. Chen and Q. K. Xue, *Adv. Mater.*, 2015, **27**, 4150.
- 171 K. Wu and J. Cui, *J. Mater. Sci. Mater. Electron.*, 2018, **29**, 15643.
- 172 G. Hema Chandra, J. Naveen Kumar, N. Madhusudhana Rao and S. Uthanna, *J. Cryst. Growth*, 2007, **306**, 68.
- 173 A. Aljarb, Z. Cao, H. L. Tang, J. K. Huang, M. Li, W. Hu, L. Cavallo and L. J. Li, *ACS Nano*, 2017, **11**, 9215.
- 174 J. Jiang, T. Xu, J. Lu, L. Sun and Z. Ni, *Research*, 2019, **2019**, 4641739.
- 175 R. K. Harris, *Chem. Soc. Rev.*, 1976, **5**, 1.
- 176 D. W. H. Rankin, N. W. Mitzel and C. A. Morrison, *Structural Methods in Molecular Inorganic Chemistry*, John Wiley & Sons, Ltd, Chichester, First Edn., 2013.
- 177 R. K. Harris, E. D. Becker, S. M. C. De Menezes, R. Goodfellow and P. Granger, *Solid State Nucl. Magn. Reson.*, 2002, **22**, 458.
- 178 F. D. Uhlig and H. C. Marsmann, in *Si NMR Some Practical Aspects*, Eigenverlag, Morrisville, Silicon Co., 2003, vol. 2, pp. 208–222.
- 179 J. Mason, *Multinuclear NMR*, Plenum Press, New York, 1987.
- 180 M. Weller, T. Overton, J. Rourke and F. Armstrong, *Inorganic Chemistry*, Oxford University Press Inc., Oxford, Sixth Edn., 2014.
- 181 C. Wang, S. Yang and Y. Chen, *R. Soc. Open Sci.*, 2019, **6**, 181193.
- 182 S. Kobayashi, *Rigaku J.*, 2010, **26**, 3.
- 183 NIST Inorganic Crystal Structure Database, NIST Standard Reference Database Number 3,

National Institute of Standards and Technology, Gaithersburg MD, 20899,
DOI: <https://doi.org/10.18434/M32147>, (retrieved September 2019).

- 184 T. Mitsunaga, *Rigaku J.*, 2009, **25**, 7.
- 185 Rigaku, *Rigaku J.*, 2010, **26**, 23.
- 186 P. Scherrer and N. G. W. Göttingen, *Math.-Phys. Klasse 2*, 1918, 96.
- 187 F. Izumi and T. Ikeda, *Adv. Ceram. Res. Cent. Annu. Rep.*, 2014, **3**, 33.
- 188 A. R. Stokes and A. . . C. Wilson, *Proc. Cambridge Philos. Soc.*, 1944, **40**, 197.
- 189 N. C. Halder and C. N. J. Wagner, *Adv. X-Ray Anal.*, 1966, **9**, 91.
- 190 N. C. Halder and C. N. J. Wagner, *Acta Crystallogr.*, 1966, **20**, 312.
- 191 K. Nagao and E. Kagami, *Rigaku J.*, 2011, **27**, 6.
- 192 A. K. Brisdon, *Inorganic Spectroscopic Methods*, Oxford University Press Inc., New York, 1998.
- 193 H. Zhao, Y. Mao, X. Mao, X. Shi, C. Xu, C. Wang, S. Zhang and D. Zhou, *Adv. Funct. Mater.*, 2018, **28**, 1704855.
- 194 H. Ardebili, J. Zhang and M. G. Pecht, in *Encapsulation Technologies for Electronic Applications*, William Andrew Publishing, Cambridge, Second Edi., 2018, p. 317.
- 195 J. C. Russ, *Fundamentals of Energy Dispersive X-Ray Analysis*, Butterworths & Co Ltd, London, 1984.
- 196 D. K. Schroder, *Semiconductor Material and Device Characterisation*, Wiley, New York, Second Edn., 1998.
- 197 D. E. Newbury and N. W. M. Ritchie, *Scanning*, 2013, **35**, 141.
- 198 H. Arwin, *Sensors Actuators, A Phys.*, 2001, **92**, 43.
- 199 L. J. van der Pauw, *Philips Res. Reports*, 1958, **13**, 1.
- 200 L. J. van der Pauw, *Philips Tech. Rev.*, 1958, **20**, 220.

Chapter 2 Group 14 Metal Chalcogenide Single Source Precursor Synthesis and Characterisation

2.1 Introduction

The deposition of semiconducting material thin films is of enormous technological importance for a vast array of applications. These include: optoelectronics, photovoltaic cells, battery materials, microelectronic circuits, photonics, phase change memory materials, topological crystalline insulators, photodetectors and thermoelectronics.¹⁻⁹ The fabrication of these devices rely on the variety of deposition techniques possible. The selection of which deposition technique is right for the intended application depends upon the specific requirements of the material deposited and the requirements of the device in question. Firstly, the chemistry of the elements comprising the material is important when determining possible methods for deposition. Secondly, the thickness of the material that is required for the device may need to be very specific and thus control over this will be important in the deposition technique selection. Thirdly, the growth mechanism of the material or materials may be relevant for some applications, for example when very thin (mono- or few-layer) films or other specific morphologies like nanowires are required. These considerations, along with cost effectiveness, scalability and energy requirements are all important for selecting the most suitable deposition technique. However, the precursor requirements of that deposition process are of utmost importance. The precursors may require a combination of specific reactivity, stability, volatility, toxicity, purity, ease of handling, *etc.*, so that the precursor is optimised for the deposition technique.

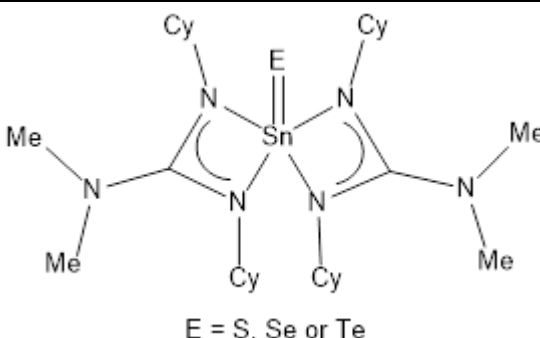
The utilisation of single source precursors for chemical vapour deposition (CVD) can be beneficial for several reasons. Firstly, having all the required elements present in one molecular species can allow for a more precise balance of the stoichiometry, when compared to a dual source system, for example. Secondly, the properties of the precursor can be altered and tuned to aid in the optimisation process. This can be achieved by altering the volatility of the precursor by reducing or increasing the molecular weight to modify the vapour pressure and boiling point of the precursor. Another modification to the precursors is to adapt the chemical structure, oxidation state, bonding type and stability, for example by moving from an octahedral dative covalently bonded complex to a covalently bonded tetrahedral compound. Altering these properties of the precursor can affect its stability and the actual material or phase that is deposited. Finally, the substituents on the precursor can be altered to change properties such as volatility, the decomposition pathways possible and thus the stability of the precursor. Preferably, the

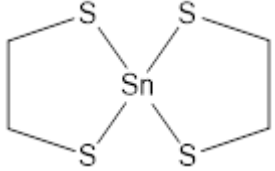
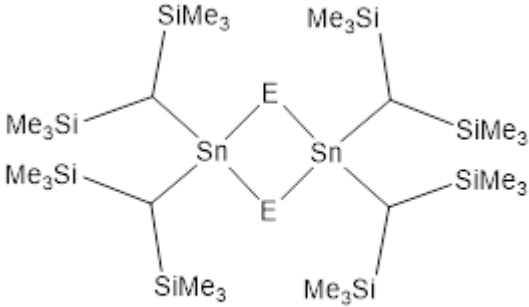
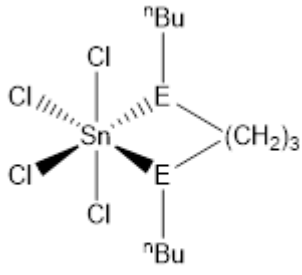
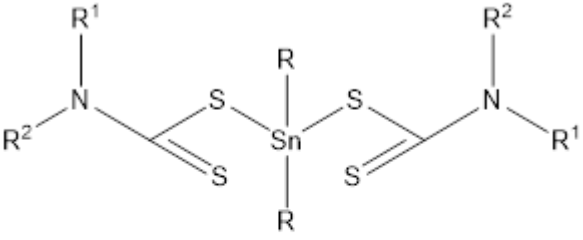
properties of the precursor can be modified such that the volatility is great enough to easily be vaporised and transported to the deposition zone, but not so volatile that it is difficult to handle, while the stability is sufficient for the precursor to remain intact until the time it is deposited, but not so stable that a particularly high temperature is required. In fact, this might be impractical for certain deposition techniques or device targets and material deposited must be continuous if electrical measurements are to be carried out.

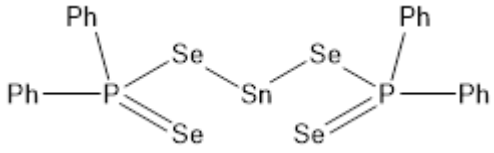
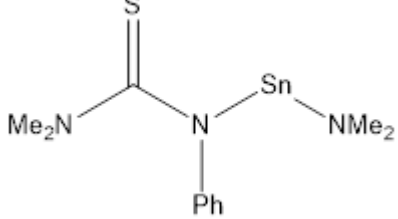
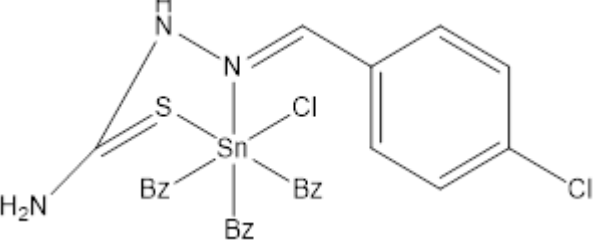
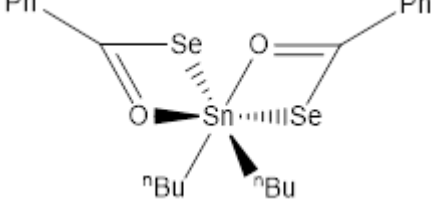
2.1.1 Precursor systems

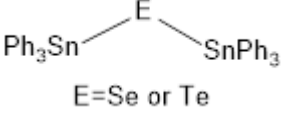
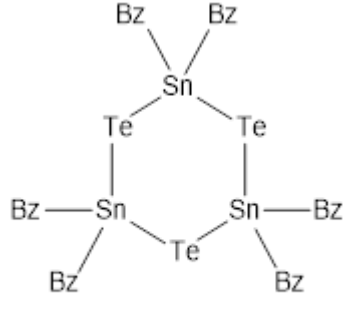
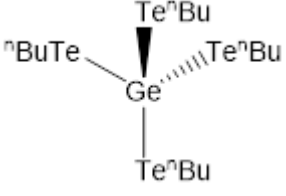
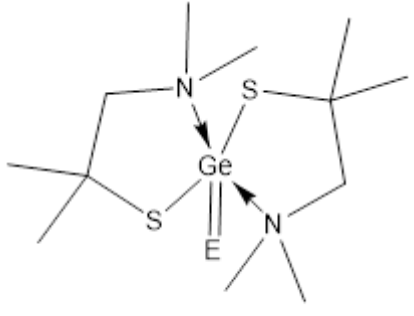
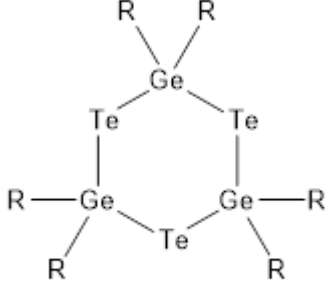
Effective precursor design is key to the deposition of high-quality semiconducting materials. As discussed, different deposition techniques have very different demands on the properties of the precursor or precursors involved. Some different precursor systems used for Group 14 chalcogenides, the deposition method and conditions employed have been tabulated below.

Table 2-1: Precursors used for the deposition of tin chalcogenide thin films a)-j) or tin chalcogenide powders k) and l) and the deposition technique used. Precursors used for the deposition of germanium chalcogenide thin films m) or germanium chalcogenide powders or crystals n) and o) and the deposition technique used. p) Large scale CVD process described for the production of Si_2Te_3 thin films and q) CVD of Si_2Te_3 nanoplates and nanoribbons.

Precursor(s)	Deposition conditions	Deposition technique
a) $\text{SnCl}_4 + \text{H}_2\text{S}$	300-500 °C for SnS_2 , 525 °C for Sn_2S_3 and 545 °C yielded SnS.	Atmospheric pressure chemical vapour deposition (APCVD). ¹⁰
b)  E = S, Se or Te	300-400 °C for all materials with a gas flow pressure of 10 bar.	AACVD of SnS, SnSe and SnTe films. ¹¹

c) 	400-550 °C.	AACVD of SnS, Sn ₂ S ₃ and SnS ₂ films. ¹²
d)  E=Se or Te	300-600 °C and 1 Torr under a flow of 1:1 He/H ₂ .	MOCVD of SnSe and SnTe films. ¹³
e)  E= S or Se	286 for SnS ₂ , 480-500 °C for SnSe ₂ , 588 °C for SnSe and 558 °C for SnS under a pressure of 0.02 mmHg for - 3 hours.	LPCVD of SnS ₂ , SnSe ₂ and at elevated temperatures, SnS and SnSe. ¹⁴ The same precursor was also used in the liquid injection CVD growth of SnSe nanowires and nanoribbons. ^{15,16}
f)  (1) R = ⁿ Bu, R ¹ = Et, R ² = Et (2) R = ⁿ Bu, R ¹ = Me, R ² = ⁿ Bu (3) R = ⁿ Bu, R ¹ = ⁿ Bu, R ² = ⁿ Bu (4) R = ⁿ Bu, R ¹ = Me, R ² = ⁿ Hex	400-530 °C, argon flow rate of 140 sccm, using a toluene solution of the precursors	AACVD of SnS. ¹⁷

g) 	400 and 450 °C with an Ar flow rate of 180 sccm for 45 min using a THF solution of the precursor.	AACVD of SnSe. ¹⁸
h) 	Deposition at 300 °C yielded cubic SnS and depositions at above 350 °C yielded orthorhombic SnS. Depositions onto Mo substrates, toluene used to dissolve precursor and the carrier gas used was Ar or N ₂ .	AACVD. ¹⁹
i)  Bz = Benzyl group	375-475°C.	AACVD of SnS. ²⁰
j) 	0.2 g of precursor dissolved in THF, carrier gas Ar with furnace temperature of 200 °C.	AACVD of SnSe. ²¹

k) <div style="text-align: center;">  <p>E=Se or Te</p> </div>	300 °C.	Pyrolysis to produce SnSe and SnTe powders. ²²
l) <div style="text-align: center;">  <p>Bz = Benzyl group</p> </div>	200-400 °C.	Thermolysis, producing SnTe powder. ²³
m) <div style="text-align: center;">  </div>	450 °C, 0.02 mmHg for 15-20 mins.	LPCVD of GeTe. ²⁴
n) <div style="text-align: center;">  <p>E= Se or Te</p> </div>	270-350 °C for 1 hour.	Thermal decomposition in solution to produce GeSe and GeTe powders. ²⁵
o) <div style="text-align: center;">  <p>R= Et or nBu</p> </div>	300 °C for 1 hour.	Thermal decomposition in solution to produce GeTe crystals. ²⁶
p) <div style="text-align: center;"> $\text{SiO}_2 + \text{Te}$ </div>	630 °C at 9.12 Torr under a flow rate of Ar/H ₂ at 15 sccm for 35 mins	CVD of Si ₂ Te ₃ . ²⁷

q)	Si + Te	425-680 °C at between 0.1-15 Torr with Ar flow of 15 sccm for 1 h.	CVD of Si ₂ Te ₃ nanoplates and nanoribbons. ³
----	---------	---	---

The majority of the precursors known within the literature for the deposition of tin and germanium chalcogenide materials have high molecular weights, leading to too poor volatility and thermal stability, to be applicable with an LPCVD procedure. This issue has been overcome in these cases by using Aerosol Assisted CVD (AACVD) or direct liquid injection CVD, which first solvate the precursor molecules, then the precursor solution is either nebulised and transported to the reaction chamber via a flow gas or injected in a solution to the reaction chamber, thus negating the need for high volatility. However, precursors that have properties which lend themselves to LPCVD have the potential to be optimised for selective depositions onto patterned substrates and adapted to other deposition techniques. The use of binary precursor systems is also undesirable as the control over stoichiometry is reduced and the requirement for often highly toxic gaseous compounds, like hydrogen sulfide, is increased. One of the common features of the single source precursors shown in Table 2-1 is the rational design of their decomposition pathways, whether that be a reductive elimination step, the elimination of ethenylbenzene or butene via β -hydride elimination, or the elimination of a guanidinato group. To ensure that the final material produced does not include any impurities, any elements not desired in the final material should be avoided and the decomposition pathway should preferably be well established.

When designing a precursor for chalcogenide-based materials, the different chemistry of chalcogen based ligands is an important consideration. Some key ligand types are chalcogenoether ligands, as seen in Table 2-1e, and chalcogenolate ligands, Table 2-1c and j. Chalcogenoether ligands, ER₂, donate a lone pair of electrons to a metal centre to form a dative covalent bond. The strength of this dative covalent bond is related to the donor ability of the ligand and the Lewis acidity of the group 14 fragment. Thus, the order is opposite to that of the electronegativity (e.g. M-TeR₂ > M-SeR₂ > M-SR₂). It is important to separate the kinetic and thermodynamic factors here (i.e. bond stability vs bond lability).²⁸ Chalcogenolate ligands, RE⁻, form a covalent bond with stabilities in the order of M-SR > M-SeR > M-TeR. The strength of the chalcogenolate bonds reflects the relative Lewis basicity of the chalcogens, in line with their electronegativity.

One key feature of any SSP is its high purity, as this will likely affect the material deposition and certainly the yield and purity of the deposited material. This can be achieved by consideration of purification techniques and the preparation steps required. The preparation of a SSP, especially if it is to be used in a scaled up process such as a commercial one, needs to be possible on large enough scales of at least several grams. Also imperative to a commercial SSP is a preparation with as few steps as possible, this will greatly improve both the yield and the purity of the final SSP, thus, reducing costs.²⁹

2.1.2 Film growth

Film growth occurs by several different mechanisms depending on the conditions, deposition process utilised and the chemistry of the precursors involved. This can be problematic for CVD processes as the continuity of the films produced is defined by the growth mechanism and thus may never yield continuous films in some instances. This can also help to produce very thin continuous films by CVD if the mechanism is epitaxial growth, where the crystallite growth occurs with a strong preferred orientation with respect to the crystalline substrate. A more in-depth overview of growth mechanisms, how to control them and some of the things that can be selected through controlling the material growth can be found in section **1.8**.

2.1.3 Material deposition

The deposition techniques relevant to the work presented in this chapter are LPCVD and a larger scale procedure using a commercial CVD/ ALD system, a Picosun R200 Advanced deposition rig. A description of these deposition techniques can be found in Section **1.5**. For the purposes of this chapter more details of the different precursor requirements for these techniques are required. LPCVD allows for a high output of samples across a range of conditions for analysis, this includes information on the temperature range that deposition is possible within and, therefore, informs the optimisation process rapidly. The deposition rig used for the LPCVD in this work consists of a fused quartz CVD tube, connected to a vacuum line, positioned inside a Lenton tube furnace (model: LTF 12/50/300). As mentioned, this set up has many advantages afforded by its simplicity. There are, however, several limitations to the process used in this work. Namely, the inability to achieve fine control of the internal pressure, rate of precursor delivery and the inability to introduce different individual precursors, not as mixtures, without significant adaptation to the setup. To produce several different thin film layers for example, the current LPCVD set up needs to be disassembled, the substrates removed and placed into a new LPCVD tube, which contains the next precursor desired. This means that the processing of multiple layered depositions is far more time consuming than in some other deposition methods where several precursor inlets are

possible. This may be achievable using an adapted CVD tube with segmented precursor bulbs which can be opened and closed during the deposition process but is likely difficult to achieve and would limit the number of layers substantially.

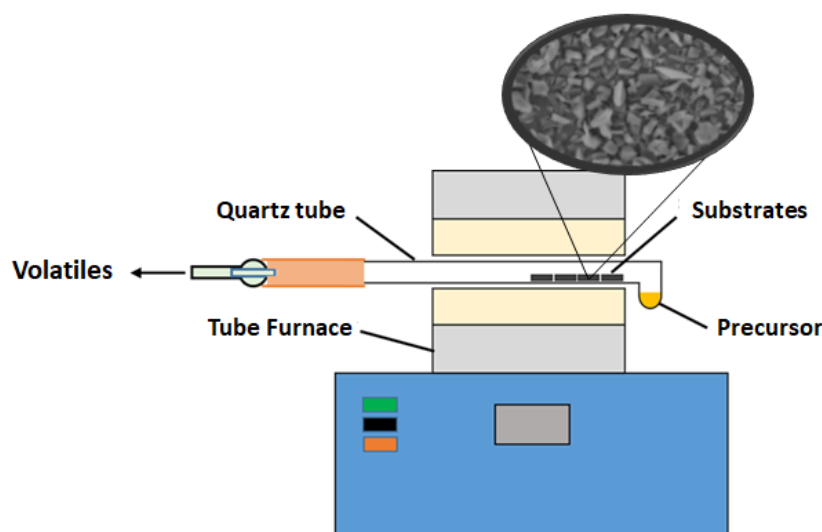


Figure 2-1: Schematic of the LPCVD set up with a portion of an SEM image of a sample of a tin selenide thin film deposited using this equipment.

Firstly, the commercial scale set up, using full 6 inch wafers in a Picosun R200 Advanced rig, requires a slightly increased vapour pressure of the single source precursor compared to that which is appropriate for LPCVD. This is due to the precursor needing to travel through lines connecting the precursor vessels to the reaction chamber under the flow of nitrogen gas in the commercial scale CVD system. Also, of greater importance for the larger scale depositions, using the alternative commercial rig, is the stability of the precursor molecules. This is due to the undesirable possibility of depositing material inside the precursor lines. However, the higher precursor specificity required for this procedure is more than made up for by the additional control over the precursor delivery and substrate temperature, two factors which are of great importance in material growth.

The depositions that were performed from these precursors will be discussed in later chapters. The purpose of this chapter is to focus on the chemistry of the precursors, their characterisation and the evaluation of their properties for different deposition processes.

2.2 Experimental

2.2.1 Precursor preparation and characterisation

All reactions were performed under an inert atmosphere using Schlenk, vacuum line and glove box techniques under a dry nitrogen atmosphere. The solvents used (ethanol, THF and hexane) were dried by distillation from sodium wire prior to use and NMR solvents were stored in a glovebox over molecular sieves. ${}^n\text{Bu}_3\text{SnCl}$, ${}^n\text{Bu}_2\text{SnCl}_2$ (Alfa Aesar) and butane thiol (Aldrich) were stored in a glovebox and used as received. All ${}^1\text{H}$, ${}^{13}\text{C}\{^1\text{H}\}$, ${}^{77}\text{Se}\{^1\text{H}\}$ (referenced against neat SeMe_2), ${}^{119}\text{Sn}\{^1\text{H}\}$ (referenced against neat SnMe_4), ${}^{125}\text{Te}\{^1\text{H}\}$ (referenced against neat TeMe_2) and 2D HMQC NMR spectra were collected on a Bruker AV400 spectrometer in CDCl_3 at room temperature. No relaxation agent was required for use in the NMR spectra of any of the SSPs explored, this is likely a result of the high symmetry around the covalently bonded NMR active nuclei. Microanalyses were obtained *via* the London Metropolitan University elemental analysis service.

All boiling points were measured using thermogravimetric analysis (TGA) using a temperature ramp rate of $5\text{ }^\circ\text{C min}^{-1}$ measured from $29\text{ }^\circ\text{C}$ to $600\text{ }^\circ\text{C}$ under the flow of argon gas at 20 mL min^{-1} . The vapour pressures stated were measured using an isothermal step experiment on the TGA which consisted of a fast temperature ramp rate of $5\text{ }^\circ\text{C min}^{-1}$ followed by 1 hour at the given temperature between 50 and $125\text{ }^\circ\text{C}$ in $25\text{ }^\circ\text{C}$ steps whilst under argon gas at a flow rate of 60 mL min^{-1} . These experiments were used to measure the rate of mass loss at a given temperature. In all cases the sample (between 10 - 30 mg) was held in an alumina crucible. The reference compound, tetrabutyltin, was purchased from Sigma Aldrich and used as received. It was selected as it is similar in chemistry to the single source precursors and has known Antoine constants, meaning that the vapour pressure can be estimated accurately at a given temperature.

The vapour pressure approximations were obtained using an isothermal step experiment using TGA to obtain the rate of mass lost at 50 , 75 , 100 and $125\text{ }^\circ\text{C}$ under the flow of argon gas at a flow rate of 60 mL min^{-1} . All temperatures were stabilised for 1 h and ramp rates to each temperature were $5\text{ }^\circ\text{C min}^{-1}$. This was initially performed for the reference compound, tert-n-butyltin. As values for the vapour pressure of tert-n-butyltin are available within the literature,³⁰ the values given were then used to calculate the instrument constants related to the equipment, at which point the vapour pressures of the single source precursors could be obtained using the calculations below, as demonstrated by Wang *et al.*³¹

$$\begin{array}{l}
 1. \quad \frac{1}{a} \cdot \frac{dm}{dt} = p\alpha \sqrt{\frac{M}{2\pi RT}} \\
 2. \quad k = \frac{\sqrt{2\pi R}}{\alpha} \\
 3. \quad v = \frac{1}{a} \cdot \frac{dm}{dt} \sqrt{\frac{T}{M}} \\
 4. \quad p = kv
 \end{array}$$

Where k , the instrument factor, which includes α , the vapour coefficient and R , the ideal gas constant. The sample dependent factor, v , which concerns the area of the sample containing vessel, a , the rate of mass loss, $\frac{dm}{dt}$, the temperature T and the relative molecular mass, M . Using these the final equation gives the vapour pressure, p . At each of the temperatures measured the value of k was first calculated using the experimentally determined value for v and the known value for p .³⁰ Using the value for k gained in this method, the vapour pressures of all of the single source precursors could be gained.

2.2.2 Precursor synthesis

[SnⁿBu₃(SⁿBu)]: Butane thiol (0.949 g, 1.05×10^{-2} mol, 1.1 eq.) was added to a solution of sodium metal (0.242 g, 1.05×10^{-2} mol, 1.1 eq.) dissolved in anhydrous ethanol (20 mL) and stirred vigorously for 2 h. Removal of volatiles from this colourless solution gave a white powder. THF (20 mL) was then added, followed by a solution of tributyltin chloride (3.877 g, 9.49×10^{-3} mol, 1 eq.) in THF (20 mL), which was added dropwise over the course of 5 min., resulting in a cloudy white suspension, which was stirred for 12 h. The reaction mixture was then filtered, producing a clear, colourless solution. After the THF had been removed under vacuum, the clear colourless liquid remaining was washed in anhydrous hexane (30 mL), filtered to remove particulates and dried *in vacuo*. Yield: 2.618 g, 73%. Elemental analysis: calc. for C₁₆H₃₆SSn ($379.20 \text{ g mol}^{-1}$): C 50.66, H 9.57%. Found: C 50.89, H 10.13%. ¹H NMR (CDCl₃): δ /ppm = 0.84 (two overlapping t, $J = 8.00$ Hz, [12H], CH₃), 1.06 (t with ¹¹⁹Sn satellites, [6H], CH₂Sn), 1.26 (overlapping m, [8H], CH₂), 1.50 (overlapping m, [8H], CH₂) 2.48 (t, [2H], CH₂S). ¹³C {¹H} NMR (CDCl₃): δ /ppm = 13.33 (¹J_{119Sn13C} = 333 Hz, ¹J_{117Sn13C} = 317 Hz, CH₂), 13.60 (CH₃), 13.62 (CH₃), 21.84 (CH₂), 26.40 (CH₂), 27.06 (²J_{119Sn13C} = 60 Hz, CH₂), 28.65 (³J_{119Sn13C} = 21 Hz, CH₂), 37.03 (²J_{119Sn13C} = 12 Hz CH₂). ¹¹⁹Sn {¹H} NMR (CDCl₃): δ /ppm = 75.2 (s).

[SnBu₂(SBu)₂]: Butane thiol (0.878 g, 9.73×10^{-3} mol, 2 eq.) was added to a solution of sodium metal (0.224 g, 9.73×10^{-3} mol, 2 eq.) dissolved in anhydrous ethanol (20 mL) and stirred vigorously for 1 h. This colourless solution was then taken to dryness *in vacuo*, leaving a white powder. This white powder was then suspended in THF (15 mL) and a solution of dibutyltin dichloride (1.478 g, 4.86×10^{-3} mol, 1 eq.), in THF (15 mL), was added dropwise over the course of

Chapter 2

5 min., resulting in a cloudy white suspension, which was stirred for 12 h. The reaction mixture was then filtered, producing a clear colourless solution. After the THF had been removed under vacuum, a colourless oil remained, which was washed with anhydrous hexane (20 mL) and dried *in vacuo*. Yield: 1.407 g, 70%. Elemental analysis: calc. for $C_{16}H_{36}S_2Sn$ (411.26 gmol^{-1}): C 46.73, H 8.82 %. Found: C 45.96. H 9.44 %. 1H NMR ($CDCl_3$): $\delta/ppm = 0.91$ (two overlapping t, $J = 8.00$ Hz, [12H], CH_3), 1.39 (overlapping tquart, tt and t with ^{119}Sn satellites, [12H], CH_2 and $SnCH_2$), 1.58 (overlapping tquart and tt, [8H], CH_2), 2.69 (t, [8H], SCH_2). $^{13}C\{^1H\}$ NMR ($CDCl_3$): $\delta/ppm = 13.52$ (CH_3), 13.59 (CH_2), 17.79 ($^1J_{119Sn13C} = 377$ Hz, $^1J_{117Sn13C} = 360$ Hz, CH_3), 21.77 (CH_2), 26.70 ($^2J_{119Sn13C} = 73$ Hz, $^2J_{117Sn13C} = 70$ Hz CH_2), 26.98 ($^3J_{119Sn13C} = 16$ Hz CH_2), 28.24 ($^2J_{119Sn13C} = 25$ Hz, CH_2), 36.51 ($^3J_{119Sn13C} = 14$ Hz, CH_2). $^{119}Sn\{^1H\}$ NMR ($CDCl_3$ at room temperature): $\delta/ppm = 127.6$ (s).

[SnBu₃(SeBu)]: Selenium shot (2.041 g, 2.59×10^{-2} mol, 1.1 eq.) was ground into a fine powder under an inert atmosphere in a glovebox and suspended in THF (30 mL). The suspension was then frozen in liquid nitrogen before the dropwise addition of nBuLi solution in hexanes (15 mL, 2.43×10^{-2} mol). After the mixture had thawed and been allowed to stir, a colour change from a black suspension to a yellow solution and then to a deep red solution was observed. Further nBuLi solution (1 mL, 1.60×10^{-3} mol) was then added dropwise until a pale yellow colour persisted. A solution of nBu_3SnCl (7.650 g, 2.35×10^{-2} mol, 1 eq.) in THF (30 mL) was then added dropwise to the cooled ($0^\circ C$) solution of nBuSeLi . The reaction mixture was then stirred vigorously overnight. The reaction mixture was then concentrated under vacuum, hexane (30 mL) was added, at which point the solution turned cloudy with the precipitation of $LiCl$. The mixture was filtered by cannula filter, before concentrating under vacuum, washing with further hexane (30 mL), filtering once more and finally drying *in vacuo*, leaving a yellow/orange oil. Yield: 7.936 g, 79%. Elemental analysis: calc. for $C_{16}H_{36}SeSn$ (426.11 gmol^{-1}): C 45.10, H 8.52 %. Found: C 45.29. H 8.95 %. 1H NMR ($CDCl_3$): $\delta/ppm = 0.88$ (two overlapping t, $J = 8.00$ Hz, [12H], CH_3), 1.13 (t with ^{119}Sn satellites, [6H], $SnCH_2$), 1.29 - 1.40 (overlapping dt, [8H], CH_2), 1.54 - 1.62 (overlapping dt, [8H], CH_2), 2.53 (overlapping t with ^{77}Se satellites, [2H], $SeCH_2$). $^{13}C\{^1H\}$ NMR ($CDCl_3$): $\delta/ppm = 13.07$ ($^1J_{119Sn13C} = 318$ Hz, $^1J_{117Sn13C} = 305$ Hz, CH_2), 13.45 (CH_2), 13.54 (CH_3), 16.79 ($^3J_{77Se13C} = 14$ Hz, CH_2), 22.90 (CH_2), 26.98 ($^2J_{119Sn13C} = 62$ Hz, $^2J_{117Sn13C} = 60$ Hz, CH_2), 28.94 ($^3J_{119Sn13C} = 21$ Hz, CH_2), 36.70 ($^3J_{119Sn13C} = 11$ Hz, CH_2). $^{77}Se\{^1H\}$ NMR ($CDCl_3$): $\delta/ppm = -213.8$ (s, $^1J_{77Se119Sn} = 1050$ Hz). $^{119}Sn\{^1H\}$ NMR ($CDCl_3$): $\delta/ppm = 51.9$ (s, $^1J_{77Se119Sn} = 1056$ Hz).

[SnEt₃(SeBu)]: Selenium shot (1.268 g, 1.61×10^{-2} mol, 1.1 eq.) was ground into a fine powder under an inert atmosphere in a glovebox before being suspended in THF (30 mL). The suspension was then frozen in liquid nitrogen before the dropwise addition of nBuLi solution in hexanes (9 mL, 1.45×10^{-2} mol). After the mixture had thawed and been allowed to stir for 1 h and the colour change from a black suspension to yellow and then to red had been observed. Further nBuLi

solution (1 mL, 1.6×10^{-2} mol) was then added dropwise until a pale-yellow colour persisted. A solution of Et_3SnCl (3.529 g, 1.46×10^{-2} mol, 1 eq.) in THF (30 mL) was then added dropwise to the cooled (0°C) solution of ${}^n\text{BuSeLi}$. The reaction mixture was then stirred vigorously overnight, before being concentrated under vacuum. Hexane (30 mL) was then added to the solution turning it cloudy with the precipitation of LiCl . The mixture was filtered by cannula filter before concentrating under vacuum, washing with further hexane (30 mL), filtering once more and finally drying *in vacuo* leaving a yellow/orange oil. Yield: 3.967 g, 79%. Elemental analysis: calc. for $\text{C}_{10}\text{H}_{24}\text{SeSn}$ ($341.95 \text{ g mol}^{-1}$): C 35.13, H 7.07 %. Found: C 35.73, H 7.48 %. ${}^1\text{H}$ NMR (CDCl_3): $\delta/\text{ppm} = 0.89$ (t, $J = 8.00$ Hz, [3H], CH_3), 1.13 (q with ${}^{119}\text{Sn}$ satellites, [6H], SnCH_2), 1.24 (t, [9H], CH_3), 1.39 (tquart, [2H], CH_2), 1.62 (tt, [2H], CH_2), 2.55 (overlapping t with ${}^{77}\text{Se}$ satellites, [2H], SeCH_2). ${}^{13}\text{C}\{{}^1\text{H}\}$ NMR (CDCl_3): $\delta/\text{ppm} = 4.44$ (${}^1J_{119\text{Sn}13\text{C}} = 324$ Hz, ${}^1J_{117\text{Sn}13\text{C}} = 310$ Hz, CH_2), 10.91 (${}^2J_{119\text{Sn}13\text{C}} = 24$ Hz, CH_3), 13.48 (CH_3), 16.60 (${}^1J_{77\text{Se}13\text{C}} = 55$ Hz, ${}^2J_{119\text{Sn}13\text{C}} = 14$ Hz, CH_2), 22.93 (CH_2), 36.83 (${}^2J_{77\text{Se}13\text{C}} = 10$ Hz, CH_2). ${}^{77}\text{Se}\{{}^1\text{H}\}$ NMR (CDCl_3): $\delta/\text{ppm} = -226.5$ (s, ${}^1J_{77\text{Se}119\text{Sn}} = 1040$ Hz). ${}^{119}\text{Sn}\{{}^1\text{H}\}$ NMR (CDCl_3): $\delta/\text{ppm} = 63.5$ (s, ${}^1J_{77\text{Se}119\text{Sn}} = 1065$ Hz).

[SnBu₃(TeBu)]: Tellurium granules (2.846 g, 2.23×10^{-2} mol, 1.05 eq.) were ground into a fine powder under an inert atmosphere in the glovebox before being suspended in THF (30 mL). The suspension was then frozen in liquid nitrogen before the dropwise addition of ${}^n\text{BuLi}$ solution in hexanes (13 mL, 2.18×10^{-2} mol). After the mixture had slowly thawed, the solution initially turned yellow and then red. Further ${}^n\text{BuLi}$ solution (0.3 mL, 5.03×10^{-4} mol) was then added dropwise until a pale yellow colour persisted. A solution of ${}^n\text{Bu}_3\text{SnCl}$ (6.856 g, 2.11×10^{-3} mol, 1 eq.) in THF (30 mL) was then added dropwise to the cooled (0°C) solution. The reaction mixture was stirred vigorously for 24 h, leaving an orange solution. The volatiles were then removed *in vacuo* and the orange oily residue was then washed twice with hexane (30 mL), leading to the precipitation of LiCl . This was removed by cannula filtration before the filtrate was taken to dryness *in vacuo*, leaving an orange oil. The compound is somewhat moisture sensitive and was therefore handled and stored under an inert atmosphere to avoid degradation, although it can be handled briefly in air. Yield 8.608 g, 86%. Elemental analysis: calc. for $\text{C}_{16}\text{H}_{36}\text{SnTe}$ (474.85): C 40.48, H 7.64 %. Found: C 41.60, H 7.76 %. ${}^1\text{H}$ NMR (CDCl_3): $\delta/\text{ppm} = 0.90$ (two overlapping t, $J = 8.00$ Hz, [12H], CH_3), 1.19 (t with ${}^{119}\text{Sn}$ satellites, [6H], SnCH_2), 1.34 (overlapping m, [8H], CH_2), 1.55 and 1.65 (overlapping m, [8H], CH_2), 2.52 (t with overlapping ${}^{125}\text{Te}$ satellites, [2H], TeCH_2). ${}^{13}\text{C}\{{}^1\text{H}\}$ NMR (CDCl_3): $\delta/\text{ppm} = -7.05$ (${}^1J_{125\text{Te}13\text{C}} = 133$ Hz, ${}^2J_{119\text{Sn}13\text{C}} = 13$ Hz, CH_2), 12.54 (${}^1J_{119\text{Sn}13\text{C}} = 299$ Hz, ${}^1J_{117\text{Sn}13\text{C}} = 286$ Hz, CH_2), 13.27 (CH_3), 13.61 (CH_3), 25.01 (CH_2), 26.96 (${}^2J_{119\text{Sn}13\text{C}} = 63$ Hz, CH_2), 29.69 (${}^3J_{119\text{Sn}13\text{C}} = 21$ Hz, CH_2), 37.34 (${}^3J_{125\text{Te}13\text{C}} = 8$ Hz CH_2). ${}^{119}\text{Sn}\{{}^1\text{H}\}$ NMR (CDCl_3): $\delta/\text{ppm} = -15.6$ (${}^1J_{119\text{Sn}125\text{Te}} = 2765$ Hz). ${}^{125}\text{Te}\{{}^1\text{H}\}$ NMR (CDCl_3): $\delta/\text{ppm} = -536.5$ (${}^1J_{119\text{Sn}125\text{Te}} = 2704$ Hz).

[GeⁿBu₃(SⁿBu)]: Butane thiol (0.227 g, 2.52×10^{-3} mol, 1 eq.) was added to a solution of sodium metal (0.076 g, 2.52×10^{-3} mol, 1 eq.) dissolved in anhydrous ethanol (15 mL) and stirred vigorously over the course of 2 h. This colourless solution was then placed under vacuum and the volatiles removed, leaving a white powder. This white powder was then stirred in THF (15 mL) and a solution of tributylgermanium chloride (0.704 g, 2.52×10^{-3} mol, 1 eq.), in THF (15 mL), was added dropwise over the course of 5 min., resulting in a clear reaction mixture, which was stirred for 1 h before being refluxed at 70 °C. The then cloudy white reaction mixture was then reduced in volume under vacuum and washed in hexane (15 mL) before being filtered, producing a clear colourless solution. After the solvent had been removed under vacuum, the clear colourless liquid was washed in anhydrous hexane (20 mL) and dried under vacuum. Yield: 0.607 g, 72%. Elemental analysis: calc for C₁₆H₃₆GeS (333.12 gmol⁻¹). C 57.69, H 10.89 %. Found: C 57.54, H 10.93 %. ¹H NMR (CDCl₃): δ/ppm = 0.90 (t, *J* = 8.00 Hz, [12H], CH₃) 1.01 (t, [6H], CH₂) 1.35-1.42 (two tq and a tt, [14H], CH₂), 2.47 (t, [2H], CH₂) 3.65 (t, [2H], CH₂). ¹³C {¹H} NMR (CDCl₃) δ/ppm = 13.62 (CH₃), 13.67 (CH₃), 15.72 (CH₂), 21.89 (CH₂), 26.19 (CH₂), 26.26 (CH₂), 27.06 (CH₂), 35.61 (CH₂).

[GeⁿBu₂(SⁿBu)₂]: Butane thiol (1.623 g, 1.8×10^{-2} mol, 2.2 eq.) was added to a solution of sodium metal (0.415 g, 1.8×10^{-2} mol, 2.2 eq.) dissolved in anhydrous ethanol (15 mL) and stirred vigorously until the sodium metal had fully reacted and dissolved. The volatiles were then removed under vacuum leaving a white powder. This white powder was then stirred in THF (15 mL) and a solution of dibutylgermanium dichloride (2.117 g, 8.21×10^{-3} mol, 1 eq.), in THF (15 mL), was added dropwise over the course of five minutes resulting in a cloudy white suspension which was stirred for 2 h before being refluxed at 70 °C for 5 h. The cloudy white reaction mixture was then condensed and washed in hexane (15 mL) before being filtered producing a clear, colourless solution. After the solvent had been removed under vacuum, a clear colourless liquid remaining was washed in anhydrous hexane (20 mL). After removing the volatiles under vacuum, the product was distilled to produce a clear, colourless liquid. Yield: 1.807 g, 60%. Elemental analysis: calc. for C₁₆H₃₆GeS₂ (366.21 gmol⁻¹): C 52.63, H 9.94 %. Found: C 52.98, H 10.05 %. ¹H NMR (CDCl₃): δ/ppm = 0.89 (two overlapping t, *J* = 8.00 Hz, [12H], CH₃), 1.25 (t, [4H], GeCH₂), 1.36-1.44 (overlapping tq and two tt, [12H], CH₂), 1.59 (t, [4H], CH₂), 2.60 (t, [4H], SCH₂). ¹³C {¹H} NMR (CDCl₃): δ/ppm = 13.58 (2CH₃), 19.32 (CH₂), 21.82 (CH₂), 25.73 (CH₂), 26.82 (CH₂), 27.10 (CH₂), 34.97 (CH₂).

[GeⁿBu₃(SeⁿBu)]: Selenium granules (0.229 g, 2.89×10^{-3} mol, 1.1 eq.) were ground into a fine powder inside of a glovebox before being suspended in THF (20 mL). The solution was then frozen in liquid nitrogen before the dropwise addition of ⁿBuLi solution in hexanes (1.1 mL, 1.76×10^{-3} mol). After the mixture had thawed and been allowed to stir, the solution turned initially pale yellow and then to red. Further ⁿBuLi solution (0.6 ml, 9.64×10^{-4} mol) was then

added dropwise until the pale-yellow colour persisted. A solution of ${}^n\text{Bu}_3\text{GeCl}$ (0.735 g, 2.63×10^{-3} mol, 1 eq.) in THF (10 mL) was then added dropwise to the pale-yellow solution followed by a further portion of THF (10 mL) used to rinse the Schlenk containing the ${}^n\text{Bu}_3\text{GeCl}$. The reaction mixture was then refluxed at 85 °C and stirred vigorously over the course of 12 h. Upon allowing the yellow solution to cool, removing the solvent *in vacuo* and adding hexane (30 mL), the solution turned cloudy with the precipitation of LiCl. The mixture was filtered by cannula filter before pumping down, washing with further hexane (30 mL) and then dried under vacuum, leaving a yellow oil. Yield 0.767 g, 77 %. Elemental analysis: calc. for $\text{C}_{16}\text{H}_{36}\text{GeSe}$ ($380.03 \text{ g mol}^{-1}$): C 50.57, H 9.55 %. Found: C 51.11, H 9.67 %. ${}^1\text{H}$ NMR (CDCl_3): $\delta/\text{ppm} = 0.89$ (two overlapping t, $J = 8.00$ Hz, [12H], CH_3) 1.04 (t, [6H], GeCH_2) 1.29 - 1.46 (overlapping tt, tquart and tt, [14H] CH_2) 1.62 (tquart, [2H], CH_2) 2.47 (t with overlapping ${}^{77}\text{Se}$ satellites, [2H], SeCH_2). ${}^{13}\text{C}$ $\{^1\text{H}\}$ NMR (CDCl_3): $\delta/\text{ppm} = 13.50$ (CH_3), 13.65 (CH_2), 16.18 (CH_3), 17.36 (CH_2), 22.95 (CH_2), 26.11 (CH_2), 27.43 (CH_2), 35.53 (CH_2). ${}^{77}\text{Se}$ $\{^1\text{H}\}$ NMR (CDCl_3): $\delta/\text{ppm} = -144.8$ (s).

[$\text{Ge}^n\text{Bu}_3(\text{Te}^n\text{Bu})$]: Tellurium granules (0.297 g, 2.33×10^{-3} mol) were ground into a fine powder under an inert atmosphere in the glovebox before being suspended in THF (20 mL). The solution was then frozen in liquid nitrogen before the dropwise addition of ${}^n\text{BuLi}$ solution in hexanes (1 mL, 1.60×10^{-3} mol). After the mixture had thawed and been allowed to stir, the solution initially turned yellow and then to red. ${}^n\text{BuLi}$ solution (0.5 mL, 8.0×10^{-4} mol) was added dropwise until the pale yellow colour persisted. A solution of ${}^n\text{Bu}_3\text{GeCl}$ (0.651 g, 2.33×10^{-3} mol) in THF (10 mL), followed by a further rinse of THF (10 mL) to ensure that no residual ${}^n\text{Bu}_3\text{GeCl}$ remained, was then added dropwise to the pale yellow solution. The reaction mixture was then refluxed to 90 °C and stirred vigorously for 24 h, leaving an amber solution. Upon allowing the solution to cool, removing the volatiles *in vacuo* and adding hexane (30 mL), the solution turned cloudy with the precipitation of LiCl. The mixture was filtered by cannula filter before having the volatiles removed under vacuum, being washed with further hexane (30 mL) and then brought to dryness under vacuum leaving a reddish orange oil. Yield 0.836 g, 84 %. Elemental analysis: calc. for $\text{C}_{16}\text{H}_{36}\text{GeTe}$ ($428.77 \text{ g mol}^{-1}$): C 44.83, H 8.46 %. Found: C 44.05, H 8.07 %. ${}^1\text{H}$ NMR (CDCl_3): $\delta/\text{ppm} = 0.90$ (two overlapping t, $J = 8.00$ Hz, [12H], CH_3) 1.11 (t, [6H], GeCH_2) 1.36 and 1.40 (overlapping tq, tq and t, [14H], CH_2) 1.65 (tq, [2H], CH_2) 2.47 (t, [2H], TeCH_2). ${}^{13}\text{C}$ $\{^1\text{H}\}$ NMR (CDCl_3): $\delta/\text{ppm} = -5.51$ (CH_2), 13.31 (CH_2), 13.70 (CH_3), 16.68 (CH_2), 25.01 (CH_2), 26.02 (CH_2), 28.32 (CH_2), 36.37 (CH_2). ${}^{125}\text{Te}$ $\{^1\text{H}\}$ NMR (CDCl_3): $\delta/\text{ppm} = -400.1$ (s).

[$\text{GeBu}_2(\text{TeBu})_2$]: Tellurium granules (2.1784 g, 1.71×10^{-2} mol, 2.2 eq.) were ground into a fine powder under an inert atmosphere in the glovebox before being suspended in THF (20 mL). The suspension was then frozen in liquid nitrogen before the dropwise addition of ${}^n\text{BuLi}$ solution in hexanes (10 mL, 1.60×10^{-2} mol). After the mixture had thawed, the solution initially turned

yellow and then red. Further ${}^n\text{BuLi}$ solution (1 mL, 1.6×10^{-2} mol) was added dropwise until a pale yellow colour persisted. A solution of ${}^n\text{Bu}_2\text{GeCl}_2$ (2.000 g, 7.76×10^{-3} mol, 1 eq.) in THF (20 mL) was then added dropwise, while it was cooled using an ice bath. The reaction mixture was stirred vigorously for 24 h, leaving an orange solution. The volatiles were then removed *in vacuo* and the orange oily residue was then washed twice with hexane (30 mL), leading to the precipitation of LiCl. This was removed by cannula filtration before the filtrate was taken to dryness *in vacuo*, leaving an orange oil. Yield 4.001 g, 93%. Elemental analysis: calc. for $\text{C}_{16}\text{H}_{36}\text{GeTe}_2$ (556.47 g mol^{-1}): C 34.55, H 6.52 %. Found: C 34.52, H 6.51 %. ${}^1\text{H}$ NMR (CDCl_3): $\delta/\text{ppm} = 0.89$ (two overlapping t, $J = 8.00$ Hz, [12H], CH_3), 1.37-1.49 (two overlapping tt and two t quart [16H], GeCH_2 and CH_2), 1.69 (overlapping t quart, [4H], CH_2), 2.58 (t with overlapping ${}^{125}\text{Te}$ satellites, [4H], TeCH_2). ${}^{13}\text{C}\{{}^1\text{H}\}$ NMR (CDCl_3): $\delta/\text{ppm} = 1.97$ (${}^1J_{125\text{Te}13\text{C}} = 138$ Hz, CH_2), 13.34 (CH_3), 13.58 (CH_3), 21.52 (CH_2), 25.01 (CH_2), 25.29 (CH_2), 29.36 (CH_2), 35.55 (${}^3J_{125\text{Te}13\text{C}} = 16$ Hz, CH_2). ${}^{125}\text{Te}\{{}^1\text{H}\}$ NMR (CDCl_3): $\delta/\text{ppm} = -294.9$ (s).

Attempted synthesis of $[\text{Si}^n\text{Bu}_3(\text{S}^n\text{Bu})]$: Butane thiol (0.687 g, 7.62×10^{-3} mol, 1.1 eq.) was added to a solution of sodium metal (0.175 g, 7.62×10^{-3} mol, 1.1 eq.) dissolved in anhydrous ethanol (15 mL) and stirred vigorously until the sodium metal had fully reacted and dissolved. This colourless solution was then pumped down to dryness leaving a white powder. This white powder was then stirred in THF (15 mL) and a solution of tri-*n*-butylsilyl chloride (1.628 g, 6.93×10^{-3} mol, 1 eq.), in THF (15 mL), was added dropwise over the course of five minutes resulting in a cloudy white suspension which was then refluxed at 70 °C for 5 h. The cloudy white reaction mixture was then condensed and washed in hexane (15 mL) before being filtered producing a clear, colourless solution. After the solvent had been removed under vacuum, a clear colourless liquid remaining was washed in anhydrous hexane (20 mL). After removing the volatiles under vacuum, the product was distilled to produce a clear, colourless liquid. Yield: 1.807 g, 60%. ${}^1\text{H}$ NMR (CDCl_3): $\delta/\text{ppm} = 0.88$ (t, $J = 8.00$ Hz, [6H], SiCH_2), 0.90 (overlapping t's, [12H], CH_3), 1.25-1.48 (overlapping t quart and two tt, [14H], CH_2), 1.63 (dt, [2H], CH_2), 2.46 (t, [2H], SCH_2). ${}^{13}\text{C}\{{}^1\text{H}\}$ NMR (CDCl_3): $\delta/\text{ppm} = 13.58$ (2 CH_3), 19.32 (CH_2), 21.82 (CH_2), 25.73 (CH_2), 26.82 (CH_2), 27.10 (CH_2), 34.97 (CH_2). ${}^{29}\text{Si}\{{}^1\text{H}\}$ NMR (CDCl_3): $\delta/\text{ppm} = 33.0$ (s) corresponds to remaining starting material, 19.0 (s) major peak, -21.15 (s).

$[\text{Si}^n\text{Bu}_3(\text{Se}^n\text{Bu})]$: Selenium granules (0.777 g, 9.83×10^{-3} mol, 1.1 eq.) were ground to a fine powder inside of a glovebox and suspended in THF (20 mL). The solution was then frozen in liquid nitrogen before the dropwise addition of ${}^n\text{BuLi}$ solution in hexanes (6 mL, 9.67×10^{-3} mol). After the mixture had thawed and been allowed to stir, the solution turned initially pale yellow and then to red. Further ${}^n\text{BuLi}$ solution (0.6 mL, 9.64×10^{-4} mol) was then added dropwise until the pale-yellow colour persisted. A solution of ${}^n\text{Bu}_3\text{SiCl}$ (2.100 g, 8.94×10^{-3} mol, 1 eq.) in THF (20 mL)

was then added dropwise followed, by a further rinse of THF (10 mL) to ensure no residue of ${}^n\text{Bu}_3\text{SiCl}$ remained, was then added dropwise to the pale-yellow solution. The reaction mixture was then stirred vigorously over the course of 12 h. The solvent was then removed *in vacuo* and hexane (30 mL) was added, the solution then turned cloudy with the precipitation of LiCl. The mixture was filtered by cannula filter before reducing the volume under vacuum, washing with further hexane (30 mL) and finally removal of the volatiles under vacuum, leaving a light orange oil. Yield 2.667 g, 89 %. ${}^1\text{H}$ NMR (CDCl_3): $\delta/\text{ppm} = 0.88$ (t, $J = 8.00$ Hz, [6H], SiCH_2), 0.90 (overlapping t's, [12H], CH_3), 1.25-1.48 (overlapping t quart and two tt, [14H], CH_2), 1.63 (dt, [2H], CH_2), 2.46 (t, [2H], SeCH_2). ${}^{13}\text{C}$ $\{{}^1\text{H}\}$ NMR (CDCl_3): $\delta/\text{ppm} = 13.49$ (CH_3), 13.70 (CH_3), 14.56 (${}^2J_{13\text{C}77\text{Se}} = 50$ Hz, SiCH_2), 17.56 (${}^1J_{13\text{C}77\text{Se}} = 52$ Hz, SeCH_2), 22.94 (CH_2), 26.20 (CH_2), 26.40 (CH_2), 35.14 (${}^2J_{13\text{C}77\text{Se}} = 9$ Hz, CH_2). ${}^{29}\text{Si}$ $\{{}^1\text{H}\}$ NMR (CDCl_3): $\delta/\text{ppm} = 20.9$ (s). ${}^{77}\text{Se}$ $\{{}^1\text{H}\}$ NMR (CDCl_3): $\delta/\text{ppm} = -156.8$ (s).

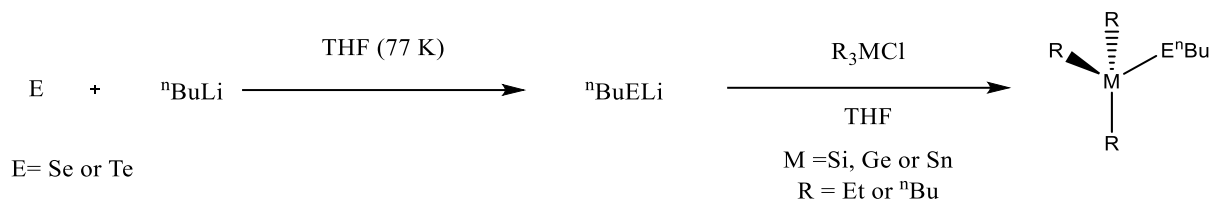
[SiBu₃(TeBu)]: Tellurium granules (0.7299 g, 5.72×10^{-3} mol, 1.1 eq.) were ground into a fine powder under an inert atmosphere in the glovebox before being suspended in THF (20 mL). The suspension was then frozen in liquid nitrogen before the dropwise addition of ${}^n\text{BuLi}$ solution in hexanes (2.6 mL, 4.16×10^{-3} mol). After the mixture had thawed, the solution initially turned yellow and then red. Further ${}^n\text{BuLi}$ solution (1 mL, 1.6×10^{-2} mol) was added dropwise until a pale yellow colour persisted. A solution of ${}^n\text{Bu}_3\text{SiCl}$ (1.2219 g, 5.20×10^{-3} mol, 1 eq.) in THF (20 mL) was then added dropwise, while it was cooled using an ice bath. The reaction mixture was stirred vigorously for 24 h, leaving an amber solution. The volatiles were then removed *in vacuo* and the amber oily residue was washed twice with hexane (30 mL), leading to the precipitation of LiCl. This was removed by cannula filtration before the filtrate was taken to dryness *in vacuo*, leaving a clear amber oil. Yield 1.7420 g, 87%. Elemental analysis: calc. for $\text{C}_{16}\text{H}_{36}\text{SiTe}$ ($384.22 \text{ g mol}^{-1}$): C 50.03, H 9.45 %. Found: C 50.01, H 10.09 %. ${}^1\text{H}$ NMR (CDCl_3): $\delta/\text{ppm} = 0.90$ (3 overlapping t, $J = 8.00$ Hz, [18H], CH_3 and SiCH_2), 1.37 (2 overlapping tt and t quart, [14H], CH_2), 1.65 (t quart, [2H], CH_2), 2.42 (t with overlapping ${}^{125}\text{Te}$ satellites, [2H], TeCH_2). ${}^{13}\text{C}\{{}^1\text{H}\}$ NMR (CDCl_3): $\delta/\text{ppm} = -4.82$ (${}^1J_{125\text{Te}13\text{C}} = 130$ Hz, CH_3), 13.29 (CH_3), 13.71 (CH_3), 15.37 (${}^2J_{125\text{Te}13\text{C}} = 49$ Hz, CH_2), 25.00 (CH_2), 26.28 (CH_2), 26.67 (CH_2), 36.03 (${}^3J_{125\text{Te}13\text{C}} = 18$ Hz CH_2). ${}^{29}\text{Si}$ $\{{}^1\text{H}\}$ NMR (CDCl_3): $\delta/\text{ppm} = 10.98$ (s). ${}^{125}\text{Te}$ $\{{}^1\text{H}\}$ NMR (CDCl_3): $\delta/\text{ppm} = -427.6$ (s).

2.3 Results and Discussion

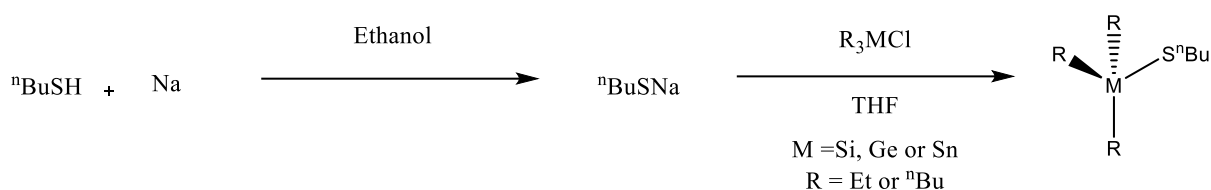
2.3.1 Group 14 chalcogenide single source precursor preparation

The synthetic routes to the precursors used in this work, shown in the below Schemes 2-1, 2-2 and 2-3, consist of the initial formation of an alkyl lithium or alkyl sodium chalcogenolate, followed by the salt metathesis reaction with a group 14 chloride, as reported previously for

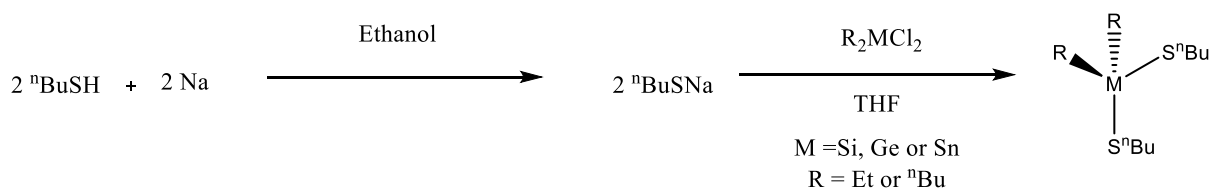
[SnⁿBu₃(SⁿBu)] and **[SnⁿBu₂(SⁿBu)₂]**.³² The salt metathesis reaction worked best when performed initially at 0 °C and the reaction mixture was allowed to warm to room temperature. The reactions worked well producing good yields of between 60-93 % and unlike the alternative synthesis method which used dry liquid ammonia, contain fewer harmful reactants.³³



Scheme 2-1: Synthetic routes to **[SiⁿBu₃(SeⁿBu)]**, **[SiⁿBu₃(TeⁿBu)]**, **[GeⁿBu₃(SeⁿBu)]**, **[GeⁿBu₃(TeⁿBu)]**, **[SnⁿBu₃(SeⁿBu)]**, **[SnⁿBu₃(TeⁿBu)]** and **[SnEt₃(SeⁿBu)]**.



Scheme 2-2: Synthetic routes to **[SiⁿBu₃(SⁿBu)]**, **[GeⁿBu₃(SⁿBu)]** and **[SnⁿBu₃(SⁿBu)]**.



Scheme 2-3: Synthetic route to **[GeⁿBu₂(SⁿBu)₂]** and **[SnⁿBu₂(SⁿBu)₂]**.

The n-butyl substituent was selected, as discussed in literature published from within the group, because of its clean decomposition pathway by β -hydride elimination and reductive elimination.^{14,34} This decomposition likely proceeds via the elimination of butene and either butane or hydrogen gas. As all the waste decomposition products produced are highly volatile, they are easily removed *in vacuo* during the LPCVD procedure. The relatively low mass of the butyl substituent also gives the single source precursors a vapour pressure that is reasonable for the LPCVD procedure. The general form of the single source precursors is **[MⁿBu₃(EⁿBu)]**, where M is Si, Ge or Sn and E is S, Se or Te. However, in the case of **[SnⁿBu₂(SⁿBu)₂]**, the increased sulfur content provided from the second SⁿBu⁻ group was introduced as a result of the sulfur deficiency observed within the SnS films deposited from **[SnⁿBu₃(SⁿBu)]**.

For the scale up of a deposition process, a single source precursor will ideally have a simple preparation consisting of only a few steps. This is a feature of the family of SSPs presented here. The synthesis was also able to be scaled up to a much larger scale. In the case of **[SnⁿBu₃(SeⁿBu)]**

this was performed on a 20 g scale in a good yield and in the case of **[SnⁿBu₃(TeⁿBu)]** and **[SnEt₃(SeⁿBu)]** on 10 g scales similarly in good yields.

Of high importance for material deposition processes is the purity of the SSPs used, as this will affect the deposited material. Throughout all of the work performed herein one of the major means of determining the purity of the SSPs was using NMR spectroscopy. This can be used to determine that there are no other contributions from other ¹H or ¹³C environments, as shown in Figure 2-2 and Figure 2-3, respectively.

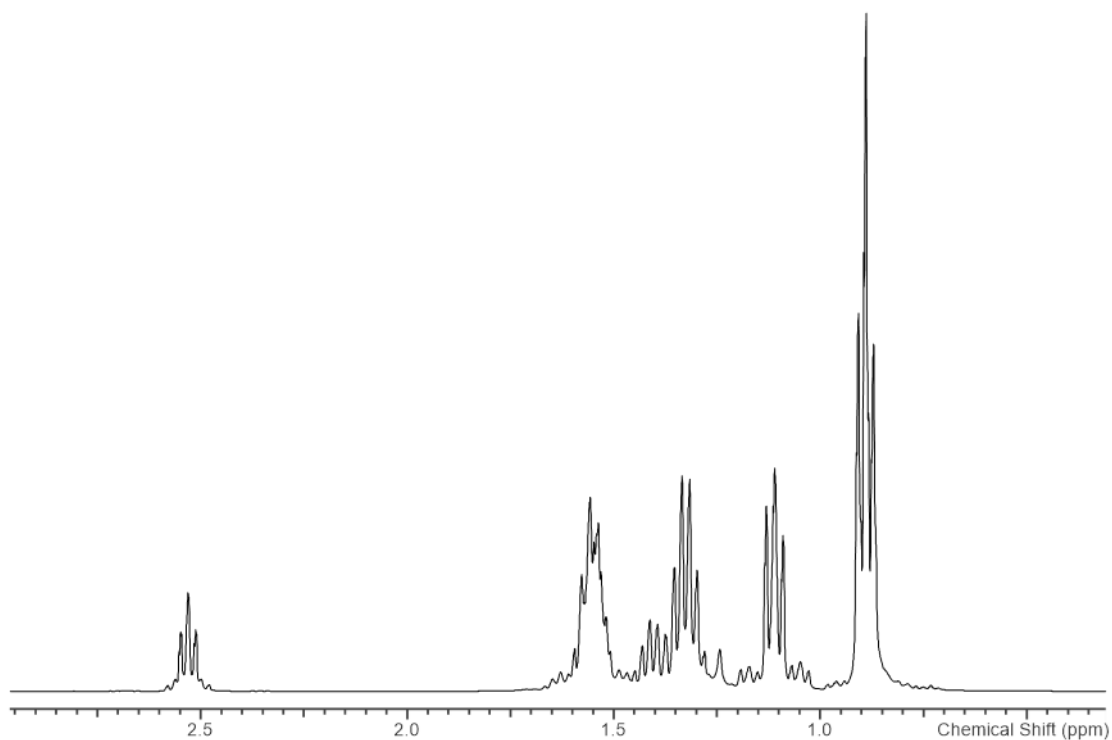


Figure 2-2: ¹H NMR spectrum for **[SnⁿBu₃(SⁿBu)]**, showing the clean SSP with no impurities.

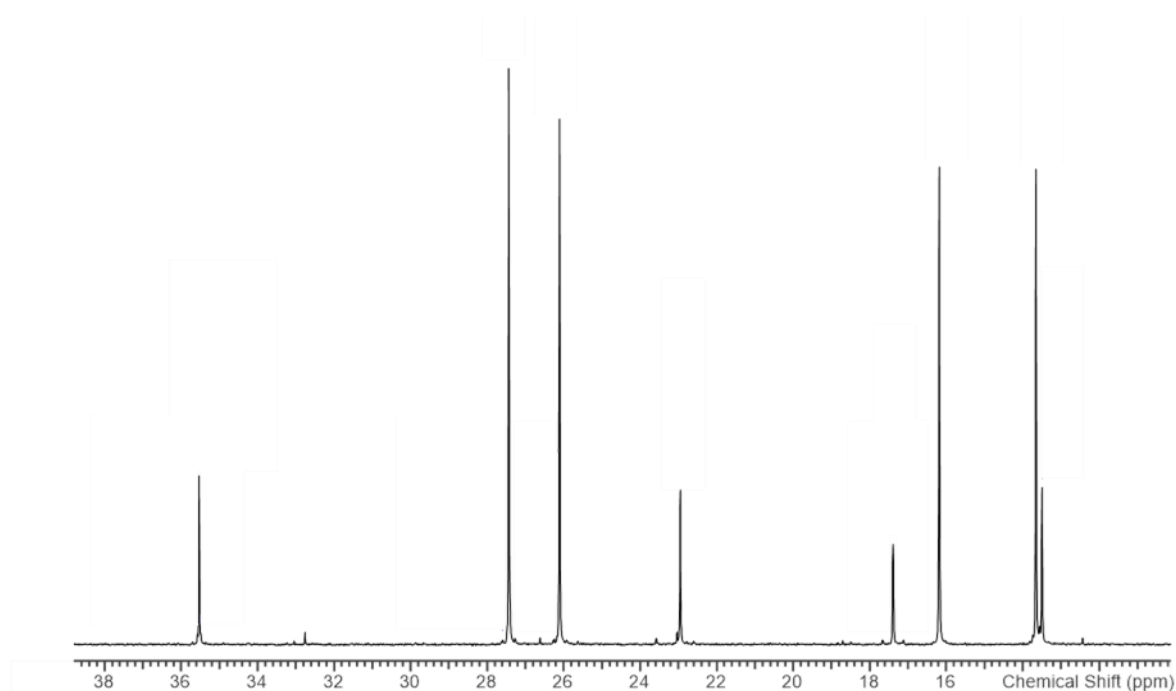


Figure 2-3: $^{13}\text{C}\{^1\text{H}\}$ NMR spectrum for $[\text{Ge}^n\text{Bu}_3(\text{Se}^n\text{Bu})]$, showing the clean SSP with 8 well defined ^{13}C environments with no impurities.

In SSPs where two NMR active heteroatoms are bonded together, such as in $[\text{Sn}^n\text{Bu}_3(\text{Se}^n\text{Bu})]$, $[\text{SnEt}_3(\text{Se}^n\text{Bu})]$, $[\text{Sn}^n\text{Bu}_3(\text{Te}^n\text{Bu})]$ and $[\text{Si}^n\text{Bu}_3(\text{Te}^n\text{Bu})]$, it may be possible to observe satellites in the NMR of the respective NMR active heteroatoms. In occurrences where this is possible, the coupling constants of the satellites observed in each NMR spectrum will be equivalent if the elements are in fact bonded together. This can be seen highlighted in Figure 2-4, for $^{77}\text{Se}\{^1\text{H}\}$ and Figure 2-5 for $^{119}\text{Sn}\{^1\text{H}\}$ NMR spectra for $[\text{Sn}^n\text{Bu}_3(\text{Se}^n\text{Bu})]$.

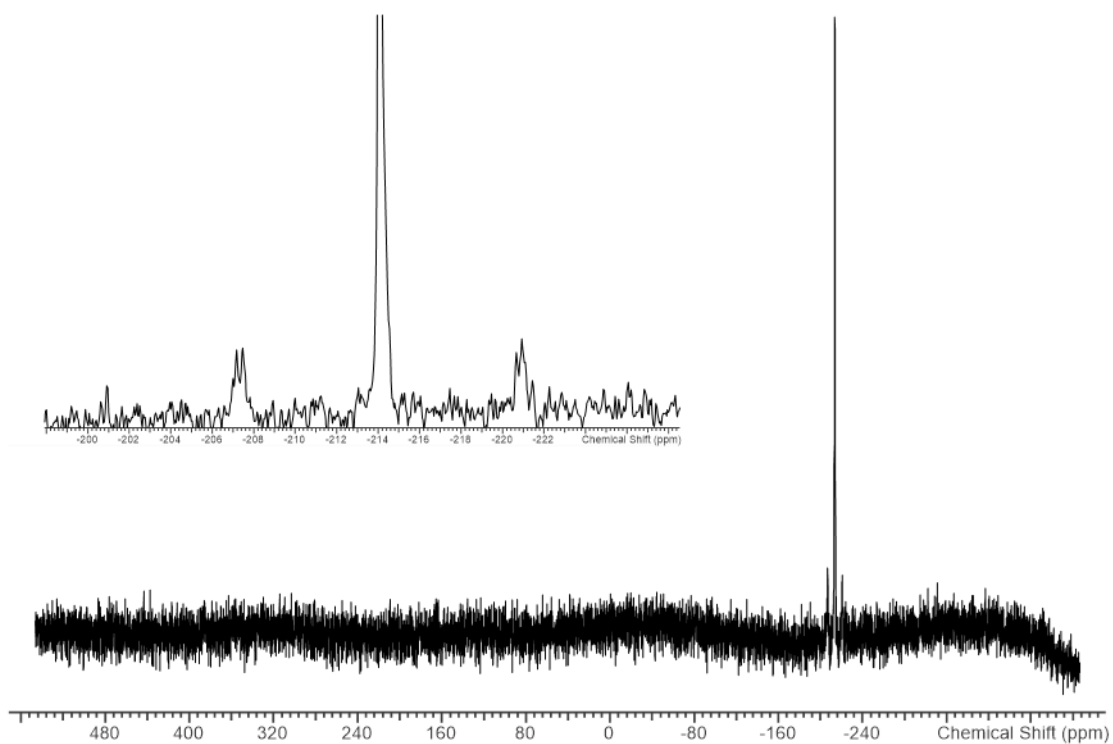


Figure 2-4: $^{77}\text{Se}\{^1\text{H}\}$ NMR spectrum for $[\text{Sn}^n\text{Bu}_3(\text{Se}^n\text{Bu})]$, showing the clean SSP. The inset image is of a zoomed in section of the spectrum showing well-defined satellites from the adjacent ^{119}Sn and ^{117}Sn .

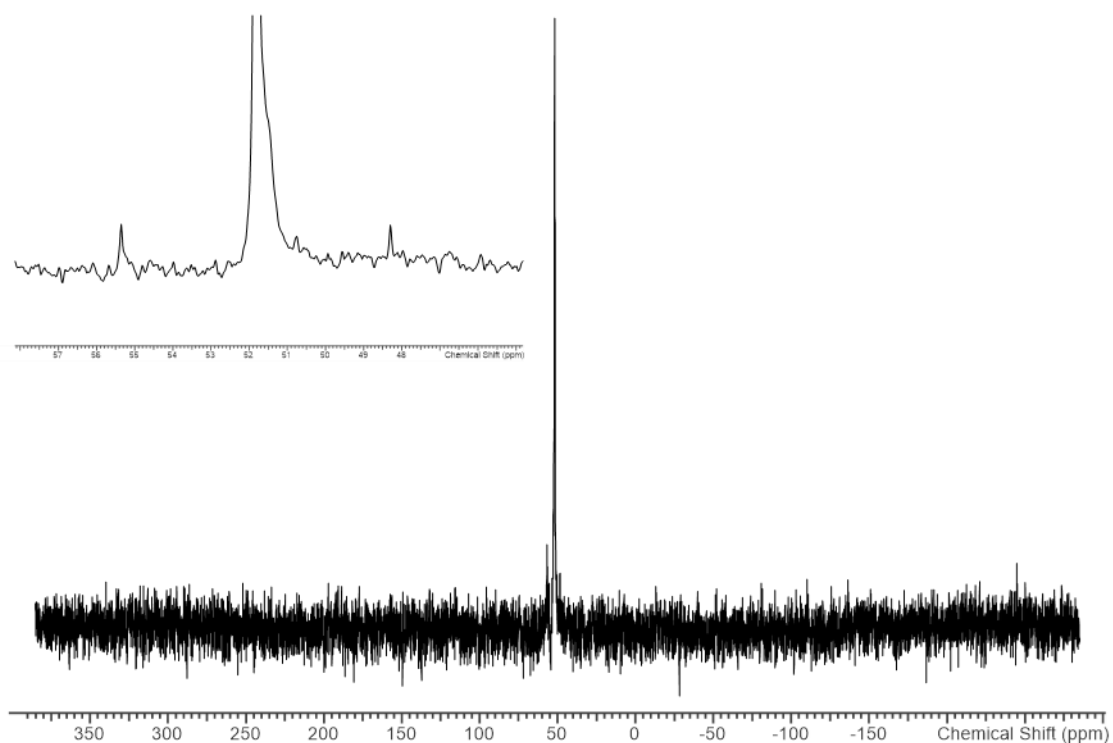
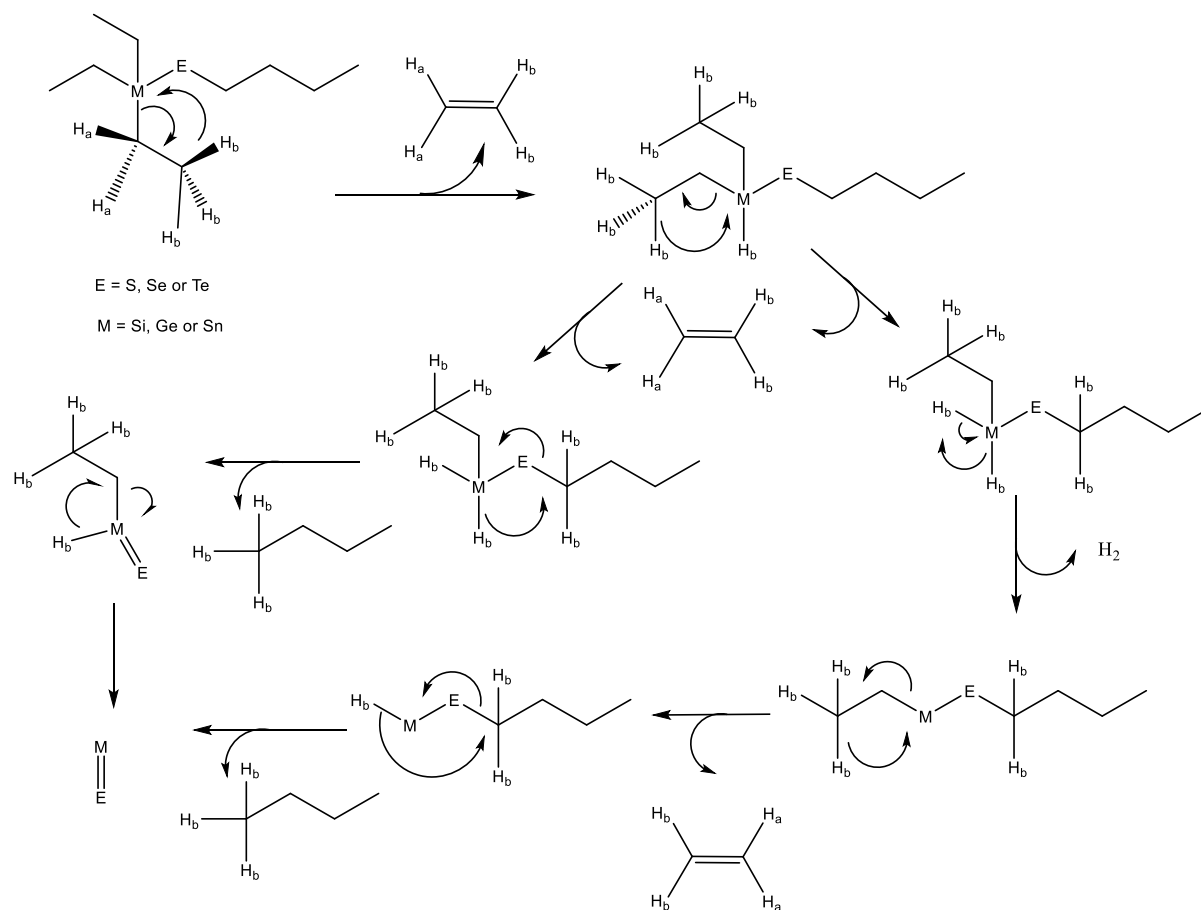


Figure 2-5: $^{119}\text{Sn}\{^1\text{H}\}$ NMR spectrum for $[\text{Sn}^n\text{Bu}_3(\text{Se}^n\text{Bu})]$, showing the clean SSP. The inset image is of a zoomed in section of the spectrum showing well-defined satellites from the adjacent ^{77}Se .

2.3.2 Single source precursor evaluation

The development of the ethyl substituted precursor, $[\text{SnEt}_3(\text{Se}^n\text{Bu})]$ was undertaken to increase the vapour pressure compared to the $[\text{M}^n\text{Bu}_3(\text{E}^n\text{Bu})]$. This was necessary for the precursors to be adapted for use in a Picosun Advanced- 200 ALD rig, used in the scaled up CVD process described in section 1.3.2 and Chapter 5. The increased vapour pressure improved the coverage of the substrate by the deposit and allowed for more straightforward quantification of the amount of precursor entering the reaction chamber. This increased vapour pressure was the reason for the alteration of the precursors used for the scaled up CVD process. The same decomposition pathways are possible for the ethyl-substituted precursors and thus this is still likely the mechanism for the deposition of the thin films produced in this way. Possible decomposition pathways can be seen suggested in Scheme 2-4. The results from these depositions can be found discussed in full in section 5.4.1.



Scheme 2-4: Proposed routes for the thermal decomposition of the single source precursors.

The proposed decomposition pathways shown in **Scheme 2-4** for the thermal decomposition of $[\text{MEt}_3(\text{E}^n\text{Bu})]$ shows the elimination of either 2 equivalents of ethene, one equivalent of butane and one equivalent of ethane or 3 equivalents of ethene, one equivalent of hydrogen and one

equivalent of butane. In this study no experimental work has been performed to confirm either of these routes, however, this could be undertaken by tracking the elimination of these by-products. This could be investigated using a trap in liquid nitrogen, the contents of which could then be probed by either NMR or IR spectroscopy. This would show the presence of some of these by-products and validate these proposed mechanisms.

An important step in assuring the clean decomposition of the precursors used is the quantification of any carbon impurity contained within the deposited material. This can be achieved using EDX, WDS, XPS and microanalysis on the deposited material.

The TGA results, shown in Figure 2-6, concerning the standard temperature ramp experiments showed that for all of the precursors studied in this work, full evaporation occurred between 140 and 245 °C. This suggests that LPCVD is a suitable deposition technique. The experiments also allowed for a good determination of likely optimal temperatures for the deposition experiments.

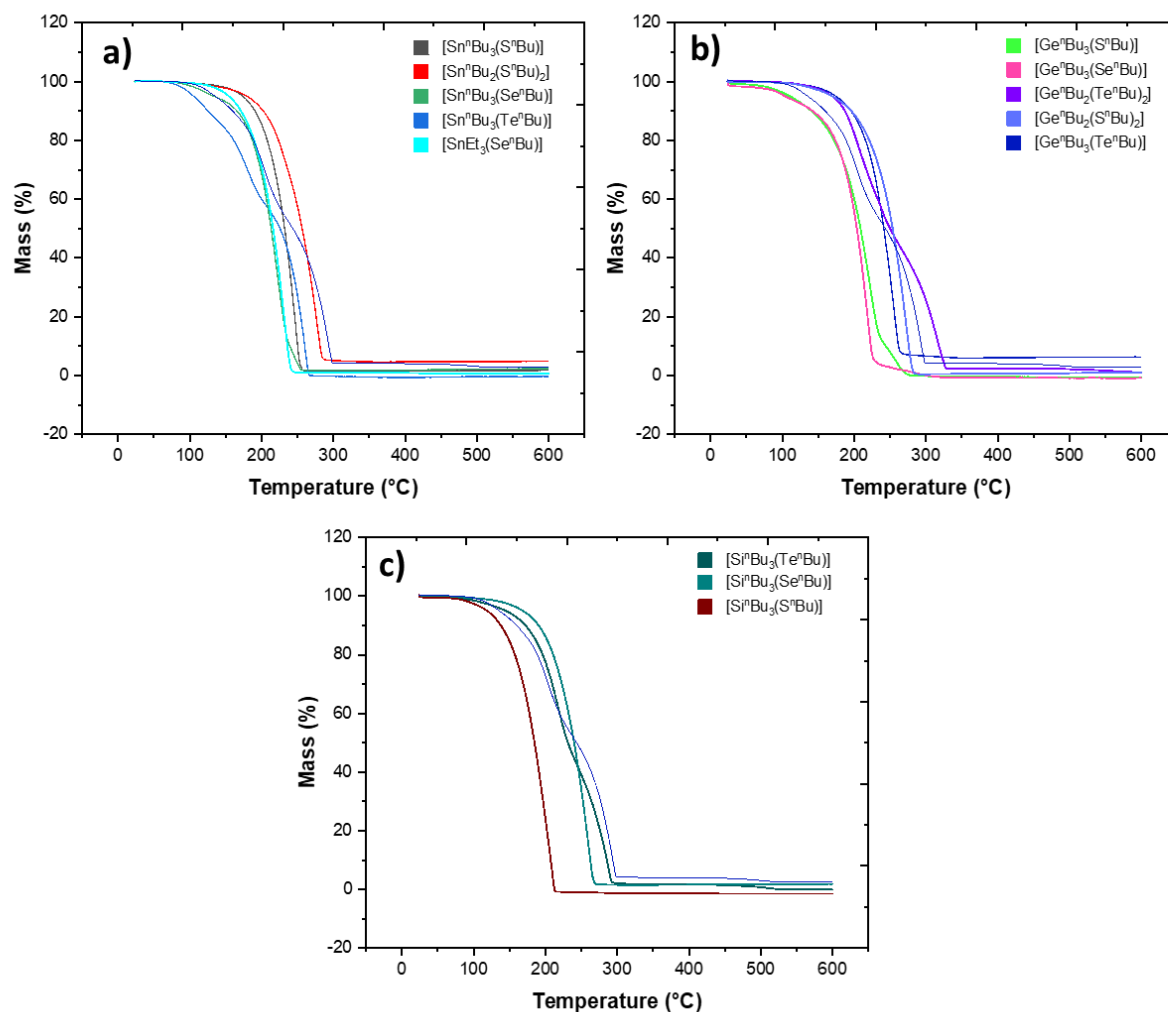


Figure 2-6: TGA results compiled for all group 14 chalcogenide SSPs showing the boiling point range and clean volatilisation for the a) tin, b) germanium and c) silicon containing precursors.

The heteronuclear NMR studies performed, shown in Table 2-2, in this work primarily serve the purpose of supplying further evidence for the successful synthesis of the single source precursors discussed, as well as the purity of the product and in cases where two NMR active heteroatoms are adjacent with a precursor molecule the matching coupling constants are evidence of these being bonded together. They also allow for some insights to be gained on the bonding nature of some of the elements involved, whether that be the electronegativity or electropositivity, the degree of polarity across the metal chalcogen bond or the degree of covalent or ionic nature of the bonds involved.

In the case of group 14, the degree of electronegativity does not change linearly down the group but, instead, moving from silicon to germanium, the electronegativity increases before reducing from germanium to tin, as shown in Figure 2-7. Interestingly, only in $[\text{Sn}^n\text{Bu}_3(\text{Te}^n\text{Bu})]$ is the Sn

environment more shielded than the ^{119}Sn NMR reference compound, SnMe_4 , despite Te being more electronegative than Sn, this is due to the heavy atom effect.

C	O
2.50	3.50
Si	S
1.74	2.44
Ge	Se
2.02	2.48
Sn	Te
1.72	2.01

Figure 2-7: Electronegativity values for group 14 and the chalcogens period 2 to 5. The values stated use the Pauling scale.³⁵

Table 2-2: Heteronuclear NMR data and, when applicable, coupling constants for starting reagents and single source precursors prepared in this work.

Compound	$\delta^{77}\text{Se}\{^1\text{H}\} / \text{ppm}$ ($^1J_{\text{SnSe}} / \text{Hz}$)	$\delta^{119}\text{Sn}\{^1\text{H}\} / \text{ppm}$ ($^1J_{\text{SnSe}} / \text{Hz}$ or $^1J_{\text{SnTe}} / \text{Hz}$)	$\delta^{125}\text{Te}\{^1\text{H}\} / \text{ppm}$ ($^1J_{\text{SnTe}} / \text{Hz}$)
[Sn ⁿ Bu ₃ Cl]	-	154.8	-
[Sn ⁿ Bu ₃ (S ⁿ Bu)]	-	75.3	-
[Sn ⁿ Bu ₃ (Se ⁿ Bu)]	-212.6 (1050)	51.9 (1056)	-
[Sn ⁿ Bu ₃ (Te ⁿ Bu)]	-	-15.3 (2765)	-536.1 (2704)
[Sn ⁿ Bu ₂ Cl ₂]	-	126.0	-
[Sn ⁿ Bu ₂ (S ⁿ Bu) ₂]	-	127.4	-
[SnEt ₃ Cl]	-	162.0	-
[SnEt ₃ (Se ⁿ Bu)]	-226.5 (1040)	63.5 (1065)	-
[Ge ⁿ Bu ₃ (Se ⁿ Bu)]	-144.7	-	-
[Ge ⁿ Bu ₃ (Te ⁿ Bu)]	-	-	-401.4
[Ge ⁿ Bu ₂ (Te ⁿ Bu) ₂]	-	-	-294.9
[Si ⁿ Bu ₃ (Te ⁿ Bu)]	-	-	-427.6

The differences in the approximate vapour pressure, displayed in Table 2-3 and Figure 2-8, show a strong relationship to the relative molecular mass of the molecule in question and the polarity of the compound implied by the electronegativity difference of the metal and chalcogen involved. However, the huge increase in vapour pressure observed when moving from butyl to ethyl substituents cannot be explained by the reduction in relative molecular weight alone. Instead the effect observed here most likely also has contributions from the poorer packing of the unsymmetrical [SnEt₃(SeⁿBu)] when compared to [SnⁿBu₃(SeⁿBu)]. The reduction in steric hindrance surrounding the tin centre in [SnEt₃(SeⁿBu)] allows for stronger repulsive interactions between positive tin centres of the polar compounds with one another and thus a higher vapour pressure is observed.

Table 2-3: Displays the vapour pressures obtained from calculations and experimental data, where tetrabutyltin was used as a reference. *Vapour pressure values stated for Sn^nBu_4 acquired from literature.³⁰ No vapour pressure experiments conducted on $[\text{Si}^n\text{Bu}_3(\text{S}^n\text{Bu})]$ as this was not isolated pure.

Compound	Molecular weight (gmol^{-1})	Vapour Pressure at 50 °C (Pa)	Vapour Pressure at 75 °C (Pa)	Vapour Pressure at 100 °C (Pa)	Vapour Pressure at 125 °C (Pa)
Bu_4Sn^*	347.15	6.74	40.05	160	861
$[\text{Sn}^n\text{Bu}_3(\text{S}^n\text{Bu})]$	379.20	4.84	28.80	96.14	244.43
$[\text{Sn}^n\text{Bu}_3(\text{Se}^n\text{Bu})]$	426.11	5.20	24.80	64.30	196.29
$[\text{Sn}^n\text{Bu}_3(\text{Te}^n\text{Bu})]$	474.85	1.23	15.0	53.28	285.05
$[\text{Sn}^n\text{Bu}_2(\text{S}^n\text{Bu})_2]$	411.26	3.75	11.82	33.49	172.57
$[\text{SnEt}_3(\text{Se}^n\text{Bu})]$	341.95	11.42	59.51	238.31	1647.64
$[\text{Ge}^n\text{Bu}_3(\text{S}^n\text{Bu})]$	333.12	4.70	18.51	36.06	184.75
$[\text{Ge}^n\text{Bu}_2(\text{S}^n\text{Bu})_2]$	366.21	0.62	13.32	40.22	123.71
$[\text{Ge}^n\text{Bu}_3(\text{Se}^n\text{Bu})]$	380.03	6.79	24.59	50.34	236.69
$[\text{Ge}^n\text{Bu}_3(\text{Te}^n\text{Bu})]$	428.77	0.91	9.84	33.09	60.59
$[\text{Ge}^n\text{Bu}_2(\text{Te}^n\text{Bu})_2]$	556.47	7.20	41.78	141.84	258.05
$[\text{Si}^n\text{Bu}_3(\text{S}^n\text{Bu})]$	288.57	-	-	-	-
$[\text{Si}^n\text{Bu}_3(\text{Se}^n\text{Bu})]$	335.48	6.18	30.61	57.55	168.71
$[\text{Si}^n\text{Bu}_3(\text{Te}^n\text{Bu})]$	384.22	0.48	32.07	107.55	258.80

The temperature of vaporisation, T_{vap} , of the precursors was determined using TGA. Whereby, a small sample of the precursor was heated at a constant rate of 1 °C/ min between 25 and 600 °C. Using the values obtained for the vapour pressures at different temperatures the enthalpy of vaporisation can be obtained by means of the Clausius–Clapeyron equation:

$$\ln\left(\frac{P_1}{P_2}\right) = \frac{\Delta H_{\text{vap}}}{R} \left(\frac{1}{T_2} - \frac{1}{T_1}\right)$$

The entropy of vaporisation can then be found simply using the equation:

$$\Delta S_{vap} = \frac{\Delta H_{vap}}{T_{vap}}$$

Table 2-4: Boiling point, T_{vap} , from Sigma Aldrich safety data sheet (SDS) and estimated from TGA data, a enthalpy of vaporisation calculated using the Clausius–Clapeyron equation and reference values given for ${}^n\text{Bu}_4\text{Sn}$, as well as the entropy of vaporisation calculated using $\Delta H_{vap}/T_{vap}$ along with reference values for ${}^n\text{Bu}_4\text{Sn}$.

Compound	T_{vap} (K)	ΔH_{vap} (kJ mol ⁻¹)	ΔS_{vap} (JK ⁻¹ mol ⁻¹)
Bu ₄ Sn*	518.15	69 ± 8 (61.3) ³⁰	137 ± 15
[Sn ⁿ Bu ₃ (S ⁿ Bu)]	498.15	62 ± 14	124 ± 29
[Sn ⁿ Bu ₃ (Se ⁿ Bu)]	463.15	55 ± 12	119 ± 27
[Sn ⁿ Bu ₃ (Te ⁿ Bu)]	473.15	67 ± 15	140 ± 32
[Sn ⁿ Bu ₂ (S ⁿ Bu) ₂]	503.15	108 ± 24	215 ± 49
[SnEt ₃ (Se ⁿ Bu)]	473.15	96 ± 21	202 ± 46
[Ge ⁿ Bu ₃ (S ⁿ Bu)]	453.15	81 ± 18	178 ± 41
[Ge ⁿ Bu ₂ (S ⁿ Bu) ₂]	498.15	74 ± 16	149 ± 34
[Ge ⁿ Bu ₃ (Se ⁿ Bu)]	453.15	76 ± 17	169 ± 39
[Ge ⁿ Bu ₃ (Te ⁿ Bu)]	493.15	38 ± 8	77 ± 19
[Ge ⁿ Bu ₂ (Te ⁿ Bu) ₂]	493.15	37 ± 8	75 ± 19
[Si ⁿ Bu ₃ (S ⁿ Bu)]	463.15	-	-
[Si ⁿ Bu ₃ (Se ⁿ Bu)]	513.15	53 ± 12	103 ± 24
[Si ⁿ Bu ₃ (Te ⁿ Bu)]	503.15	58 ± 13	120 ± 28

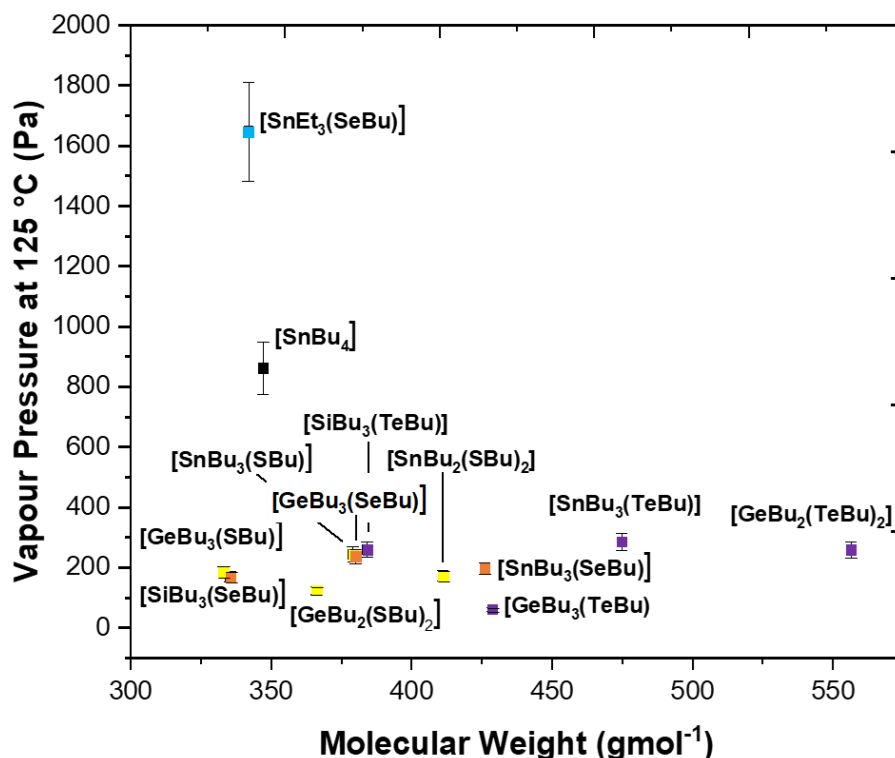


Figure 2-8: A graphical representation of the values obtained for vapour pressure at 125 °C against molecular weight for all the group 14 chalcogenide single source precursors developed in this work.

As discussed in Section 1.2.3, many of the chemical properties of materials are indicative of their thermoelectric properties. These properties are the bond strength, anharmonicity of the crystal vibrations, the energy gap, coordination number and the effective mass of the majority charge carriers. One way these properties can be altered and optimised for a material is by the formation of solid solutions, as shown for the SnS-SnSe solid solution,³⁶ or by the addition of small amounts of a dopant.³⁷ From the work done on the characterisation of the precursors it is possible to assess what combination of materials is likely to be the most advantageous and one feature that needs to be considered for the success of mixed systems is how the precursors behave when they are combined.

To optimise the process of mixed precursor systems, for the deposition of solid solutions, doped materials or superlattices, the vapour pressure of the precursors when mixed should be considered. The principle of how the mixing of ideal liquids effects the vapour pressure of the whole system is defined by Raoult's law. As shown in Figure 2-9, the behaviour predicted by Raoult's law is that the total vapour pressure of the system will be equivalent to the vapour pressure of liquid A multiplied by the mole fraction of liquid A added to the vapour pressure of

liquid B multiplied by the mole fraction of liquid B. However, from experimental observations during the LPCVD of mixed precursor systems, the precursors used in this work show a positive deviation from Raoult's law. This means that the vapour pressure of the mixed system is higher than that expected by Raoult's law. The evidence for this is the observation that the LPCVD experiments consisting of mixed precursors had amounts of undecomposed precursor distilled through the hot zone at temperatures that would have fully decomposed either of the individual precursors used in the mixture. This distillation through the hot zone must be caused by a larger mass transportation effect caused by the higher vapour pressure of the mixed precursors. This higher vapour pressure means intrinsically that the precursors form weaker intermolecular interactions between different precursor molecules when compared to two similar precursor molecules. This is likely to occur as a result of the strongest intermolecular bonds between the precursor molecules being bipolar interactions caused by the electronegativity difference between the group 14 metal and the chalcogen involved. When the precursors are mixed, these bipolar interactions are interrupted by a molecule containing a different degree of polarisation. When a more polarised molecule interacts with a less polarised molecule, there is a larger repulsive force than if two molecules with the same degree of polarisation. This increase in repulsive forces leads to an overall increase in the vapour pressure and a positive deviation from Raoult's law.

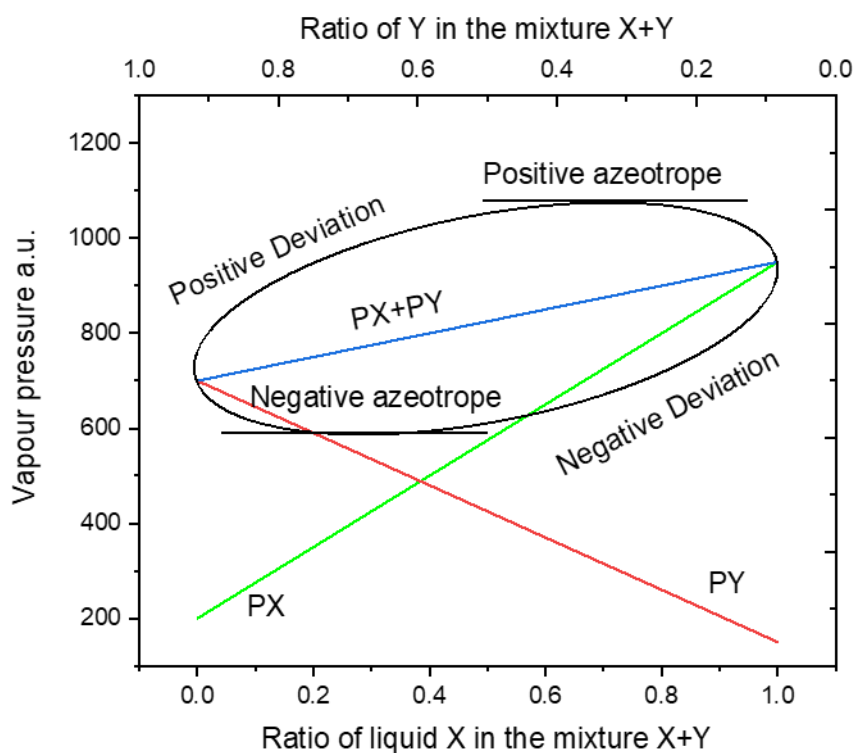


Figure 2-9: Raoult's law and a representation of positive and negative deviations from ideal behaviour.³⁸

2.4 Conclusions

A series of potential single source precursors for the deposition of ME, where M is Ge or Sn and E is S, Se or Te, as well as for Si_2Te_3 , have been designed and successfully synthesised. All the precursors mentioned have been thoroughly characterised using, where appropriate, ^1H , $^{13}\text{C}\{^1\text{H}\}$, $^{29}\text{Si}\{^1\text{H}\}$, $^{77}\text{Se}\{^1\text{H}\}$, $^{119}\text{Sn}\{^1\text{H}\}$ and $^{125}\text{Te}\{^1\text{H}\}$ NMR spectroscopy, together with elemental analysis. Potential decomposition pathways have been suggested, consisting of β -hydride elimination and reductive elimination steps.

The evaluation of the vapour pressure measurement was successfully established for the precursors in this work, using tetrabutyltin as the reference compound.³⁰ The process for these measurements was performed in an analogous way to Wang *et al.*³¹ These results were used to determine the suitability of the single source precursors for use in different CVD systems.

2.5 References

- 1 M. Wang, G. Lahti, D. Williams and K. J. Koski, *ACS Nano*, 2018, **12**, 6163.
- 2 P. Zhao, H. Yang, J. Li, H. Jin, W. Wei, L. Yu, B. Huang and Y. Dai, *J. Mater. Chem. A*, 2017, **5**, 24145.
- 3 S. Keuleyan, M. Wang, F. R. Chung, J. Commons and K. J. Koski, *Nano Lett.*, 2015, **15**, 2285.
- 4 R. J. Martín-Palma, C. G. Pantano and A. Lakhtakia, *Microelectron. Reliab.*, 2009, **49**, 460.
- 5 Z. Xie, F. Zhang, Z. Liang, T. Fan, Z. Li, X. Jiang, H. Chen, J. Li and H. Zhang, *Photonics Res.*, 2019, **7**, 494.
- 6 R. Y. Wang, M. A. Caldwell, R. G. D. Jeyasingh, S. Aloni, R. M. Shelby, H. S. P. Wong and D. J. Milliron, *J. Appl. Phys.*, 2011, **109**, 113506.
- 7 Z. Wang, J. Wang, Y. Zang, Q. Zhang, J. A. Shi, T. Jiang, Y. Gong, C. L. Song, S. H. Ji, L. L. Wang, L. Gu, K. He, W. Duan, X. Ma, X. Chen and Q. K. Xue, *Adv. Mater.*, 2015, **27**, 4150.
- 8 M. S. Mahdi, K. Ibrahim, A. Hmood, N. M. Ahmed, F. I. Mustafa and S. A. Azzez, *Mater. Lett.*, 2017, **200**, 10.
- 9 J. Yan, X. Liao, D. Yan and Y. Chen, *J. Microelectromechanical Syst.*, 2018, **27**, 1.
- 10 L. S. Price, I. P. Parkin, A. M. E. Hardy, R. J. H. Clark, T. G. Hibbert and K. C. Molloy, *Chem. Mater.*, 1999, **11**, 1792.

Chapter 2

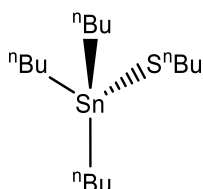
- 11 I. Y. Ahmet, M. S. Hill, P. R. Raithby and A. L. Johnson, *Dalton Trans.*, 2018, **47**, 5031.
- 12 I. P. Parkin, L. S. Price, T. G. Hibbert and K. C. Molloy, *J. Mater. Chem.*, 2001, **11**, 1486.
- 13 I. S. Chuprakov, K. H. Dahmen, J. J. Schneider and J. Hagen, *Chem. Mater.*, 1998, **10**, 3467.
- 14 C. Gurnani, S. L. Hawken, A. L. Hector, R. Huang, M. Jura, W. Levason, J. Perkins, G. Reid and G. B. G. Stenning, *Dalton Trans*, 2018, **47**, 2628.
- 15 F. Davitt, H. G. Manning, F. Robinson, S. L. Hawken, S. Biswas, N. Petkov, M. van Druenen, J. J. Boland, G. Reid and J. D. Holmes, *Adv. Mater. Interfaces*, 2020, 2000474.
- 16 F. Davitt, K. Stokes, T. W. Collins, M. Roldan-gutierrez, F. Robinson, H. Geaney, S. Biswas, S. L. Y. Chang, K. M. Ryan, G. Reid and J. D. Holmes, *ACS Appl. Energy Mater.*, 2020, **3**, 6602.
- 17 K. Ramasamy, V. L. Kuznetsov, K. Gopal, M. A. Malik, J. Raftery, P. P. Edwards and P. O'Brien, *Chem. Mater.*, 2013, **25**, 266.
- 18 P. Kevin, S. N. Malik, M. A. Malik and P. O'Brien, *Chem. Commun.*, 2014, **50**, 14328.
- 19 I. Y. Ahmet, M. S. Hill, A. L. Johnson and L. M. Peter, *Chem. Mater.*, 2015, **27**, 7680.
- 20 B. P. Bade, S. S. Garje, Y. S. Niwate, M. Afzaal and P. O'Brien, *Chem. Vap. Depos.*, 2008, **14**, 292.
- 21 M. D. Khan, M. Aamir, M. Sohail, M. Sher, N. Baig, J. Akhtar, M. A. Malik and N. Revaprasadu, *Dalton Trans.*, 2018, **47**, 5465.
- 22 P. Boudjouk, D. J. Seidler, S. R. Bahr and G. J. McCarthy, *Chem. Mater.*, 1994, **6**, 2108.
- 23 P. Boudjouk, M. P. Remington, D. G. Grier, W. Triebold and B. R. Jarabek, *Organometallics*, 2002, **18**, 4534.
- 24 S. L. Hawken, R. Huang, C. H. de Groot, A. L. Hector, M. Jura, W. Levason, G. Reid and G. B. G. Stenning, *Dalton Trans*, 2019, **48**, 117.
- 25 H. S. Kim, E. A. Jung, S. H. Han, J. H. Han, B. K. Park, C. G. Kim and T. M. Chung, *Inorg. Chem.*, 2017, **56**, 4084.
- 26 G. Gupta, T. M. Jeong, C. G. Kim and J. Kim, *Mater. Lett.*, 2015, **156**, 121.
- 27 X. Song, Y. Ke, X. Chen, J. Liu, Q. Hao, D. Wei and W. Zhang, *Nanoscale*, 2020, **12**, 11242.
- 28 E. G. Hope and W. Levason, *Coord. Chem. Rev.*, 1993, **122**, 109.

- 29 M. A. Malik, M. Afzaal and P. O'Brien, *Chem. Rev.*, 2010, **110**, 4417.
- 30 D. Hawker, *Chemosphere*, 1992, **25**, 427.
- 31 C. Wang, S. Yang and Y. Chen, *R. Soc. Open Sci.*, 2019, **6**, 181193.
- 32 M. Wakasa and T. Kugita, *Organometallics*, 1999, **18**, 2941.
- 33 R. C. Mehrotra, V. D. Gupta and D. Sukhani, *J. Inorg. Nucl. Chem*, 1967, **29**, 1577.
- 34 S. L. Benjamin, C. H. de Groot, C. Gurnani, A. L. Hector, R. Huang, K. Ignatyev, W. Levason, S. J. Pearce, F. Thomas and G. Reid, *Chem. Mater.*, 2013, **25**, 4719.
- 35 E. J. Little and M. M. Jones, *J. Chem. Educ.*, 1960, **37**, 231.
- 36 Y. M. Han, J. Zhao, M. Zhou, X. X. Jiang, H. Q. Leng and L. F. Li, *J. Mater. Chem. A*, 2015, **3**, 4555.
- 37 H. Wang, X. Cao, Y. Takagiwa and G. J. Snyder, *Mater. Horizons*, 2015, **2**, 323.
- 38 W. D. Bancroft and H. L. Davis, *J. Phys. Chem.*, 1929, **33**, 361.

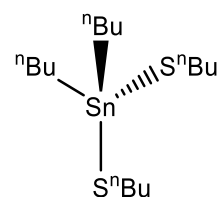
Chapter 3 CVD and Thermoelectric Properties of Tin Chalcogenide Thin Films

3.1 Single source precursors used

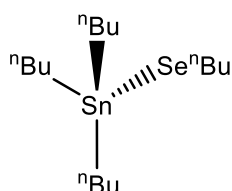
$[\text{Sn}^n\text{Bu}_3(\text{S}^n\text{Bu})]$: Tri-n-butyltin n-butyl thiolate



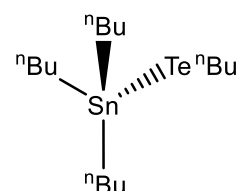
$[\text{Sn}^n\text{Bu}_2(\text{S}^n\text{Bu})_2]$: Di-n-butyltin bis-n-butyl thiolate



$[\text{Sn}^n\text{Bu}_3(\text{Se}^n\text{Bu})]$: Tri-n-butyltin n-butyl selenolate



$[\text{Sn}^n\text{Bu}_3(\text{Te}^n\text{Bu})]$: Tri-n-butyltin n-butyl tellurolate



3.2 Introduction

The tin monochalcogenides, SnE ($E = \text{S}, \text{Se}$ or Te), form a subset of the group 14 monochalcogenides, ME ($M = \text{Pb}, \text{Sn}, \text{Ge}$; $E = \text{S}, \text{Se}, \text{Te}$), which are well established semiconducting materials with applications in many technological fields. The materials comprised in this series, at room temperature, either adopt a cubic rock salt structure, in the case of the heavier elements, or a layered orthorhombic structure with the only exception being the rhombohedral structure adopted by GeTe . The layered orthorhombic structure materials here show many similarities to graphite or black phosphorus with respect to their structure and the van der Waals interactions which are the dominating factor in the inter-layer bonding. The distinguishing factor, which gives the Group 14 monochalcogenides some advantages for electronic applications, is the tunability of their band gap through manipulation of the M and E involved. These materials have proven themselves useful specifically for thermoelectric applications since the early 1960s with the use of PbTe in the SNAP-10A thermoelectric generator used by NASA.^{1,2}

The importance of the tin monochalcogenides arises from their reduced toxicity, when compared to that of the lead containing material alternatives, the high abundance of the elements involved,

with the exception of tellurium, and some very promising thermoelectric properties. SnTe is perhaps the obvious alternative to the existing lead chalcogenide-based systems because of their similarities in both crystal and electronic structure.³⁻⁵ However, due to the intrinsic tin vacancies in tin telluride leading to a very high charge carrier concentration, the thermal conductivity is increased and its Seebeck coefficient is decreased, reducing its applicability to the field of thermoelectrics.⁶ Some approaches to combat these factors can be found in Section 1.3, however, the undoped pristine material is unsuitable for these reasons. The more abundant tin selenide, with its lower symmetry layered orthorhombic crystal structure, exhibits ultralow thermal conductivity, due to the anharmonicity of its lattice vibrations, and a large Seebeck coefficient.⁷⁻⁹ The final member of the tin monochalcogenides, tin sulfide has also sparked much investigation as a cheap and abundant thermoelectric material, mostly stemming from its similarities in crystal and electronic structure with tin selenide. Tin sulfide, however, in its unoptimized binary form exhibits low carrier concentration and a high electrical resistivity hindering its thermoelectric performance.¹⁰ Tin sulfide is, however, of great interest as a semiconducting material for solar power due to its compatible band gap for this application.^{11,12}

3.2.1 Structure

The differences in structure from tin selenide to tin telluride stem from the quenched s^2 electron pair on the tin atoms in tin telluride. This quenching of the electron pair means that it is not expressed in the crystal structure of the material.¹³ The cause of the quenching is the larger tellurium atoms surrounding the tin centre, which induce too much repulsion on one another to allow for them to be destabilised in order for the lone pair orbital to be stabilised in energy. In the distorted structure adopted by tin sulfide and tin selenide, the stereochemically active lone pair occupies an energetically stabilised position while the sulfur or selenium atoms are destabilised to accommodate this. This effect contributes to the larger energy gaps of tin sulfide and selenide when compared to tin telluride. A comparison of the energy levels in these two structure types can be seen in Figure 3-1.

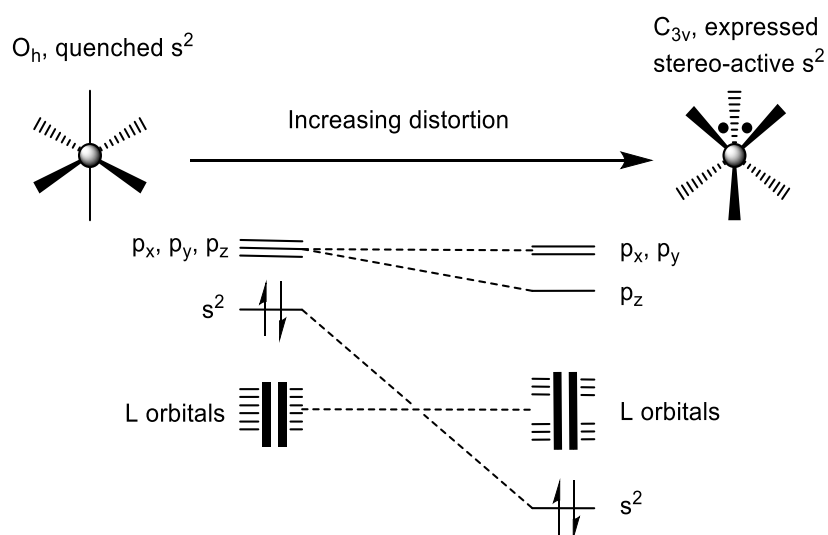


Figure 3-1- Molecular orbital diagram for an octahedral (O_h) ML_6 fragment and a distorted (C_{3v}). The orbitals of the ligands adjust to allow for the expression of the s^2 lone pair and the energy of the s^2 lone pair is reduced meaning the L orbitals become the HOMO. The degree to which the s^2 orbital is stabilised is proportional to the degree of distortion of the fragment.¹³

Some related structural properties of the tin monochalcogenides are presented in Table 3-1. The larger Grüneisen parameter relates to a smaller thermal conductivity, as is evident in the lower thermal conductivity of tin selenide. Another relationship between parameters is that of the band gap and the Seebeck maxima.¹⁴ Thus, the largest band gap and the largest Seebeck coefficient maxima both belong to tin sulfide, while the smallest band gap and Seebeck coefficient maxima both belong to tin telluride. The relationship between these parameters can be seen discussed further in sections **1.2.3.2** and **1.2.3.4**.

Table 3-1: Data pertaining to tin chalcogenide materials for the crystal structure in the form of the unit cell lattice parameters, the unitless Grüneisen parameter, which provides information about the volume expansion with temperature, the electronic band gap and the Seebeck coefficient maxima.

Material	Lattice Parameters (Å) (a, b, c)	Grüneisen Anharmonicity parameter (a, b, c)	Thermal conductivity minima (W m ⁻¹ K ⁻¹)	Band gap (eV)	Seebeck maxima (μV K ⁻¹)
SnS	11.180(6), 3.982(2), 4.329(3) ¹⁵	3.9, 2.1, 2.3 ¹⁶	0.64 ¹⁷	1.3 ¹⁸	750 ¹⁷
SnSe	11.49417(12), 4.15096(5), 4.44175(7) ¹⁹	4.1, 2.1, 2.3 ²⁰	0.46 ^{7,21}	0.829 ²²	537 ^{7,21}
SnTe	6.318(3) ^{3,23}	2 ^{24,25}	2.7 ¹⁴	0.15 ²⁶	ca. 150 ²⁷

Displayed in Figure 3-2 are the structures of the tin monochalcogenides with the layered structure highlighted for SnS and SnSe. It is simple to imagine the process of obtaining monolayers of these van der Waals bounded layers by disassembling the bulk, via: exfoliation, mechanical separation, etching or sonication, or by a carefully controlled deposition process, like PVD or CVD.

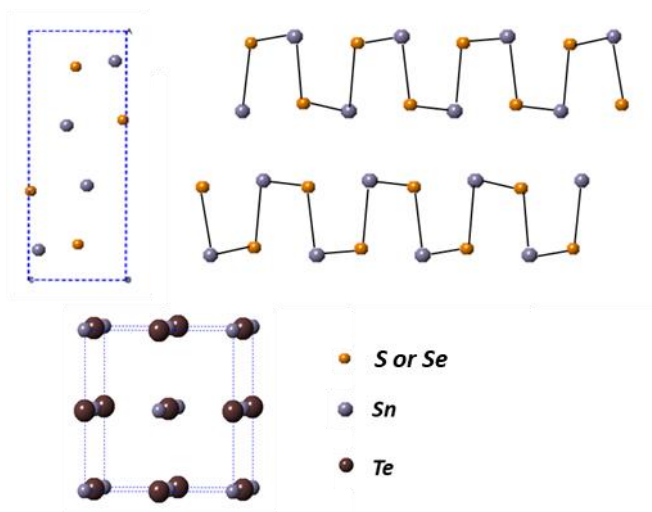


Figure 3-2: Crystal structures of a) SnS²⁸ or SnSe⁷ and b) SnTe.³

3.2.2 Applications of SnE based materials

Additional to their thermoelectric properties, the tin monochalcogenides are known for a number of properties and are important for a multitude of different technological applications. These include, in the case of SnTe; topological crystalline insulators,^{29,30} IR detection and radiation receivers^{31,32} and in near IR photovoltaics²⁷ and in the case of SnSe and SnS; battery

materials,^{20,33,34} photonics,^{20,35} photoelectronics,^{36–38} photovoltaics,^{20,39–42} optoelectronics^{28,40,43,44} and as supercapacitors.^{20,35,45,46}

In the fabrication process for a device, polycrystalline films are more attractive for energy harvesting when compared to single crystals due to the fragility and inflexibility of the single crystals as well as the more stringent conditions required in their synthesis. The optimum operation temperature, for the pristine tin monochalcogenides, can be seen from the profile of the unitless figure of merit, ZT, against temperature in Figure 3-3.

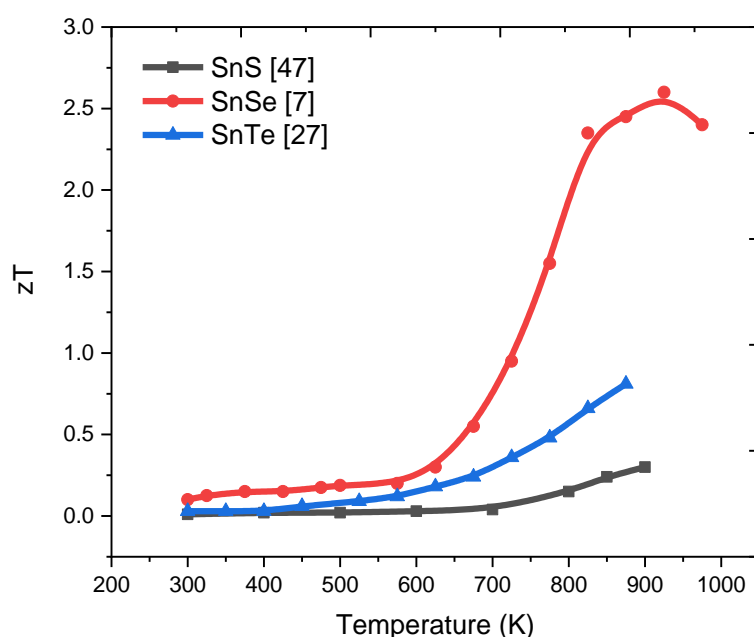


Figure 3-3- Compilation of the ZT values for polycrystalline pristine SnS, the b axis of single crystal SnSe and pristine SnTe, recreated using literature sources.^{7,27,47}

For all of the pristine tin chalcogenide materials the optimum operation temperature is between 700-900 K. One feature that is undesirable about these ZT profiles is how sharp the peak is, meaning that the optimum performance is only obtainable within a small temperature window. Since the temperature range for combustion engine automotive systems is between 500 K and 900 K, processes that require combustion engines are likely a good fit for light weight, low toxicity, high abundance and low cost thin film devices to scavenge some of the otherwise wasted heat energy. The challenges to this application, along with maintaining the optimum heat difference across the device, are the optimisation of the thermoelectric device to ensure the power output is sufficient for them to be viable.

3.2.3 Deposition of SnE

Tin monochalcogenide thin films have previously been produced using many different techniques. These include: dip deposition, chemical bath deposition, flash evaporation, thermal evaporation, molecular beam epitaxy (MBE), atmospheric pressure chemical vapour deposition (APCVD), aerosol assisted chemical vapour deposition (AACVD), metal organic chemical vapour deposition (MOCVD), plasma enhanced chemical vapour deposition (PECVD), low pressure chemical vapour deposition (LPCVD) and atomic layer deposition (ALD).^{38,41,55–60,44,48–54} It is difficult to determine which technique is superior as each holds their own merits, as discussed in more detail in section 1.3, whether it be orientation control offered by MBE and LPCVD, fine control over the film thickness in the case of ALD particularly, polymorph selectivity in the cases cited for MBE and AACVD, or the ease of producing samples quickly for many of the CVD processes. The technique chosen should always be determined by the requirements of the deposited material for the desired process and the compatibility of the precursor chemistry with that technique. The process with the strictest precursor requirements is ALD, as highlighted in the introductory chapter. It requires a minimum of two highly reactive gaseous precursors that do not self-react and can undergo chemisorption to the substrate surface in sequence to build layers up one atomic layer at a time. There are some examples of pseudo-ALD processes concerning the deposition of tin selenide reported within the literature.^{60,61} These processes do show a linear trend in the thickness of the deposited material with time or number of precursor cycles, but as the deposition occurs via thermal decomposition and not chemisorption, the deposition is not limited in each cycle and cannot be considered to be atomic layer growth and thus are pseudo-ALD processes.

3.2.3.1 Comparison of previously reported single source SnE precursors

The design of the precursors used for CVD procedures in the literature consists of simple, highly volatile and highly toxic components for binary precursor systems, stannic chloride and hydrogen sulfide for example or larger more complicated compounds with low volatility. The binary system mentioned has been adopted for APCVD and PECVD. Although the chemicals used in these binary precursor processes are commercially available, they are undesirable for any upscaling procedure due to their reactivity and toxicity.

The larger, more complicated compounds, which do not volatilise completely without decomposition, are unsuited to many deposition techniques. However, these can still be used in AACVD as the nebulisation of a solution containing the precursor negates the requirement for stability and vapour pressure of the precursor or using MOCVD with a high carrier gas flow rate. However, this does also reduce the control over the thickness and coverage of the films produced and can in some cases cause grain sizes and morphologies that are more dependent on the

evaporation or droplet formation of the solvent, rather than the decomposition of the precursors. MBE allows for the production of very elementally pure deposits due to the ultrahigh vacuum and lack of flow gas involved. The very slow rate of growth of the films is what allows for their epitaxial growth and thus strict control over the thickness is possible. The distorted octahedral tin (IV) chloride thio and selenoether precursors displayed in Figure 3-4 were developed for LPCVD of tin disulfide and tin diselenide but can produce the tin (II) chalcogenides at elevated temperatures.⁵⁷ In the case of these precursors the elevated temperatures required leads to higher energy demands and may be linked to the discontinuity of the tin monoselenide films produced. The ability of these precursors to access both the tin mono and dichalcogenides may also lead to the formation of mixed phase systems and thus lower control over the material composition. One of the simpler procedures considering the equipment required is that of LPCVD. It has been selected for the work within this chapter as:

- i. It enables a large number of samples to be produced in short period of time when compared to many of the other deposition techniques.
- ii. It allows for orientational control in some cases.
- iii. It can also enable the selective deposition onto patterned substrates.
- iv. Gives some control over grain size and film thickness.
- v. The design of single source precursors appropriate for LPCVD is quite simple.

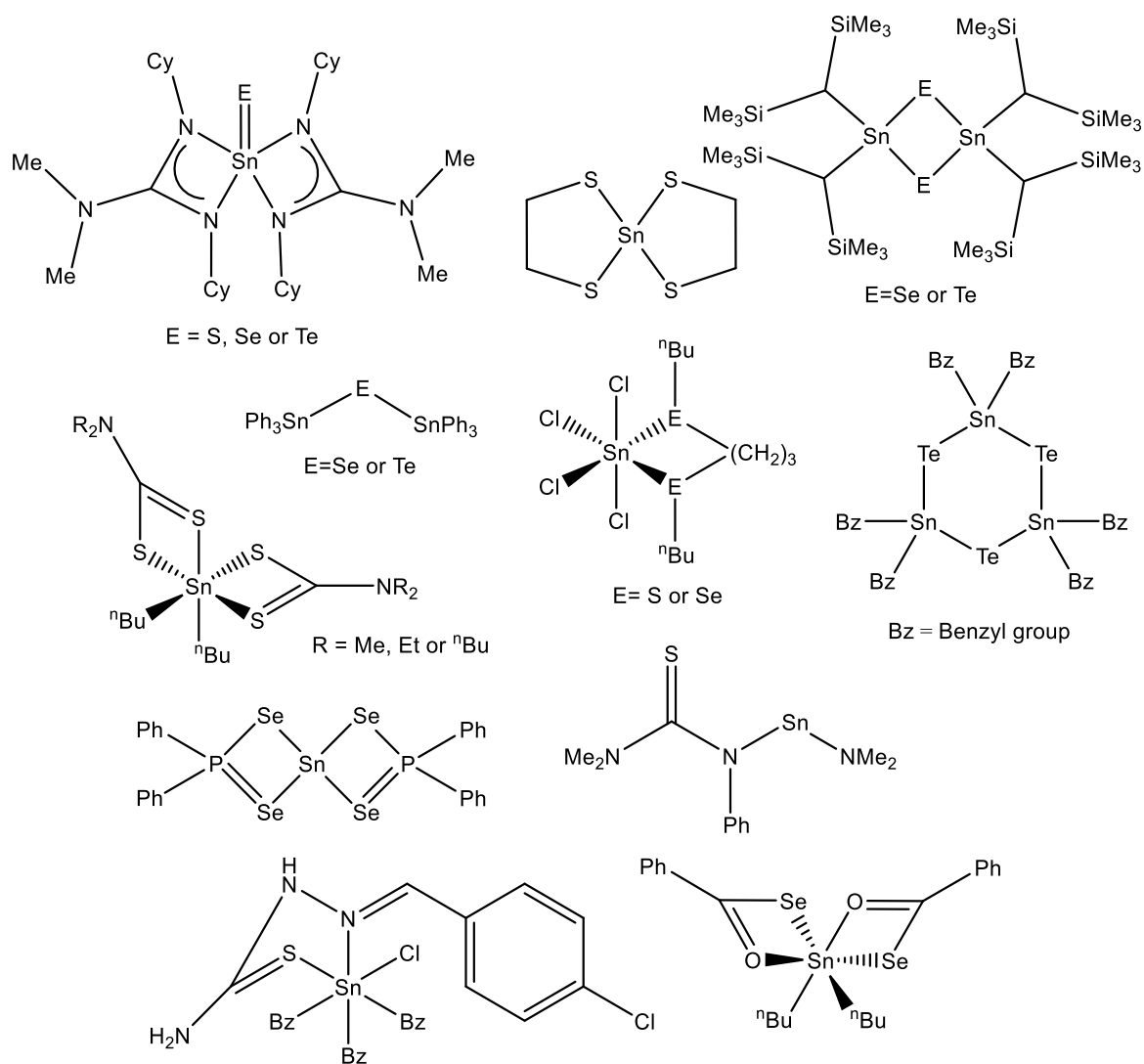


Figure 3-4: Examples of some of the single source precursors available in the literature.^{54,56,69,57,62–68}

3.2.4 Optimisation

Complementary to the incorporation of nanostructuring techniques, like the approach of thin film fabrication used in this work, are a great number of optimisation techniques that have been shown to improve tin monochalcogenide thermoelectric performance, as discussed in section 1.5. One of the methods shown to have profound effects on thermoelectric performance for a vast number of materials, and in particular SnTe, is band engineering. A good example of this being applied is by aliovalent doping, for example, with the incorporation of indium into tin sites in $\text{In}_x\text{Sn}_{1-x}\text{Te}$, which when paired with nanostructuring has been shown to greatly improve performance. An enhancement in ZT of 333%, when compared to pristine SnTe, was observed by Zhang *et al.* which was attributed to resonant valance bands provided by the indium enhancing the Seebeck coefficient and the reduced thermal conductivity from both the nanostructuring and point defect phonon scattering.⁷⁰ Another example of band engineering improving the

performance of SnTe was observed by Tan *et al.* in cadmium doped SnTe.⁴ In this case, rather than an enhancement caused by resonant valence bands increasing the degeneracy of the band structure, the enhanced performance was caused by reducing the energy separation between the light and heavy-hole valence bands. This leads to an increase in the Seebeck coefficient through the increased band gap which also reduces the occasions of phonon to electron scattering events improving the electrical conductivity. Similar band engineering techniques are described by He *et al.* with the investigation of $\text{SnS}_{1-x}\text{Se}_x$.⁷¹ Here the inclusion of selenium into SnS causes the coalescence of valence bands, improving band degeneracy and increasing the band gap thus improving the thermoelectric performance. The band degeneracy is one part of the Fermi complexity and, as discussed in section 1.2.2.2, is important for increasing the Seebeck coefficient.

Other forms of electrical optimisation concern themselves with the charge carrier mobility, concentration and electrical conductivity effective mass. As discussed in the Chapter 1, optimisation of charge carrier concentration is a delicate balance between maximising the electrical conductivity and not reducing the Seebeck by too large an extent. The charge carrier mobility is dependent on maximisation of the time of relaxation or scattering and the minimisation of the effective mass concerning electrical conductivity. Thus, charge carrier concentration is of high importance but cannot be used as a handle on the selection of high-performance thermoelectric materials. However, the electrical conductivity effective mass, and therefore the charge carrier mobility, can be manipulated to produce better materials for thermoelectric applications. Notably, this reduction in the conductivity effective mass causing a vast improvement in charge carrier mobility is stated as the source of performance enhancement in a model concerning monolayered SnSe.³⁵

Another approach to the optimisation of the electronic properties through both band engineering and charge carrier concentration optimisation is through the reduction of the thermal conductivity through the increase of phonon scattering within the system. A more detailed description of how each of these techniques can help improve thermoelectric performance can be found in section 1.4. Manipulation of this can be seen as described by Moshwan *et al* in the structural engineering of SnTe utilising lattice distortion, crystal imperfections and nanoprecipitates to increase the phonon scattering events and reduce the thermal conductivity.⁷²

3.2.4.1 Nanostructuring

Since the early 1990s, the concept of reducing the thermal conductivity through the reduction of one or more dimensions of the material has been a very exciting prospect.^{73–75} As previously discussed, this method, known as nanostructuring, describes the formation of thin films,

nanowires or quantum dots. In terms of advances in thermoelectric performance for tin monochalcogenide materials, these have been used alongside alloying and solid solutions to produce enhanced thermoelectric performances. Nanostructured materials based on tin sulfide, tin selenide and tin telluride have been discussed within the literature.^{70,76–78} Despite the fact that nanostructuring of a material should lower its lattice thermal conductivity, and thus improve the ZT value, no SnSe polycrystalline sample has been able to outperform that reported for the single crystal described by Zhao *et al.*⁷ One possible explanation for this issue has been discussed by Wei *et al.* and describes the discrepancy in density of the ‘single crystals’ used in the work published by Zhao *et al.* with that expected from powder and neutron diffraction data.⁷⁹ The communications presented by Wei *et al.* outlines that the density of the single crystals used by Zhao *et al.* was around 10% lower than expected and that vacancies and interstitials alone could not explain, at room temperature, the discrepancy in density. The other potential source for the difference in thermoelectric performance of the work of Zhao *et al.* on single crystals when compared with polycrystalline films is oxidation, as SnO and SnO₂ have a much higher thermal conductivity. This as well as the removal of these oxide layers is discussed by Li *et al.*⁸⁰ In this work Li *et al.* also present a very high ZT value for their treated SnSe of 2.5, much higher than other polycrystalline samples reported. This evidence does certainly seem convincing as a major contributor towards the lower ZT values reported for polycrystalline SnSe. However, as the ZT value for the chemically reduced sample reported by Wei *et al.* still has a lower ZT value, other factors must also play a role in the high performance reported by Zhao *et al.* Another potential contributing factor is that of the single crystalline samples being off-stoichiometric, as is proposed by Wu *et al.*⁸¹ All of these factors really highlight the importance of investigating the stoichiometry of the samples reported and investigating the presence of any possible impurities as part of the standard characterisation.

3.2.4.2 Solid solutions

The use of solid solutions has been shown, both experimentally and theoretically, to increase phonon scattering. This occurs as fluctuations in the mass of the elements comprising the material cause the scattering of phonons at point defects within the material. The technique of reducing the thermal conductivity using solid solutions has been demonstrated for a number of tin chalcogenide based systems, as shown for PbSe-SnSe, SnSe-SnS and MgTe-SnTe.^{26,82,83}

3.2.4.3 Superlattice

Another source for phonon scattering events is the interface between two materials. An easy way to have lots of material interfaces is in a repeating layered material known as a superlattice or by the layering of different materials atop one another, such as in heterostructures. Although some

superlattices containing tin monochalcogenide layers have been reported within the literature, little is reported on this technique being used to enhance thermoelectric performance.⁸⁴ However, multi-layered materials containing tin monochalcogenide materials have shown meaningful enhancements to thermoelectric performance.⁸⁵

3.2.4.4 Mesostructure

Phonon scattering also occurs at grain boundaries and thus the mesostructuring of materials is another powerful technique for the reduction of thermal conductivity on a sub-micron scale. This can be performed by simply increasing the proportion of the material that is on a grain boundary within the system or with the inclusion of pores to maximise the scattering events that occur by this mechanism. Consideration of the mesoscale scattering, when coupled with other scale scattering techniques, has been shown for Gd doped SnTe to improve performance and SnTe alloyed with MnTe.^{86,87} An example of mesoscale scattering greatly improving the thermoelectric performance of a material is in Hg doped SnTe. Here a large portion of the reduced thermal conductivity was attributed to the grain boundaries, which can be seen in Figure 3-5.⁸⁸

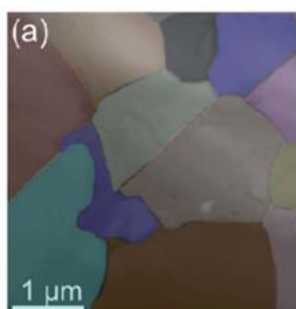


Figure 3-5: Low magnification TEM image of Hg doped SnTe showing the individual grains and thus the mesostructure of the material.⁸⁸ The colours added to the image are to aid in the visualisation of individual grains. Reproduced with permission from

3.2.4.5 Panoscopic approach

For a system to be truly optimised all of these different techniques should be used simultaneously, sometimes referred to as the panoscopic approach.⁸⁹ This involves a series of different solid solutions combined to optimise the phonon scattering from: point defects, nanoprecipitates, material interfaces, structural modulations and grain boundaries, shown in Figure 3-6, whilst also optimising the electrical properties: charge carrier concentration, mobility and band degeneracy. This is made a little simpler as, an important technique for electrical optimisation, doping, also plays a role in the reduction of the thermal conductivity by creating point defects.⁹⁰ Nano and microscale scattering enhancements could be achieved by the formation of alloys made out of electrically optimised solid solutions. However, this will likely also

affect the electrical properties of the individual materials and thus lots of further research is fundamental to the realisation of panoscopically optimised thermoelectric materials.

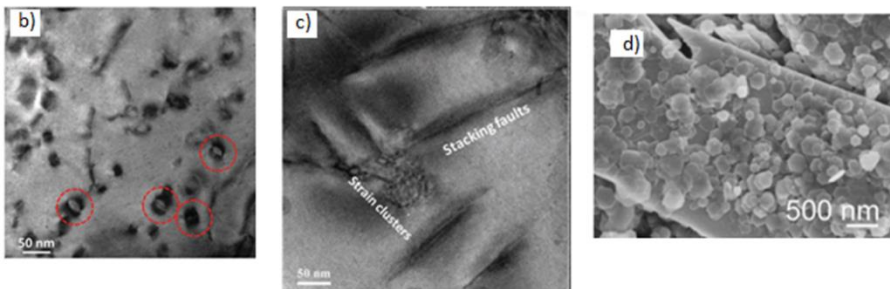
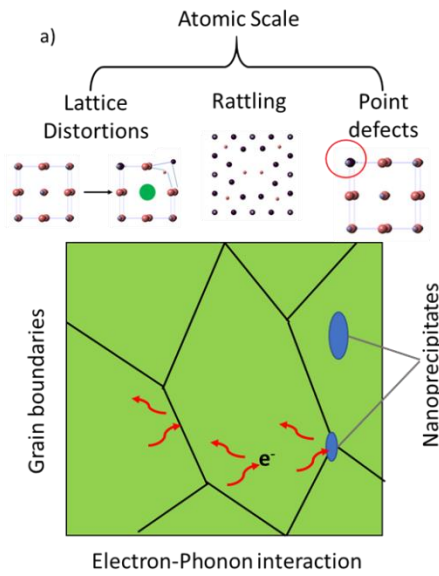


Figure 3-6: Multiscale phonon scattering displayed in a) showing the different scale features that can be used for phonon scattering. Examples of these features in b) nanoprecipitates of MnTe in SnTe, c) dislocations in the form of stacking faults and strain clusters in a MnTe-SnTe alloy and d) heterostructure of SnS₂ nanoplates deposited onto SnS flakes providing further grain boundaries.^{87,91–93} Images b), c) and d) reproduced with permissions from the Royal Society of Chemistry, John Wiley and Sons and Elsevier.

3.2.4.6 Anharmonicity

As discussed in Chapter 1, one approach to reducing the thermal conductivity is to increase the phonon scattering caused by anharmonic bonds. This is one of the features of SnSe which results in its low thermal conductivity.⁸ Increasing the anharmonicity of the crystal lattice has been reported for lead doped SnSe and, along with strain engineering, showed an increased thermoelectric performance when compared to pristine samples produced in the same work.⁹⁴

3.2.5 Aims

The aims of the work presented in this chapter were to explore the deposition of stoichiometric thin films of tin monochalcogenide (SnS, SnSe and SnTe) using the precursors developed in Chapter 2. Once the deposition of these thin films was proved to be successful by characterisation of the films, by grazing incidence XRD, scanning electron microscopy (SEM) with energy dispersive X-ray spectroscopy (EDX) and Raman spectroscopy, the thermoelectric properties would be measured. These thermoelectric properties would then be compared with physical properties of the films to see if there was any control to be gained over performance. Finally, the possibility of selective deposition onto patterned substrates would be explored to determine if a thermoelectric device could be fabricated in this manner.

3.3 Experimental

3.3.1 Thin film growth by low pressure CVD onto fused silica substrates

The silica substrates (8 mm x 20 mm) were first washed with deionized water then ethanol, before being dried thoroughly in an oven before use. In a typical LPCVD experiment, the precursor (5-50 mg) and silica substrates were loaded into a silica CVD tube inside the glovebox. The precursor was loaded into the precursor bulb at the closed end of the tube and the substrates were positioned end-to-end lengthways (0-4 cm away from the precursor bulb) along the silica tube. The tube was positioned horizontally in the furnace and held in place such that the precursor bulb was protruding from the end of the furnace. The tube was evacuated to *ca.* 0.01-0.05 mmHg. The furnace was heated to the required temperature and allowed to stabilise. The tube was then repositioned so that the precursor was close enough to the furnace for evaporation to be observed. This position was then maintained until all of the precursor had evaporated, typically between 10- 30 mins. Depositions from $[\text{Sn}^n\text{Bu}_2(\text{S}^n\text{Bu})_2]$, however, were maintained in the hot zone for as short a period of time as was required for all of the precursor to vaporise, typically less than 3 mins. Once the deposition was complete, the tube was removed from the furnace and allowed to cool to room temperature before being transferred to the glovebox, where the substrates were removed and stored for characterisation.

The LPCVD experiments produced grey films of SnS, dark grey films of SnSe and silvery films of SnTe. All of the precursors produced good continuous films with coverages of at least 3 cm², for SnTe, and 6 cm² for SnS and SnSe.

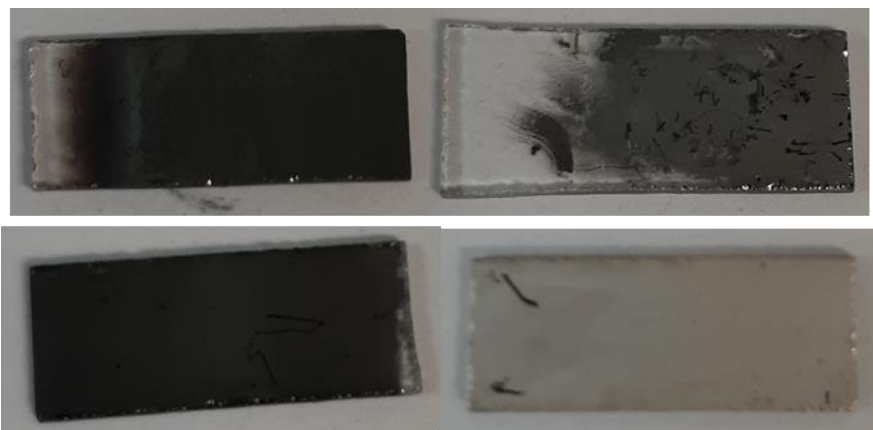


Figure 3-7: Examples of deposits on silica substrates of SnS from $[\text{Sn}^n\text{Bu}_3(\text{S}^n\text{Bu})]$, SnS from $[\text{Sn}^n\text{Bu}_2(\text{S}^n\text{Bu})_2]$, SnSe and SnTe (top left to bottom right).

3.3.2 Thin film growth by low pressure CVD onto patterned SiO_2/TiN substrates

TiN/ SiO_2 patterned substrates (8 mm × 20 mm) were prepared as described previously.⁹⁵ These were loaded lengthways into a closed end silica tube containing < 3 mg of the $[\text{Sn}^n\text{Bu}_3(\text{Te}^n\text{Bu})]$ precursor. The deposition process parallels that onto the unpatterned substrates, with the only changes being the lower precursor loading and the position of the tube causing the slower volatilisation of the precursor (and hence better discrimination of the TiN vs. SiO_2 surfaces), thus the duration of the depositions were longer (30-45 mins).

3.4 Results and Discussion

3.4.1 Synthesis and Characterisation of SSPs for LPCVD

The incorporation of *n*-butyl substituents into molecular compounds for use as CVD precursors for semiconductor materials has proved to be a very effective strategy to achieve clean deposition of many target semiconductor materials, for example InSb, CdSe, SnE_2 (E = S, Se), M_2E_3 (M = Sb, Bi; E = Se, Te), etc., as these substituents facilitate a clean, low energy deposition pathway via β -hydride elimination pathway.^{57,95,96} Previous work has corroborated that thin film deposition from CVD precursors containing *n*-butyl and other alkyl substituents containing β -hydrogen atoms can often involve β -hydride elimination³⁴ of alkene and reductive elimination of hydrogen gas or alkane. Previously it has been demonstrated within the group that $[\text{SnCl}_4\{\text{BuE}(\text{CH}_2)_n\text{E}^n\text{Bu}\}]$ (E = S, Se; n = 2, 3) can be used as SSPs for SnS and SnSe, respectively, at elevated temperatures, although they are better suited for deposition of the dichalcogenide phases, SnS_2 and SnSe_2 .⁵⁷ The target SSPs for clean SnE thin film growth via CVD in this work were based upon the organometallic complexes, $[\text{Sn}^n\text{Bu}_3(\text{E}^n\text{Bu})]$ (E = S, Se, Te), and $[\text{Sn}^n\text{Bu}_2(\text{S}^n\text{Bu})_2]$. Moreover, ⁿBu

groups can also enhance the prospects of highly area selective deposition of metal chalcogenides onto patterned substrates.^{26,27}

The synthesis of the precursors proceeded via the reaction of the appropriate sodium or lithium butyl chalcogenolate (prepared *in situ* from n-butyl mercaptan with Na or by insertion of elemental Se or Te into ⁿBuLi in thf at low temperature, to increase control and prevent formation of ⁿBu₂Te₂⁹⁷) with the appropriate alkyltin chloride. Schemes describing these reactions, along with a more in depth discussion of the synthesis can be found in section 2.3.1.

The complexes were obtained in good yield and were characterised by multinuclear NMR spectroscopy (¹H, ¹³C{¹H}, ⁷⁷Se{¹H} and ¹²⁵Te{¹H}) and elemental analysis, as well as by thermogravimetric analysis (TGA) in order to establish the volatility of the precursors and to guide the temperature range for the low pressure CVD experiments. The TGA data show that complete evaporation, or vast majority evaporation, occurs in all cases, with the temperature associated with the onset of evaporation being lowest for **[SnⁿBu₃(TeⁿBu)]** (*ca.* 100 °C) and increasing progressively for **[SnⁿBu₃(SeⁿBu)]** and then **[SnⁿBu₃(SⁿBu)]** and **[SnⁿBu₂(TeⁿBu)₂]**, with the evaporation onset occurring at *ca.* 200-220 °C for the thiolate precursors. This can be seen displayed in Figure 3-8. A small residual mass, *ca.* 4%, can be observed for the TGA experiment conducted using **[SnⁿBu₂(SⁿBu)₂]**. This may be evidence for some decomposition of the precursor prior to total vaporisation in **[SnⁿBu₂(SⁿBu)₂]**. However, the small size of this residual mass proves that the precursor is almost completely vaporised; 4% mass does not correspond to any decomposition products (e.g. SnS₂, Sn₂S₃, SnS, Sn or S). The TGA experiments conducted were at atmospheric pressure and determined only that the precursors were volatile with a certain temperature window, the experiments do not inform the decomposition window of the precursors. For this reason, higher temperatures are required for material depositions and at temperatures below the decomposition temperatures but above the required temperature for the precursor to boil, precursor could be observed distilled through the hot zone of the furnace.

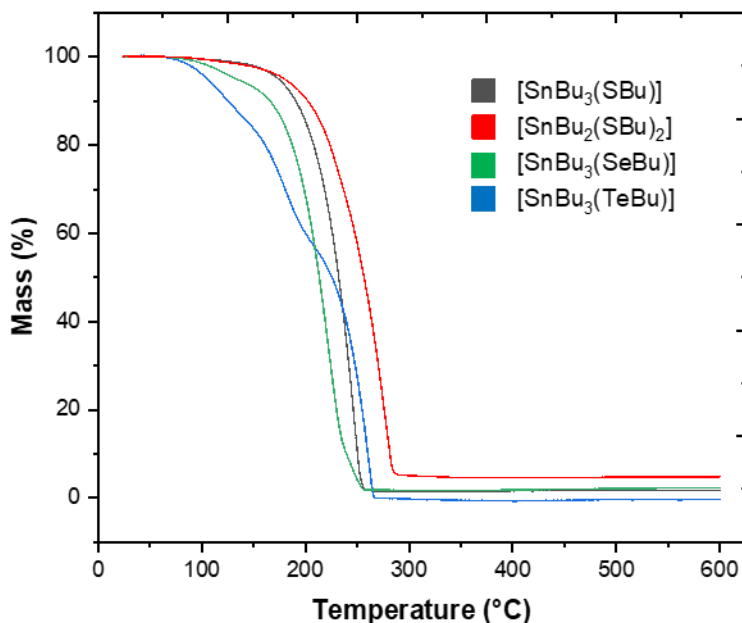


Figure 3-8: TGA results, for all the precursors used in this chapter, showing suitable volatility in the range of 30- 600 °C with no, or less than 5%, residual mass left in the crucible after the experiment.

3.4.2 Low Pressure Chemical Vapour Deposition Experiments

The suitability of the new precursors for the deposition of high quality SnS, SnSe and SnTe thin films was established via preliminary TGA experiments and low pressure CVD experiments onto fused silica substrates (8 mm by 20 mm by 1 mm) and resulted in continuous films and good substrate coverage. The temperatures selected for the LPCVD experiments were informed by the TGA experiments performed beforehand. The TGA experiments highlight the boiling temperature range and the stability of the SSP in question and thus the temperature of the experiment as well as the position of the CVD tube within the tube furnace were based on these experimental results.

Depositions from **[SnⁿBu₃(SⁿBu)]** produced sulfur deficient thin films of tin sulfide, typically between 30 and 45% sulfur by EDX analysis, Table 3-2. The grazing incidence XRD patterns collected were consistent with the material being SnS and the Raman spectra also were consistent with that of SnS described in published literature. The films showed good continuous coverages of 2- 3 cm by 1 cm in area. The temperature range for the depositions seen occurred between 439- 530 °C and the pressure for these depositions was between 0.2 and 0.5 mmHg. Duration of deposition, meaning the time for the precursor to fully vaporise at which point the tube was removed from the furnace, was between 12 and 21 minutes.

Since $[\text{Sn}^n\text{Bu}_3(\text{S}^n\text{Bu})]$ produced sulfur-deficient films, the iteration to this precursor was to increase the sulfur content by moving from a mono-thiolate substituted precursor to the bis-thiolate substituted precursor, $[\text{Sn}^n\text{Bu}_3(\text{S}^n\text{Bu})]$. Initial depositions from $[\text{Sn}^n\text{Bu}_3(\text{S}^n\text{Bu})]$ produced sulfur deficient films. However, by reducing the time the substrates were in the hot zone stoichiometric tin sulfide was successfully produced. This was achieved by increasing the rate of volatilisation of $[\text{Sn}^n\text{Bu}_3(\text{S}^n\text{Bu})]$ by moving the precursor bulb into a position further into the hot zone and thus a hotter region. The stoichiometric tin sulfide produced was deposited in the temperature range 376- 491 °C, at a pressure of 0.01 mmHg and took 3 minutes for the deposition to take place once at temperature and the precursor bulb had been positioned 2 cm inside the hot zone of the furnace. This deposition used only 16 mg of precursor to ensure a quick deposition time and thus quite thin films were produced. The films were continuous and had coverages of about 1 cm².

Table 3-2: Energy dispersive X-ray analysis results for some SnS depositions.

Tile	Precursor	O%	Si%	S%	Sn%
Dep. 1 tile 1	$[\text{Sn}^n\text{Bu}_3(\text{S}^n\text{Bu})]$	7.8	1.2	36.4	54.6
Dep. 2 tile 1	$[\text{Sn}^n\text{Bu}_3(\text{S}^n\text{Bu})]$	-	-	40.2	59.8
Dep. 2 tile 2	$[\text{Sn}^n\text{Bu}_3(\text{S}^n\text{Bu})]$	-	-	39.9	60.1
Dep. 3 tile 1	$[\text{Sn}^n\text{Bu}_3(\text{S}^n\text{Bu})]$	6.6	1.3	40.8	51.3
Dep. 4 tile 1	$[\text{Sn}^n\text{Bu}_3(\text{S}^n\text{Bu})]$	-	0.7	44.2	55.0
Dep. 5 tile 1	$[\text{Sn}^n\text{Bu}_3(\text{S}^n\text{Bu})]$	13.4	24.1	31.2	31.2
Dep. 5 tile 2	$[\text{Sn}^n\text{Bu}_3(\text{S}^n\text{Bu})]$	12.3	12.5	37.2	38.1

The deposition of tin selenide from $[\text{Sn}^n\text{Bu}_3(\text{Se}^n\text{Bu})]$ produced stoichiometric films of tin selenide, Table 3-3, with good continuous coverages around 3 cm by 1 cm. These films were deposited within the temperature range of 352- 431 °C, at a pressure of 0.01 mmHg, using between 20- 41 mg of precursor and the depositions took between 5- 9 minutes to complete.

Table 3-3: Energy dispersive X-ray analysis results for SnSe depositions

Tile	%C	%O	% Si	%Se	%Sn
Dep. 1 tile 1	-	11.3	29.4	29.1	30.2
Dep. 2 tile 1	17.4	10.1	-	35.4	37.1
Dep. 3 tile 1	-	7.54	4.2	44.4	43.9
Dep. 4 tile 1	11.7	7.1	-	38.9	42.3
Dep. 5 tile 1	12.2	8.0	7.1	37.5	35.2

The deposition of tin telluride from **[SnⁿBu₃(TeⁿBu)]** produced stoichiometric films, Table 3-4, with good continuous coverages around 2 cm by 1 cm on average. These films were deposited within the temperature range of 355- 434 °C, at a pressure of 0.01 mm Hg, using between 31- 60 mg of precursor and the depositions took between 15- 18 minutes to complete.

Table 3-4: Energy dispersive X-ray analysis results for SnTe depositions. The large values observed for the O% is likely in part due to the overlap of characteristic X-rays of oxygen with minor lines from Sn and Te.

Tile	O%	Si%	Sn%	Te%
Dep. 1 Tile 1	16.4	2.1	41.4	40.1
Dep. 2 Tile 1	16.9	2.2	41.1	39.8
Dep. 2 Tile 2	15.8	0.7	41.9	41.6
Dep. 3 Tile 1	23.5	2.3	37.5	36.7

All of the deposited materials were characterised by grazing incidence X-ray diffraction (XRD), scanning electron microscopy (SEM), energy dispersive X-ray spectroscopy (EDX) and Raman spectroscopy. The variable temperature electrical and Seebeck properties have also been explored to evaluate the potential for these thin film materials to be used in TE devices.

3.4.3 Tin sulfide (SnS) thin films

Initial depositions produced films of highly sulfur deficient SnS, or alternatively tin rich. These films had unusual morphologies which contained long wires with diameters of *ca* 1 μm, as can be seen in Figure 3-9. The XRD patterns collected matched that of SnS and the lattice parameters: a =

11.1846(15), $b = 3.9717(6)$ and $c = 4.3001(7)$ Å are in good agreement with the literature values of: $a = 11.180(6)$, $b = 3.982(2)$ and $c = 4.329(3)$ Å.¹⁵

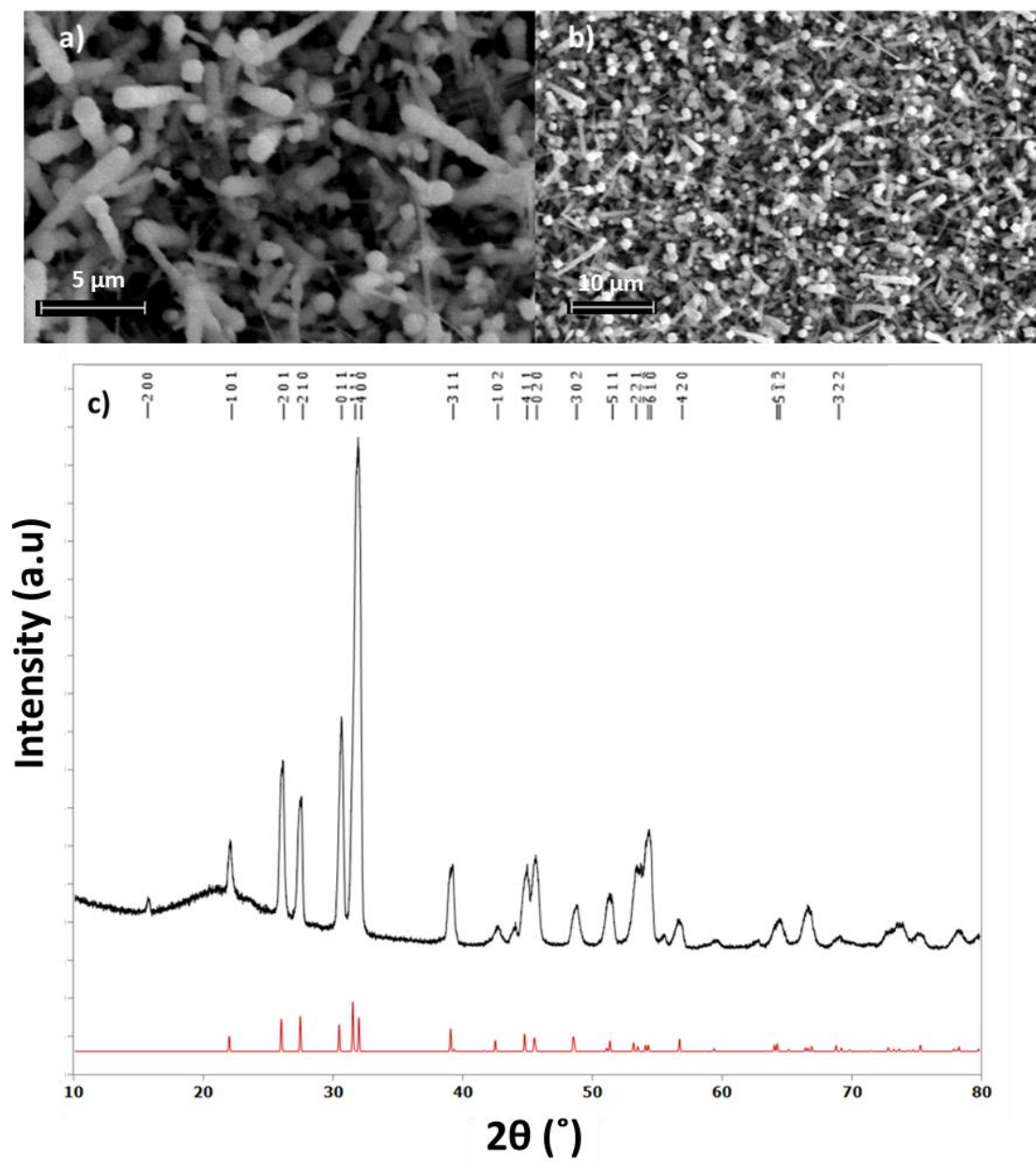


Figure 3-9: Top down SEM images a) and b) of two thin films of sulfur deficient SnS deposited using $[\text{Sn}^n\text{Bu}_3(\text{S}^n\text{Bu})]$ and c) a GIXRD pattern (black) for the film seen in b) matched to a bulk literature pattern (red).¹⁵

The film depicted in Figure 3-9 was found to contain 40% sulfur by EDX analysis. Despite multiple attempts, reducing the furnace temperature and attempting to speed up the deposition process all of the films produced from this precursor were sulfur deficient. However, since the GIXRD data does not show a reduced unit cell compared with the literature data, these deposits are likely tin rich. This might also explain the unusual morphology, seen in the SEM image seen in Figure 3-9a

and b, which may be nanowires produced in the VLS growth mechanism. It was for this reason that depositions using the alternative, more sulfur rich precursor, $[\text{Sn}^n\text{Bu}_2(\text{S}^n\text{Bu})_2]$, were explored.

The grazing incidence XRD pattern, shown in Figure 3-10, shows a deposition made using $[\text{Sn}^n\text{Bu}_2(\text{S}^n\text{Bu})]$. The GIXRD pattern shows a single phase of Pnma- tin sulfide, as can be seen by the bulk literature pattern displayed for comparison.¹⁵ The refined lattice parameters for the XRD pattern below are: $a = 11.271(1) \text{ \AA}$, $b = 4.0134(7) \text{ \AA}$ and $c = 4.3331(8) \text{ \AA}$ in good agreement with the literature values.¹⁵ Also of note, the intensity distribution of the pattern is similar to that of the literature bulk pattern. This suggests that the polycrystalline film has randomly orientated crystallites.

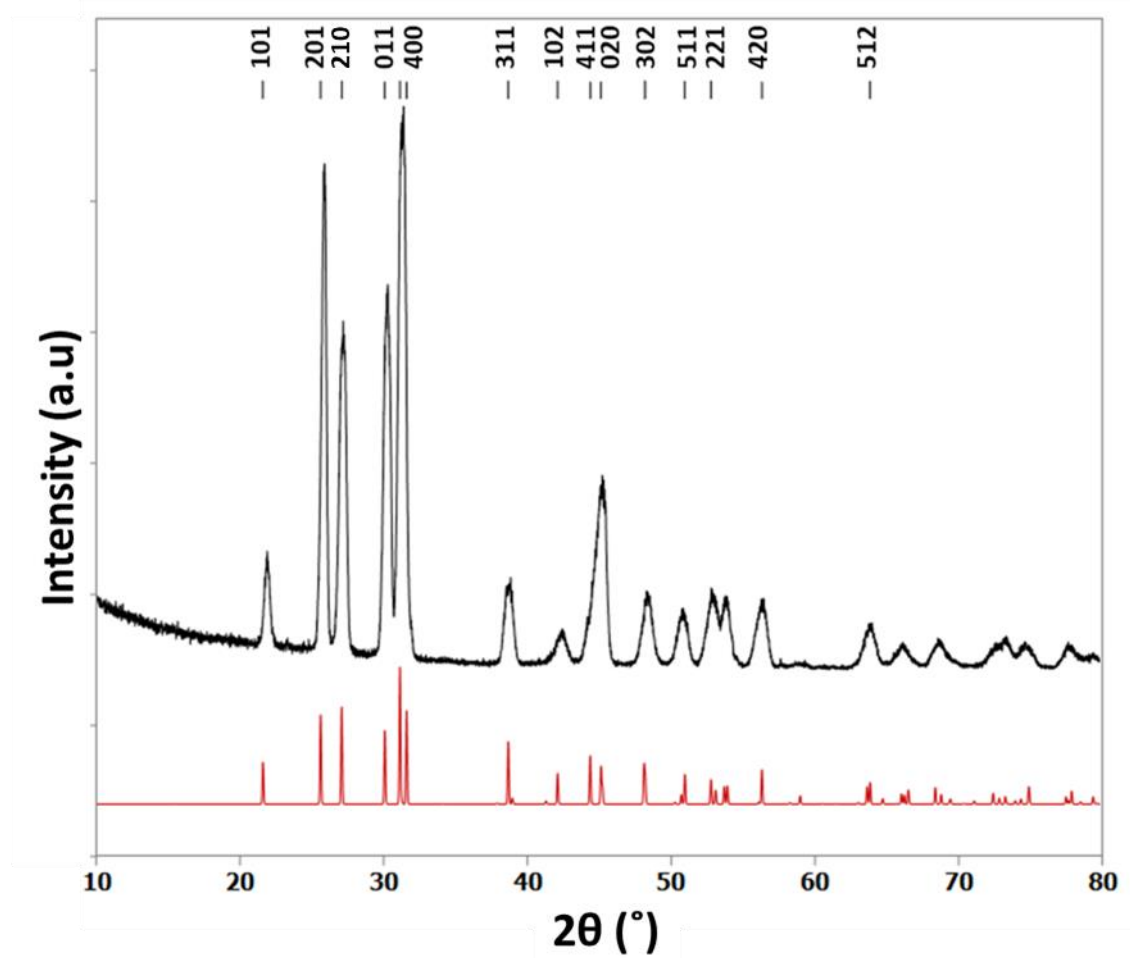
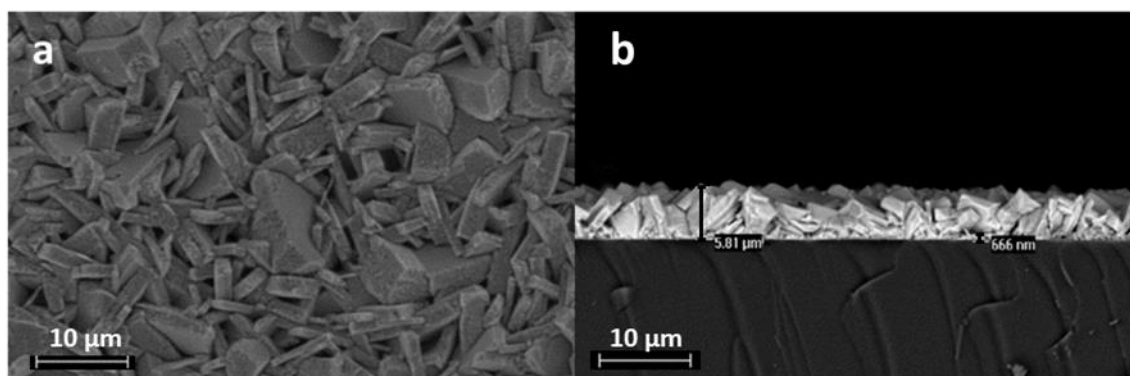


Figure 3-10: Top down SEM image (a), cross sectional SEM image (b) and grazing incidence XRD pattern for SnS thin film obtained by low pressure CVD using $[\text{Sn}^n\text{Bu}_2(\text{S}^n\text{Bu})_2]$ (red = XRD pattern for bulk SnS^{15}) with a thickness of around 6 μm .

The use of this precursor did overall increase the sulfur content of the films produced but the conditions under which stoichiometric tin sulfide could be produced were quite constrained. Only when performing the deposition at as fast a rate as possible using a small quantity of $[\text{Sn}^n\text{Bu}_2(\text{S}^n\text{Bu})_2]$ was it possible to produce three tiles of stoichiometric tin sulfide, shown by EDX analysis to contain between 49-50% of sulfur (spectrum of one deposition shown in Figure 3-11). It is likely that the requirement for such a fast deposition time and small amount of precursor is

that this reduces the time that the films are at temperature under low pressure. This may reduce the amount of volatile sulfur that can be removed from the films once they have deposited.

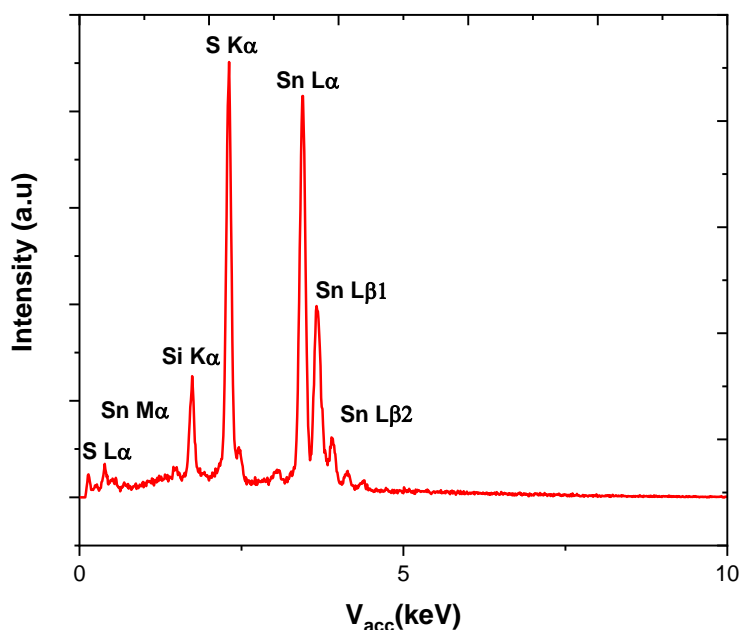


Figure 3-11: EDX spectrum obtained for a stoichiometric deposition of SnS, signal from the Si is from the underlying substrate material and is indicative of a thin film.

The grazing incidence XRD pattern (Figure 3-12c), as with depositions using $[\text{SnBu}_2(\text{SBu})_2]$, shows a single phase of Pnma- tin sulfide.¹⁵ The refined lattice parameters for the XRD pattern above are: $a = 11.271(1) \text{ \AA}$, $b = 4.0134(7) \text{ \AA}$ and $c = 4.3331(8) \text{ \AA}$, in good agreement with the literature values of: $a = 11.180(6) \text{ \AA}$, $b = 3.982(2) \text{ \AA}$ and $c = 4.329(3) \text{ \AA}$.¹⁵ The pattern in Figure 3-12c clearly shows a highly orientated, or textured, film of SnS. This orientational effect is the cause of the enhanced intensity of the 201 reflection, as compared to other peaks within the pattern. This orientation is further corroborated by inspection of the SEM images which clearly show crystallites lying flat forming interconnected plates atop the substrate. Ideally to explore this effect further pole figure measurements would be collected, however, thus far this has not been possible.

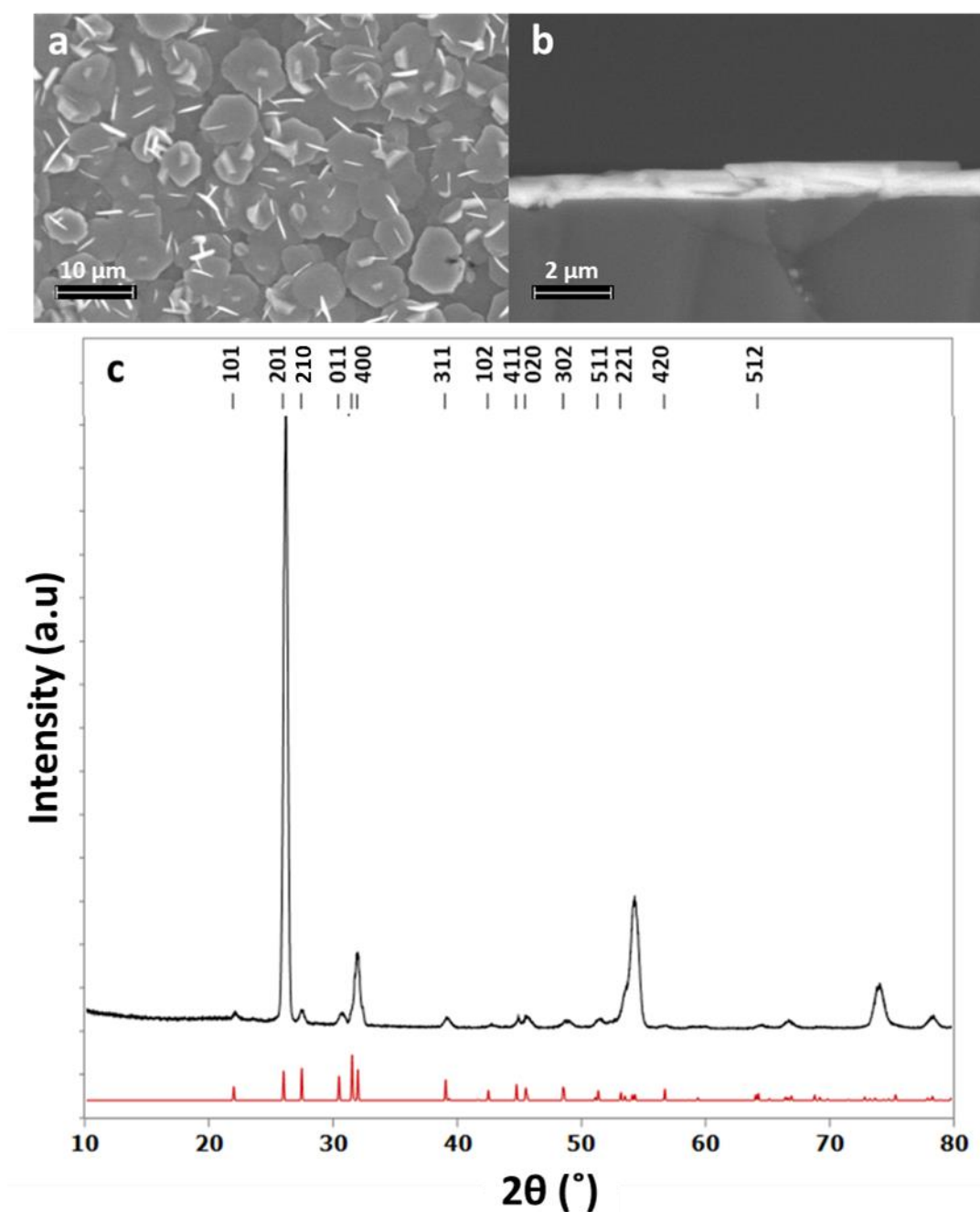


Figure 3-12: Top down SEM image (a), cross sectional SEM image (b) and grazing incidence XRD pattern for SnS thin film obtained by low pressure CVD using $[\text{Sn}^n\text{Bu}_2(\text{S}^n\text{Bu})_2]$ (red = XRD pattern for bulk SnS^{15}) with a thickness of *ca.* 700 nm.

The Raman spectrum (Figure 3-13) is also consistent with SnS; the peak at 98, 190 and 222 cm^{-1} corresponds to the A_g mode whereas the 190 cm^{-1} peak is associated with the B_{2g} mode.^{98,99}

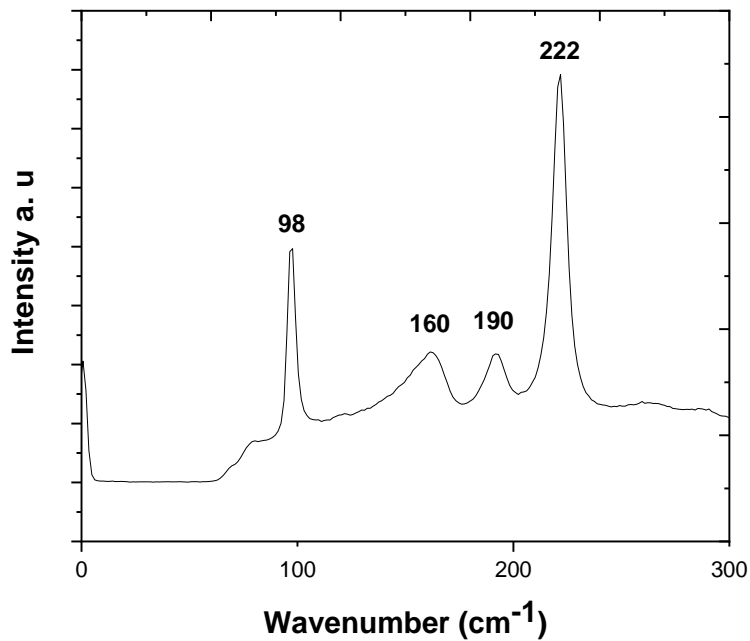


Figure 3-13: Raman spectrum with the data highlighting the A_g and B_{2g} modes.

3.4.4 Tin mono-selenide (SnSe) thin films

The film displayed in Figure 3-15 corresponds to Dep. 3 tile 1 in Table 3-3, which is a sample within the error for stoichiometric tin selenide. Control over the stoichiometry proved much simpler than in the case of the tin sulfide depositions, likely as a result of the lower volatility of the selenium compared to the sulfur. The depositions were produced stoichiometrically and with no impurities as can be observed in the EDX spectrum shown in Figure 3-14.

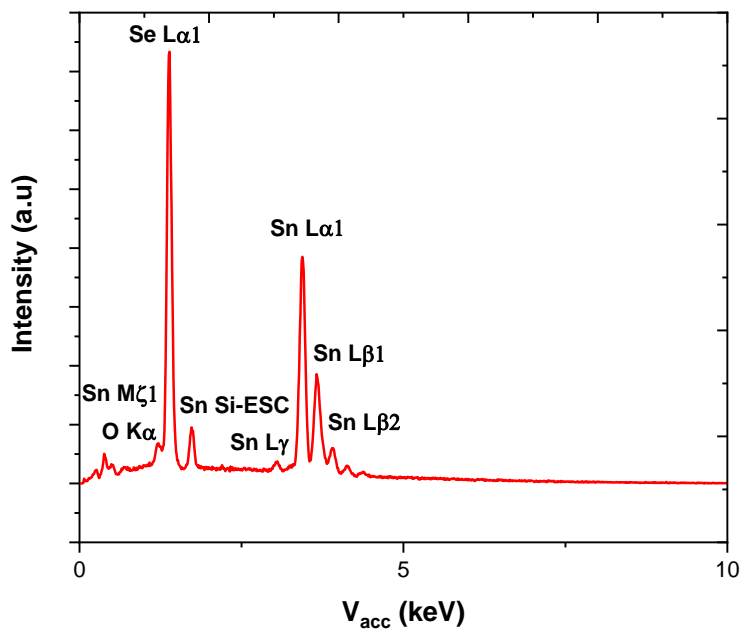


Figure 3-14: EDX Spectrum collected for a stoichiometric sample of SnSe.

The grazing incidence XRD pattern shown in Figure 3-15c is in good agreement with the literature pattern for orthorhombic SnSe in space group $Pnma$. The refined lattice parameters are: $a = 11.4844 (18) \text{ \AA}$, $b = 4.1555 (7) \text{ \AA}$ and $c = 4.4289 (10) \text{ \AA}$ (literature: $a = 11.49417 (12) \text{ \AA}$, $b = 4.15096 (5) \text{ \AA}$ and $c = 4.44175 (7) \text{ \AA}$).¹⁹ The diffraction pattern can be seen in Figure 3-15c.

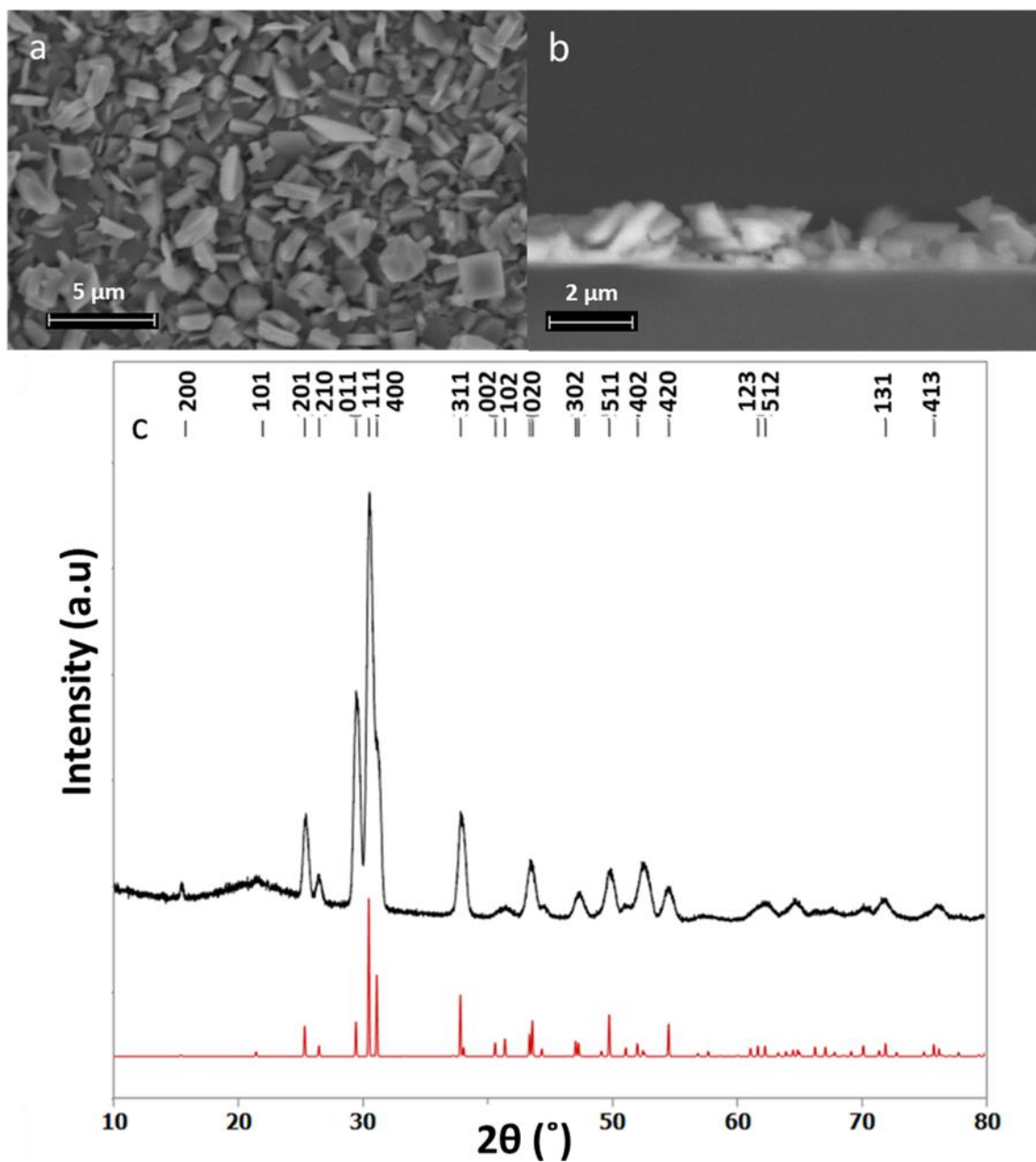


Figure 3-15: Grazing incidence XRD pattern for SnSe thin film (black) and the pattern for bulk Pnma SnSe (red).¹⁹

The Raman spectrum (Figure 3-16) of the SnSe film shows the expected peaks at 152, 130 and 110 cm^{-1} , corresponding to the A_{3g} , A_{2g} and B_{3g} modes, respectively.³⁷ The very weak feature at 186 cm^{-1} may indicate the presence of a small amount of SnSe_2 , although this is not visible in the XRD data.

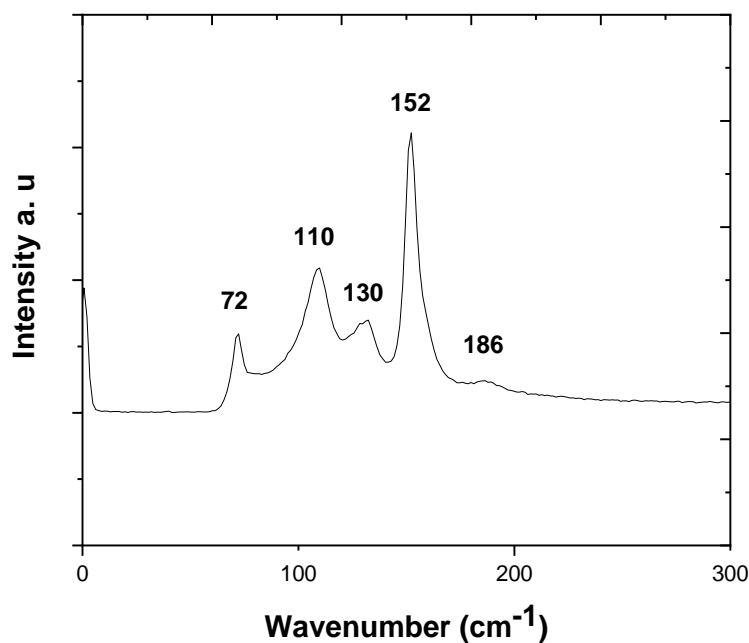


Figure 3-16: Raman spectra of an SnSe thin film with the peaks at 152, 130, 72 and 110 cm^{-1} , corresponding to the A_g , A_g , A_g and B_{3g} modes highlighted. Also highlighted is the small feature at 186 cm^{-1} which is likely SnSe_2 .³⁷

3.4.5 Tin mono-telluride (SnTe) thin films

The grazing incidence XRD pattern (Figure 3-17a) agrees with the literature pattern for bulk SnTe (red).³ The broad feature centred at around 21° is caused by the underlying silica substrate. The refined lattice parameter, $a = 6.3033(5) \text{ \AA}$ for this cubic system, which is in good agreement with the bulk literature ($a = 6.318(3) \text{ \AA}$).³

The scanning electron microscopy (SEM) analysis (Figure 3-17b and c) showed uniformly distributed arrays of continuous polycrystalline films comprised of block-like particles. The cross-sectional SEM analysis determined the film thicknesses to be around *ca.* 1-2 μm and the grain sizes to be around 1 μm .³

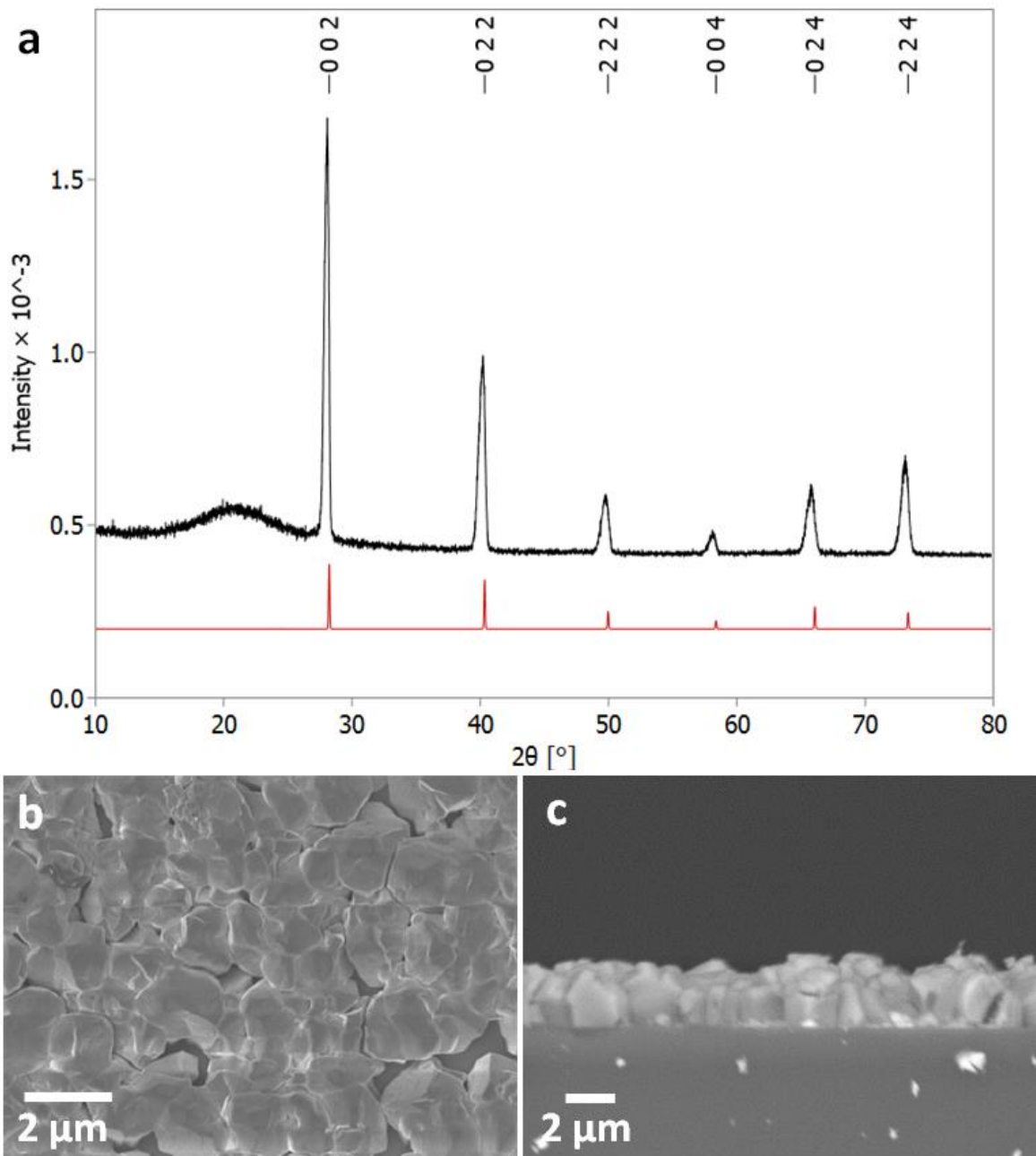


Figure 3-17: (a) grazing incidence XRD pattern for SnTe thin film (thickness *ca.* 1 μm) with XRD pattern for bulk cubic SnTe (Fm-3m) (red),³ (b) Top down and (c) cross sectional SEM images.

Crystallite sizes of between 100(10) to 210(110) nm were measured using the Halder-Wagner method, using a LaB₆ standard to account for instrumental peak broadening effects. The sizes measured using this method are smaller than those seen in the SEM images, which indicates that those observed in the SEM images are most likely particles of crystalline aggregates rather than individual crystallites.

As with the tin selenide depositions, the control over the stoichiometry of the tin telluride films was much simpler than for the tin sulfide deposition. Even in the case of longer depositions for thicker films, the tellurium content of the deposited films was between 48- 50 % by EDX analysis.

The EDX spectra displayed in Figure 3-18a shows that the SnTe film deposited contains only elements from the SnTe film or from the SiO₂ substrate and no other observable impurities. The presence of the *Si K α* peak indicates that the film was thin enough for the electron beam to penetrate to the substrate underlying the deposit. The Raman spectrum observable in Figure 3-18b of the SnTe film shows the expected peaks at 124 and 143 cm⁻¹, corresponding to the A₁ and E stretches, respectively.^{29,100} The lack of other peaks in the SnTe Raman spectra bellow indicates the absence of any surface impurities.

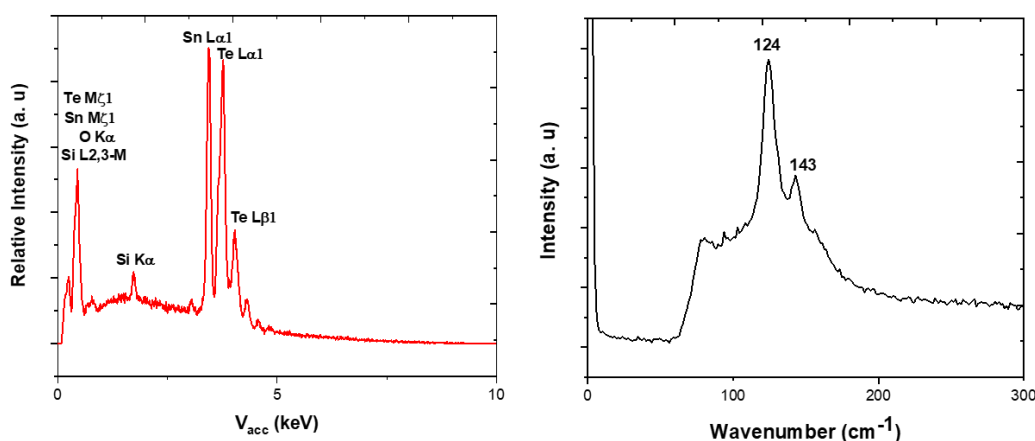


Figure 3-18: (a) EDX spectrum highlighting the elements present within the SnTe film, the silicon present is attributed to the substrate. (b) Raman spectrum with the data highlighting the A₁ and E modes at 124 and 143 cm⁻¹, respectively.^{29,100}

3.4.6 Thermoelectric performance

In order to evaluate the thermoelectric performance of the deposited films, Seebeck coefficient and Hall effect measurements were employed. These methods have been discussed in greater detail in sections 1.8.3.1 and 1.8.3.2. Here the electrical resistivity, charge carrier mobility, charge carrier concentration, Hall effect coefficient, Seebeck coefficient and power factor for the as deposited films of SnS (both stoichiometric and sulfur-poor), SnSe and SnTe are reported.

3.4.6.1 Tin Sulfide

Manual thermoelectric measurements were gathered by Daniel Newbrook. As described in section 3.4.3, non-stoichiometric depositions of SnS were produced using depositions from [SnBu₃(SBu)] and [SnBu₂(SBu)₂] and stoichiometric SnS was successfully produced using

[SnBu₂(SBu)₂] with rapid deposition times. This allowed for a comparison of the properties of both the stoichiometric and sulfur poor depositions, however, to date only SnS samples from [SnBu₂(SBu)₂] have had their thermoelectric properties explored. The electrical conductivity of the sulfur deficient deposition, SnS_{0.9}, are greatly improved due to the increase in charge carrier concentration and mobility, compared to stoichiometric SnS. This enhancement of the charge carrier concentration, and subsequently the electrical conductivity, for the sulfur-deficient deposition is a little counterintuitive, as this would typically lead to n-type doping and thus lower p-type conductivity. The increased electrical conductivity seen for SnS_{0.9} results in an increased power factor, to ca. 6 μWK⁻²·cm⁻¹, higher than reported for even some doped polycrystalline SnS samples.^{10,101,102} A graphical representation of these findings can be seen in Figure 3-19. The undoped stoichiometric SnS films have a limited thermoelectric performance caused by the low carrier concentration and large bandgaps.^{103,104} Such shortcomings can be addressed by including doping or alloying which have been successfully demonstrated in several pioneering works,^{47,101,105–108} resulting in high ZT values.

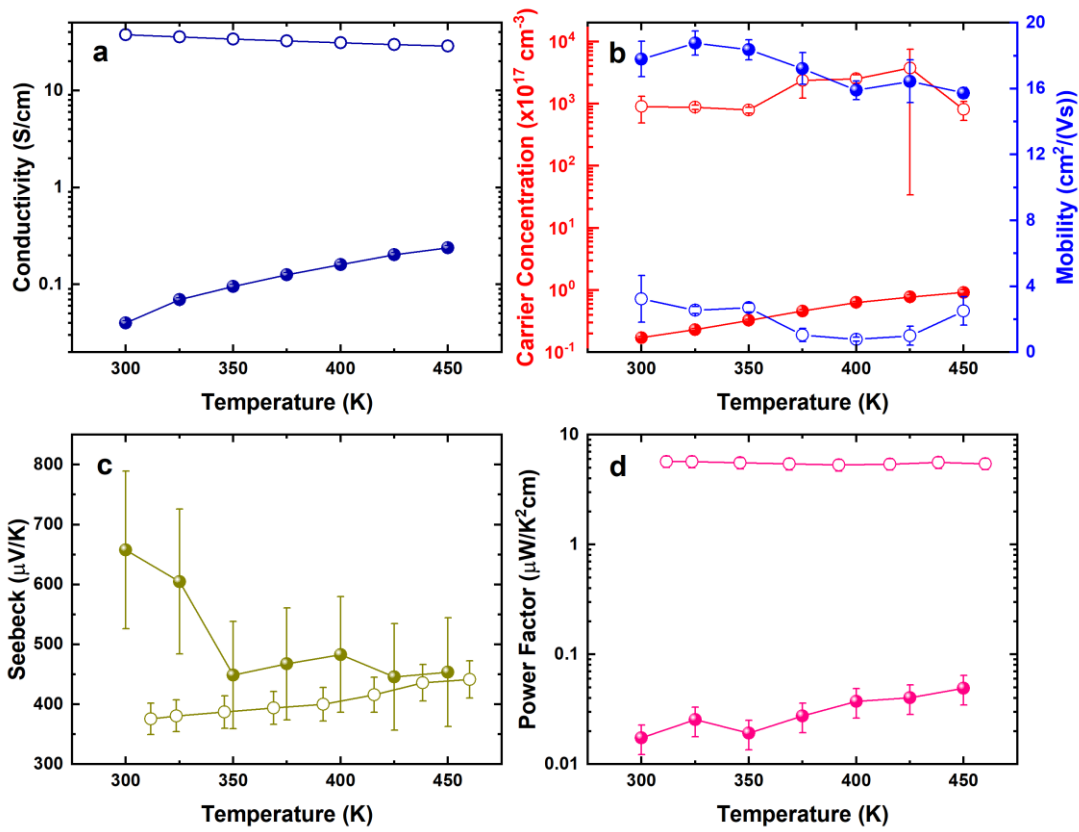


Figure 3-19: Comparison of stoichiometric SnS, filled circles, and SnS_{0.9}, empty circles, for a) conductivity, b) carrier concentration, red, and mobility, blue, c) Seebeck coefficient and d) power factor.

3.4.6.2 Tin Selenide

The electrical measurements confirm that the SnSe deposit displays semiconductor like conductivity, as can be seen in Figure 3-20a. The electrical conductivity is low, with a room temperature value of 0.1 Scm^{-1} . This low observed electrical conductivity in SnSe is attributable to its low charge carrier concentration of $2 \times 10^{17} \text{ cm}^{-3}$. A high Seebeck coefficient, as compared to the literature,^{7,80,109,110} is displayed in Figure 3-20c. It is this value which leads to the competitive value obtained for the power factor of the measured SnSe. The peak power factor value of $\sim 0.55 \mu\text{WK}^{-2}\text{cm}^{-1}$ at 400 K matches literature examples of polycrystalline thin films of SnSe.^{106,111} Due to the low resistivity of SnSe the temperature regime is restricted to 300- 450 K, as this is the overlapping region of the Seebeck tool and the Hall effect tool described in section 1.9.3.

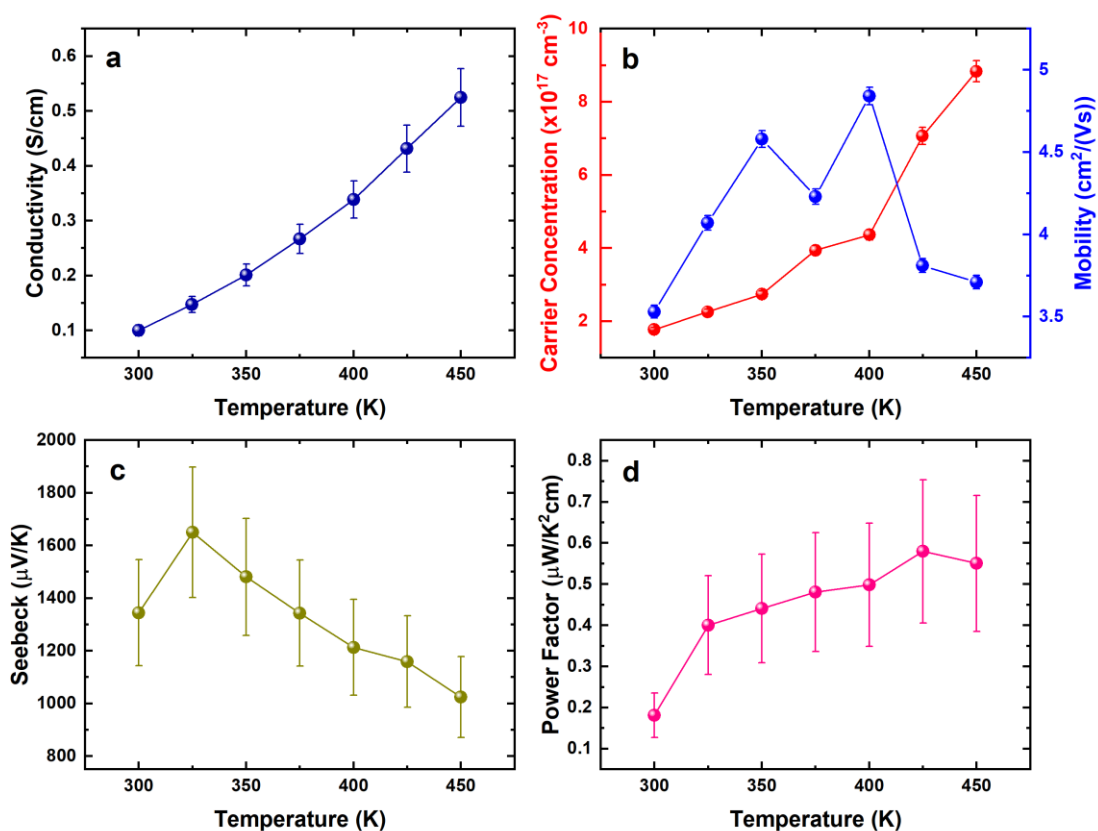


Figure 3-20: a) Electrical conductivity, b) the carrier concentration in red and the mobility in blue, c) the Seebeck coefficient and d) the power factor for the SnSe deposited using $[\text{SnBu}_3(\text{SeBu})]$.

3.4.6.3 Tin Telluride

The electrical conductivity measurements, displayed in Figure 3-21, from both tools showed good agreement and showed that the deposited films of SnTe exhibited metallic transportation behaviour. The room temperature electrical conductivity displayed is 2400 S cm^{-1} . This high

electrical conductivity is likely the result of intrinsic Sn vacancies causing a high p-type carrier concentration.⁶ This is further evidenced by the high charge carrier concentration value measured using the Hall effect method, in the range of $(4 - 5) \times 10^{21} \text{ cm}^{-3}$. The charge carrier concentration remains fairly constant within the temperature of 100- 450 K but the charge carrier mobility decreases with temperature. This decrease in mobility is likely a result of stronger scattering effects at elevated temperatures, resulting in the metallic type conductivity observed.

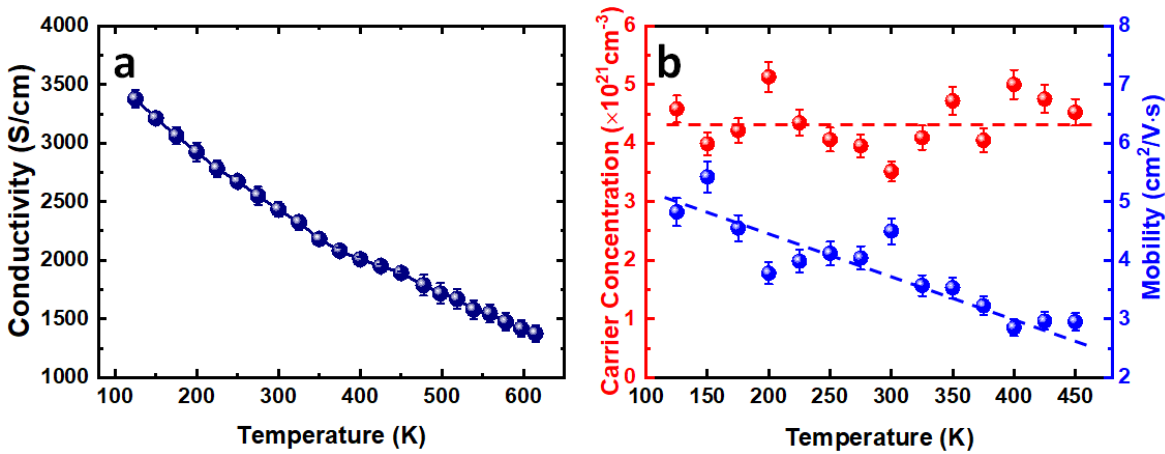


Figure 3-21: Temperature dependence of (a) the electrical conductivity, (b) carrier concentration and mobility for SnTe. The lines connecting the electrical conductivity and the dotted trendlines of the carrier concentration and mobility are to guide the eyes.

The Seebeck coefficient measured for the as-deposited films of SnTe further confirm the p-type identification as the Seebeck coefficients measured were all positive. The Seebeck coefficient measured is *ca.* $12 \mu\text{V}/\text{K}$ at room temperature and is increased to *ca.* $78 \mu\text{V}/\text{K}$ at higher temperature (615 K), as shown in Figure 3-22a and the power factor displays a peak value of $8.3 \mu\text{W}/\text{K}^2\cdot\text{cm}$ at 615 K, Figure 3-22b. These values are comparable to undoped polycrystalline literature samples previously reported.^{6,113–115} This provides additional evidence for the high quality of the precursors and their clean decomposition during the deposition process. The performance reported here are for undoped and unoptimized polycrystalline thin films of SnTe. Therefore, as mentioned in previous sections, large improvements are possible by implementing doping and alloying to induce band engineering or more specifically band convergence of the light and heavy hole valance bands.^{72,116,117} In the undoped films these bands have a relatively large energy separation of around 0.3- 0.4 eV,⁷² but using carefully selected dopants these can be made to converge. This increases the band degeneracy which greatly improves performance, as discussed in **1.2.2.3**.

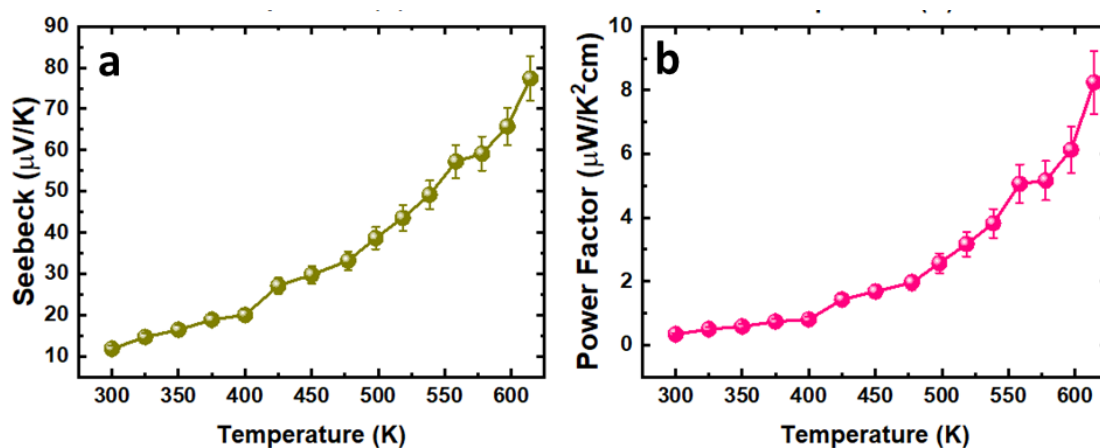


Figure 3-22: Temperature dependence of the Seebeck coefficient and power factor with connective lines to guide the eyes.

3.4.7 Selective deposition of tin telluride

The selective deposition process and the method of fabrication for the patterned substrates is covered in more detail in Section 1.4. Previous investigations into selective depositing materials has shown that materials with higher electrical conductivity display better selectivity onto lithographically patterned substrates.³⁹ For this reason SnTe was selected as a likely candidate for the selective deposition into TiN wells in a SiO₂ matrix. The other tin chalcogenide deposition, SnS and SnSe, likely have too high electrical resistivity to be selectively deposited in this manner.¹¹⁸ The selective deposition of SnTe is demonstrated in Figure 3-23. Here the deposition can be seen inside one TiN well where crystalline material can clearly be seen. EDX elemental mapping also corroborates this, as only Sn and Te can be seen inside the well whereas O can be seen outside the well in the SiO₂ matrix. The higher electrical conductivity and hydrophobicity of TiN compared to SiO₂ has been discussed previously as a likely cause of this selective behaviour.^{118,119} This selective deposition behaviour provides great positional control over the growth of SnTe and therefore provides evidence that this process can be transferred to the fabrication of μ -TEGs.⁴²

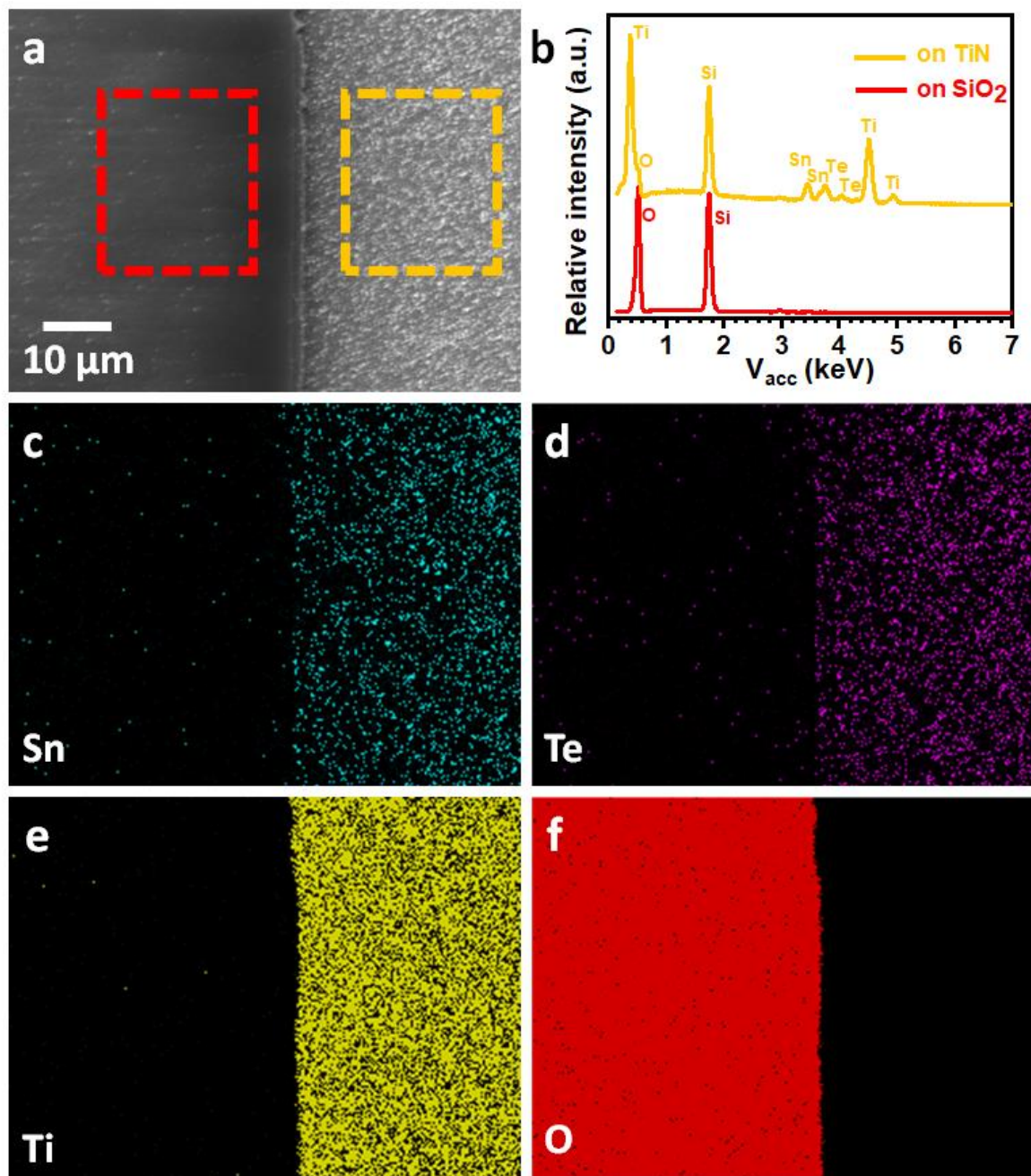


Figure 3-23: (a) Top-view SEM image of a TiN/SiO₂ patterned substrate with SnTe selectively deposited on the TiN surface (right). (b) EDX spectra taken from the rectangular areas indicated in (a). EDX element mapping of (c) Sn, (d) Te, (e) Ti and (f) O.

3.5 Conclusions

The series of single source precursors, of the form $[\text{SnBu}_3(\text{EBu})]$, were determined by TGA to be suitable for LPCVD. The precursors used in the LPCVD procedure established for sulfur poor SnS, SnSe and SnTe and the precursor $[\text{SnBu}_2(\text{SBU})_2]$ was successfully developed for the deposition of stoichiometric SnS.

The deposited films were fully characterised using GIXRD, SEM with EDX and Raman spectroscopy. The thermoelectric and electrical properties were also measured using variable temperature Seebeck, resistivity and variable temperature Hall effect measurements were gathered using the van der Pauw method. The measurements were compared to those from the literature and shown to be competitive with those of polycrystalline samples. The performance of the sulfur deficient deposition described was far superior to that of the stoichiometric samples, but further studies are required to develop a rationale for this improved performance.

The selective deposition of tin telluride onto patterned SiO_2/TiN substrates was also investigated due to its much larger electrical conductivity. The success of these attempts was determined using SEM with EDX mapping. The success of these selective deposition experiments is an important step towards the fabrication of a device, as this means that there is potential to selectively deposit into a device template. Thus, this procedure may be used for the deposition of a μ -TEG.

3.6 References

- 1 C. Wood, *Reports Prog. Phys.*, 1988, **51**, 459.
- 2 A. Polozine, S. Sirovinskaya and L. Schaeffer, *Mater. Res.*, 2014, **17**, 1260.
- 3 P. Bauer Pereira, I. Sergueev, S. Gorsse, J. Dadda, E. Müller and R. P. Hermann, *Phys. status. Solidi B*, 2013, **250**, 1300.
- 4 G. Tan, L. D. Zhao, F. Shi, J. W. Doak, S. H. Lo, H. Sun, C. Wolverton, V. P. Dravid, C. Uher and M. G. Kanatzidis, *J. Am. Chem. Soc.*, 2014, **136**, 7006.
- 5 J. Zhai, T. Wang, H. Wang, W. Su, X. Wang, T. Chen and C. Wang, *Chinese Phys. B*, 2018, **27**, 047406.
- 6 A. Banik, S. Roychowdhury and K. Biswas, *Chem. Commun.*, 2018, **54**, 6573.
- 7 L.-D. Zhao, S.-H. Lo, Y. Zhang, H. Sun, G. Tan, C. Uher, C. Wolverton, V. P. Dravid and M. G. Kanatzidis, *Nature*, 2014, **508**, 373.
- 8 C. W. Li, J. Hong, A. F. May, D. Bansal, S. Chi, T. Hong, G. Ehlers and O. Delaire, *Nat. Phys.*, 2015, **11**, 1063.
- 9 Y. Xiao, C. Chang, Y. Pei, D. Wu, K. Peng, X. Zhou, S. Gong, J. He, Y. Zhang, Z. Zeng and L. D. Zhao, *Phys. Rev. B*, 2016, **94**, 125203.
- 10 Z. Wang, D. Wang, Y. Qiu, J. He and L. D. Zhao, *J. Alloys Compd.*, 2019, **789**, 485.

Chapter 3

- 11 P. K. Nair, A. R. Garcia-Angelmo and M. T. S. Nair, *Phys. Status Solidi Appl. Mater. Sci.*, 2016, **213**, 170.
- 12 P. K. Nair, E. Barrios-Salgado and M. T. S. Nair, *Phys. Status Solidi Appl. Mater. Sci.*, 2016, **213**, 2229.
- 13 W. G. Zeier, A. Zevalkink, Z. M. Gibbs, G. Hautier, M. G. Kanatzidis and G. J. Snyder, *Angew. Chem. Int. Ed.*, 2016, **55**, 6826.
- 14 R. Al Rahal Al Orabi, N. A. Mecholsky, J. Hwang, W. Kim, J. S. Rhyee, D. Wee and M. Fornari, *Chem. Mater.*, 2016, **28**, 376.
- 15 S. Del Bucchia, J. C. Jumas and M. Maurin, *Acta Cryst.*, 1981, **B37**, 1903.
- 16 S. Hao, V. P. Dravid, M. G. Kanatzidis and C. Wolverton, *APL Mater.*, 2016, **4**, 104505.
- 17 Q. Tan and J.-F. Li, *J. Electron. Mater.*, 2014, **43**, 2435.
- 18 S. Lopez and A. Ortiz, *Semicond. Sci. Technol.*, 1994, **9**, 2130.
- 19 M. Sist, J. Zhang and B. B. Iversen, *Acta Cryst.*, 2016, **B72**, 310.
- 20 W. Shi, M. Gao, J. Wei, J. Gao, C. Fan, E. Ashalley, H. Li and Z. Wang, *Adv. Sci.*, 2018, **5**, 1700602.
- 21 S. Li, X. Li, Z. Ren and Q. Zhang, *J. Mater. Chem. A*, 2018, **6**, 2432.
- 22 G. Shi and E. Kioupakis, *J. Appl. Phys.*, 2015, **117**, 065103.
- 23 I. Lefebvre, M. Szymanski, J. Olivier-Fourcade and J. Jumas, *Phys. Rev. B - Condens. Matter Mater. Phys.*, 1998, **58**, 1896.
- 24 T. F. Smith, J. A. Birch and J. G. Collins, *J. Phys. C Solid State Phys.*, 1976, **9**, 4375.
- 25 C. W. Li, J. Ma, H. B. Cao, A. F. May, D. L. Abernathy, G. Ehlers, C. Hoffmann, X. Wang, T. Hong, A. Huq, O. Gourdon and O. Delaire, *Phys. Rev. B - Condens. Matter Mater. Phys.*, 2014, **90**, 214303.
- 26 A. Banik, U. S. Shenoy, S. Anand, U. V Waghmare and K. Biswas, *Chem. Mater.*, 2015, **27**, 581.
- 27 R. Moshwan, L. Yang, J. Zou and Z. G. Chen, *Adv. Funct. Mater.*, 2017, **27**, 30.
- 28 J. R. Brent, D. J. Lewis, T. Lorenz, E. A. Lewis, N. Savjani, S. J. Haigh, G. Seifert, B. Derby and P. O'Brien, *J. Am. Chem. Soc.*, 2015, **137**, 12689.
- 29 N. Berchenko, R. Vitchev, M. Trzyna, R. Wojnarowska-Nowak, A. Szczerbakow, A. Badyła, J. Cebulski and T. Story, *Appl. Surf. Sci.*, 2018, **452**, 134.
- 30 J. Shen and J. J. Cha, *Nanoscale*, 2014, **6**, 14133.
- 31 D. J. Lewis, P. Kevin, O. Bakr, C. A. Muryn, M. A. Malik and P. O'Brien, *Inorg. Chem. Front.*, 2014, **1**, 577.
- 32 H. Zhang, B. Man and Q. Zhang, *ACS Appl. Mater. Interfaces*, 2017, **9**, 14067.
- 33 M. Zhang, D. Lei, X. Yu, L. Chen, Q. Li, Y. Wang, T. Wang and G. Cao, *J. Mater. Chem.*, 2012, **22**, 23091.
- 34 L. Zhang, L. Lu, D. Zhang, W. Hu, N. Wang, B. Xu, Y. Li and H. Zeng, *Electrochim. Acta*, 2016,

- 209**, 423.
- 35 Z. Xie, F. Zhang, Z. Liang, T. Fan, Z. Li, X. Jiang, H. Chen, J. Li and H. Zhang, *Photonics Res.*, 2019, **7**, 494.
- 36 T. Subba Rao and A. K. Chaudhuri, *J. Phys. D. Appl. Phys.*, 1985, **18**, L35.
- 37 W. Gao, C. Wu, M. Cao, J. Huang, L. Wang and Y. Shen, *J. Alloys Compd.*, 2016, **688**, 668.
- 38 A. Tanuševski, *Semicond. Sci. Technol.*, 2003, **18**, 501.
- 39 R. E. Banai, M. W. Horn and J. R. S. Brownson, *Sol. Energy Mater. Sol. Cells*, 2016, **150**, 112.
- 40 F. K. Butt, M. Mirza, C. Cao, F. Idrees, M. Tahir, M. Safdar, Z. Ali, M. Tanveer and I. Aslam, *CrystEngComm*, 2014, **16**, 3470.
- 41 A. Sánchez-Juárez, A. Tiburcio-Silver and A. Ortiz, *Thin Solid Films*, 2005, **480–481**, 452.
- 42 P. D. Antunez, J. J. Buckley and R. L. Brutchey, *Nanoscale*, 2011, **3**, 2399.
- 43 C. Wang, Y. D. Li, G. H. Zhang, J. Zhuang and G. Q. Shen, *Inorg. Chem.*, 2000, **39**, 4237.
- 44 M. S. Mahdi, K. Ibrahim, A. Hmood, N. M. Ahmed, F. I. Mustafa and S. A. Azzez, *Mater. Lett.*, 2017, **200**, 10.
- 45 X. Wang, B. Liu, Q. Xiang, Q. Wang, X. Hou, D. Chen and G. Shen, *ChemSusChem*, 2014, **7**, 308.
- 46 H. Wang, D. Chao, J. Liu, J. Lin and Z. X. Shen, *2D Mater.*, 2018, **5**, 031005.
- 47 H. Wu, X. Lu, G. Wang, K. Peng, H. Chi, B. Zhang, Y. Chen, C. Li, Y. Yan, L. Guo, C. Uher, X. Zhou and X. Han, *Adv. Energy Mater.*, 2018, **8**, 1800087.
- 48 S. C. Ray, M. K. Karanjai and D. Dasgupta, *Thin Solid Films*, 1999, **350**, 72.
- 49 G. Hema Chandra, J. Naveen Kumar, N. Madhusudhana Rao and S. Uthanna, *J. Cryst. Growth*, 2007, **306**, 68.
- 50 S. Xu, W. Zhu, H. Zhao, L. Xu, P. Sheng, G. Zhao and Y. Deng, *J. Alloys Compd.*, 2018, **737**, 167.
- 51 Z. Wang, J. Wang, Y. Zang, Q. Zhang, J. A. Shi, T. Jiang, Y. Gong, C. L. Song, S. H. Ji, L. L. Wang, L. Gu, K. He, W. Duan, X. Ma, X. Chen and Q. K. Xue, *Adv. Mater.*, 2015, **27**, 4150.
- 52 C. J. Carmalt, I. P. Parkin and E. S. Peters, *J. Mater. Chem.*, 2000, **10**, 527.
- 53 L. S. Price, I. P. Parkin, T. G. Hibbert and K. C. Molloy, *Chem. Vap. Depos.*, 1998, **4**, 222.
- 54 I. Y. Ahmet, M. S. Hill, P. R. Raithby and A. L. Johnson, *Dalton Trans.*, 2018, **47**, 5031.
- 55 I. P. Parkin, L. S. Price, T. G. Hibbert and K. C. Molloy, *J. Mater. Chem.*, 2001, **11**, 1486.
- 56 I. S. Chuprakov, K. H. Dahmen, J. J. Schneider and J. Hagen, *Chem. Mater.*, 1998, **10**, 3467.
- 57 C. Gurnani, S. L. Hawken, A. L. Hector, R. Huang, M. Jura, W. Levason, J. Perkins, G. Reid and G. B. G. Stenning, *Dalton Trans*, 2018, **47**, 2628.
- 58 P. Sinsermuksakul, J. Heo, W. Noh, A. S. Hock and R. G. Gordon, *Adv. Energy Mater.*, 2011, **1**, 1116.

Chapter 3

- 59 J. Y. Kim and S. M. George, *J. Phys. Chem. C*, 2010, **114**, 17597.
- 60 V. E. Drozd, I. O. Nikiforova, V. B. Bogevolnov, A. M. Yafyasov, E. O. Filatova and D. Papazoglou, *J. Phys. D. Appl. Phys.*, 2009, **42**, 125306.
- 61 S. Afrin, N. Kuperman and R. Solanki, "Atomic layer Deposition of 2-dimensional, Semiconducting SnSe Thin Films," *2018 IEEE 13th Nanotechnology Materials and Devices Conference (NMDC)*, 2018, pp. 1-4, doi: 10.1109/NMDC.2018.8605911
- 62 P. Boudjouk, M. P. Remington, D. G. Grier, W. Triebold and B. R. Jarabek, *Organometallics*, 2002, **18**, 4534.
- 63 I. P. Parkin, L. S. Price, T. G. Hibbert and K. C. Molloy, *J. Mater. Chem.*, 2001, **11**, 1486.
- 64 P. Boudjouk, D. J. Seidler, S. R. Bahr and G. J. McCarthy, *Chem. Mater.*, 1994, **6**, 2108.
- 65 K. Ramasamy, V. L. Kuznetsov, K. Gopal, M. A. Malik, J. Raftery, P. P. Edwards and P. O'Brien, *Chem. Mater.*, 2013, **25**, 266.
- 66 M. D. Khan, M. Aamir, M. Sohail, M. Sher, N. Baig, J. Akhtar, M. A. Malik and N. Revaprasadu, *Dalton Trans.*, 2018, **47**, 5465.
- 67 B. P. Bade, S. S. Garje, Y. S. Niwate, M. Afzaal and P. O'Brien, *Chem. Vap. Depos.*, 2008, **14**, 292.
- 68 P. Kevin, S. N. Malik, M. A. Malik and P. O'Brien, *Chem. Commun.*, 2014, **50**, 14328.
- 69 I. Y. Ahmet, M. S. Hill, A. L. Johnson and L. M. Peter, *Chem. Mater.*, 2015, **27**, 7680.
- 70 Q. Zhang, B. Liao, Y. Lan, K. Lukas, W. Liu, K. Esfarjani, C. Opeil, D. Broido, G. Chen and Z. Ren, *Proc. Natl. Acad. Sci.*, 2013, **110**, 13261.
- 71 W. He, D. Wang, H. Wu, Y. Xiao, Y. Zhang, D. He, Y. Feng, Y.-J. Hao, J.-F. Dong, R. Chetty, L. Hao, Chen, D. Qin, Jianfei, Q. Yang, X. Li, J.-M. Song, Y. Zhu, W. X. C. Niu, X. Li, G. Wang, C. Liu, M. Ohta, S. J. Pennycook, J. He, J.-F. Li⁴ and L.-D. Zha, *Science*, 2019, **365**, 1418.
- 72 R. Moshwan, W. Di Liu, X. L. Shi, Y. P. Wang, J. Zou and Z. G. Chen, *Nano Energy*, 2019, **65**, 104056.
- 73 H. L.D. and D. M.S., *Phys. Rev. B*, 1993, **47**, 12727.
- 74 L. Hicks, T. Harman, X. Sun and M. S. Dresselhaus, *Phys. Rev. B*, 1996, **53**, R10493.
- 75 G. Chen, M. S. Dresselhaus, G. Dresselhaus, J.-P. Fleurial and T. Caillat, *Int. Mater. Rev.*, 2013, **48**, 45.
- 76 H. Guo, H. Xin, X. Qin, J. Zhang, D. Li, Y. Li, C. Song and C. Li, *J. Alloys Compd.*, 2016, **689**, 87.
- 77 H. Reith, K. Nielsch, O. Falkenbach, J. Tinz, A. S. Schulze, E. Mueller and S. Schlecht, *Phys. Status Solidi Appl. Mater. Sci.*, 2016, **213**, 699.
- 78 G. Han, R. Zhang, S. R. Popuri, H. F. Greer, M. J. Reece, J. W. G. Bos, W. Zhou, A. R. Knox and D. H. Gregory, *Materials (Basel)*, 2017, **10**, 233.
- 79 P. C. Wei, S. Bhattacharya, J. He, S. Neeleshwar, R. Podila, Y. Y. Chen and A. M. Rao, *Nature*, 2016, **539**, E1.
- 80 Y. K. Lee, Z. Luo, S. P. Cho, M. G. Kanatzidis and I. Chung, *Joule*, 2019, **3**, 719.

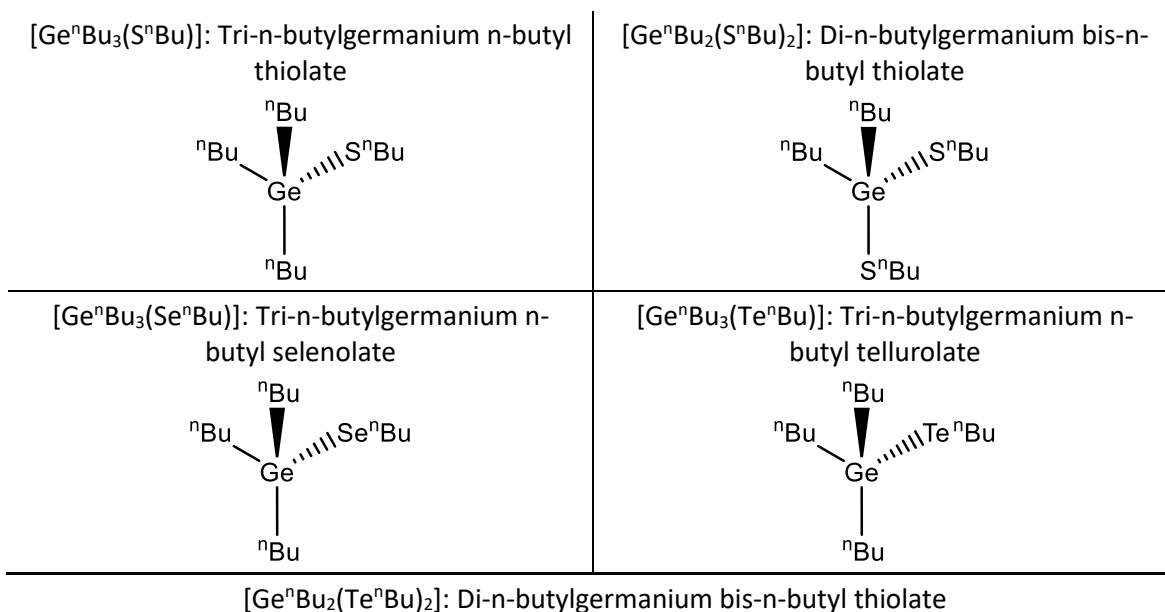
- 81 D. Wu, L. Wu, D. He, L. D. Zhao, W. Li, M. Wu, M. Jin, J. Xu, J. Jiang, L. Huang, Y. Zhu, M. G. Kanatzidis and J. He, *Nano Energy*, 2017, **35**, 321.
- 82 C.-F. Wu, T.-R. Wei and J.-F. Li, *Phys. Chem. Chem. Phys.*, 2015, **17**, 13006.
- 83 Y. M. Han, J. Zhao, M. Zhou, X. X. Jiang, H. Q. Leng and L. F. Li, *J. Mater. Chem. A*, 2015, **3**, 4555.
- 84 A. You, M. A. Y. Be and I. In, *J. Appl. Phys.*, 2017, **61**, 206.
- 85 H. Ju, D. Park and J. Kim, *Nanoscale*, 2019, **11**, 16114.
- 86 L. Zhang and J. L. Wang, *J. Mater. Chem. A*, 2016, **4**, 7936.
- 87 H. Wu, C. Chang, D. Feng, Y. Xiao, X. Zhang, Y. Pei, L. Zheng, D. Wu, S. Gong, Y. Chen, J. He, M. G. Kanatzidis and L. D. Zhao, *Energy Environ. Sci.*, 2015, **8**, 3298.
- 88 G. Tan, F. Shi, J. W. Doak, H. Sun, L. D. Zhao, P. Wang, C. Uher, C. Wolverton, V. P. Dravid and M. G. Kanatzidis, *Energy Environ. Sci.*, 2015, **8**, 267.
- 89 L. D. Zhao, V. P. Dravid and M. G. Kanatzidis, *Energy Environ. Sci.*, 2014, **7**, 251.
- 90 Z. H. Ge, D. Song, X. Chong, F. Zheng, L. Jin, X. Qian, L. Zheng, R. E. Dunin-Borkowski, P. Qin, J. Feng and L. D. Zhao, *J. Am. Chem. Soc.*, 2017, **139**, 9714.
- 91 T. Zhu, Y. Liu, C. Fu, J. P. Heremans, J. G. Snyder and X. Zhao, *Adv. Mater.*, 2017, **29**, 1605884.
- 92 F. Guo, B. Cui, Y. Liu, X. Meng, J. Cao, Y. Zhang and R. He, *Small*, 2018, **14**, 1802615.
- 93 X. Hu, G. Song, W. Li, Y. Peng, L. Jiang, Y. Xue, Q. Liu, Z. Chen and J. Hu, *Mater. Res. Bull.*, 2013, **48**, 2325.
- 94 G. Tang, J. Liu, J. Zhang, D. Li, K. H. Rara, R. Xu, W. Lu, J. Liu, Y. Zhang and Z. Feng, *ACS Appl. Mater. Interfaces*, 2018, **10**, 30558.
- 95 C. H. de Groot, C. Gurnani, A. L. Hector, R. Huang, M. Jura, W. Levason and G. Reid, *Chem. Mater.*, 2012, **24**, 4442.
- 96 S. L. Benjamin, C. H. de Groot, C. Gurnani, A. L. Hector, R. Huang, K. Ignatyev, W. Levason, S. J. Pearce, F. Thomas and G. Reid, *Chem. Mater.*, 2013, **25**, 4719.
- 97 E. G. Hope, T. Kemmlitt and W. Levason, *Organometallics*, 1987, **6**, 206.
- 98 V. R. Minnam Reddy, S. Gedi, C. Park, M. R.w and R. R. Ramakrishna, *Curr. Appl. Phys.*, 2015, **15**, 588.
- 99 S. Gedi, V. R. M. Reddy, J. yoon Kang and C. W. Jeon, *Appl. Surf. Sci.*, 2017, **402**, 463.
- 100 C. An, K. Tang, B. Hai, G. Shen, C. Wang and Y. Qian, *Inorg. Chem. Commun.*, 2003, **6**, 181.
- 101 B. Zhou, S. Li, W. Li, J. Li, X. Zhang, S. Lin, Z. Chen and Y. Pei, *ACS Appl. Mater. Interfaces*, 2017, **9**, 34033.
- 102 Q. Tan, L. D. Zhao, J. F. Li, C. F. Wu, T. R. Wei, Z. B. Xing and M. G. Kanatzidis, *J. Mater. Chem. A*, 2014, **2**, 17302.
- 103 R. Guo, X. Wang, Y. Kuang and B. Huang, *Phys. Rev. B*, 2015, **92**, 115202.
- 104 Y. Li, M. Wu, D. K. Song, T. Ding, F. Liu, J. Li, H. Zhang and H. Xie, *ACS Appl. Energy Mater.*,

2020, **3**, 6946.

- 105 L. D. Zhao, G. Tan, S. Hao, J. He, Y. Pei, H. Chi, H. Wang, S. Gong, H. Xu, V. P. Dravid, C. Uher, G. J. Snyder, C. Wolverton and M. G. Kanatzidis, *Science*, 2016, **351**, 141.
- 106 L. D. Zhao, C. Chang, G. Tan and M. G. Kanatzidis, *Energy Environ. Sci.*, 2016, **9**, 3044.
- 107 Z. Wang, D. Wang, Y. Qiu, J. He and L. D. Zhao, *J. Alloys Compd.*, 2019, **789**, 485.
- 108 Q. Zhao, B. Qin, D. Wang, Y. Qiu and L. D. Zhao, *ACS Appl. Energy Mater.*, 2020, **3**, 2049.
- 109 J. O. M. Ferreira, D. E. Diaz-droguett, D. Celentano, J. S. Reparaz, C. M. S. Torres, S. Ganguli and T. Luo, *Appl. Therm. Eng.*, 2017, **111**, 1426.
- 110 L.-D. Zhao, G. Tan, S. Hao, J. He, Y. Pei, H. Chi, H. Wang, S. Gong, H. Xu and V. P. Dravid, *Science*, 2016, **351**, 141.
- 111 Y. K. Lee, K. Ahn, J. Cha, C. Zhou, H. S. Kim, G. Choi, S. I. Chae, J. H. Park, S. P. Cho, S. H. Park, Y. E. Sung, W. B. Lee, T. Hyeon and I. Chung, *J. Am. Chem. Soc.*, 2017, **139**, 10887.
- 112 F. Robinson, D. W. Newbrook, P. Curran, C. H. (Kees) de Groot, D. Hardie, A. L. Hector, R. Huang and G. Reid, *Dalton Trans.*, 2021, **50**, 998.
- 113 Q. Jiang, H. Hu, J. Yang, J. Xin, S. Li, G. Viola and H. Yan, *ACS Appl. Mater. Interfaces*, 2020, **12**, 23102.
- 114 Z. Ma, C. Wang, J. Lei, D. Zhang, Y. Chen, J. Wang, Z. Cheng and Y. Wang, *ACS Appl. Energy Mater.*, 2019, **2**, 7354.
- 115 A. Doi, S. Shimano, D. Inoue, T. Kikitsu, T. Hirai, D. Hashizume, Y. Tokura and Y. Taguchi, *APL Mater.*, 2019, **7**, 091107.
- 116 L. Zhao, J. J. Wang, J. Li, J. Liu, C. Wang, J. J. Wang and X. Wang, *Phys. Chem. Chem. Phys.*, 2019, **21**, 17978.
- 117 R. Huang, S. L. Benjamin, C. Gurnani, Y. Wang, A. L. Hector, W. Levason, G. Reid and C. H. de Groot, *Sci. Rep.*, 2016, **6**, 27593.
- 118 H. Park, S. Go, C. Lee, H. Nam, J. K. Lee and J. Lee, *Jpn. J. Appl. Phys.*, 2013, **52**, 10MCB08.

Chapter 4 CVD of Germanium (II) Chalcogenide Thin Films and Thermoelectric Properties of GeTe

4.1 Precursors used



4.2 Introduction

The series of germanium monochalcogenides, GeE (E= S, Se or Te), are a promising group of semiconducting materials with exciting thermoelectric properties. Showing many similarities to their wider semiconductor family, the group 14 metal chalcogenides, the germanium monochalcogenides have many structural properties that have sparked interest for thermoelectric applications. They mainly adopt layered orthorhombic structures, while the only rhombohedral member is germanium telluride (GeTe).¹ Although the low natural abundance of germanium (ca. 1 ppm in the earth's crust)² may seem to make the series less favourable for commercial applications, the potential for reduced material demands when coupled with nanostructuring and alloying help to make germanium monochalcogenide based materials of great interest for electrical applications.^{3,4}

The exploration of the germanium monochalcogenides for thermoelectric applications is a relatively recent development. Interest in them stems from the structural similarities of germanium telluride at high temperature with lead telluride, a well-known thermoelectric material.⁵⁻⁷ At high temperature germanium, tin and lead telluride all adopt a cubic structure and have a similar band structure. In particular, GeTe has been discussed as a promising material for a number of applications because of its high electrical conductivity, reversible amorphous–crystalline phase transition behaviour and its applications for phase change random access memory (PRAM).⁸⁻¹⁰ The high electrical conductivity of GeTe is attributed to its high charge carrier concentration, caused by inherent germanium vacancies.¹¹ This also contributes to the relatively low Seebeck coefficient of $\sim +135 \mu\text{V K}^{-1}$ at 720 K.^{12,13} The performance capabilities of pristine GeTe are, therefore, limited by its poor Seebeck coefficient and its high thermal conductivity. Both of these factors have strong correlations with the charge carrier concentration, as discussed in Chapter 1. Thus, the thermoelectric properties of GeTe can be greatly enhanced by the rational selection of dopants. The lighter members of the series, germanium sulfide (GeS) and selenide (GeSe), both adopt a layered orthorhombic structure at atmospheric temperature and pressure, similar to that of tin sulfide and selenide.¹⁴ Conversely to GeTe, GeS and GeSe have very low charge carrier concentrations which result in high Seebeck coefficients, but very poor electrical conduction.^{1,15,16} Thus, all of the series require optimisation to operate well for thermoelectric applications.

Along with the interest in the thermoelectric potential for the GeE series are a number of other technological applications, including photovoltaic devices, lithium ion batteries and phase change non-volatile memory (PCRAM).¹⁷⁻²³

4.2.1 Crystal structures

The structures shown in Figure 4-1 highlight the similarities between the layered orthorhombic structures of germanium sulfide, germanium selenide and phosphorene, a monolayer of black phosphorus. Phosphorene is a well-known semiconducting material which, due to its structural similarities and dissimilar conduction properties to those of graphene, has gained much interest.²⁴ The benefit of using the isostructural tin and germanium monochalcogenides is the ease with which their properties, such as energy gap and electrical conductivity, can be tuned by selection of the elements involved. This tunability gives an advantage of the group 14 metal chalcogenide layered orthorhombic materials over similarly structured graphene and phosphorene. Another disadvantage of xenes (graphene, silicene, phosphorene, etc.) is their comparably lower stabilities in air to that of ME van der Waals layered materials.²⁵

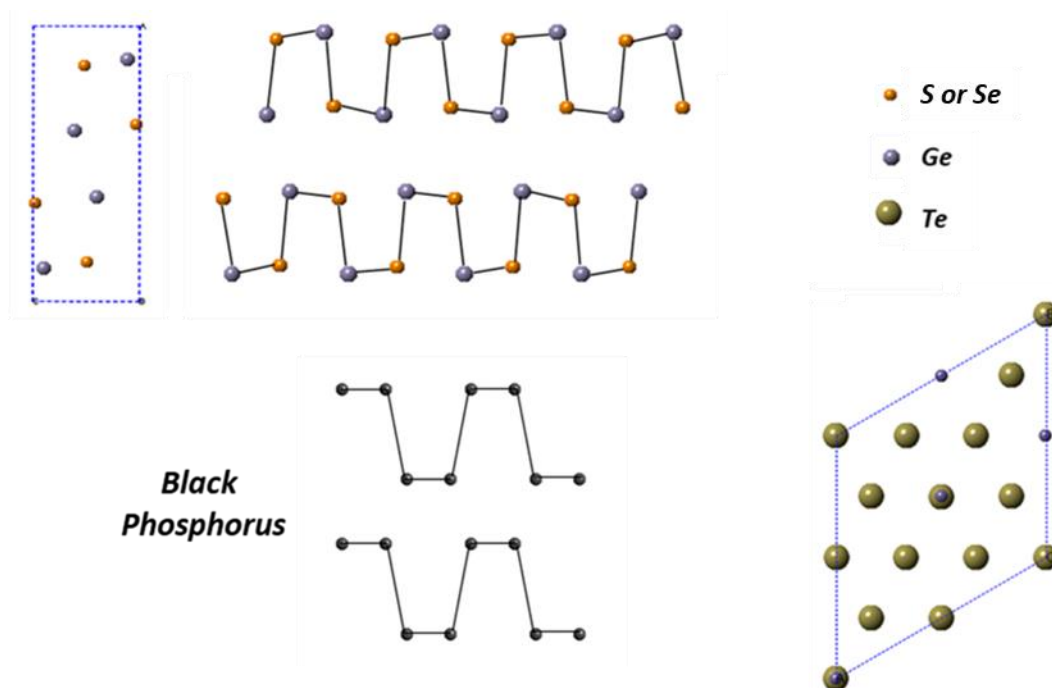


Figure 4-1: The view looking down the axis of GeS,²⁶ GeSe²⁷ and black phosphorus²⁸ to highlight the similarities in their structure and the structure of rhombohedral GeTe.²⁹

As discussed in Chapter 3, the transition in structure when moving from GeS and GeSe to GeTe is caused by the relative stability of the lone s^2 pair on the germanium when compared to the energy of the bonding orbitals. In the case of GeS and GeSe, the s^2 electron pair is sufficiently stabilised in energy for the lower symmetry orthorhombic structure to be adopted. However, in GeTe the larger size of the tellurium atoms surrounding the germanium centre quench the s^2 orbital so that it is less energetically stabilised, but not sufficiently to result in a cubic structure to be adopted.³⁰ Thus, the intermediate rhombohedral structure is adopted exclusively by GeTe in the group 14 metal chalcogenides.^{1,5}

4.2.2 Germanium chalcogenide deposition techniques and single source precursors

There are far fewer examples of the deposition of GeE films in the literature compared to SnE films. Deposition of GeE has been performed using: electrodeposition, thermal decomposition, sputtering, evaporation deposition, thermal decomposition, molecular beam epitaxy, vapour transport deposition, CVD, PECVD and LPCVD.^{17,31,40–42,32–39} The deposition methods mentioned tend to be performed using either dual precursors or via the evaporation of bulk germanium telluride or elemental germanium and tellurium sources. In these cases, there is a low degree of control over the balancing of the stoichiometry.

The examples shown in Figure 4.2 show some of the single source precursors reported for the deposition of germanium monochalcogenides, by thermal decomposition, LPCVD or MOCVD. The benefits of using a single source precursor include fine control over the stoichiometry, as this is designed into the precursor, as discussed further in Chapter 2. The precursors displayed in Figure 4.2 are unsuitable for a large number of deposition techniques due to their high molecular weights and low volatilities, as well as poorly defined thermal decomposition pathways, or, in the case of $[\text{Ge}(\text{Te}^n\text{Bu})_4]$ the unbalanced stoichiometry, which led to some contamination by excess tellurium.³¹

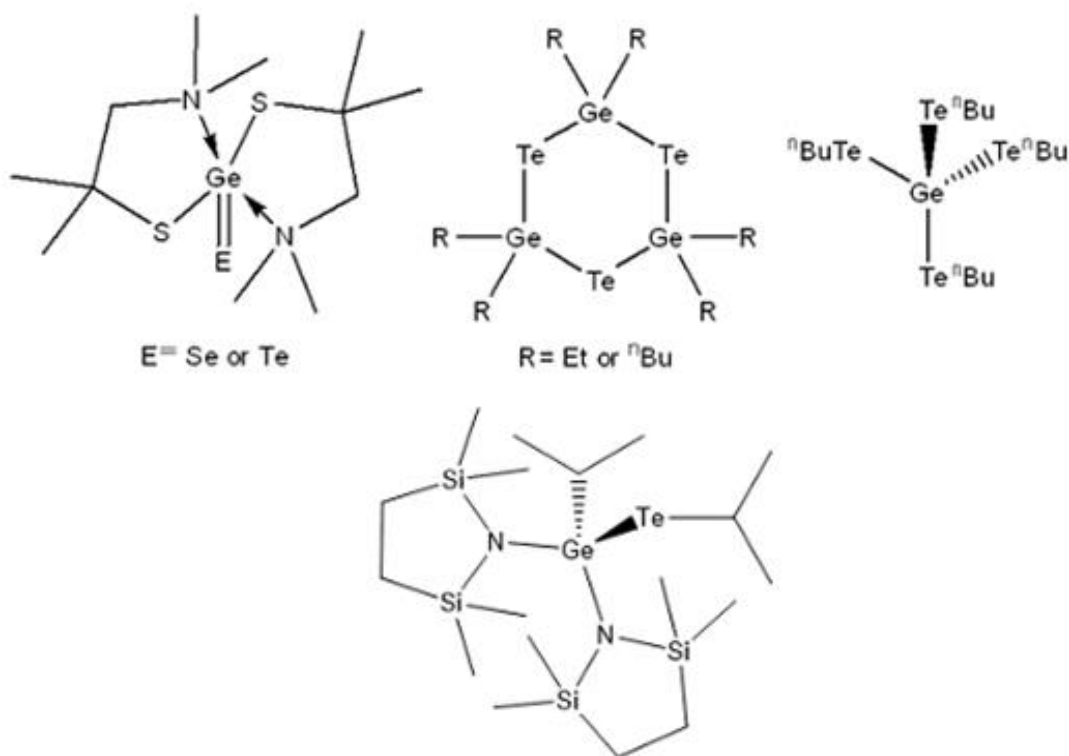


Figure 4-2: Examples of single source precursors reported for the deposition of germanium selenide and germanium telluride thin films.^{17,22,31,32}

4.2.3 Temperature regime and applications

As can be seen in Figure 4.3, the germanium monochalcogenide-based materials have often large, maximum ZT values in the mid-temperature regime window, between 450 and 850 K. This means that the optimum operation temperature is within this range. Many of the applications for thermoelectrics suited to the mid-temperature range have been discussed in section 1.2.1.1. When considering the germanium monochalcogenide materials for bulk thermoelectric applications there are some concerns. The vast majority of high-performance materials based on

germanium monochalcogenides contain both germanium and tellurium as their main constituents. These elements are of low natural abundance in the earth's crust and expensive and hence the inclusion of other dopant materials and elements can improve both the performance and sustainability simultaneously. Another way in which the application of germanium chalcogenides can be made more sustainable is using nanostructured materials such as nanodots, nanowires and thin films, all of which use much less material than their bulk counterparts.

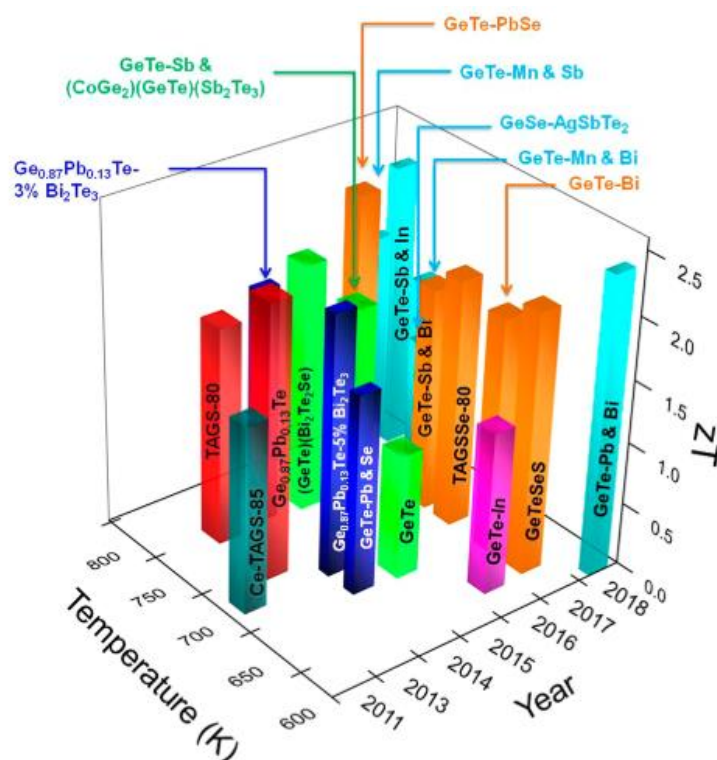


Figure 4-3: Collation of germanium monochalcogenide based thermoelectric materials with promising ZT values, plotted against both temperature at which ZT is maximised and the year or their publication.¹ This highlights the mid temperature regime and the recent surge of interest in germanium chalcogenide-based thermoelectric materials. Reproduced with permission from ACS publications.

4.2.4 Property comparison

Presented in Table 4.1 are some interrelated properties of the germanium monochalcogenide series. Comparing the lattice parameters and the thermal conductivities at 300 K reveals a similar trend to that observed for the tin chalcogenides in Chapter 3. In the case of the tin analogues, the comparison of lattice parameters with the Grüneisen parameters and the thermal conductivities showed that the selenide displays the lowest thermal conductivity, followed by the sulfide and then the material with the highest thermal conductivities, the telluride. This trend can also be

observed in the germanium series here, where similar structural trends are also observed. The difference in the sulfide and selenide structures is primarily due to the structure and bonding differences, and therefore Grüneisen parameters, as well as a contribution from the difference in the electrical conductivities between the two materials. In the case of germanium telluride, the higher thermal conductivity can be rationalised by its contributions from the lattice part, due to the higher symmetry, and thus smaller Grüneisen parameter, and to the large increase in electrical conductivity, and thus electrical contribution to the thermal conductivity. The electrical conductivity increase is connected to the high intrinsic charge carrier concentration caused by germanium vacancies. The impact of a higher charge carrier concentration on the thermal conductivity is to increase it, as the total thermal conductivity is made up by electrical and lattice contributions, as discussed in Chapter 1.⁴³ It is the combination of these factors that lead to the relatively large thermal conductivity of GeTe when compared to GeS and GeSe. A discussion of the relationship between the band gap and the Seebeck coefficient can be found in section **1.2.3.2**.

The same trend of larger energy gap relating to a larger Seebeck coefficient can be seen here too. The largest power factor, despite having the lowest Seebeck coefficient, belongs to germanium telluride. This is due to the far higher electrical conductivity when compared to that of the selenide and sulfide. Therefore, the best way to improve the power factor of the already highly performing germanium telluride is through enhancement of the Seebeck coefficient. Conversely, the best way to improve the performance of GeS and GeSe is through electrical conductivity improvements, something that has been touched upon in the literature.^{15,44}

Table 4-1: Lattice parameters, band gaps, thermal and electronic conductivities and maximum Seebeck coefficients for the germanium monochalcogenides at ambient temperature and pressure.

Material	Lattice parameters (ambient T and P) (Å)	Band gap (eV)	Thermal conductivity at 300 K ($\text{Wm}^{-1}\text{K}^{-1}$)	Electrical conductivity at 300 K (Scm^{-1})	Maximum Seebeck coefficient (μVK^{-1})
GeS	10.470(2), 3.641(1), 4.297(1) ²⁶	1.65 ^{45,46}	0.52 ¹⁶	($\sim 1 \times 10^{-7}$) ⁴⁷	769 ¹⁶
GeSe	10.9208(4), 3.8708(3), 4.4075(4) ⁴⁸	1.08 ⁴⁶	0.39 ^{15,16}	($\sim 4.7 \times 10^{-6}$) ⁴⁹	706 ¹⁶
GeTe	4.2810(5) ^{50,51}	0.55 ⁵²	8.24 ⁵³	~ 8000 ¹	167 ⁵⁴

4.2.5 Electrical band structure and engineering

As discussed in section 1.2.2 and 1.2.3, one method of affecting the Seebeck coefficient is through the careful engineering of the electronic band structure. In order to do this effectively, an understanding of the electronic band structure must be gathered through computation, supported by experimental data. A quick glance at the band structure for germanium telluride, displayed in Figure 4-4d, shows that there are multiple band maxima and minima that are close in terms of their energy. The coalescence of these increases the band degeneracy which greatly increases the Seebeck coefficient, as discussed in section 1.2.2.3.

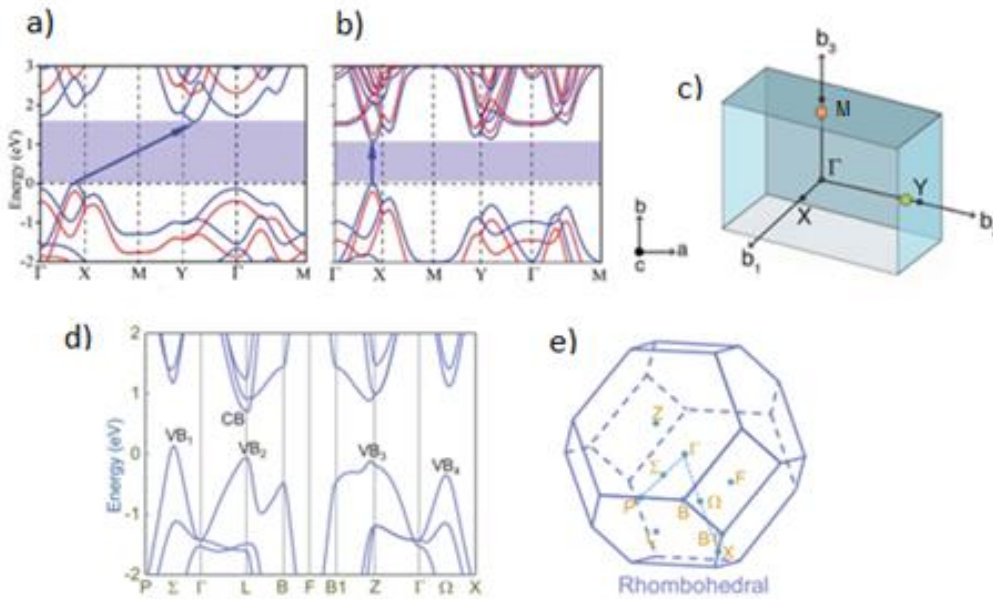


Figure 4-4: a) Electronic band structure of GeS, b) electronic band structure GeSe, c) the first Brillouin zone of orthorhombic structure adopted by GeS and GeSe and d) the electronic band structure of GeTe and e) the first Brillouin zone of rhombohedral GeTe.^{55–57} Reproduced with permissions from the Royal Society of Chemistry and John Wiley and Sons.

The electronic band structures shown in Figure 4-4 give an insight into some of the properties of the materials they represent, as well as an insight into the best mechanism for optimisation. The size of the band effective mass can be inferred from the broadness or narrowness of a peak. This means that the material’s charge carrier mobility can be compared based on the width or sharpness of the peaks in the valance and conduction bands.³⁰ The degeneracy is also obtained by observing the number or peaks at the same energy when comparing the band maxima and minima in the valance and conduction bands, respectively. Using these methods for comparing the properties of the electronic band structure by inspection, a comparison of and approach to the best method of optimisation, can be gained. In Figure 4-4 it follows that as germanium sulfide has broader bands, it has a smaller band effective mass than that of germanium selenide, and thus has a higher mobility.

As previously mentioned, one obvious way of improving the thermoelectric performance of germanium telluride is through band coalescence. This method has been cited by Wu *et al.* as the mechanism for enhancement in the 3% Bi₂Te₃ doped Ge_{0.87}Pb_{0.13}Te, which sees a huge increase in Seebeck coefficient to 273 μVK⁻¹ resulting in a ZT of 1.9 at 773 K.⁵⁴ In this specific case the addition of 3% Bi₂Te₃ increases the solubility of lead into germanium telluride, which in turn causes the

structural transition from rhombohedral to cubic. It is this structural transition that enables the valance band convergence, enhancing the thermoelectric properties.^{30,54} As described in Figure 4-5, another method for the coalescence of the valance bands is based around the alloying of germanium telluride with manganese telluride or Sb.¹

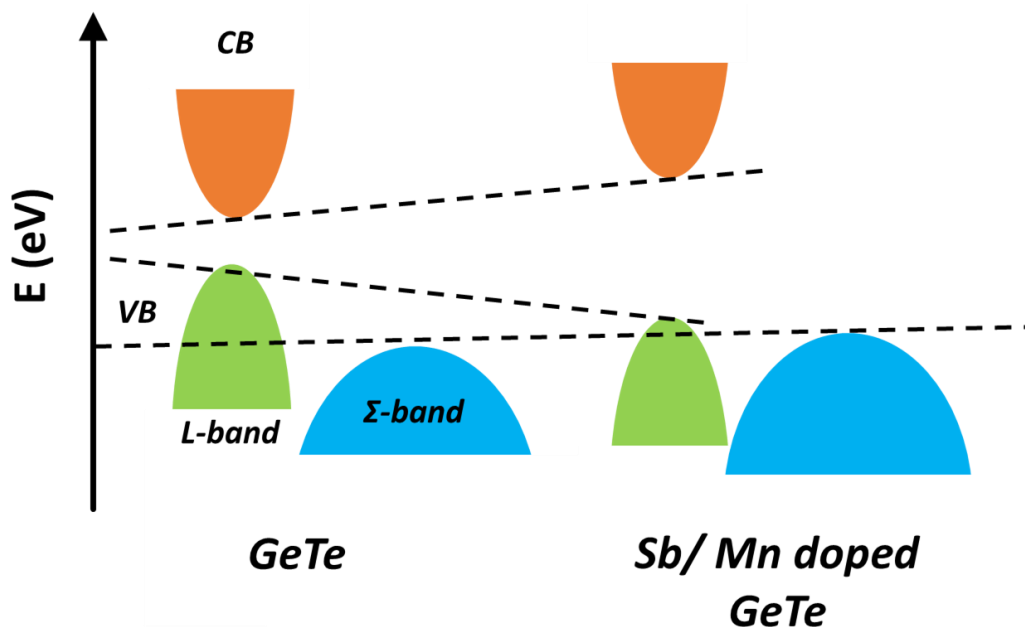


Figure 4-5: The increase in band gap and band coalescence observed when alloying GeTe with MnTe or doping with antimony.¹

The methods described in Figure 4-5 have been used in: $\text{Ge}_{0.9}\text{Sb}_{0.1}\text{Te}$, $\text{Ge}_{26}\text{MnTe}_{27}$, $\text{Ge}_{25}\text{Mn}_2\text{Te}_{16}$, $\text{Ge}_{13}\text{BiSb}_2\text{Te}_{16}$, $\text{Ge}_{0.84}\text{Mn}_{0.10}\text{Sb}_{0.06}\text{Te}$ and $\text{Ge}_{0.81}\text{Mn}_{0.15}\text{Bi}_{0.04}\text{Te}$.^{53,58-61} In each case the thermoelectric properties are shown to be enhanced through the stabilisation of the L band or light pocket and destabilisation of the heavy Σ band, causing an increase in the Seebeck coefficient due to the higher band degeneracy. This, along with the manipulation of the charge carrier concentration through doping, yield ZT values as high as 1.85.⁶⁰ Another factor that the stabilisation of a high temperature phase aids in, for materials with a phase transition inside their optimal working temperature window, is a reduction in the potential for mechanical stress facilitated faults. That is to say a material that undergoes phase transitions within a device is more likely to cause a malfunction or disconnection than one that remains a single phase for the duration of its operation, hence the suppression of this is desirable for thermoelectric applications.⁵⁹

One of the factors that detracts from the thermoelectric performance of GeTe is its inherently high charge carrier concentration due to germanium vacancies. As a result of this, the mobility and Seebeck coefficient are low and thus optimisation of these parameters through charge carrier concentration manipulation is key to improving GeTe. The inclusion of a dopant can be used to affect the charge carrier concentration and the Seebeck coefficient, whilst also reducing the

lattice thermal conductivity through point defects. This has been performed for the optimisation of GeTe, notably in: $\text{Ge}_{0.9}\text{Sb}_{0.1}\text{Te}$, $\text{Ge}_{0.935}\text{Bi}_{0.065}\text{Te}$, $\text{Ge}_{0.98}\text{In}_{0.02}\text{Te}$ and $\text{Ge}_{0.73}\text{Pb}_{0.27}\text{Te}$.^{53,62–64} The inclusion of the additional elements in these examples to produce germanium telluride based solid solutions enhances the ZT value from 0.9 for pristine GeTe to 1.9, 1.8, 1.3 and 2.3, respectively.⁵⁶

Huge advances in the performance of GeS and GeSe based materials have also been achieved using similar techniques. One example of this was from the study of the mixed germanium chalcogenide solid solution system, $(\text{GeTe})_{1-2x}(\text{GeSe})_x(\text{GeS})_x$, which greatly exceeds the performance of any of the individual pristine materials, whilst increasing the sustainability of the overall material by replacing some of the low abundance tellurium with higher abundance selenium and sulfur.⁶⁵ One example of a more earth abundant element subsidising the quantity of tellurium within a material based on germanium telluride is in $\text{Ge}_{0.9}\text{Sb}_{0.1}\text{Te}_{0.88}\text{Se}_{0.12}$. In this case, the addition of selenium leads to a large reduction in thermal conductivity, increasing the ZT value to 2.0, whilst also reducing the cost and increasing the sustainability of the material.⁵⁸

Another method that has been shown to increase the band gap and Seebeck coefficient is the reduction of one or more dimensions. This method, known as nanostructuring, is a promising optimisation mechanism for germanium chalcogenide based thermoelectric materials.⁶⁶ This has been explored computationally for GeSe where large improvements in the Seebeck coefficient, and therefore power factor and ZT, are predicted.⁶⁷ The typical aim of nanostructuring is to improve performance through the reduction of lattice thermal conductivity without reducing the electrical conductivity. Nanostructuring is a particularly enticing approach for the optimisation of germanium telluride as it has good electrical conductivity and power factor, but the ZT value is limited by the thermal conductivity. As discussed in Chapter 1, the electrical conductivity is proportional to the electrical contribution to the thermal conductivity, as described by the Wiedemann–Franz law ($\kappa_e = L\sigma T$), and so decoupling the electrical and lattice parts of the thermal conductivity allows a lot of scope for optimisation. One method of nanostructuring is through the incorporation of nanoprecipitates within the material. This requires a dopant or alloyed material to exceed some upper limit for solubility into the host system, at which point this material forms areas of their higher concentration, known as nanoprecipitates. This approach has been utilised in a number of systems based on germanium telluride containing different dopants, above their solubility limit. Good examples of this are: $(\text{Co-Ge}_2)_{0.22}(\text{GeTe})_{19}\text{Sb}_2\text{Te}_3$, $\text{Ge}_{0.87}\text{Pb}_{0.13}\text{Te}$ and $(\text{GeTe})_{80}(\text{AgSbSe}_2)_{20}$.^{66,68,69} Since the majority of the lattice thermal conductivity in lead, tin and germanium telluride is dominated by phonons with a mean free path range of 1-100 nm, nanostructuring along with point defects, is a useful technique for optimisation.^{1,70,71} The concept of reducing a material's dimensions in order to improve the performance is particularly attractive

for the layered orthorhombic members of the germanium monochalcogenide series. The weaker Van der Waals bonding, which holds the bulk material together, allow for the separation, for example, through processes such as mechanical exfoliation.⁷² How this would impact the electrical properties of germanium sulfide and selenide has been studied computationally and suggests large enhancements in thermoelectric performances.^{73,74}

All scale phonon scattering techniques should be incorporated in order to minimise the thermal conductivity, whilst also considering methods for maximising Seebeck and electrical conductivity. Some examples of different scattering events can be seen in Sections **1.3.2** and **3.2.4.5**. Although only atomic and nano-scale examples have been discussed here, examples of submicron and mesoscale phonon scattering being exploited to enhance performance can be found in the substructure of $\text{Ge}_{0.90}\text{Sb}_{0.10}\text{Te}$ and in mesostructure engineered $\text{Ge}_{0.90}\text{Bi}_{0.10}\text{Te}$.^{53,75}

This chapter presents the establishment of single source precursors for the LPCVD of GeS, GeSe and GeTe. The resultant thin films demonstrate high purity by GIXRD, SEM with EDX and Raman. In view of its importance as a thermoelectric importance, the properties of germanium telluride films were measured using van der Pauw and Seebeck coefficient measurements as discussed in section **1.8.3**.

4.3 Experimental

4.3.1 Precursor Preparation and Characterisation

The precursors used in this work consist of $[\text{Ge}^n\text{Bu}_3(\text{S}^n\text{Bu})]$, $[\text{Ge}^n\text{Bu}_2(\text{S}^n\text{Bu})_2]$, $[\text{Ge}^n\text{Bu}_3(\text{Se}^n\text{Bu})]$, $[\text{Ge}^n\text{Bu}_3(\text{Te}^n\text{Bu})]$ and $[\text{Ge}^n\text{Bu}_2(\text{Te}^n\text{Bu})_2]$. All were prepared and characterised as discussed in Chapter 2.

4.3.2 LPCVD onto fused quartz substrates

The fused quartz substrates were first washed with deionized water then ethanol before being dried thoroughly in an oven before use. In a typical LPCVD experiment, the precursor (5-50mg) and fused quartz substrates were loaded into a closed ended silica tube inside the glovebox. The precursor was loaded into the precursor bulb at the end of the sealed silica tube and the substrates were positioned end to end (0-4 cm away from the precursor bulb) down the silica tube. The tube was positioned horizontally in the furnace and held in place such that the precursor containing bulb was protruding from the end of the furnace. The tube was evacuated to 0.01- 0.4 mmHg. The furnace was heated to the necessary temperature for the experiment, as determined by TGA experiments and experimental observations, and allowed to stabilise. The

tube was positioned so that the precursor was close enough to the furnace for volatilisation to be observed. The position was then maintained until all of the precursor had volatilised. This typically took 5-10 minutes. Once the deposition was complete, the tube was removed from the furnace area and allowed to cool naturally to room temperature before being transferred to the glovebox, where the substrates were removed and stored until they could be characterised.

The LPCVD experiments produced silver white films of GeTe, grey films of GeSe and on one occasion the edge of a tile contained grey/black GeS. The GeTe and GeSe depositions were continuous and had coverages of around 1 cm².

4.3.3 Thermoelectric and electrical property measurements

The GeS and GeSe films were determined to be of too high resistivity to be easily measured using the equipment available. This does not mean that they are not of interest for thermoelectric applications especially with regards to the exploration of them as components in solid solutions. As a result of the poorer electrical conductivity of GeS and GeSe thin films, the highly electrically conductive GeTe films were the focus of the thermoelectric and electrical property investigations described here.

4.4 Results and Discussion

4.4.1 Evaluation of SSPs for LPCVD procedure

The complexes were obtained in good yield and were characterised as discussed in Chapter 2. As well as using thermogravimetric analysis (TGA) to establish the clean volatilisation of the precursors, it is also used to guide the temperature range for the low pressure CVD experiments (Figure 4-6). The TGA data indicate that the temperature associated with the onset of evaporation being lowest for **[GeⁿBu₃(SeⁿBu)]** and **[GeⁿBu₃(SⁿBu)]**, *ca.* 200 °C, then **[GeⁿBu₃(TeⁿBu)]**, *ca.* 250 °C, before **[GeⁿBu₂(TeⁿBu)₂]** and **[GeⁿBu₂(SⁿBu)₂]** at *ca.* 260 °C. From these experiments furnace temperatures were selected that would allow for the precursor bulb to reach the temperature needed for volatilisation. The TGA experiments are, however, performed at atmospheric pressures, whereas the LPCVD experiments are at reduced pressure and so adjustments based on experimental observations are necessary. However, the TGA data do provide a good basis on which a SSP can be considered suited towards LPCVD.

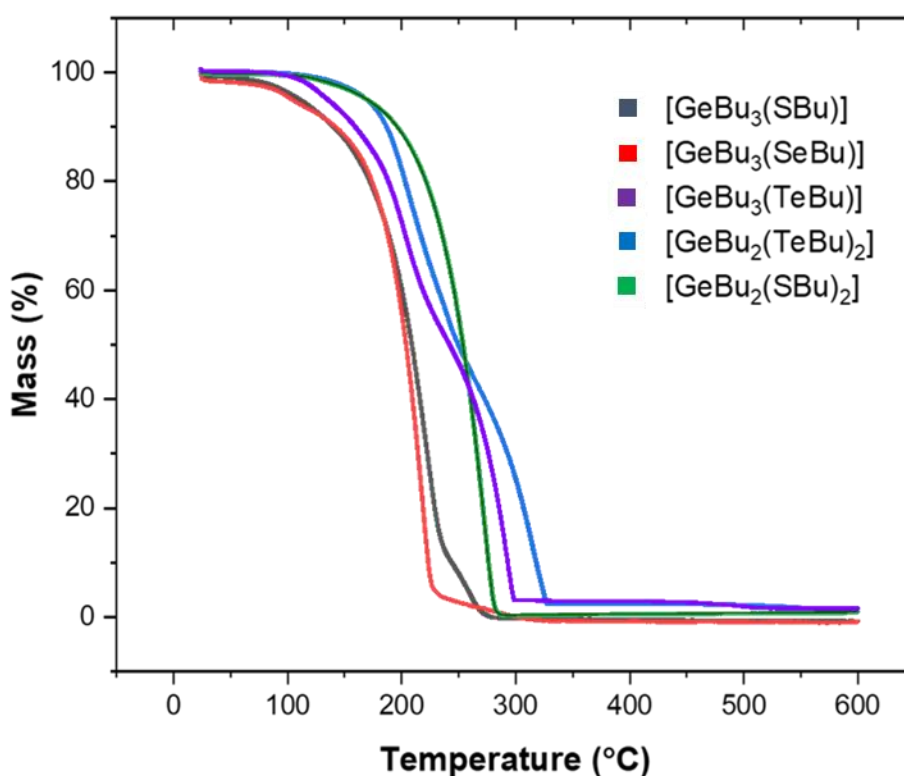


Figure 4-6: The percentage of mass lost during heating from 30- 600 °C at a fixed heating rate for $[\text{Ge}^n\text{Bu}_3(\text{S}^n\text{Bu})]$, $[\text{Ge}^n\text{Bu}_3(\text{Se}^n\text{Bu})]$, $[\text{Ge}^n\text{Bu}_3(\text{Te}^n\text{Bu})]$, $[\text{Ge}^n\text{Bu}_2(\text{Te}^n\text{Bu})_2]$ and $[\text{Ge}^n\text{Bu}_2(\text{S}^n\text{Bu})_2]$, all showing complete volatilisation.

4.4.2 Low Pressure Chemical Vapour Deposition Experiments

The temperatures selected for the depositions were determined through inspection of the vaporisation temperatures given by the TGA results, chemical intuition based on the comparative bond strengths and experimental observations. Thus, it follows that the furnace temperatures selected were: 700 °C, 600 °C, and 550-650 °C for GeS, GeSe and GeTe, respectively. The precursor that deposits at the highest temperature is $[\text{Ge}^n\text{Bu}_3(\text{S}^n\text{Bu})]$ due to its comparatively stronger germanium to chalcogen bond, when compared to $[\text{Ge}^n\text{Bu}_3(\text{Se}^n\text{Bu})]$ and $[\text{Ge}^n\text{Bu}_3(\text{Te}^n\text{Bu})]$.⁷⁶ The deposition of germanium sulfide was successful on only one occasion and was confined to an area of only a 3 mm at the end on a substrate tile, so further repeats are still necessary. Unfortunately, no successful depositions using $[\text{Ge}^n\text{Bu}_2(\text{S}^n\text{Bu})_2]$ can be reported thus far, despite numerous attempts at furnace temperatures between 550-750 °C. Germanium selenide was produced reproducibly and had a larger continuous area of deposition of about 1 cm by 0.8 cm. The sample of GeS produced was deposited at 261 °C and the samples of GeSe were deposited between 168-356 °C.

As germanium telluride is the most interesting material for thermoelectric applications, and GeS and GeSe are too resistive to easily be measured, this was the material for which thermoelectric property measurements were focussed. For this reason, multiple samples of germanium telluride were prepared using different precursor batches of both $[\text{Ge}^n\text{Bu}_3(\text{Te}^n\text{Bu})]$ and $[\text{Ge}^n\text{Bu}_2(\text{Te}^n\text{Bu})_2]$. The deposition of germanium telluride produced continuous films with coverages up to 2 cm by 0.8 cm with deposition temperatures between 336 and 554 °C.

4.4.3 Germanium sulfide sample

The success of SnS depositions prompted the use of an analogous GeS precursor, $[\text{Ge}^n\text{Bu}_2(\text{S}^n\text{Bu})_2]$. Thus far, this approach has only produced a small area of GeS film. The material produced was shown to be slightly sulfur-deficient by EDX analysis, at 45%S: 55%Ge. This sulfur-deficiency is analogous to the SnS depositions discussed in the previous chapter. The situation was improved by using $[\text{Sn}^n\text{Bu}_2(\text{S}^n\text{Bu})_2]$ in that case, as described in section 3.4.2. A similar tactic was explored here using $[\text{Ge}^n\text{Bu}_2(\text{S}^n\text{Bu})_2]$. Unfortunately, this could not be explored fully due to the time constraints caused by building closures throughout lockdown due to COVID 19.



Figure 4-7: Image of the small amount of deposited GeS (grey material at left hand side of tile).

The grazing incidence XRD pattern displayed in Figure 4-8 (black) matches well with the literature bulk pattern (red) for GeS.²⁶ The refined lattice parameters for this pattern are: $a = 10.4661(5) \text{ \AA}$, $b = 4.2792(2) \text{ \AA}$ and $3.63594(18) \text{ \AA}$ for this orthorhombic crystal system. This is in good agreement with the literature data: $a = 10.470(2) \text{ \AA}$, $b = 4.297(1) \text{ \AA}$, $c = 3.641(1) \text{ \AA}$.²⁶

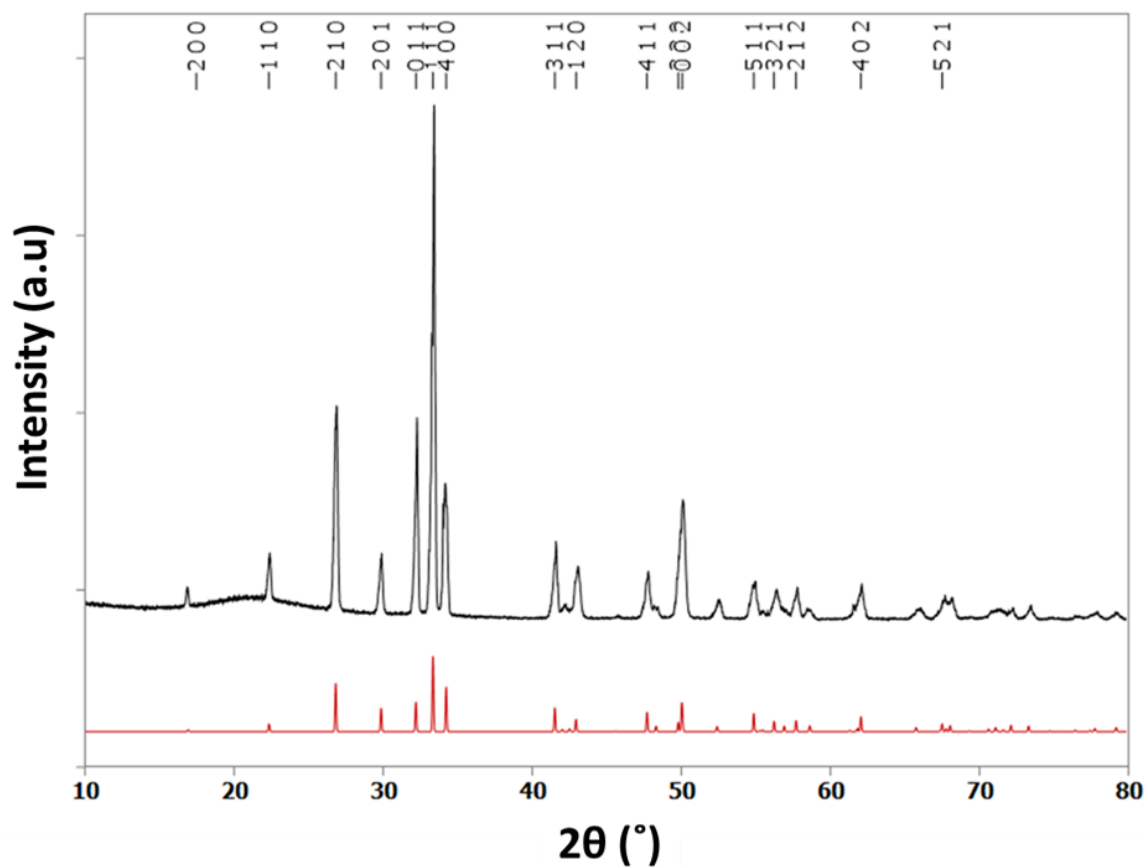


Figure 4-8: Grazing incidence XRD pattern measured for the deposited germanium sulfide (black) and the matched literature pattern (red).²⁶

The SEM image displayed in Figure 4-9 shows a polycrystalline film of GeS. Other attempts to produce films with better coverages produced discontinuous films of germanium, as determined by EDX and grazing incident XRD. It is likely that using the more sulfur rich SSP, $[\text{Ge}^n\text{Bu}_2(\text{S}^n\text{Bu})_2]$, and short deposition times would produce better films of GeS.

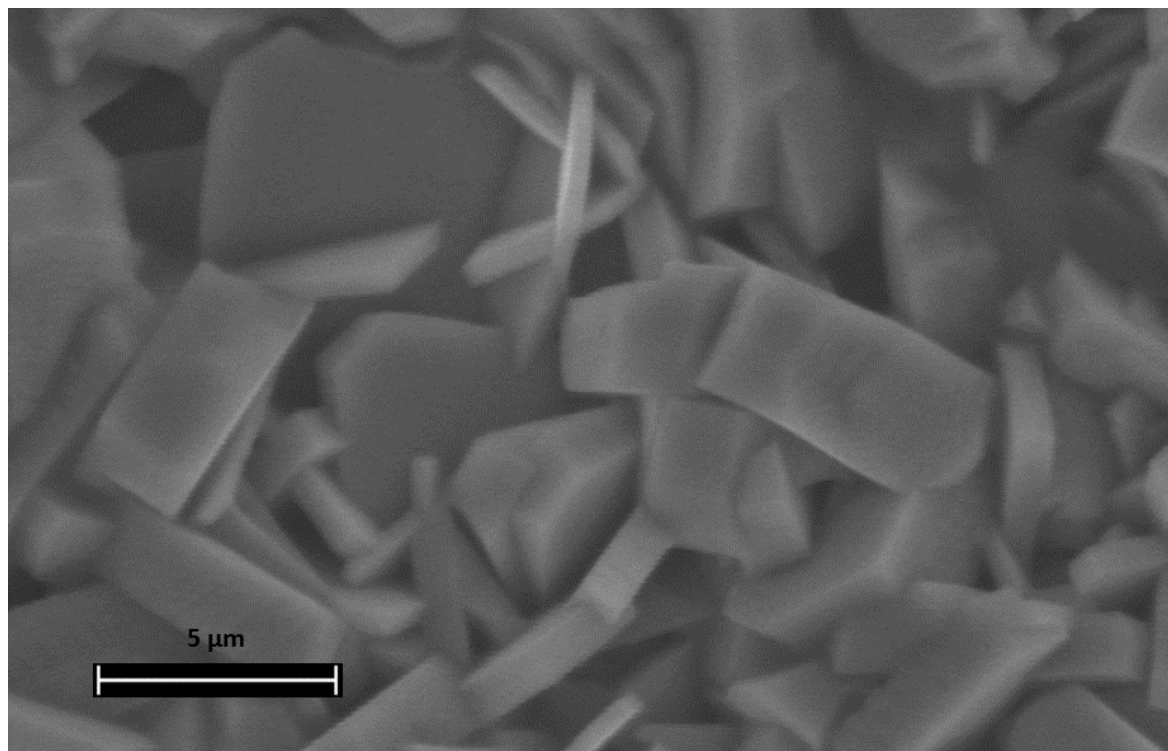


Figure 4-9: SEM image of germanium sulfide deposited from $[\text{Ge}^n\text{Bu}_3(\text{S}^n\text{Bu})]$.

The EDX analysis shows that the deposition produced was GeS and that there were no impurities present besides a small quantity of C. The deposition was performed at a 600 °C furnace temperature and over a period of 25 minutes. This is likely the cause of the slight sulfur deficiency (45.2% S to 54.8% Ge).

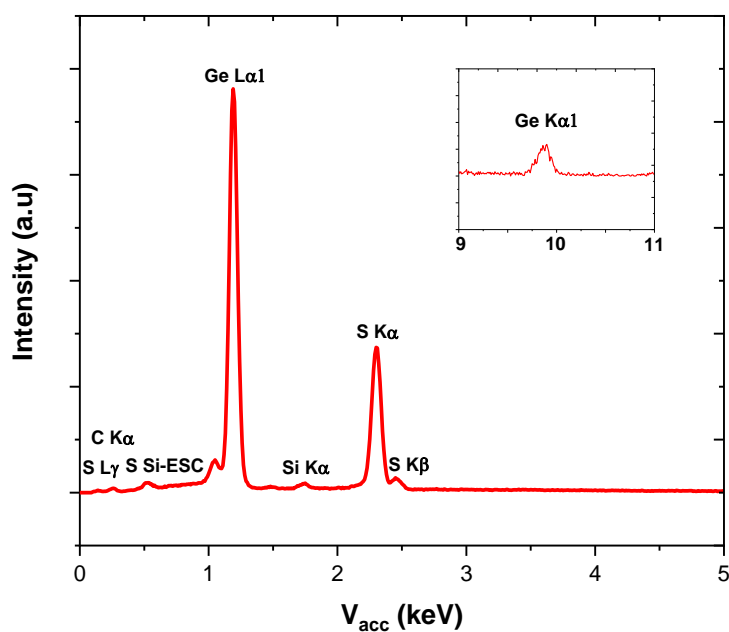


Figure 4-10: EDX spectrum collected for the GeS deposition produced using $[\text{Ge}^n\text{Bu}_3(\text{S}^n\text{Bu})]$ with region between 9-10 keV inset to highlight the Ge $K\alpha_1$ peak.

The Raman spectrum, displayed in Figure 4-10, is also consistent with GeS; the peak at 211 cm^{-1} corresponds to the B_{3g} mode, the 112 , 239 and 267 cm^{-1} peaks are associated with the A_g modes.⁷²

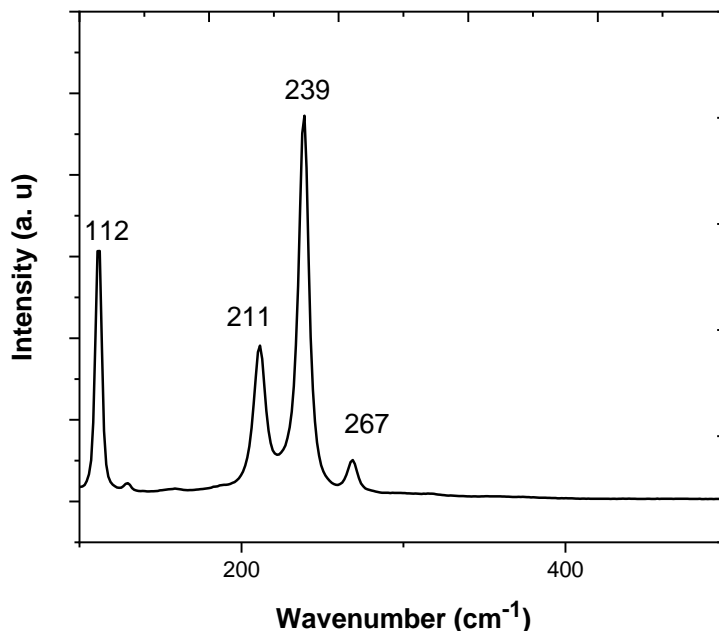


Figure 4-11: Raman spectrum of germanium sulfide, with A_g^3 , B_{3g} , A_g^1 and A_g^2 stretches at 112 , 211 , 239 and 267 cm^{-1} , respectively.⁷²

4.4.4 Germanium selenide thin films

The deposited material shown on the tile in Figure 4-12 is GeSe. The area investigated for characterisation is indicated.



Figure 4-12: Image of a tile containing highly orientated GeSe. The red cross indicates the region investigated for characterisation.

The grazing incidence XRD pattern shown in Figure 4-13 is in good agreement with the literature bulk pattern (red).²⁷ The refined lattice parameters for the pattern are: $a = 10.8089(7)\text{ \AA}$, $b = 3.8222(2)\text{ \AA}$ and $c = 4.3679(3)\text{ \AA}$ for this orthorhombic crystal system. These are in agreement with the literature values of: $a = 10.9208(4)\text{ \AA}$, $b = 3.8708(3)\text{ \AA}$ and $c = 4.4075(4)\text{ \AA}$.⁴⁸

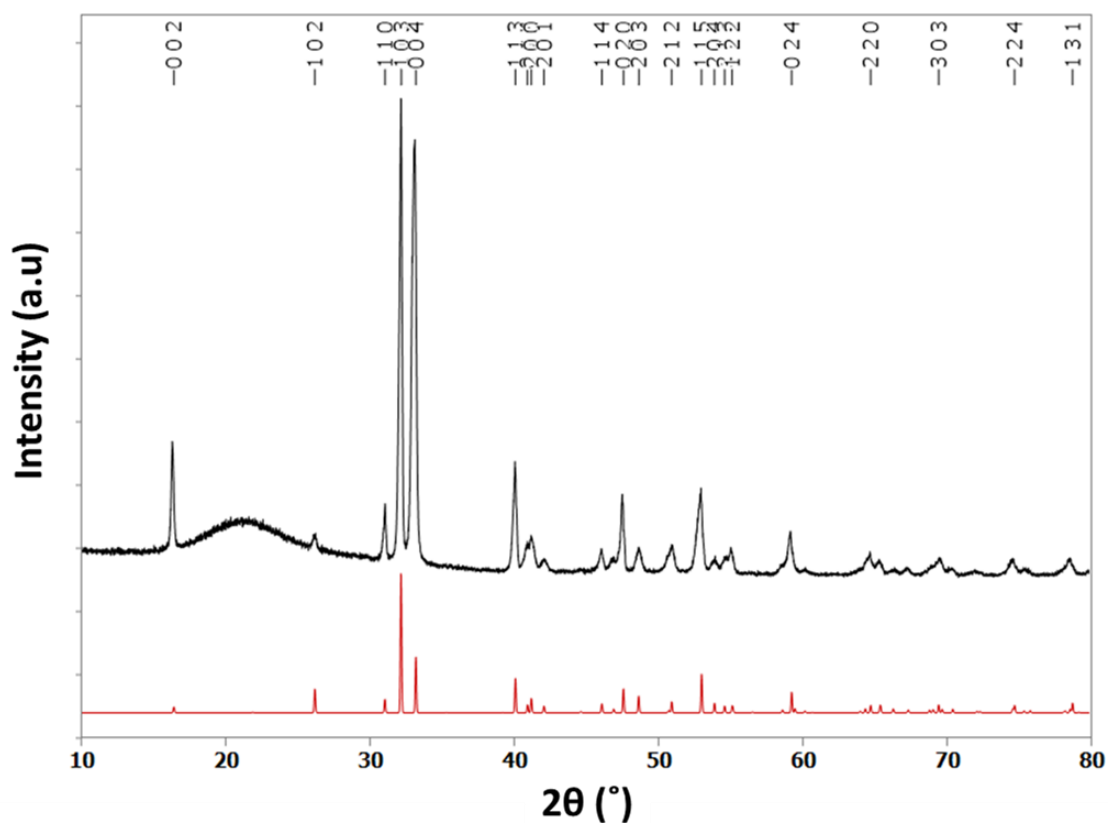


Figure 4-13: Grazing incidence XRD pattern measured for germanium selenide deposited from $[\text{Ge}^n\text{Bu}_3(\text{Se}^n\text{Bu})]$ (black) and the matched literature bulk pattern (red).²⁷ The broad feature observed around 21° is attributed to the SiO_2 substrate and it indicates that the film is relatively thin.

The EDX analysis showed the ratio of selenium to germanium to be 47%Se: 53%Ge. However, for a more accurate determination of the composition WDS or XPS could be employed. These experiments were not possible due to time restrictions and equipment constraints caused by lockdown procedures as a result of the COVID 19 pandemic. The EDX spectrum shown in Figure 4-14, indicates little to no impurities present.

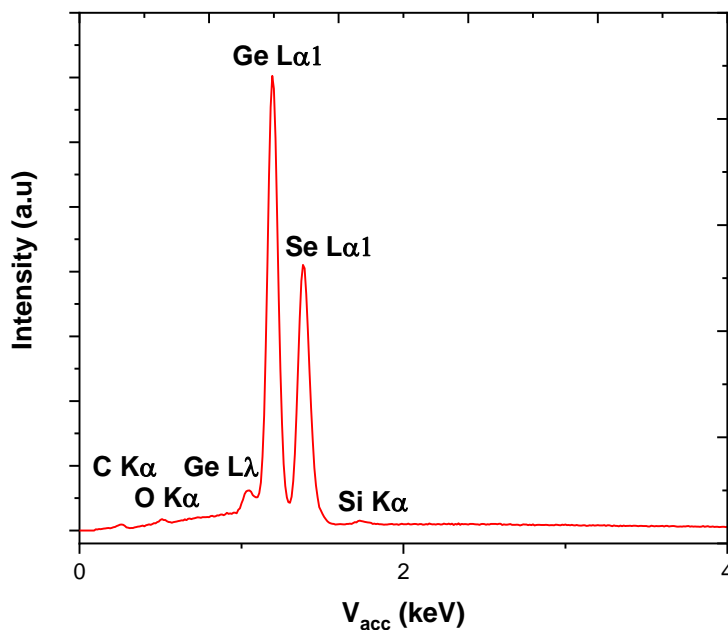


Figure 4-14: EDX spectrum collected for the GeSe deposition produced using $[\text{Ge}^n\text{Bu}_3(\text{Se}^n\text{Bu})]$.

The deposited material possesses a peculiar morphology, as shown in Figure 4-15, which may reflect a preferred orientation. Evidence for this can also be seen in the enhancement of the 002 and 004 reflections in the grazing incidence XRD spectrum in Figure 4-13. To further investigate this preferred orientation pole figure measurements could be collected.

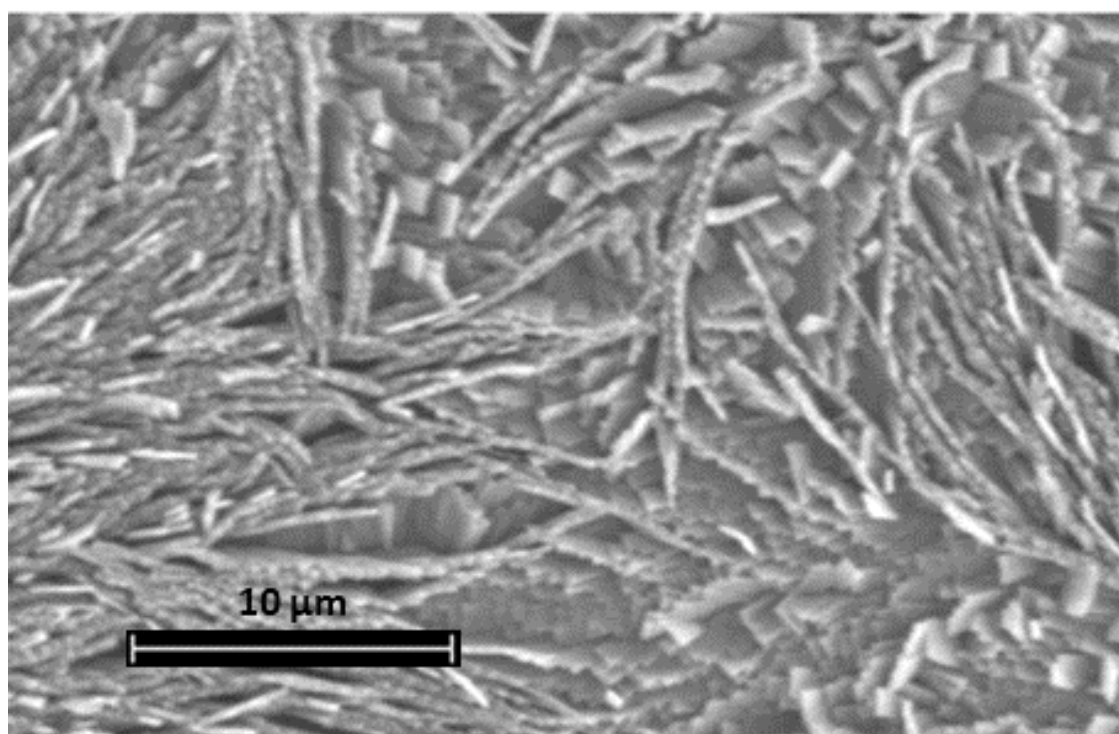


Figure 4-15: SEM images of germanium selenide, deposited from $[\text{Ge}^n\text{Bu}_3(\text{Se}^n\text{Bu})]$.

The Raman spectrum, displayed in Figure 4-16, is also consistent with GeSe; the peak at 151 cm^{-1} corresponds to the B_{3g} mode, the 175 and 189 cm^{-1} peaks are associated with the A_g modes.⁷⁷

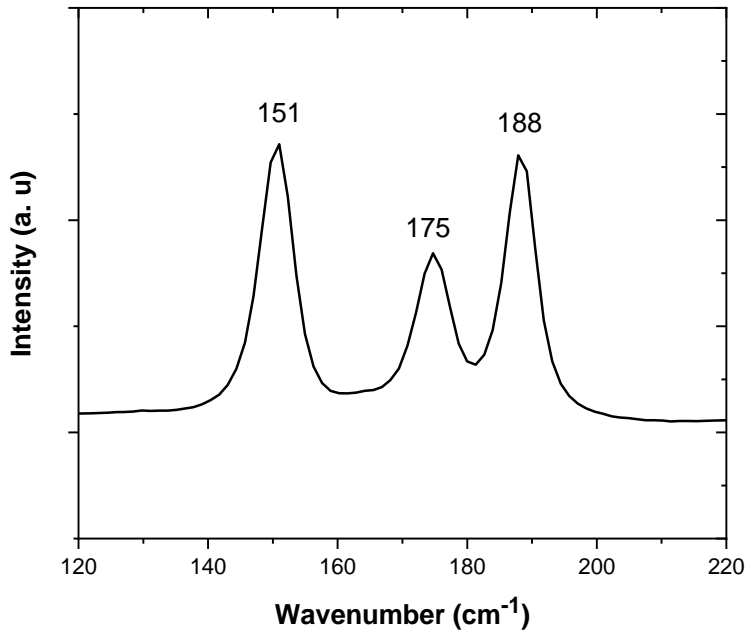


Figure 4-16: Raman spectrum of germanium selenide with B_{3g} , $A_{g(1)}$ and $A_{g(2)}$ stretches at 151 , 175 and 188 cm^{-1} , respectively.⁷⁷

The value quoted for the resistivity of GeSe is around $5 \times 10^4\ \Omega\text{cm}^{-1}$; however,¹⁵ as the value measured in this work is a sheet value, an assumed thickness of $1\ \mu\text{m}$ has been selected for comparisons. The assumed resistivity value is *ca.* an order of magnitude greater than that reported for GeSe. The charge carrier concentration is also *ca.* an order of magnitude greater than that reported in the literature, 3×10^{14} .⁷⁸

Table 4-2: Room temperature Van der Pauw electrical measurements for a film of GeSe and the deposition temperature. Note that the measurements inside the brackets have been calculated using an assumed thickness of $1\ \mu\text{m}$.

Tile	Hall effect coefficient (m^2C^{-1})	Sheet Resistivity (Ωsq^{-1})	Mobility ($\text{cm}^2\text{V}^{-1}\text{s}^{-1}$)	Charge carrier concentration (cm^{-2})
GeSe deposit	5230	2.235×10^7 (2235 Ωcm^{-1})	2.34	1.193×10^{11} ($1.193 \times 10^{15}\text{ cm}^{-3}$)

4.4.5 Germanium telluride thin films

The GeTe films produced are continuous and with coverages of between 1 cm by 0.8 cm and 2 cm by 0.8 cm. The material deposited was shown to be stoichiometric germanium telluride by EDX analysis, Raman spectroscopic analysis and grazing incidence XRD analysis. An example of one such deposit is displayed in Figure 4-17.



Figure 4-17: Image of a tile containing GeTe. (Note: the scratch marks occurred during the electrical and thermoelectrical measurements).

The grazing incidence XRD pattern shown in Figure 4-18 (black) is in good agreement with the literature pattern from bulk α -GeTe (red). The refined lattice parameters for the above pattern are: $a = 4.1778(5) \text{ \AA}$ and $c = 10.6866(14) \text{ \AA}$, which are in good agreement with the literature: $a = b = 4.156(3) \text{ \AA}$ and $c = 10.663(5)$.⁷⁹ There is a significant enhancement of the 003 reflection compared to the literature bulk system. This suggests that this sample is textured and should be further investigated by means of pole figure measurements in order to better understand the orientation of the crystallites with respect to the surface normal. Due to building closures and slow engineer works on vital instruments, resulting from COVID 19 restrictions, these experiments were not possible.

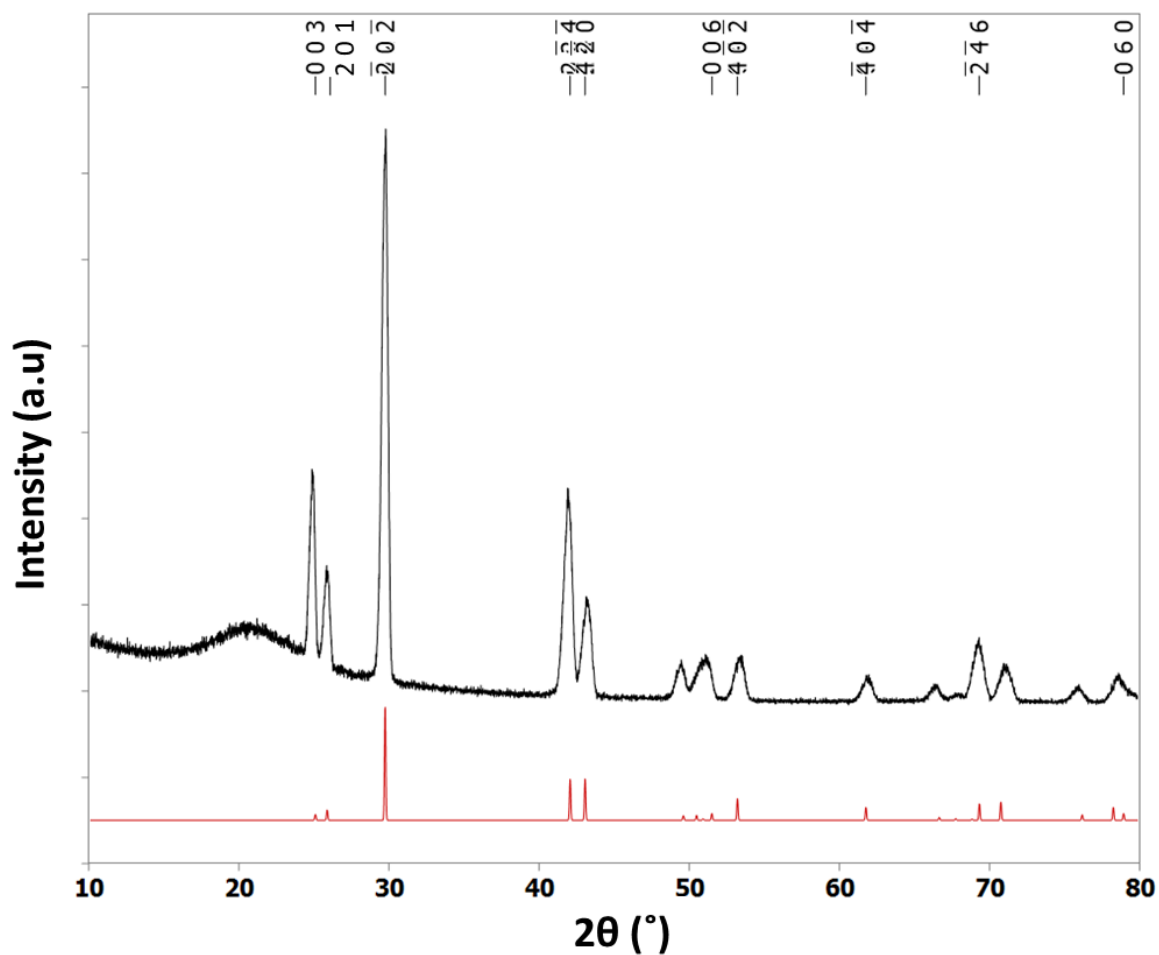


Figure 4-18: Grazing incidence XRD pattern measured for a deposit of GeTe (black) and the matched literature pattern (red).²⁹ The broad artifact around 22 ° corresponds to the underlaying fused quartz substrate.

The SEM images shown in Figure 4-19 show a good continuous film of germanium telluride which was shown to contain an equal amount of germanium and tellurium by EDX. The top down SEM images in Figure 4-19a and b show clearly defined grains with diameters of approximately 6 μm .

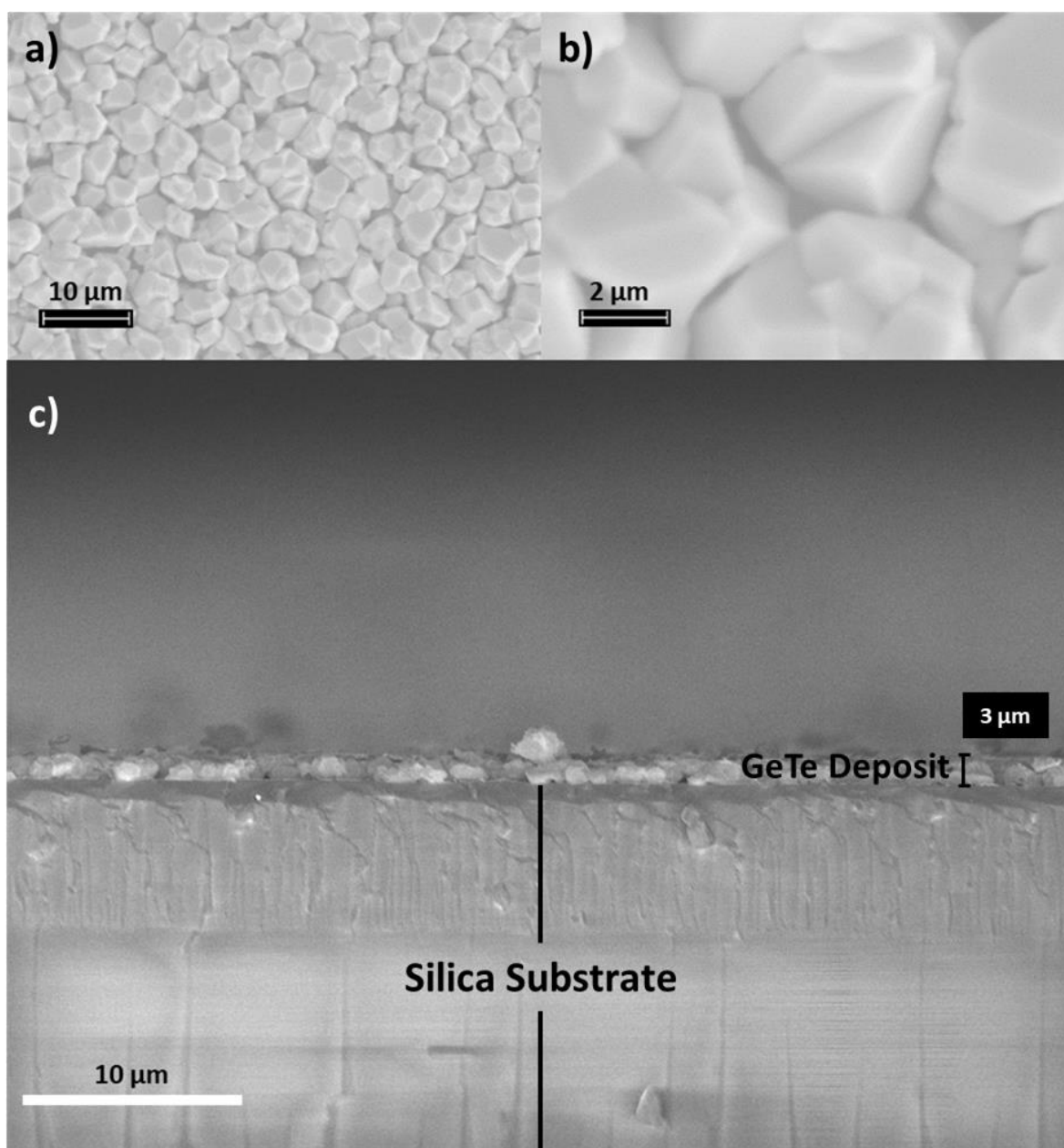


Figure 4-19: Top down SEM images of germanium telluride, deposited from $[\text{Ge}^n\text{Bu}_3(\text{Te}^n\text{Bu})]$, at 2,000 (top left) and 5,000 \times magnification (top right) and a cross sectional SEM image showing the film thickness to be *ca.* 3 μm .

The EDX spectra collected showed films of GeTe with little to no impurities. A representative sample can be seen in Figure 4-20. The peaks seen at 0.822 and 0.572 keV correspond to M series characteristic X-rays for Te which coincide with the K_α lines of O and C, respectively.

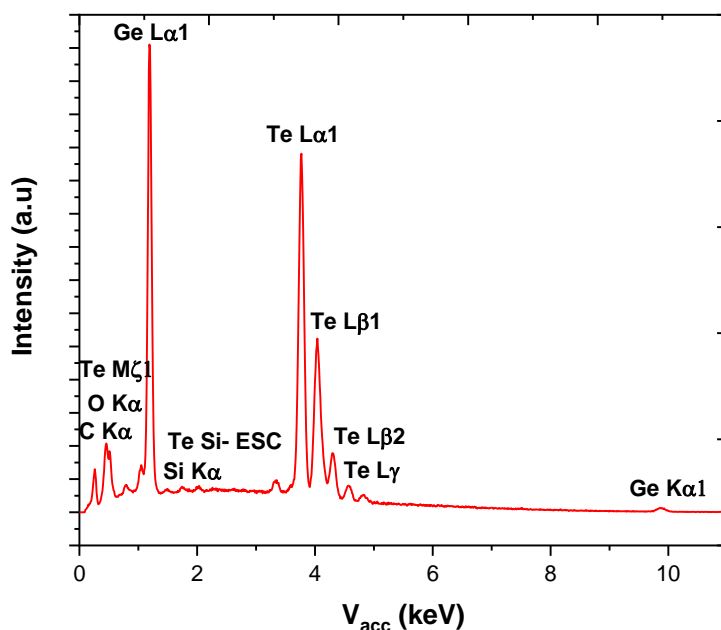


Figure 4-20: EDX spectrum collected for the GeTe deposition produced using $[\text{Ge}^n\text{Bu}_3(\text{Te}^n\text{Bu})]$.

Displayed in Table 4-3 are a number of different films of GeTe deposited from both $[\text{Ge}^n\text{Bu}_3(\text{Te}^n\text{Bu})]$ and $[\text{Ge}^n\text{Bu}_2(\text{Te}^n\text{Bu})_2]$. The EDX quantification results show good reproducibility in the deposition of high quality stoichiometric GeTe from both precursors. As mentioned, the overlap in the M lines of Te with the K_α lines of O and C lead to an exaggeration in their observed atom percentage.

Table 4-3: Table of EDX analysis results for GeTe films deposited using $[\text{Ge}^n\text{Bu}_3(\text{Te}^n\text{Bu})]$, (1), and $[\text{Ge}^n\text{Bu}_2(\text{Te}^n\text{Bu})_2]$, (2).

Deposit	Precursor	%C	%O	%Si	%Ge	%Te
Deposit 1	(1)	4.1	-	4.5	45.4	46.0
Deposit 2	(2)	17.0	11.9	0.6	34.3	36.3
Deposit 3	(2)	5.3	-	6.4	44.5	43.8
Deposit 4 tile 1	(1)	14.0	12.7	1.0	35.8	36.5
Deposit 4 tile 2	(1)	5.6	13.9	3.5	39.1	37.9
Deposit 5	(1)	3.7	-	1.3	46.9	48.2
Deposit 6	(1)	-	10.9	0.9	45.6	42.6

The Raman spectrum, seen in Figure 4-21, is also consistent with GeTe; the peak at 86 cm^{-1} corresponds to the E mode and the peak at 123 cm^{-1} are associated with the A_{1g} mode.⁸⁰

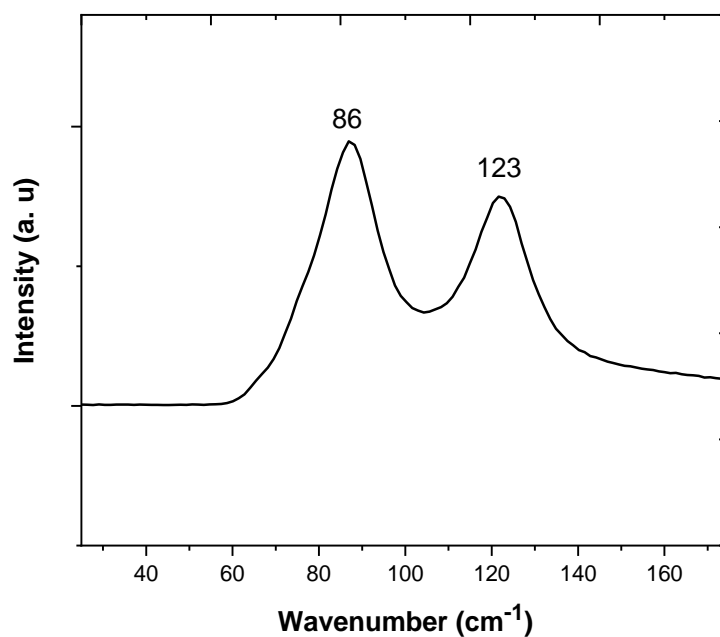


Figure 4-21: Raman spectrum for germanium telluride, deposited using $[\text{Ge}^n\text{Bu}_3(\text{Te}^n\text{Bu})]$, with E and A_{1g} stretches at 86 and 123 cm^{-1} , respectively.⁸⁰

A shift in the A_{1g} stretching mode with differing deposition temperature of the GeTe films can be seen in Figure 4-22.

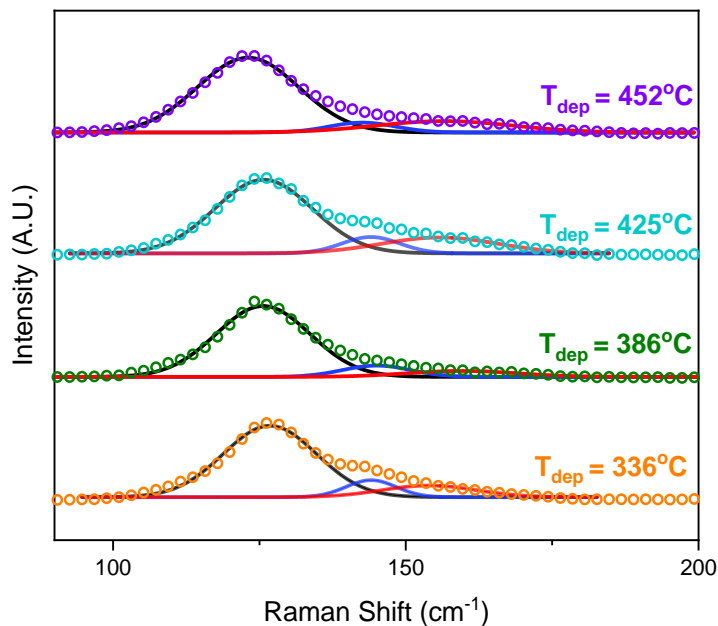


Figure 4-22: Comparison of the A_{1g} Raman stretching modes for 4 separate GeTe films deposited at different deposition temperature using $[\text{Ge}^n\text{Bu}_3(\text{Te}^n\text{Bu})]$.

4.4.6 Thermoelectric measurements of GeTe

The thermoelectric measurements acquired for GeTe, performed by Vikesh Sethi (ECS), showed high performances and a strong correlation between the deposition temperature of a film and its electrical conductivity. Some of these results can be seen displayed in Figure 4-23. The electrical conductivity is similar to that observed in the literature.¹ The Seebeck coefficients recorded are in good agreement with each other, as well as literature sources,^{13,54} and show no clear response to differing deposition temperatures. The power factors recorded show good competitive values compared with literature sources.¹³

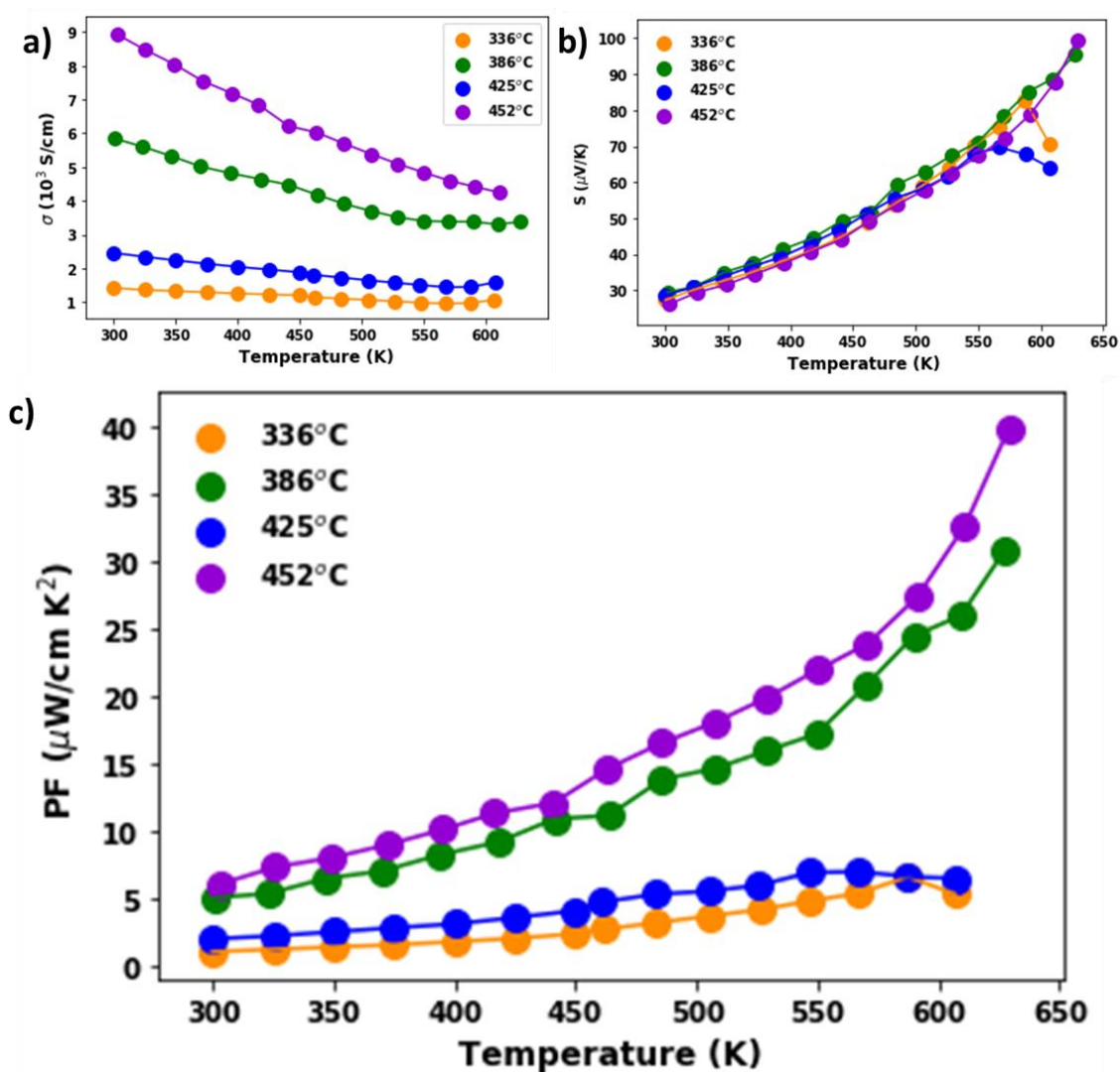


Figure 4-23: **a)** Electrical conductivity, **b)** Seebeck coefficient and **c)** power factor for four samples of GeTe deposited at different temperature, measured between \sim 300-625 K samples deposited using $[\text{Ge}^{\text{n}}\text{Bu}_3(\text{Te}^{\text{n}}\text{Bu})]$.

Hall effect measurements were also conducted in order to explore the charge carrier concentration and mobility. A clear correlation between the deposition temperature and the charge carrier concentration can be observed in Figure 4-24a. This correlation cannot clearly be seen in the charge carrier mobility graph, Figure 4-24b. This is likely due to differences in the grain size between the different deposits, as this will lead to different degrees of charge carrier scattering and thus will have an impact on the mobility. The correlation between the measured GeTe crystallite size and mobility can be seen in Figure 4-24c.

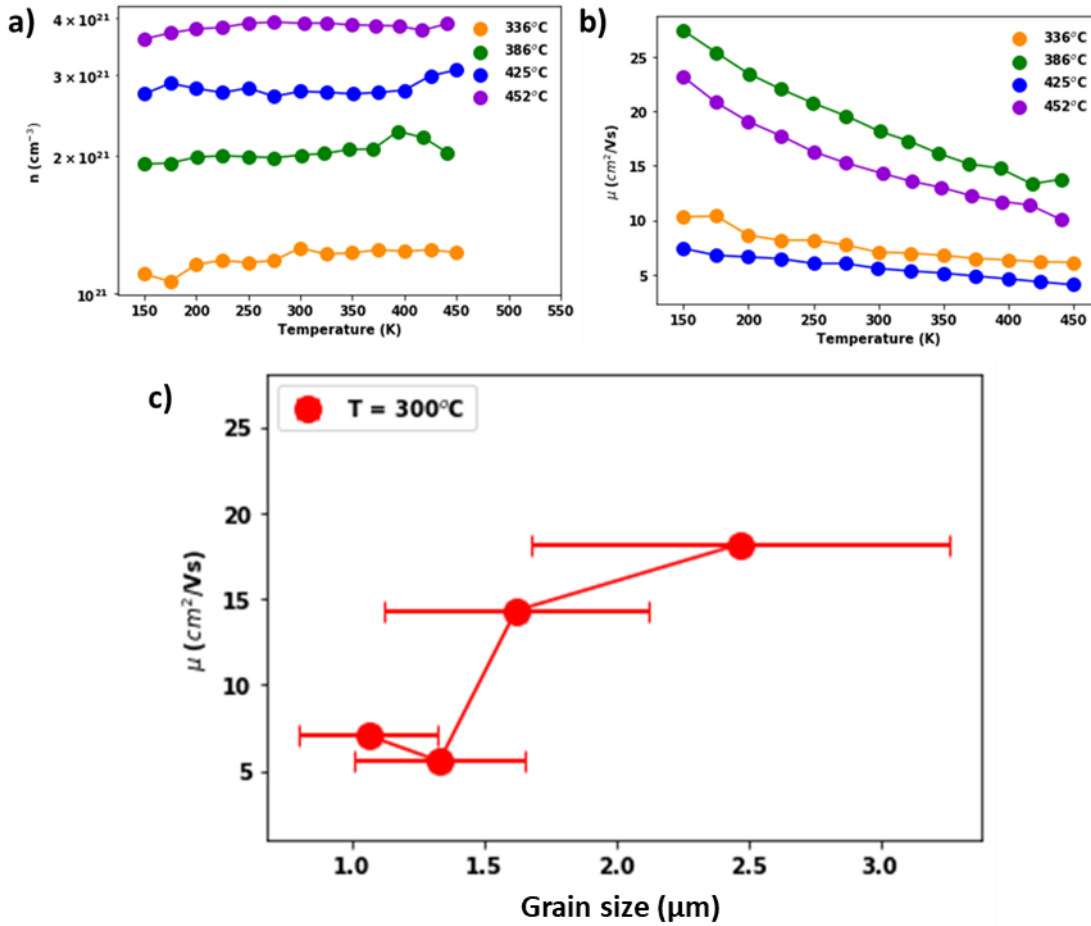


Figure 4-24: **a)** Charge carrier concentration and **b)** the charge carrier mobility versus temperature and **c)** the mobility at 300 °C versus grain size for GeTe measured between ~125- 450 K samples deposited using **[GeⁿBu₃(TeⁿBu)]**.

The relationship between the Lorentz number and the electronic contribution to the thermal conductivity, as well as its calculation, is described in Section 1.9.3.2.

Unsurprisingly, the trend observed for the κ_e of the deposits is in line with that seen for their electrical conductivities. With the order of the films in terms of their electrical conductivities being identical to their order with respect to the κ_e . These calculated results are shown in Figure 4-25.

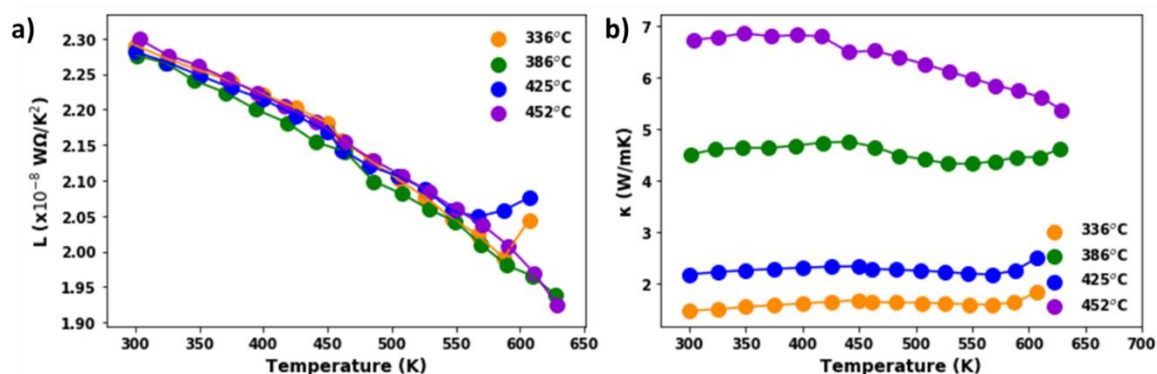


Figure 4-25: **a)** The Lorentz number and **b)** the calculated electronic contribution to the thermal conductivity factor for four samples of GeTe deposited at different temperature, between ~ 300 - 625 K samples deposited using $[\text{Ge}^n\text{Bu}_3(\text{Te}^n\text{Bu})]$.

Using the values acquired for κ_e , a ZT value can be calculated. By also assuming the value of the lattice contribution to the thermal conductivity to be $0.5 \text{ Wm}^{-1}\text{K}^{-1}$. This approximation leads to a calculated approximate peak value for ZT at *ca.* 0.45 at 625 K for the film deposited at 452 °C. The values obtained for ZT, shown in Figure 4-26, are in keeping with those recorded in the literature for bulk GeTe.⁸¹ The different profiles observed for the films deposited at 336 and 425 °C is possibly a result of their higher resistivity leading to current crowding effects which can affect the Seebeck coefficient.

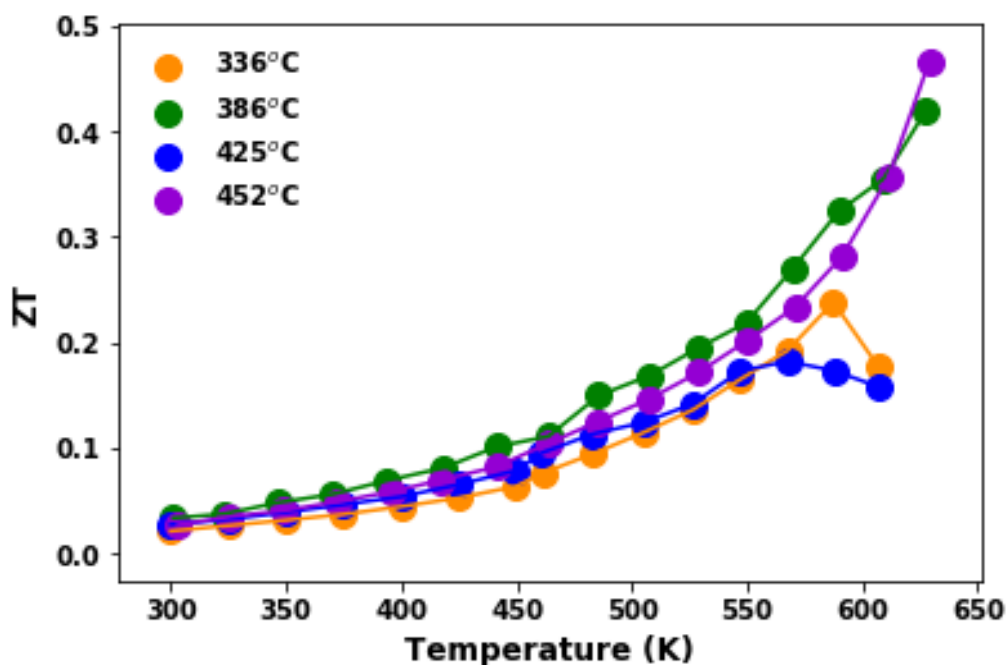


Figure 4-26: ZT values acquired using the calculated electronic contribution to the thermal conductivities shown in Figure 4-25b and the measured power factors displayed in Figure 4-23c.

4.5 Conclusions

SSPs for the deposition of GeE (E= S, Se and Te) have been assessed for their potential in LPCVD procedures. All of the precursors assessed have been shown to produced deposits of GeE, although in the case of **[GeⁿBu₃(SⁿBu)]** a sulfur deficient deposit with a small coverage area was produced. The successful characterisation of all the deposits produced has also been presented, including grazing incidence XRD, Raman spectroscopic data and SEM with EDX analysis. The thin films produced are of good quality with little to no contamination, as shown by the EDX and Raman analysis.

Some parameters of interest were measured for a GeSe deposit using the Hall effect measurement set up described. The data collected for a deposit of GeSe imply an enhanced electronic performance and a strong preferred orientation. Further measurements are required to investigate these findings more thoroughly.

No differences were found between deposits of GeTe produced using **[GeⁿBu₃(TeⁿBu)]** and **[GeⁿBu₂(TeⁿBu)₂]**. Measurements conducted on the GeTe thin films, deposited using **[GeⁿBu₃(TeⁿBu)]**, indicated that the films were competitive with the bulk literature data. Also identified is a correlation between the deposition temperature and the performance of the deposits. This could be further investigated by the deposition of further samples at different temperatures. It is possible that this observed effect could be exploited, to tune the thermoelectric properties, by using the deposition temperature and mass of precursor to influence the grain size and electrical properties.

4.6 References

- 1 S. Roychowdhury, M. Samanta, S. Perumal and K. Biswas, *Chem. Mater.*, 2018, **30**, 5799.
- 2 S. A. E. Wardani, *Geochim. Cosmochim. Acta*, 1957, **13**, 5.
- 3 H. L.D. and D. M.S., *Phys. Rev. B*, 1993, **47**, 12727.
- 4 G. Chen, M. S. Dresselhaus, G. Dresselhaus, J.-P. Fleurial and T. Caillat, *Int. Mater. Rev.*, 2013, **48**, 45.
- 5 S. Perumal, S. Roychowdhury and K. Biswas, *J. Mater. Chem. C*, 2016, **4**, 7520.
- 6 C. Wood, *Reports Prog. Phys.*, 1988, **51**, 459.
- 7 A. Polozine, S. Sirotinskaya and L. Schaeffer, *Mater. Res.*, 2014, **17**, 1260.
- 8 S. Raoux, W. Wetnic and D. Lelmini, *Chem. Rev.*, 2010, **110**, 240.
- 9 M. Chen, K. A. Rubin and R. W. Barton, *Appl. Phys. Lett.*, 1986, **49**, 502.

- 10 M. Wuttig and N. Yamada, *Nat. Mater.*, 2007, **6**, 824.
- 11 M. Sist, H. Kasai, E. M. J. Hedegaard and B. B. Iversen, *Phys. Rev. B*, 2018, **97**, 094116.
- 12 Y. Gelbstein, O. Ben-Yehuda, E. Pinhas, T. Edrei, Y. Sadia, Z. Dashevsky and M. P. Dariel, *J. Electron. Mater.*, 2009, **38**, 1478.
- 13 E. M. Levin, M. F. Besser and R. Hanus, *J. Appl. Phys.*, 2013, **114**, 083713.
- 14 M. Durandurdu, *Phys. Rev. B*, 2005, **72**, 144106.
- 15 X. Zhang, J. Shen, S. Lin, J. Li, Z. Chen, W. Li and Y. Pei, *J. Mater.*, 2016, **2**, 331.
- 16 G. Ding, G. Gao and K. Yao, *Sci. Rep.*, 2015, **5**, 9567.
- 17 H. S. Kim, E. A. Jung, S. H. Han, J. H. Han, B. K. Park, C. G. Kim and T. M. Chung, *Inorg. Chem.*, 2017, **56**, 4084.
- 18 F. Paquin, J. Rivnay, A. Salleo, N. Stingelin and C. Silva, *RSC Adv.*, 2014, **4**, 15695.
- 19 Y. J. Cho, H. S. Im, Y. Myung, C. H. Kim, H. S. Kim, S. H. Back, Y. R. Lim, C. S. Jung, D. M. Jang, J. Park, E. H. Cha, M. S. Song and W. Il Cho, *Chem. Commun.*, 2013, **49**, 4661.
- 20 D. D. Vaughn, R. J. Patel, M. A. Hickner and R. E. Schaak, *J. Am. Chem. Soc.*, 2010, **132**, 15170.
- 21 D. D. Vaughn and R. E. Schaak, *Chem. Soc. Rev.*, 2013, **42**, 2861.
- 22 T. Chen, W. Hunks, P. S. Chen, G. T. Stauf, T. M. Cameron, C. Xu, A. G. DiPasquale and A. L. Rheingold, *Eur. J. Inorg. Chem.*, 2009, 2047.
- 23 K. A. Campbell and C. M. Anderson, *Microelectronics J.*, 2007, **38**, 52.
- 24 Y. Hong, J. Zhang, X. Huang and X. C. Zeng, *Nanoscale*, 2015, **7**, 18716.
- 25 W. Tao, N. Kong, X. Ji, Y. Zhang, A. Sharma, J. Ouyang, B. Qi, J. Wang, N. Xie, C. Kang, H. Zhang, O. C. Farokhzad and J. S. Kim, *Chem. Soc. Rev.*, 2019, **48**, 2891.
- 26 G. Bissert and K.-F. Hesse, *Acta Crystallogr. Sect. B Struct. Crystallogr. Cryst. Chem.*, 2002, **34**, 1322.
- 27 A. Okazaki, *J. Phys. Soc. Japan*, 1958, **13**, 1151.
- 28 W. A. Crichton, M. Mezouar, G. Monaco and S. Falconi, *Powder Diffr.*, 2003, **18**, 155.
- 29 S. Schulz, S. Heimann, K. Kaiser, O. Prymak, W. Assenmacher, J. T. Brüggemann, B. Mallick and A. V. Mudring, *Inorg. Chem.*, 2013, **52**, 14326.
- 30 W. G. Zeier, A. Zevalkink, Z. M. Gibbs, G. Hautier, M. G. Kanatzidis and G. J. Snyder, *Angew. Chem. Int. Ed.*, 2016, **55**, 6826.
- 31 S. L. Hawken, R. Huang, C. H. de Groot, A. L. Hector, M. Jura, W. Levason, G. Reid and G. B. G. Stenning, *Dalton Trans*, 2019, **48**, 117.
- 32 G. Gupta, T. M. Jeong, C. G. Kim and J. Kim, *Mater. Lett.*, 2015, **156**, 121.
- 33 S. K. Bahl and K. L. Chopra, *J. Appl. Phys.*, 1970, **41**, 2196.
- 34 D. Bräuhaus, C. Schindler, U. Böttger and R. Waser, *Thin Solid Films*, 2008, **516**, 1223.

Chapter 4

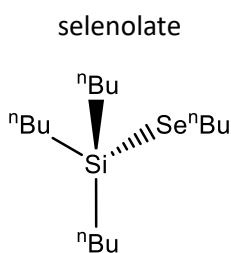
- 35 P. J. Whitham, D. P. Strommen, L. D. Lau and R. G. Rodriguez, *Plasma Chem. Plasma Process.*, 2011, **31**, 251.
- 36 S. Murugesan, P. Kearns and K. J. Stevenson, *Langmuir*, 2012, **28**, 5513.
- 37 D. Reso, M. Silinskas, M. Lisker, A. Schubert and E. P. Burte, *Appl. Phys. Lett.*, 2011, **98**, 151901.
- 38 C. C. Huang, D. W. Hewak and J. V. Badding, *Opt. Express*, 2004, **12**, 2501.
- 39 E. G. Turitsyna and S. Webb, *Electron. Lett.*, 2005, **40**, 863.
- 40 P. Nagels, *Semiconductors*, 1998, **32**, 855.
- 41 A. Giussani, K. Perumal, M. Hanke, P. Rodenbach, H. Riechert and R. Calarco, *Phys. Status Solidi Basic Res.*, 2012, **249**, 1939.
- 42 D. Yu, J. Wu, Q. Gu and H. Park, *J. Am. Chem. Soc.*, 2006, **128**, 8148.
- 43 A. Shakouri, *Annu. Rev. Mater. Res.*, 2011, **41**, 399.
- 44 S. Hao, F. Shi, V. P. Dravid, M. G. Kanatzidis and C. Wolverton, *Chem. Mater.*, 2016, **28**, 3218.
- 45 J. D. Wiley, D. Thomas, E. Schönherr and A. Breitschwerdt, *J. Phys. Chem. Solids*, 1980, **41**, 801.
- 46 M. Taniguchi, R. L. Johnson, J. Ghijsen and M. Cardona, *Phys. Rev. B*, 1990, **42**, 3634.
- 47 R. P. Dias, M. Kim and C. S. Yoo, *Phys. Rev. B*, 2016, **93**, 104107.
- 48 S. Roychowdhury, T. Ghosh, R. Arora, U. V. Waghmare and K. Biswas, *Angew. Chem. Int. Ed.*, 2018, **57**, 15167.
- 49 P. D. Antunez, J. J. Buckley and R. L. Brutchey, *Nanoscale*, 2011, **3**, 2399.
- 50 T. Nonaka, G. Ohbayashi, Y. Toriumi, Y. Mori and H. Hashimoto, *Thin Solid Films*, 2000, **370**, 258.
- 51 J. Goldak, C. S. Barrett, D. Innes and W. Youdelis, *J. Chem. Phys.*, 1966, **44**, 3323.
- 52 G. Xing, J. Sun, Y. Li, X. Fan, W. Zheng and D. J. Singh, *J. Appl. Phys.*, 2018, **123**, 195105.
- 53 S. Perumal, S. Roychowdhury, D. S. Negi, R. Datta and K. Biswas, *Chem. Mater.*, 2015, **27**, 7171.
- 54 D. Wu, L.-D. Zhao, S. Hao, Q. Jiang, F. Zheng, J. W. Doak, H. Wu, H. Chi, Y. Gelbstein, C. Uher, C. Wolverton, M. Kanatzidis and J. He, *J. Am. Chem. Soc.*, 2014, **136**, 11412.
- 55 P. Zhao, H. Yang, J. Li, H. Jin, W. Wei, L. Yu, B. Huang and Y. Dai, *J. Mater. Chem. A*, 2017, **5**, 24145.
- 56 M. Hong, J. Zou and Z. G. Chen, *Adv. Mater.*, 2019, **31**, 1807071.
- 57 J. Yan, P. Gorai, B. Ortiz, S. Miller, S. A. Barnett, T. Mason, V. Stevanović and E. S. Toberer, *Energy Environ. Sci.*, 2015, **8**, 983.
- 58 J. Li, X. Zhang, S. Lin, Z. Chen and Y. Pei, *Chem. Mater.*, 2017, **29**, 605.
- 59 Z. Zheng, X. Su, R. Deng, C. Stoumpos, H. Xie, W. Liu, Y. Yan, S. Hao, C. Uher, C. Wolverton,

- M. G. Kanatzidis and X. Tang, *J. Am. Chem. Soc.*, 2018, **140**, 2673.
- 60 Z. Liu, J. Sun, J. Mao, H. Zhu, W. Ren, J. Zhou, Z. Wang, D. J. Singh, J. Sui, C. W. Chu and Z. Ren, *Proc. Natl. Acad. Sci. U. S. A.*, 2018, **115**, 5332.
- 61 S. Perumal, P. Bellare, U. S. Shenoy, U. V. Waghmare and K. Biswas, *Chem. Mater.*, 2017, **29**, 10426.
- 62 J. Li, Z. Chen, X. Zhang, Y. Sun, J. Yang and Y. Pei, *NPG Asia Mater.*, 2017, **9**, e353.
- 63 L. Wu, X. Li, S. Wang, T. Zhang, J. Yang, W. Zhang, L. Chen and J. Yang, *NPG Asia Mater.*, 2017, **9**, e343.
- 64 J. Li, Z. Chen, X. Zhang, H. Yu, Z. Wu, H. Xie, Y. Chen and Y. Pei, *Adv. Sci.*, 2017, **4**, 1700341.
- 65 M. Samanta and K. Biswas, *J. Am. Chem. Soc.*, 2017, **139**, 9382.
- 66 Y. Gelbstein, J. Davidow, S. N. Girard, D. Y. Chung and M. Kanatzidis, *Adv. Energy Mater.*, 2013, **3**, 815.
- 67 B. Ul Haq, S. AlFaify, A. Laref, R. Ahmed and M. F. M. Taib, *Ceram. Int.*, 2019, **45**, 15122.
- 68 F. Fahrnbauer, D. Souchay, G. Wagner and O. Oeckler, *J. Am. Chem. Soc.*, 2015, **137**, 12633.
- 69 M. Samanta, S. Roychowdhury, J. Ghatak, S. Perumal and K. Biswas, *Chem. Eur. J.*, 2017, **23**, 7438.
- 70 M. Hong, Z. G. Chen, L. Yang, Y. C. Zou, M. S. Dargusch, H. Wang and J. Zou, *Adv. Mater.*, 2018, **30**, 1705942.
- 71 S. Lee, K. Esfarjani, T. Luo, J. Zhou, Z. Tian and G. Chen, *Nat. Commun.*, 2014, **5**, 3525.
- 72 D. Tan, H. E. Lim, F. Wang, N. B. Mohamed, S. Mouri, K. Sandhaya, W. Zhang, Y. Miyauchi, M. Ohfuchi and K. Matsuda, *Nano Res.*, 2016, **10**, 546.
- 73 H. Zhao, Y. Mao, X. Mao, X. Shi, C. Xu, C. Wang, S. Zhang and D. Zhou, *Adv. Funct. Mater.*, 2018, **28**, 1704855.
- 74 B. Ul Haq, S. Alfaify and A. Laref, *J. Phys. Chem. C*, 2019, **123**, 18124.
- 75 S. Perumal, S. Roychowdhury and K. Biswas, *Inorg. Chem. Front.*, 2016, **3**, 125.
- 76 M. A. Popescu, in *Non-Crystalline Chalcogenides*, Springer, Dordrecht, 2000, p. 103.
- 77 A. Taube, A. Łapińska, J. Judek, N. Wochtman and M. Zdrojek, *J. Phys. D. Appl. Phys.*, 2016, **49**, 315301.
- 78 D. Sidharth, A. S. Alagar Nedunchezian, A. Rajamani, A. Shrivastava, B. Srinivasan, P. Immanuel, R. Rajkumar, N. Yalini Devi, M. Arivanandhan, C.-J. Liu, G. Anbalagan, S. Ramasamy and J. Ramasamy, *Sustain. Energy Fuels*, 2021, **5**, 1734.
- 79 P. Bauer Pereira, I. Sergueev, S. Gorsse, J. Dadda, E. Müller and R. P. Hermann, *Phys. status. Solidi B*, 2013, **250**, 1300.
- 80 A. Pawbake, C. Bellin, L. Paulatto, K. Béneut, J. Biscaras, C. Narayana, D. J. Late and A. Shukla, *Phys. Rev. Lett.*, 2019, **122**, 145701.
- 81 K. Biswas, *Chem. Mater.*, 2015, **27**, 7171.

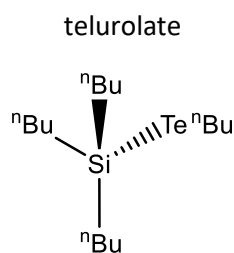
Chapter 5 Application of $[\text{Si}^n\text{Bu}_3(\text{E}^n\text{Bu})]$ as Single Source Precursors for the Deposition of Silicon Chalcogenide Thin Films

5.1 Single source precursors used

$[\text{Si}^n\text{Bu}_3(\text{Se}^n\text{Bu})]$: Tri-n-butylsilyl n-butyl



$[\text{Si}^n\text{Bu}_3(\text{Te}^n\text{Bu})]$: Tri-n-butylsilyl n-butyl



5.2 Introduction

The silicon chalcogenides are a lesser investigated group of semiconductor materials, when compared to the tin or germanium chalcogenides. This, however, does not reflect the large number of useful applications associated to the silicon chalcogenide family and in particular silicon telluride. Silicon telluride has an indirect band gap of 1 eV and a direct band gap of 2 eV, which are comparable to the most commonly used semiconducting material silicon.¹⁻⁵ A number of exciting physical properties have been identified for silicon telluride such as: high electrical conductivity, low thermal conductivity, broad photoluminescence in the near infrared region and undergoes a phase change at elevated pressure.^{1,5-7} Due to its photoluminescence in the near infrared range, silicon telluride is of interest as an infrared detector material which, due to the higher toxicity of mercury and cadmium containing materials that are widely used currently, would be desirable.⁸⁻¹⁰

Despite investigations into SiTe no material synthesis has been possible thus far. This contrasts with the typical form of the materials discussed in previous chapters of this work, i.e. the Group 14 monochalcogenides, ME (M = Ge or Sn). In this chapter on silicon telluride thin film growth and the exploration of silicon chalcogenolate SSPs, the chemical composition discussed is Si_2Te_3 , the structure most stable at room temperature and pressure. The reason for this 2:3 phase dominating the chemistry of silicon telluride is the relative instability of SiTe, due to the small size of the silicon atoms and the large size of the tellurium atoms. Although computational studies have suggested that SiTe may be stable at higher pressures, this is not viable for applications.¹¹

Si_2Te_3 adopts a hexagonal close-packed Te sub-lattice with disordered Si-Si dumb-bells evenly distributed between $2/3$ of the octahedral vacancies in every second layer of Te atoms.¹¹ The bonding between the tellurium layers is very weak and leads to the ease in mechanical separation of the layers.⁵ The 1:2, SiTe_2 has also been reported and adopts a similar structure to Si_2Te_3 with silicon atoms occupying the octahedral holes of the close-packed Te layers.¹² These features have been emphasised in Figure 5-1.

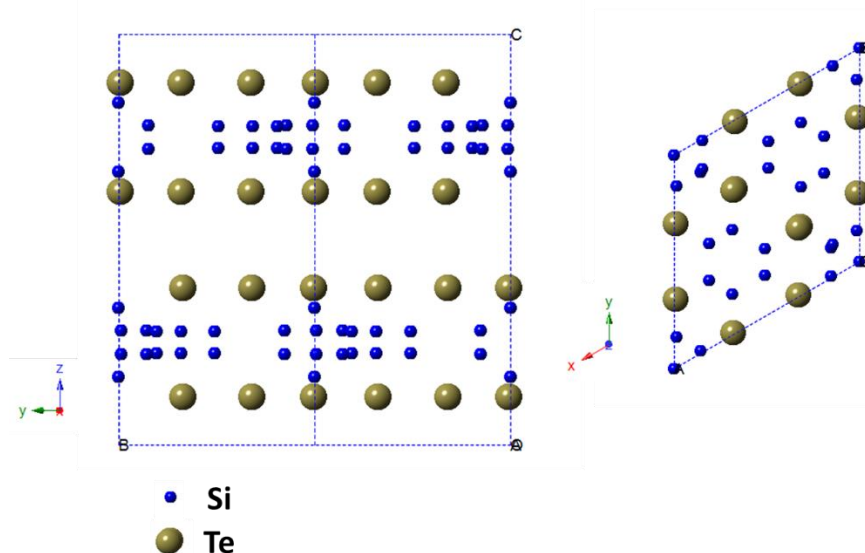


Figure 5-1: Crystal structure of Si_2Te_3 looking down the a axes to visualise the layers and down the c axis to emphasise the hexagonal structure of the Te slabs and the Si dumb-bells in the octahedral sites.¹³

The very different structure of Si_2Te_3 compared to that of the other Group 14 tellurides leads to some unique behaviour. Investigations into the electronic structure have shown that the orientation of the Si-Si dumb-bells impacts the magnitude of the bandgap.^{11,14} The alignment of these dumbbells is affected by the temperature and also any strain on the material. Si_2Te_3 is also able to withstand very high uniaxial tensile strain, higher than any other 2D material reported, including graphene.¹⁵ This allows for a degree of control over the electronic properties and makes Si_2Te_3 a good candidate for mechanical, optical and memristive devices.¹⁴

The thermoelectric properties of Si_2Te_3 are relatively unexplored, with the exception of theoretical work, which predicts the high performance of n-doped Si_2Te_3 .¹⁶ The tuneable band gap and anisotropic layered structure of Si_2Te_3 indicate good potential as a thermoelectric material.

There are few examples of Si_2Te_3 depositions, and especially for thin films. The examples are comprised of nanoribbons,⁵ nanoplates,⁸ nanotapers,¹⁷ nanowires,¹⁸ thin film¹⁹ and single crystals.¹³ However, all of these material synthesis methods occur via the direct combination of pure Si and pure Te, either in the gas phase, as described for nanoplates²⁰ and thin films of

Si_2Te_3 ,¹⁹ or combined and heated under vacuum in ampoules.¹³ Examples of some of the morphologies of Si_2Te_3 can be seen in Figure 5-2. The evaporation of Si and Te requires a considerable amount of energy and thus high temperatures, 800 °C,⁹ are required. The single source precursor described in the present study, as well as the deposition method, are therefore unique within the published literature. The use of a single source precursor opens up lots of potential areas to explore, as discussed in Section 2.1.

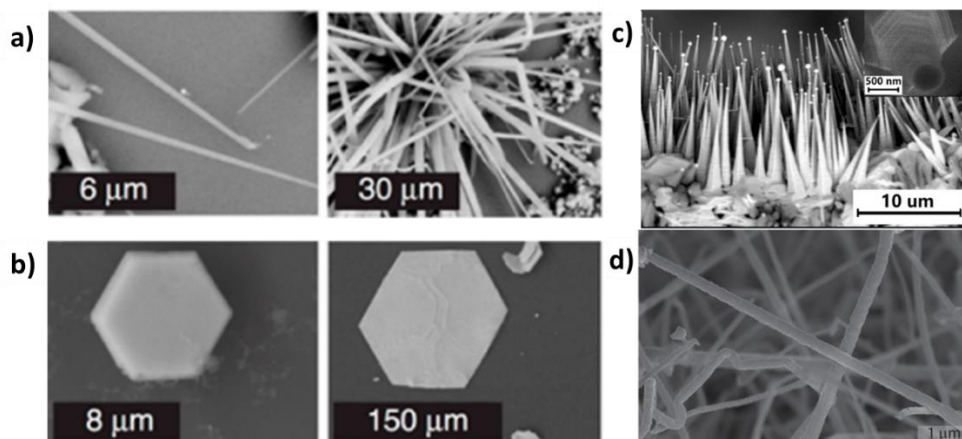


Figure 5-2: SEM images of; a) nanoribbons,⁵ b) nanoplates,⁸ c) nanotapers¹⁷ and d) nanowires,¹⁸ of Si_2Te_3 . Figures reproduced with permission from the American Chemical Society, AIP Publishing, Springer Nature and AIP publishing, respectively.

The other Si chalcogenide materials differ from Si_2Te_3 in structure and composition at ambient temperature and pressure. The sulfide and selenide both adopt an orthorhombic, *Ibam*, structure with the composition SiE_2 , under ambient conditions, as displayed in Figure 5-3.

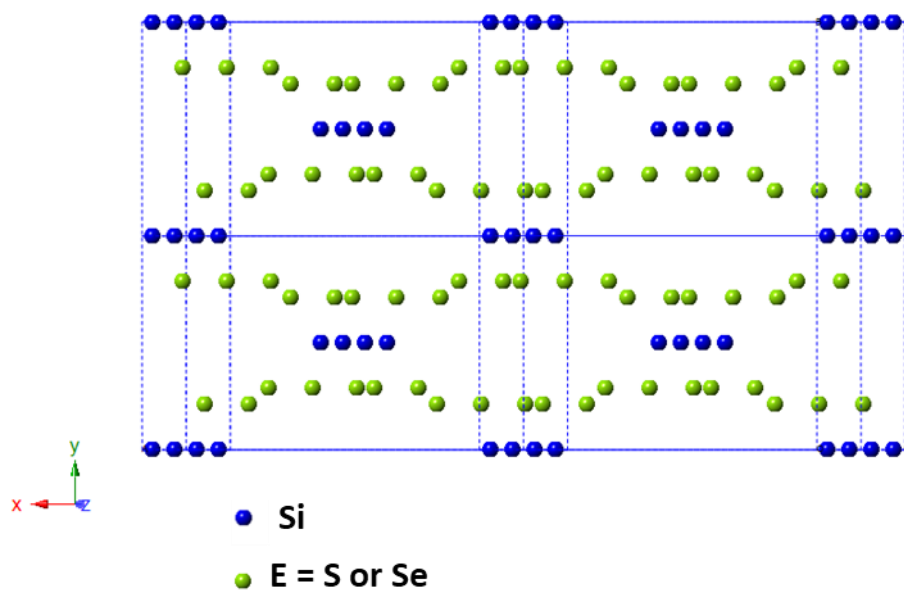


Figure 5-3: Crystal structure of SiS_2 and SiSe_2 .²¹

Few experimental investigations of the silicon sulfides and selenides exist in the literature, besides some mention of their pertinence to photovoltaics²² and optoelectronic properties.²³ There are, however, numerous mentions of different silicon chalcogenides within theoretical works. These computational experiments indicate exciting potential within thermoelectrics,²⁴ photovoltaics²⁵ and battery materials.^{26,27}

The good predicted thermoelectric performances of the silicon monochalcogenides mean that the potential for incorporating silicon chalcogenide into other group 14 chalcogenides could lead to some exciting novel thermoelectric materials. For this reason, the development of a new group of SSPs, analogous to ones which produce other group 14 chalcogenide thin films, for some of the silicon chalcogenides is of considerable interest.

The aim of this chapter is to explore the possibility of extending the pre-established SSP family from Chapters 2, 3 and 4 to the silicon chalcogenides. If this was possible, once the SSPs had been fully characterised, these would establish the first examples of SSPs for silicon chalcogenide material deposition. These would allow for the deposition of thin films at lower temperatures than those required for direct reaction of the elements in the case of Si_2Te_3 , or establish the first methods for thin film deposition for silicon sulfide and selenide. Once deposited these films would be characterised. The potential of the deposition process for orientational control of films of silicon chalcogenide as well their preliminary electrical properties would then be assessed.

5.3 Experimental

5.3.1 LPCVD onto fused quartz substrates

The fused quartz substrates were first washed with deionized water then ethanol before being dried thoroughly in an oven at 75 °C before use. In a typical LPCVD experiment, the precursor (5-50 mg) and 6 fused quartz substrates were loaded end to end into a closed end silica tube inside the glovebox. The precursor was loaded into the precursor bulb at the end of the sealed silica tube and the substrates were positioned end to end (0-4 cm away from the precursor bulb) down the silica tube. The tube was positioned horizontally in the furnace and held in place such that the precursor containing bulb was protruding from the end of the furnace. The tube was evacuated to 0.01- 0.40 mmHg. The furnace was heated to the necessary temperature as determined by TGA experiments and experimental observations, 700 °C, for the CVD experiment and allowed to stabilise. The tube was positioned so that the precursor was close enough to the furnace for sublimation to be observed. The position was then maintained until all of the precursor had sublimed. This typically took 3-15 min. Once the deposition was complete, the tube was removed

from the furnace area and allowed to cool naturally to room temperature, before being transferred to the glovebox, where the substrates were removed and stored until they could be characterised. The temperature at the substrates, where material had been successfully deposited, was obtained using a temperature probe to profile the internal temperature within the tube furnace.

The LPCVD experiments produced black films of Si_2Te_3 with around 2 by 1 cm coverage. Deposition temperatures between 374 and 539 °C were recorded for these depositions.



Figure 5-4: Example of Si_2Te_3 deposited onto a silica substrate.

Deposition attempts using $[\text{Si}^n\text{Bu}_3(\text{Se}^n\text{Bu})]$ and $[\text{Si}^n\text{Bu}_3(\text{S}^n\text{Bu})]$ proved unsuccessful. In all cases it was typical to observe some liquid distilled through the CVD tube, most likely unreacted precursor.

5.4 Results and discussion

5.4.1 Synthesis and Characterisation of SSPs for LPCVD

The precursor synthesis proceeded well and produced a reddish orange oil, in the case of $[\text{Si}^n\text{Bu}_3(\text{Te}^n\text{Bu})]$, a light orange oil, $[\text{Si}^n\text{Bu}_3(\text{Se}^n\text{Bu})]$ and a clear colourless oil $[\text{Si}^n\text{Bu}_3(\text{S}^n\text{Bu})]$, all in good yields. However, $[\text{Si}^n\text{Bu}_3(\text{S}^n\text{Bu})]$ synthesis retained unreacted $[\text{Si}^n\text{Bu}_3\text{Cl}]$. The precursors were shown to be of high purity by multinuclear NMR spectroscopy, microanalysis and their TGA are displayed in Figure 5-5. More detail about the synthesis process can be found in Sections 2.2.2 and 2.3.1 and details of the vapour pressure, enthalpy of vaporisation and entropy of vaporisation of $[\text{Si}^n\text{Bu}_3(\text{Te}^n\text{Bu})]$ can be found in Section 2.3.2.

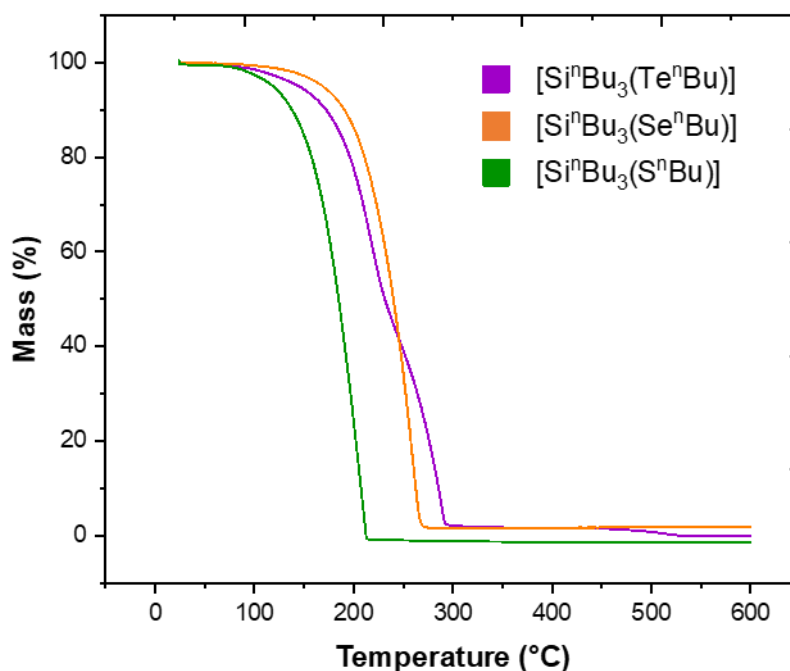


Figure 5-5: TGA of $[\text{Si}^n\text{Bu}_3(\text{S}^n\text{Bu})]$, $[\text{Si}^n\text{Bu}_3(\text{Se}^n\text{Bu})]$ and $[\text{Si}^n\text{Bu}_3(\text{Te}^n\text{Bu})]$ showing clean evaporation with no residue remaining.

The preparation of silicon thiolates proved particularly difficult. These required the reaction to be heated in order to cause reaction of the NaS^nBu with $[\text{Si}^n\text{Bu}_3\text{Cl}]$. This behaviour is likely to be the result of the poorer nucleophilicity of the RS^- group compared to that of RSe^- or RTe^- . This, combined with the steric crowding around the small Si, led to the higher temperature requirements and some unreacted silicon chloride was evident in all preparations of silicon thiolate compounds.

The bond enthalpies displayed in Table 5-1 provide some rationale for the difficulties in the deposition of silicon sulfide, silicon selenide (and germanium sulfide). In every CVD process there is a deposition temperature window. Below this temperature threshold there is not enough energy to promote the decomposition process or pre-reactions of the precursor(s). At temperatures above the temperature window the substrate surface is too hot to allow for adsorption of the deposition material. The relatively high bond enthalpies observed for Si-C, Si-S, Si-Se, Ge-C and Ge-S are expected to lead to higher activation energy requirements for decomposition to occur. Thus, the deposition temperature window is likely to be narrower for these materials.

Chalcogen/ group 14 element	Bond enthalpies (kJ mol ⁻¹) C-E	Bond enthalpies (kJ mol ⁻¹) Si-E	Bond enthalpies (kJ mol ⁻¹) Ge-E	Bond enthalpies (kJ mol ⁻¹) Sn-E
C	346	318	238	192
S	272 ^a	623	551 ± 25	464 ± 3.3
Se	234 ^a	548	489 ± 4	401.2 ± 5.9
Te	200 ^a	452 ± 8	456 ± 13	359.8

Table 5-1: Bond enthalpies for diatomic ME units, where M is C, Si, Ge or Sn and E is C, S, Se or Te. All values are stated for room temperature.²⁸ Data labelled ^a was obtained from separate literature sources.^{29,30}

5.4.2 Low Pressure Chemical Vapour Deposition Experiments using [SiⁿBu₃(TeⁿBu)]

LPCVD experiments produced deposits of different materials based on the temperature at the substrate, as highlighted in Figure 5-6. The material deposited at the lowest deposition temperature was elemental tellurium, as confirmed in Figures 5-7 and 5-8. Phase pure Si₂Te₃ was deposited adjacent to the tellurium deposition at a slightly increased deposition temperature and had typical coverages of *ca* 2 cm by 0.8 cm. One interesting feature of the deposition is the observation of the colour change of the Si₂Te₃ at temperature, immediately after deposition on removal from the furnace, versus after it has cooled. This colour change is from brown/ black to a much redder colour. This may be reflection of the silicon dumbbell orientation causing changes to the bandgap of the material, as discussed in the literature.^{11,14} At higher deposition temperatures the occurrence of Si becomes more common first as a minor impurity and then as the sole material deposited.

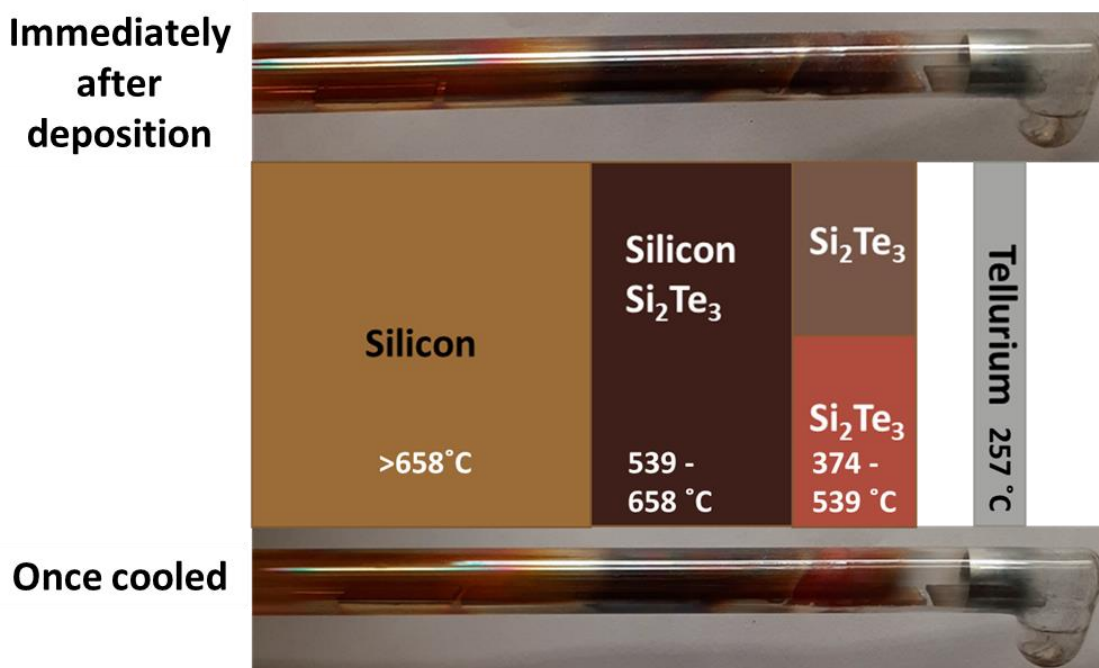


Figure 5-6: Typical appearance of the CVD tube after a LPCVD experiment using **[SiⁿBu₃(TeⁿBu)]** at a furnace temperature of 700 °C. Left to right (area of tube in the hottest region of the tube furnace to the bulb, which is external to the furnace during depositions) the deposited material highlighted by the coloured squares are elemental Te, Si₂Te₃, mixed Si and Si₂Te₃ and Si. Note the colour change observed from black/ brown to red on cooling.

The identification of these materials is highlighted in the Raman spectra and GIXRD patterns displayed in Figures 5-7 and 5-8. A more in depth investigation of the Si₂Te₃ deposition can be seen in Figures 5-9 to 5-12.

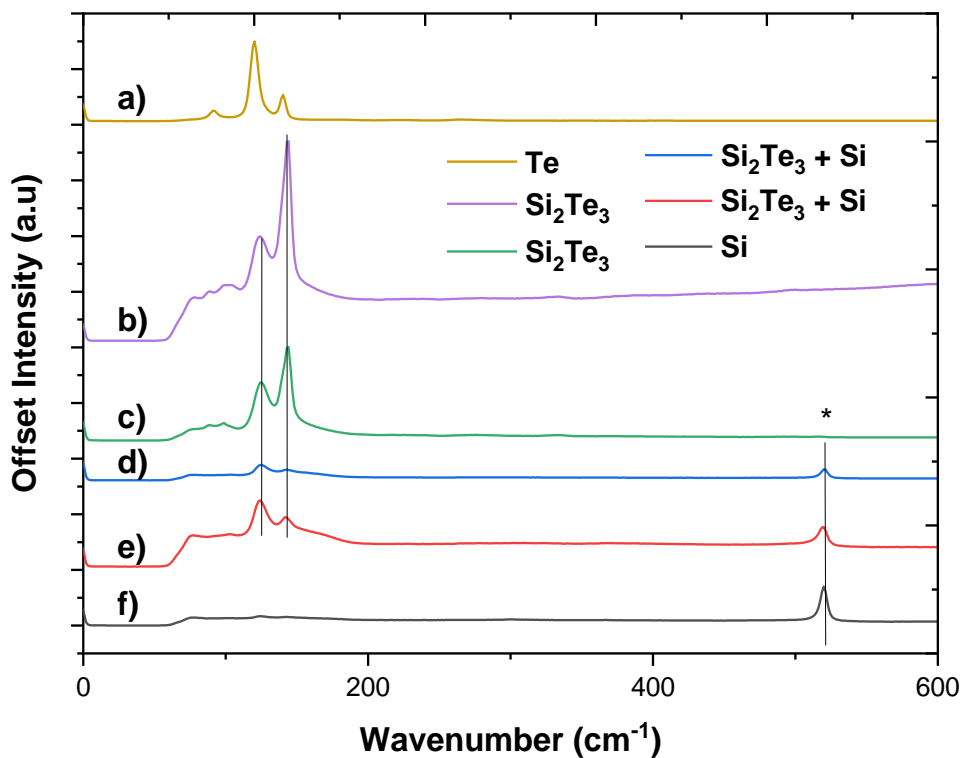


Figure 5-7: Raman spectra for different tiles in a single LPCVD experiment from $[\text{Si}^n\text{Bu}_3(\text{Te}^n\text{Bu})]$. Peak from silicon³¹ indicated with * and the stretching modes from Si_2Te_3 are highlighted also.¹⁹ Spectrum **a)** is that of the tile at the lowest deposition temperature and shows elemental Te.³² **b), c), d) and e)** all show some Si_2Te_3 . **d), e) and f)** have a stretching mode from Si.

The composition of the materials observed in Figure 5-5 were further confirmed using GIXRD, displayed in Figure 5-7. The lack of any peaks on the orange pattern indicates that there is no crystalline material on this substrate, Si can be observed in the Raman pattern for the same sample meaning that the Si on this tile must be amorphous.

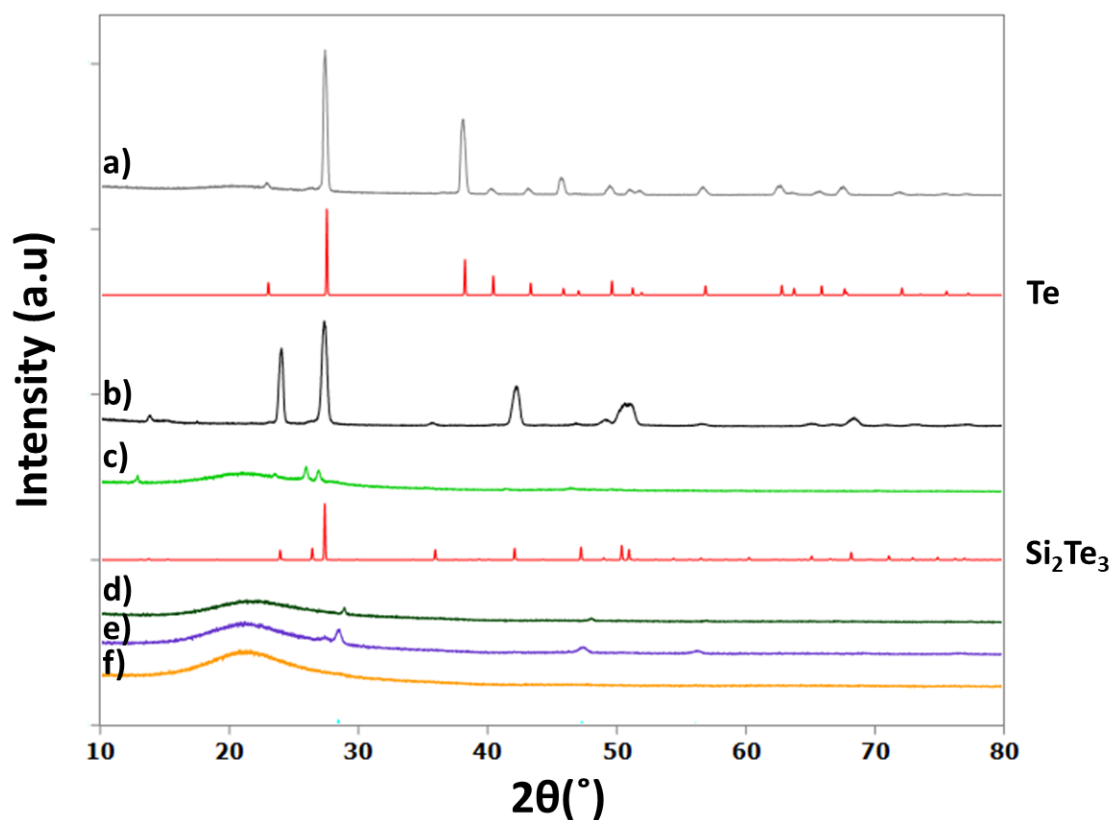


Figure 5-8: GIXRD patterns collected for individual substrates positioned at different deposition temperatures in the CVD tube shown in Figure 5-4. Literature bulk pattern of Si_2Te_3 ,¹³ bottom, and Te ,³³ top, are displayed in red. Peaks highlighted with * indicate peaks from Si .³⁴ The collected GIXRD patterns, **a)**, **b)**, **c)**, **d)**, **e)** and **f)**, are in deposition temperature order with the coolest temperature at the top, **a)**, and the hottest at the bottom, **f)**.

Depositions produced good quality films of Si_2Te_3 as confirmed by GIXRD, SEM with EDX and Raman spectroscopy. A GIXRD pattern can be seen in Figure 5-9, in black, matched to a literature bulk pattern, in red.¹³ The refined lattice parameters found are: 7.3526(11) Å, 7.3526(11) Å and 13.482(3) Å, in the space group 227: Fd-3m, which are in good agreement with the literature values: 7.430(5) Å, 7.430(5) Å and 13.482(7) Å.³⁴

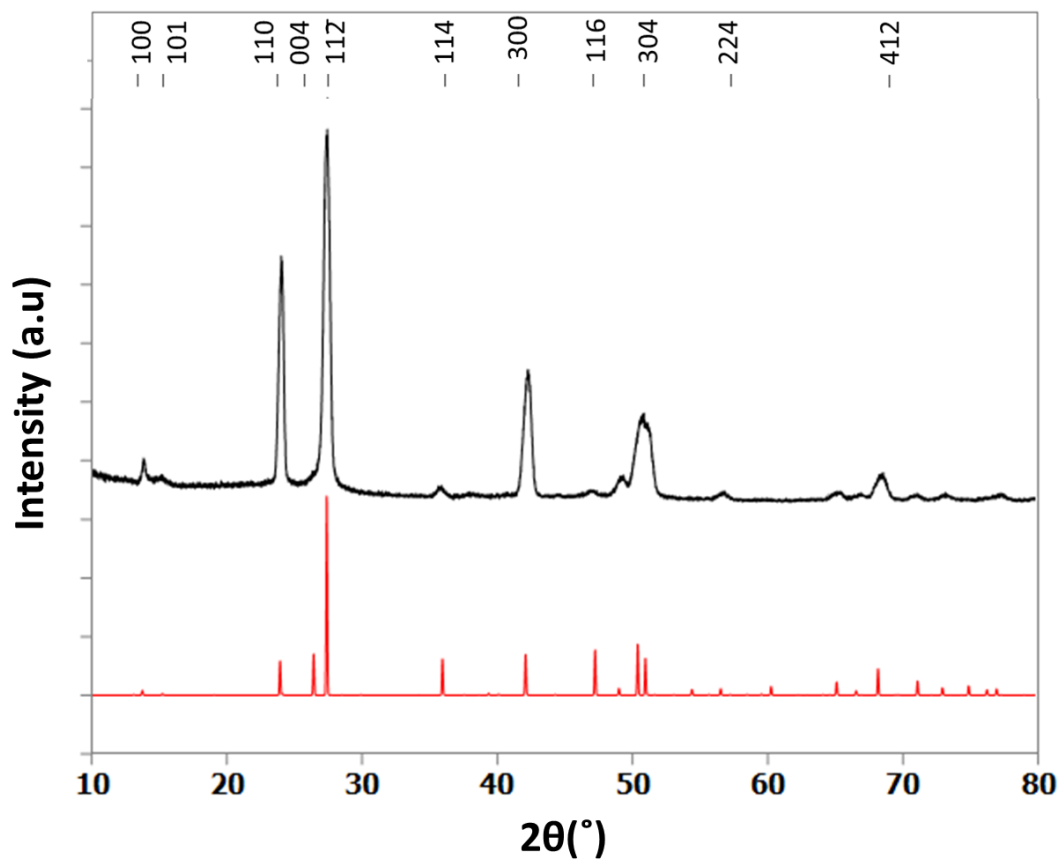


Figure 5-9: GIXRD pattern of Si_2Te_3 deposited from $[\text{Si}^n\text{Bu}_3(\text{Te}^n\text{Bu})]$ (black) and a literature bulk pattern (red).¹³

The SEM images showed uniform polycrystalline films. The SEM image, shown in Figure 5-10, does appear to indicate a textured film. This preferred orientation is also corroborated by the large enhancement of the 110 and 300 reflections in the GIXRD pattern.

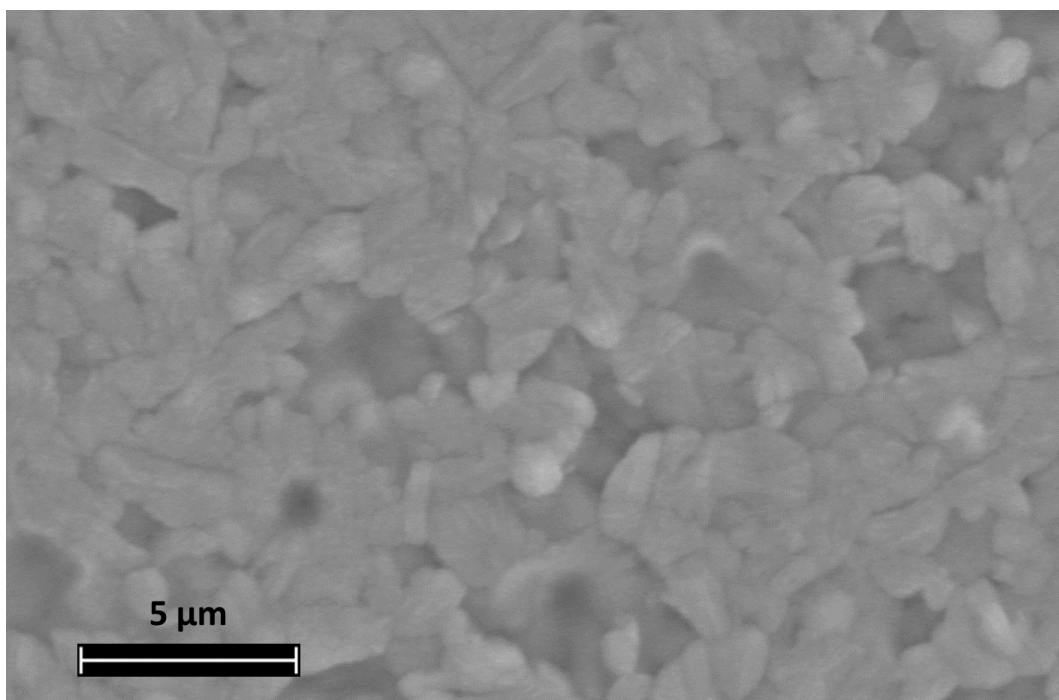


Figure 5-10: Top down SEM image of a Si_2Te_3 film deposited ($374\text{ }^\circ\text{C}/0.01\text{ mmHg}$) using $[\text{Si}^n\text{Bu}_3(\text{Te}^n\text{Bu})]$ onto a fused quartz substrate.

The EDX analysis, displayed in Figure 5-11, confirms that the only elements detected from the film deposited onto SiO_2 substrates, were Si, O and Te. Thus, no impurities could be detected in the Si_2Te_3 films. However, due to the SiO_2 substrate and the thin nature of the films the EDX analysis could not be used to quantify the material composition.

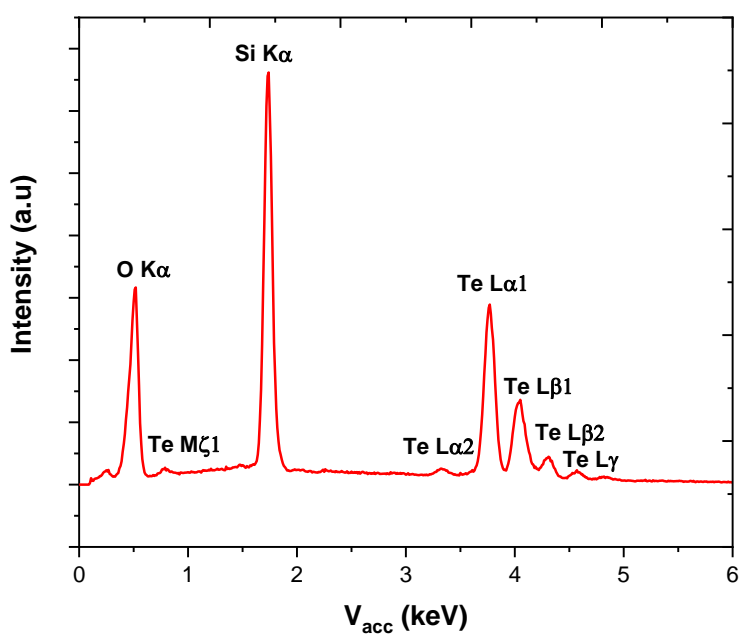


Figure 5-11: EDX spectrum for a deposition of Si_2Te_3 onto SiO_2 using $[\text{Si}^n\text{Bu}_3(\text{Te}^n\text{Bu})]$.

Chapter 5

The EDX analysis results confirm both Si and Te are present in the deposit, but do not allow for a reliable composition to be determined. Consideration of the atom% of O and attributing all of this to the substrate material, SiO₂, and therefore discounting the corresponding Si does not give the 2:3 ratio of remaining Si to Te for any of the depositions described. Since the characteristic X-rays attributed to O are very low energy, 0.53 keV, and Te exhibits X-ray emissions for M lines between 0.82 and 0.57 keV, the EDX analysis are unreliable.

As discussed in section **1.9.2.3**, the ideal method for analysing the composition of the Si₂Te₃ films would be XPS. This is due to the much smaller penetration depth of the technique. However, this was not possible at this time (due to clean-room access restrictions during COVID). Another option which would allow quantification of the film composition would be to use a substrate material which contained neither Si or Te, for example Al₂O₃, although this may also affect the deposition process.

The Raman spectra collected for the Si₂Te₃ films were in good agreement with that of the literature.^{5,19,35} An example of one such Raman spectrum can be seen in Figure 5-12. The ratio of the A_{1g} modes, at 128 and 145 cm⁻¹, has been linked to the film thickness by Song et. al. In their work, however, a different wavelength laser was used and thinner films were reported, around 8 nm.¹⁹ Despite this, the potential to investigate film thickness accurately using a non-destructive and rapid method like Raman spectroscopy is highly appealing.

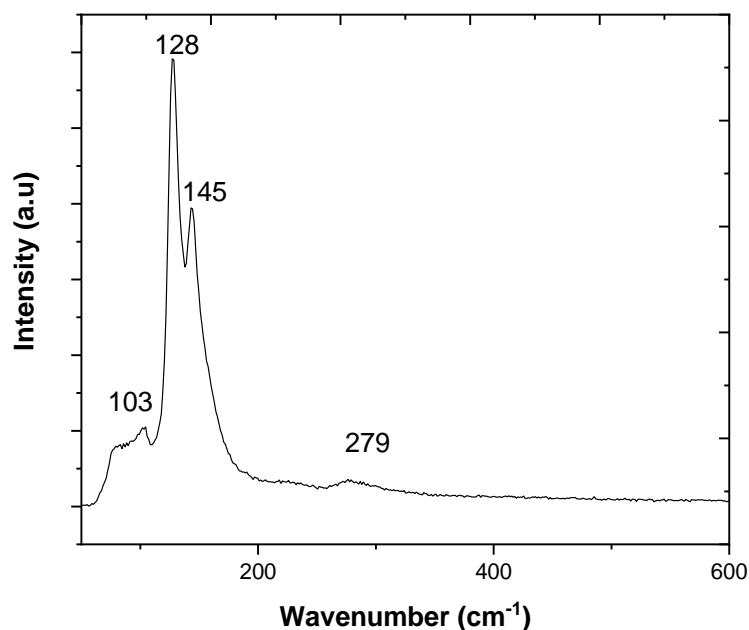


Figure 5-12: Raman spectrum of a film of Si_2Te_3 with the E_g modes, at 103 and 279 cm^{-1} , and A_{1g} modes, at 128 and 145 cm^{-1} .^{5,19,35} Note that care was taken to collect the Raman spectrum immediately after the depositions.

Due to the high resistivity of Si_2Te_3 , and limited access to equipment (due to COVID), evaluation of the electrical properties were only conducted at room temperature, the results can be seen in Table 5-2. The resistivity value obtained, using an assumed thickness of 2 μm , is in good agreement of that reported by Ziegler *et al*,³⁶ in their work emphasis was put on the importance of storing the samples in an inert atmosphere due to the hygroscopic nature of Si_2Te_3 . Additionally, the measured samples also identify the deposition as having n-type conductivity, which is unexpected for both Si_2Te_3 and elemental tellurium. However, due to the low charge carrier concentration these values may have a larger than expected error correlated to them as they are at the limit of the measurement capabilities of the Hall effect equipment.

Table 5-2: Electrical measurements obtained at room temperature using a 750 nA current for van der Pauw and 0.5 Tesla magnet for Hall effect measurements, describing sheet values as a thickness is yet to be obtained by cross sectional SEM. The resistivity values stated in parenthesis are obtained using an assumed thickness of 2 μm .

Si ₂ Te ₃ Sample	Sheet Resistivity ($\Omega \square$) (Resistivity ($\Omega \text{ cm}$))	Hall effect coefficient ($\text{m}^2 \text{ C}^{-1}$)	Charge carrier concentration (cm^{-2})	Charge carrier mobility ($\text{cm}^2 \text{ V}^{-1} \text{ s}^{-1}$)
Deposition 1 tile 1	8.189×10^5 (4.095×10^9)	-269	-2.318×10^{12} ($-1.159 \times 10^{16} \text{ cm}^{-3}$)	3.29
Deposition 2 tile 1	3.733×10^5 (1.867×10^9)	-58.6	-1.065×10^{13} ($-5.325 \times 10^{16} \text{ cm}^{-3}$)	1.57

5.5 Conclusions

The first single source precursor reported in the published literature, **[SiⁿBu₃(TeⁿBu)]**, for the deposition of Si₂Te₃ thin films has been successfully developed and characterised. These thin film deposits have also been successfully characterised using GIXRD, Raman and SEM (with EDX). An accurate analysis of the composition of the material is impossible at this time, but could be achieved by either using a different substrate material, such as alumina, or using XPS. A series of potential SSPs for the deposition of silicon sulfide and selenide have also been explored, although no successful depositions from these have been reported at this stage.

The electrical measurements performed describe Si₂Te₃, which had been exposed to air for 3 weeks, showed similar resistivity, at an assumed thickness of 2 μm , to that reported for Si₂Te₃ within the literature. The electrical results describe n-type Si₂Te₃ which is not typical and may be reflective of the high resistivity value being at the limit of the Hall effect equipment used.

5.6 References

- 1 J. W. Rau and C. R. Kannewurf, *J. Phys. Chem. Solids*, 1966, **27**, 1097.
- 2 N. Qamhieh and G. J. Adriaenssens, *J. Optoelectron. Adv. Mater.*, 2005, **7**, 1785.
- 3 M. Samanta, S. Roychowdhury, J. Ghatak, S. Perumal and K. Biswas, *Chem. Eur. J.*, 2017, **23**, 7438.

- 4 S. R. Popuri, M. Pollet, R. Decourt, F. D. Morrison, N. S. Bennett and J. W. G. Bos, *J. Mater. Chem. C*, 2016, **4**, 1685.
- 5 S. Keuleyan, M. Wang, F. R. Chung, J. Commons and K. J. Koski, *Nano Lett.*, 2015, **15**, 2285.
- 6 Q. Wang, R. Quhe, Z. Guan, L. Wu, J. Bi, P. Guan, M. Lei and P. Lu, *RSC Adv.*, 2018, **8**, 21280.
- 7 K. E. Petersen, U. Birkholz and D. Adler, *Phys. Rev. B*, 1973, **8**, 1453.
- 8 K. Wu, W. Sun, Y. Jiang, J. Chen, L. Li, C. Cao, S. Shi, X. Shen and J. Cui, *J. Appl. Phys.*, 2017, **122**, 075701.
- 9 M. Wang, G. Lahti, D. Williams and K. J. Koski, *ACS Nano*, 2018, **12**, 6163.
- 10 A. Rogalski, *Reports Prog. Phys.*, 2005, **68**, 2267.
- 11 S. Steinberg, R. P. Stoffel and R. Dronskowski, *Cryst. Growth Des.*, 2016, **16**, 6152.
- 12 K. Taketoshi and F. Andoh, *Jpn. J Appl. Phys.*, 1995, **34**, 3192.
- 13 K. Ploog, W. Stetter, A. Nowitzki and E. Schönherr, *Mat. Res. Bull.*, 1976, **11**, 1147.
- 14 X. Shen, Y. S. Puzyrev, C. Combs and S. T. Pantelides, *Appl. Phys. Lett.*, 2016, **109**, 113104.
- 15 R. Bhattarai and X. Shen, *Appl. Phys. Lett.*, 2020, **116**, 023101.
- 16 R. Juneja, T. Pandey and A. K. Singh, *Chem. Mater.*, 2017, **29**, 3723.
- 17 K. Wu and J. Cui, *J. Mater. Sci. Mater. Electron.*, 2018, **29**, 15643.
- 18 J. Chen, K. Wu, X. Shen, T. B. Hoang and J. Cui, *J. Appl. Phys.*, 2019, **125**, 024306.
- 19 X. Song, Y. Ke, X. Chen, J. Liu, Q. Hao, D. Wei and W. Zhang, *Nanoscale*, 2020, **12**, 11242.
- 20 M. Wang, G. Lahti, D. Williams and K. J. Koski, *ACS Nano*, 2018, **12**, 6163.
- 21 J. Peters and B. Krebs, *Acta Crystallogr. Sect. B Struct. Crystallogr. Cryst. Chem.*, 1982, **B38**, 1270.
- 22 C. T. Li, Y. L. Tsai and K. C. Ho, *ACS Appl. Mater. Interfaces*, 2016, **8**, 7037.
- 23 J. H. Yang, Y. Zhang, W. J. Yin, X. G. Gong, B. I. Yakobson and S. H. Wei, *Nano Lett.*, 2016, **16**, 1110.
- 24 B. Ul Haq, S. AlFaify, R. Ahmed, A. R. Chaudhry, A. Laref, F. K. Butt and K. Alam, *J. Alloys Compd.*, 2018, **769**, 413.

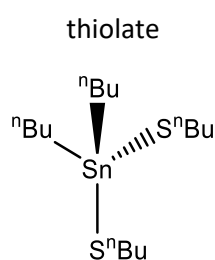
Chapter 5

- 25 C. Kamal, A. Chakrabarti and M. Ezawa, *Phys. Rev. B*, 2016, **93**, 125428.
- 26 S. Tan and B. Dai, *Int. J. Electrochem. Sci.*, 2018, **13**, 11787.
- 27 S. Karmakar, C. Chowdhury and A. Datta, *J. Phys. Chem. C*, 2016, **120**, 14522.
- 28 J. A. Kerr, *CRC Handbook of Chemistry and Physics 1999-2000 : A Ready-Reference Book of Chemical and Physical Data*, CRC Press, Florida, 81st edn., 2000.
- 29 C. E. Housecroft and A. G. Sharpe, *Inorganic Chemistry*, Pearson Education Ltd, Basel, 4th edn., 2012.
- 30 T. Chivers and R. S. Laitinen, *Chem. Soc. Rev.*, 2015, **44**, 1725.
- 31 I. De Wolf, *Spectrosc. Eur.*, 2003, **15**, 6.
- 32 N. Berchenko, R. Vitchev, M. Trzyna, R. Wojnarowska-Nowak, A. Szczerbakow, A. Badyła, J. Cebulski and T. Story, *Appl. Surf. Sci.*, 2018, **452**, 134.
- 33 P. Cherin and P. Unger, *Acta Crystallogr.*, 1967, **23**, 670.
- 34 K. C. Ross, J. A. Petrus and A. M. McDonald, *Powder Diffr.*, 2014, **29**, 337.
- 35 U. Zwick and K. H. Rieder, *Zeitschrift für Phys. B Condens. Matter*, 1976, **25**, 319.
- 36 K. Ziegler, H. -D. Junker and U. Birkholz, *Phys. Stat. Sol.*, 1976, **37**, K97.

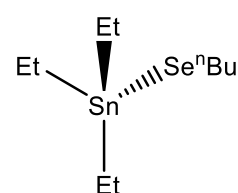
Chapter 6 Deposition of SnSe Thin Films Using a Commercial Picosun Instrument and LPCVD of Ternary Solid Solutions of the Form ME (M = Ge or Sn and E = S, Se or Te)

6.1 Precursors used

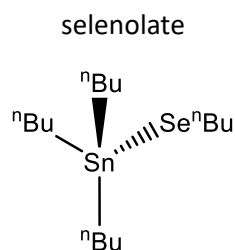
[SnⁿBu₂(SⁿBu)₂]: Di-n-butyltin bis-n-butyl



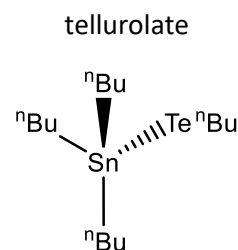
[SnEt₃(SeⁿBu)]: Triethyltin n-butyl selenolate



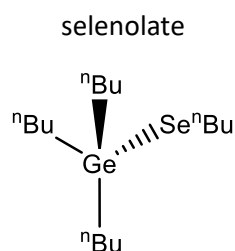
[SnⁿBu₃(SeⁿBu)]: Tri-n-butyltin n-butyl



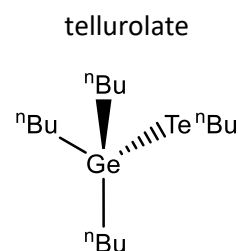
[SnⁿBu₃(TeⁿBu)]: Tri-n-butyltin n-butyl



[GeⁿBu₃(SeⁿBu)]: Tri-n-butylgermanium n-butyl



[GeⁿBu₃(TeⁿBu)]: Tri-n-butylgermanium n-butyl



6.2 Introduction

As discussed in section 1.4, there are several strategies that can be utilised to improve the performance of thermoelectric materials. Of these, the two that translate best to the process defined in this work are the formation of solid solutions and, if greater control of film thickness could be gained, the formation of nanolaminates and superlattices. This is because these methods could be applied by simply combining two of the precursors either into a mixed precursor solution or by sequential deposition of a layer of one material followed by the other.

With the intention of adapting the LPCVD process towards a full wafer scale process, the Picosun R-200 advanced rig, displayed in Figure 6-1a, at the site of Deregallera, was selected as an opportunity to assess if the process could be translated successfully. Preliminary experiments proved very promising but further experiments were halted in early 2020 due to COVID travel restrictions. A prerequisite for the use of chemicals as precursors on the ALD rig is a suitable vapour pressure. Typically, the vapour pressure needs to be higher than 100 Pa to be appropriate.¹ A discussion of how the precursor vapour pressures were assessed and a comparison of these values can be found in section 2.3.2. The adaptation of precursors to the commercial equipment could not only allow for depositions onto whole wafers, but also for the rapid deposition of up to 6 different precursors sequentially. Greater control over both the substrate temperature and the rate of precursor delivery offer the potential for much thinner and more uniform films. Once the deposition coverage can be performed uniformly across the substrate, alteration of the number of cycles and the amount of precursor delivered per cycle can be used to control the thickness of depositions, as has been shown for other systems previously.² If it is possible to control the thickness down to only a few nanometres then it would be possible to deposit ordered multi-layered structures, known as superlattices or nanolaminates depending on the layer thicknesses, and metamaterials. Superlattices have been shown to greatly increase the performance of thermoelectric materials through the quantum confinement of phonons, as discussed in more detail in section 1.4.3. A more detailed comparison of the LPCVD procedure to the enhanced CVD procedure can be found in section 2.1.3.

6.2.1 Thermoelectric performance enhancement using solid solutions

In order to explore ternary materials, and more specifically solid solutions, mixtures of two precursors, with one of the heteroatoms in common sharing a site in the crystal lattice, can be used in depositions. This means that some control over the composition of the deposited material can be achieved by altering the ratio of the precursors within the mixture. An overview of how the adoption of solid solutions enhances the thermoelectric performance of a material can be found

in section 1.4.4. A discussion of how the vapour pressures of mixtures differ between the individual precursors prepared in this work can also be found in section 2.3.2.

6.2.1.1 Techniques for identifying of solid solutions

For compositional studies, techniques including EDX, WDX and XPS, for example, can be used to detect specific elements within a sample and to quantify their ratios. However, these techniques do not identify whether a film is formed of a single phase. This is best established through the consideration of peak positions in the XRD and by careful analysis of Raman spectra. As described by Vegard's law,³ the lattice parameter of a solid solution comprised of two components is approximately a weighted mean of the two binary materials. This means that a linear relationship should be observed for a graph of lattice parameter vs. material composition if a well-distributed solid solution is present. One simple way of evaluating this is to compare the unit cell volumes/ formula unit (Z). This gives the average volume of the formula units allowing for a simple comparison between materials, even those in different crystal systems.⁴ Similarly in the Raman spectra of solid solutions, a shift in the peak position(s) relative the either of the individual components is expected when a solid solution has been successfully deposited.^{5,6}

6.2.2 Enhanced parameter control and growth

As outlined in section 1.6, material growth can be controlled by consideration of several different factors. As discussed there, these include: choice of precursor(s), temperature, substrate, pressure and the number of nucleation sites. Moving from a simple LPCVD procedure, using a tube furnace containing a quartz tube attached to a vacuum line, to the ALD reactor at Deregallera affords a greater level of control over temperature across the whole wafer substrate, pressure of the deposition and precursor delivery rate, as well as offering a means of scaling up the deposition to full wafer size.

6.3 Experimental

6.3.1 Wafer scale CVD and PECVD of SnSe using a commercial Picosun R-200 Advanced ALD reactor

Precursor bottles containing between 10 and 20 g of chosen precursor were attached to the line which was flushed prior to use. The transportation of the precursor was confirmed by monitoring the pressure within the lines when the bottles were opened, when the precursors have sufficient vapour pressure a spike can be seen. Silicon wafers (15.2 or 20.3 cm diameter), acquired from IDB Technologies who are now part of Inesto, were loaded into the reaction chamber through the

loading port at low pressure. A reaction sequence, containing sequential pulses of the selected precursor followed by a delay of up to 10 s and then either evacuation of the chamber or a pulse of hydrogen plasma to assist decomposition, followed by evacuation of the chamber. The evacuation is essential to remove the volatile by products produced during the deposition process. The substrate temperatures selected were informed from the deposition temperatures observed in LPCVD experiments, starting at a substrate temperature slightly below these temperature at 300 °C and subsequently increasing based off of experimental observations. These steps were then repeated for a predetermined number of cycles, 100, 200 or, on one occasion, 2000. The precursor bottles were held at an elevated temperature throughout the experiments, typically 200 °C. A flow rate of 50 sccm was used to deliver the precursor through the lines to the reaction chamber. The experiments took roughly 2 to 3 hours for shorter experiments of 100 to 200 cycles and around 14 hours for the 2000 cycle experiment, at which point the wafer could be removed via the loading port before the deposition was confirmed by ellipsometry at Deregallera. After transportation back to Southampton the deposits could be characterised further via GIXRD and Raman spectroscopy.

The deposits produced in these experiments were grey films of SnSe at the edge of the wafer nearest the respective precursor inlet to the chamber. These depositions proved to be continuous with coverages of about 10 cm by 5 cm and 6 cm by 1 cm, for the deposition from $[\text{Sn}^n\text{Bu}_3(\text{Se}^n\text{Bu})]$ at 300 °C and $[\text{SnEt}_3(\text{Se}^n\text{Bu})]$ at 500 °C, respectively.

6.3.2 LPCVD growth of ternary solid solutions using combined precursors

An analogous LPCVD procedure to that used in section 3.3.1 was employed. However, the mixed precursors tend to lead to increased vapour pressure, as described in section 2.3.2. This necessitates either a slightly lower furnace temperature than that used in the binary materials, or for the precursor bulb to be positioned further away from the hot zone during the deposition process, to reduce mass transport effects. The molar ratio of 1:9 was selected as a starting point for each of the mixtures. This was selected as a good starting ratio as previous materials reported have shown ratios of between 1:100 and 2:10 have displayed some enhanced thermoelectric materials, so exploring a SSP combination in this range allows for later optimisation.⁷⁻¹⁰

6.4 Results and discussion

In order for a precursor to be suitable for use in the ALD rig its vapour pressure must be sufficiently high. As SnSe is of particular interest for thermoelectrics and the temperature window for thin film deposition is typically widest for the selenolates in the work discussed in this thesis,

the precursors $[\text{Sn}^n\text{Bu}_3(\text{Se}^n\text{Bu})]$ and $[\text{SnEt}_3(\text{Se}^n\text{Bu})]$ were assessed. For a more detailed description of the characterisation and assessment of these precursors see **Chapter 2**.

6.4.1 Wafer scale chemical vapour deposition using a Picosun R-200 Advanced ALD system

The system adopted for use in the wafer scale depositions is displayed in Figure 6-1a. The system has detachable precursor bubblers, displayed in Figure 6-1b and c, which can be heated to between 40-200 °C and 40- 260 °C, respectively. The system consists of precursor source bottles connected to inlet lines which have carrier gas flow. These lines are connected to the reaction chamber either through a detachable precursor shower head, designed to give an even distribution of the precursor over the substrate, or, if the showerhead has been removed, directly from the line into the chamber. The reaction chamber is maintained at a low pressure, 0.5 HPa. The reaction chamber temperature is maintained evenly across the substrate allowing for good control and uniformity of the deposition.

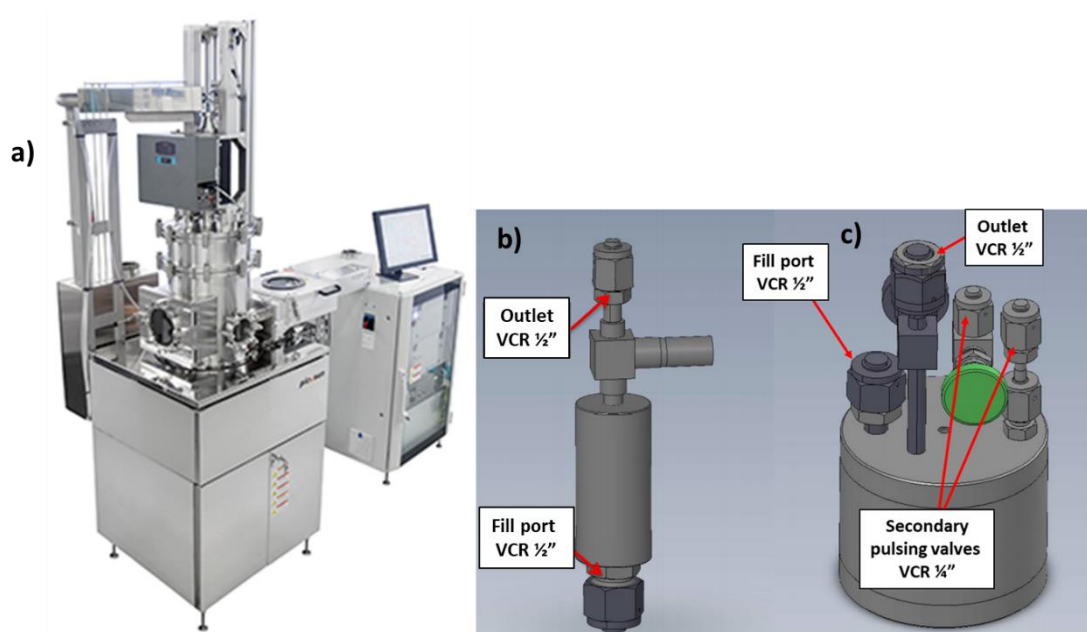


Figure 6-1: a) Image of a Picosun R-200 Advanced ALD system. Included is a separate vacuum wafer loading chamber adjacent to the control screen.¹¹ b) Illustration showing a Picohot 200 bubbler with a 40 mL capacity and c) a Picohot 300 bubbler with a 400 mL capacity.

Deposition using the enhanced CVD process involved larger scale synthesis of precursors, of between 10-20 g, to fill the precursor bottles, Picohot 200 and Picohot 300 precursor source bubblers, that attach to the inlet lines. The initial deposition attempts were performed using $[\text{Sn}^n\text{Bu}_3(\text{Se}^n\text{Bu})]$ at a reaction chamber temperature of 300 °C, this temperature was selected initially to see if lower temperatures could be used to deposit SnSe (typical deposition temperature using $[\text{Sn}^n\text{Bu}_3(\text{Se}^n\text{Bu})]$ is 352 – 431 °C in the previous LPCVD experiments). These

earlier experiments were 200 cycles long. This proved unsuccessful initially, due to the rather low vapour pressure of the precursor not allowing for sufficient precursor delivery to occur. This led to decomposition of the precursor inside the precursor showerhead only. This issue was partially resolved by removing the inlet shower head, which is used to distribute the precursor more evenly and cause a more even substrate coverage, as well as pulsing hydrogen plasma after every pulse of **[SnⁿBu₃(SeⁿBu)]** to assist in the precursor decomposition. The precursor showerhead cannot be used in experiments using plasma as this leads to the plasma collapsing on contact with the metal showerhead. The use of the hydrogen plasma in these depositions makes the process a plasma enhanced CVD (PECVD) one. After only 200 cycles, ellipsometry measurements indicated that some deposition had occurred. Following this observation, an experiment was conducted using 2000 cycles of the plasma and precursor, the results of this can be seen in Figure 6-2.

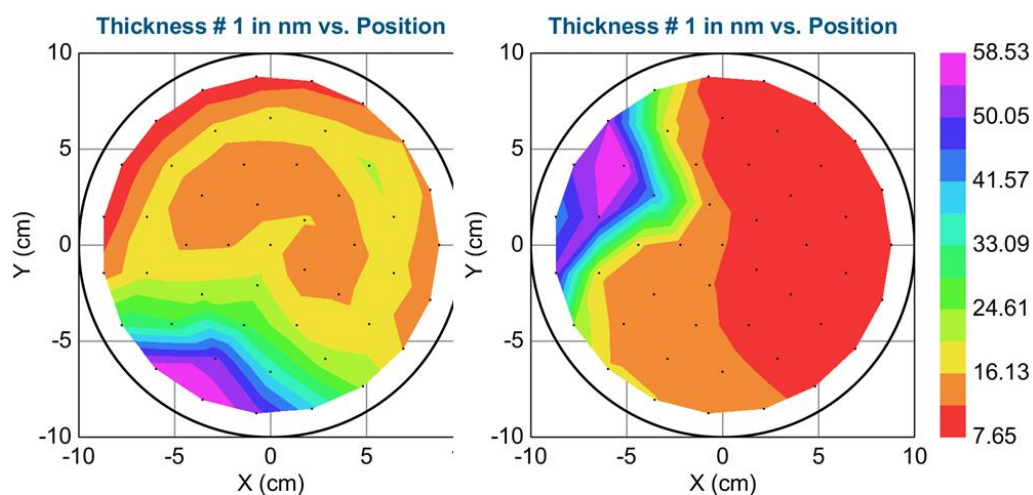


Figure 6-2: Ellipsometry of the silicon wafer after 100 cycles (left) and 2000 cycles (right) and a photograph of the wafer after the 2000 cycle experiment with deposition of material visible on the top left of the wafer. Both depositions used $[\text{Sn}^n\text{Bu}_3(\text{Se}^n\text{Bu})]$ with a reaction chamber temperature of 300 °C, precursor bubbler temperature of 200 °C and hydrogen plasma to assist in the decomposition of $[\text{Sn}^n\text{Bu}_3(\text{Se}^n\text{Bu})]$.

The material that was deposited using $[\text{Sn}^n\text{Bu}_3(\text{Se}^n\text{Bu})]$ was confirmed to be SnSe by Raman spectroscopy and GIXRD, as shown in Figure 6-3c. The refined lattice parameters for the XRD pattern are: $a = 11.614(4)$, $b = 4.1857(12)$ and $c = 4.4678(19)$ Å, which compare well with the literature values of 11.49417(12), 4.15096 (5) and 4.44175 (7) Å.¹² The sharp features observed in the GIXRD pattern in Figure 6-3c are not attributable to the Si substrate. One possible cause for these features could be the deposition of some very large highly orientated crystallites, this could occur due to an initially high barrier to nucleation which would mean fewer nucleation sites and thus much larger crystallites. The sharp features correlate with the 201, 210, 111, 311, 102, 220 and 221 peaks of SnSe. Some evidence for the potentially high barrier to nucleation is the lattice

mismatch between SnSe and Si, which crystalizes in the diamond structure with lattice parameters of : 5.4315(2) Å.¹³

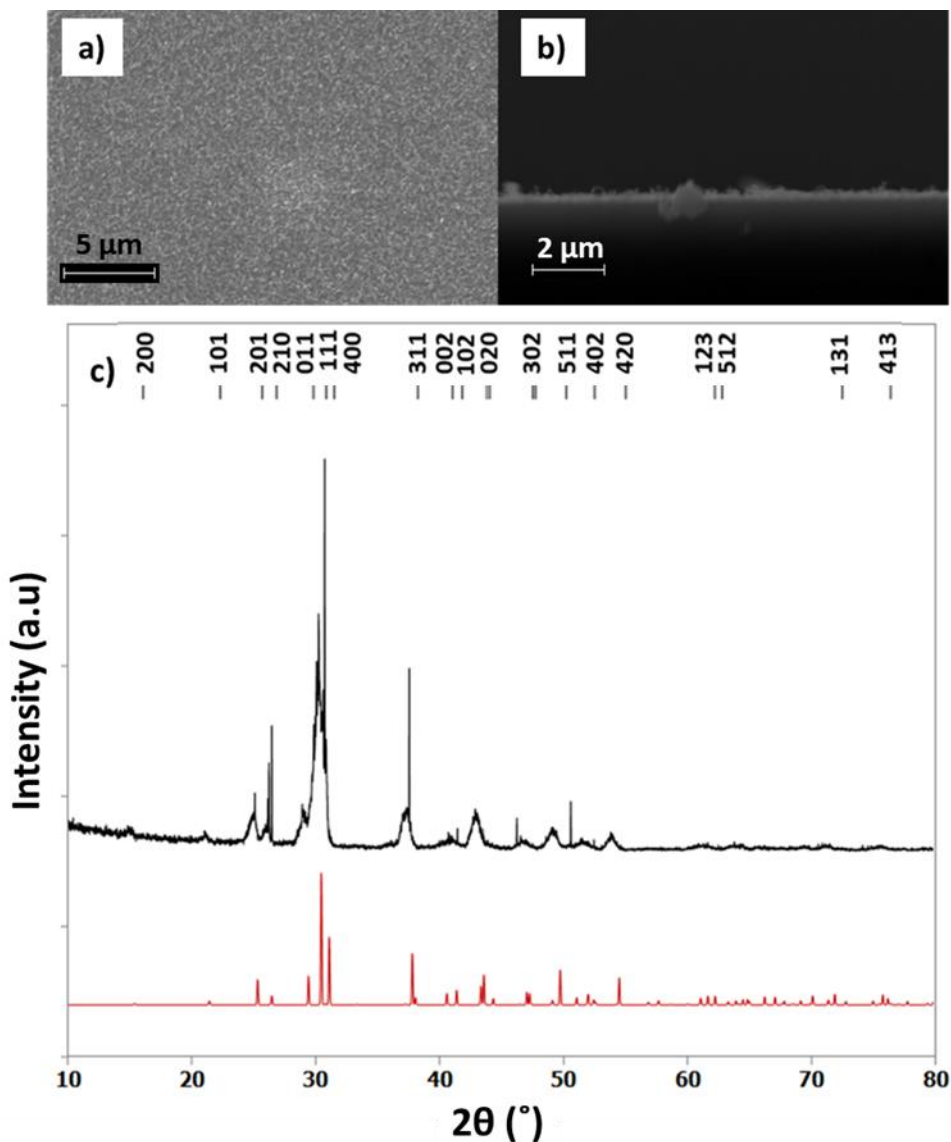


Figure 6-3: Top down and cross-sectional SEM images of a SnSe deposit grown from **[SnⁿBu₃(SeⁿBu)]** using the wafer scale CVD procedure and showing the film to be *ca.* 200 nm thick. GIXRD pattern for the same deposition, in black, and an XRD pattern from bulk SnSe.¹²

As only small amounts of material could be deposited and quite slowly using this method, a precursor with a higher vapour pressure was selected to improve the process. Thus, subsequent depositions were performed using **[SnEt₃(SeⁿBu)]**. As discussed in section 2.3.2, **[SnEt₃(SeⁿBu)]** has a vapour pressure (1647.64 Pa), more than 8 times higher than that of **[SnⁿBu₃(SeⁿBu)]** (196.29 Pa), at 125 °C.

Experiments using $[\text{SnEt}_3(\text{Se}^n\text{Bu})]$ did not require the use of a hydrogen plasma, as had been the case for the successful deposition using $[\text{Sn}^n\text{Bu}_3(\text{Se}^n\text{Bu})]$. However, even without the H_2 plasma to aid the decomposition of the precursor, the deposition of a dull grey film could be observed visibly on the wafer after just 100 cycles. Attempts to deposit material without the need for the plasma are an important step for the reactor set up used here as this would allow for the use of the showerhead inlet or some other adapted precursor inlet. This could allow for a much more even distribution of the precursor and thus lead to uniform depositions being possible. However, due to the travel restriction in place no experiments were possible to explore this. This observation in the deposition using $[\text{Et}_3\text{Sn}(\text{Se}^n\text{Bu})]$ is likely due to its higher vapour pressure allowing for a greater mass transport effect enabling the more precursor to enter the reaction chamber per pulse.

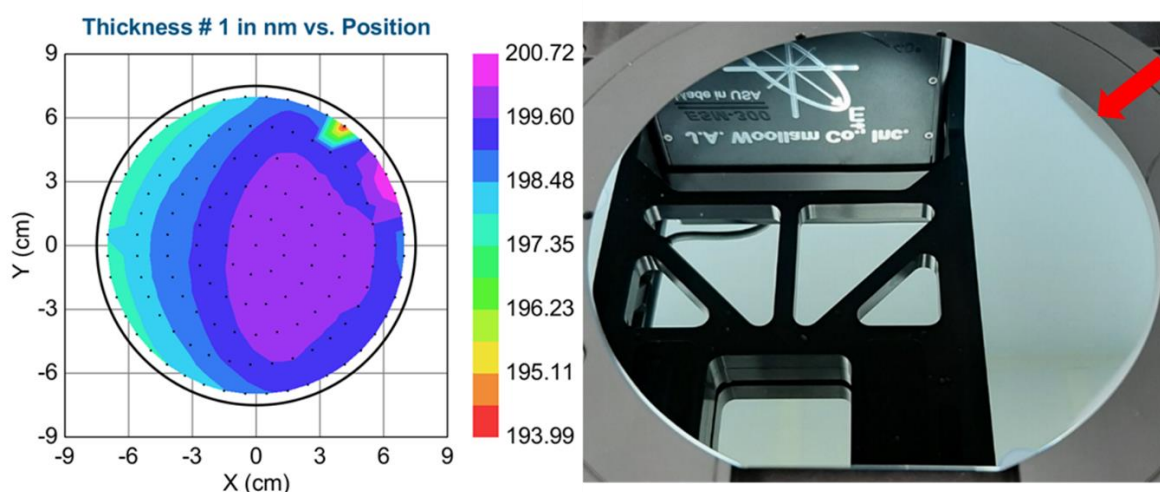


Figure 6-4: Ellipsometry thickness map showing a thicker region on the right hand side of the wafer and a photograph showing the wafer with some thicker deposit along the same edge. Note the ellipsometry measurement does not analyse within 1 cm of the edge and so the thickest part of the deposition is missed. The red arrow indicates the region characterised.

The deposited material was determined to be SnSe using Raman spectroscopy, GIXRD and SEM with EDX. The GIXRD pattern, displayed in Figure 6-5c, is in good agreement with the literature pattern and the refined lattice parameters: 11.518(3), 4.1705(13) and 4.4020(18) Å.

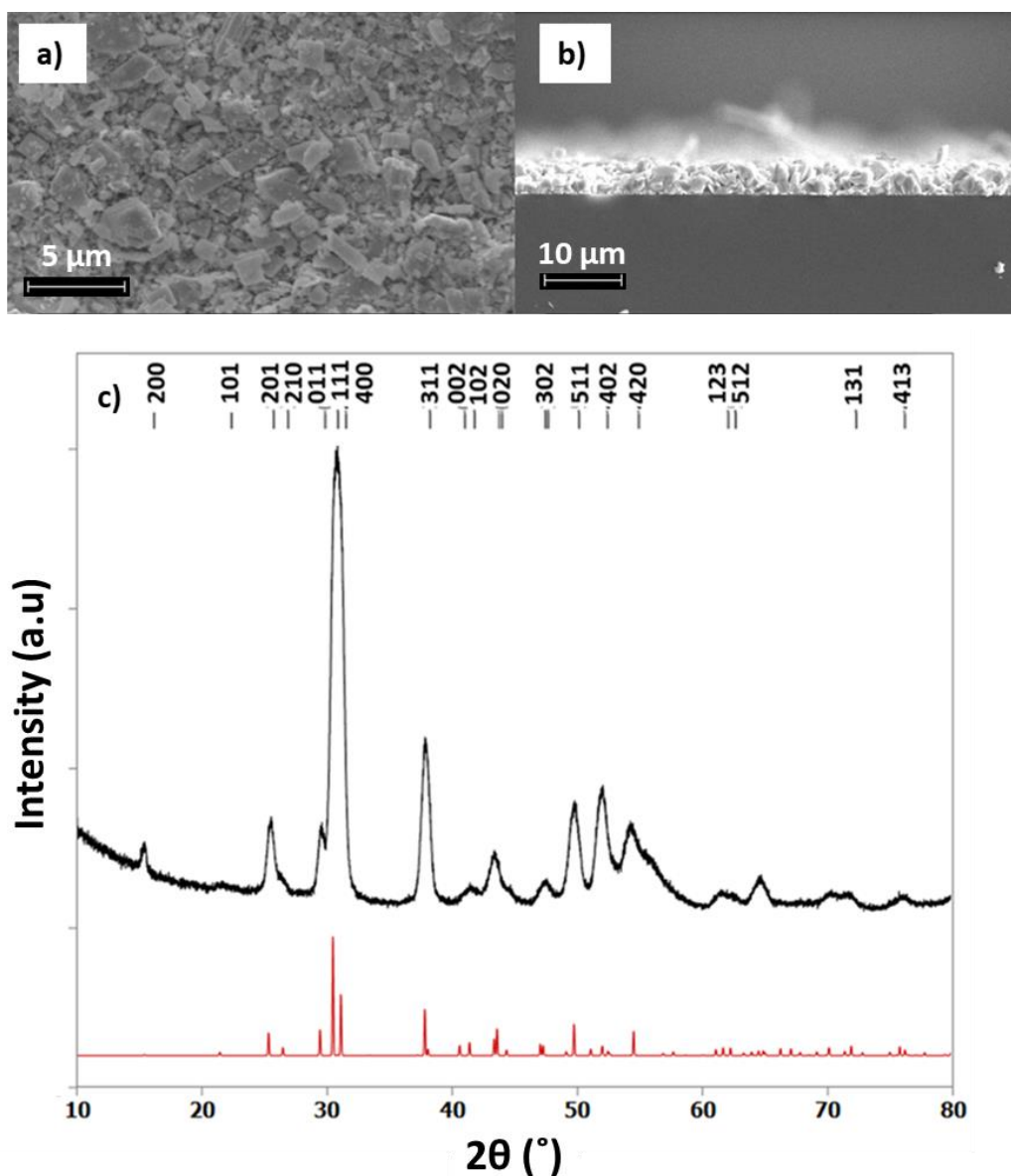


Figure 6-5: a) Top down and b) cross-sectional SEM images of a thin film deposited from $[\text{SnEt}_3(\text{Se}^n\text{Bu})]$ using the enhanced CVD procedure showing the film to be around 5 μm thick, an area not observed by the ellipsometry measurement. c) GIXRD pattern for the same deposition, in black, and a literature bulk pattern of SnSe.¹²

The EDX values displayed in Table 6-1 further show the difference in thickness of the two deposits as the major signal in the deposition from $[\text{Sn}^n\text{Bu}_3(\text{Se}^n\text{Bu})]$ with hydrogen plasma is from the silicon substrate. The two deposited materials show stoichiometric SnSe. However, the quality of the materials is not equivalent. The EDX analysis also indicates that there is a large quantity of C in both deposits, but particularly that deposited from $[\text{Sn}^n\text{Bu}_3(\text{Se}^n\text{Bu})]$. This is very likely exaggerated by the overlap of minor characteristic X-rays from both Sn with C. However, this presence of carbon could be a result of the lower evacuation of the volatile by-products produced in the decomposition compared to the LPCVD procedure, which is under vacuum throughout the experiment, rather than held at pressure and pulsed between precursor and vacuum exposure.

This slower evacuation may allow for the further decomposition of the volatile carbon containing species into carbon particulates. For this reason, further analysis of the carbon content is required to determine if the reported values are genuine. This could be performed using WDS, XPS or microanalysis. However, due to building restrictions caused by COVID regulations this was not possible at this time. If the C contamination proves genuine then attempts to minimise this could be factored into the deposition process, for example by allowing longer evacuation pulses or also introducing a hydrogen plasma when using $[\text{SnEt}_3(\text{Se}^n\text{Bu})]$. The EDX spectra in question can be seen in Figure 6-6a and b with quantitative analysis data displayed in Table 6-1.

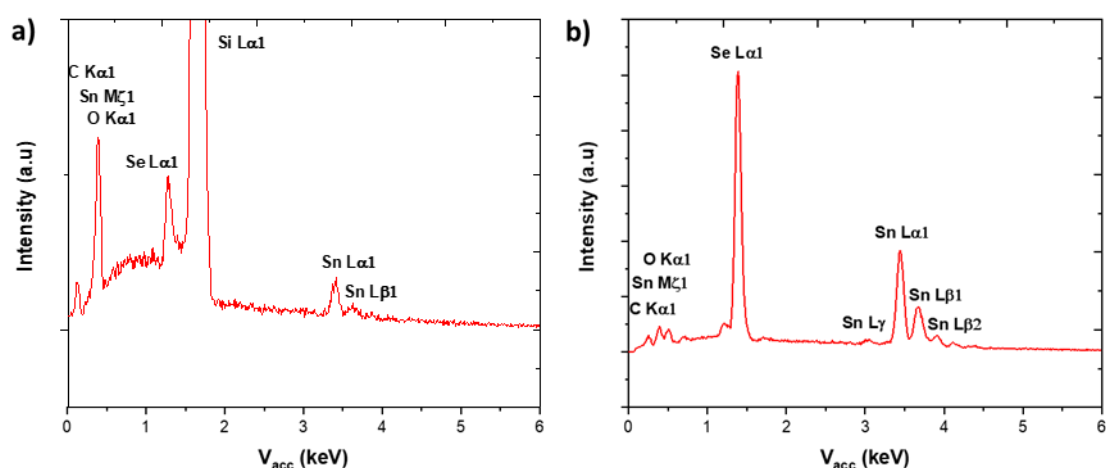


Figure 6-6: EDX spectra for SnSe depositions onto silicon wafer using the enhanced CVD approach, using a) $[\text{Sn}^n\text{Bu}_3(\text{Se}^n\text{Bu})]$ with a hydrogen plasma and b) $[\text{SnEt}_3(\text{Se}^n\text{Bu})]$, respectively.

Precursor used	Approximate film thickness (nm)	%C	%O	%Si	%Se	%Sn
$[\text{Sn}^n\text{Bu}_3(\text{Se}^n\text{Bu})]$ with hydrogen plasma	~200	14.2	6.5	77.7	0.5	1.1
$[\text{SnEt}_3(\text{Se}^n\text{Bu})]$	~5000	23.2	-	-	37.1	39.7

Table 6-1: Atom percent measured using EDX for the deposited SnSe onto silicon wafer.

The Raman spectrum of the deposit obtained from $[\text{Sn}^n\text{Bu}_3(\text{Se}^n\text{Bu})]$ using an incident laser power of 2.5 mW, shown in Figure 6-7a, shows the presence of SnSe, SnO_2 , at 304 cm^{-1} and features due to the silicon substrate, at 521 cm^{-1} .¹⁴ The Raman spectrum confirms that the primary deposited material is SnSe, however, in this case some impurities are also evident. The Raman spectra collected for the deposit from both precursors confirm the presence of SnSe.¹⁵ However, using $[\text{SnEt}_3(\text{Se}^n\text{Bu})]$ produces a film formed of SnSe only. In the case of the deposition made using

[SnⁿBu₃(SeⁿBu)], there is substantial evidence of underlying silicon from the substrate, due to the thin nature of this deposit, and a tin oxide layer. The SnO₂ observed for this deposition is likely a result of exposure to air in the transportation and storage of the wafer.

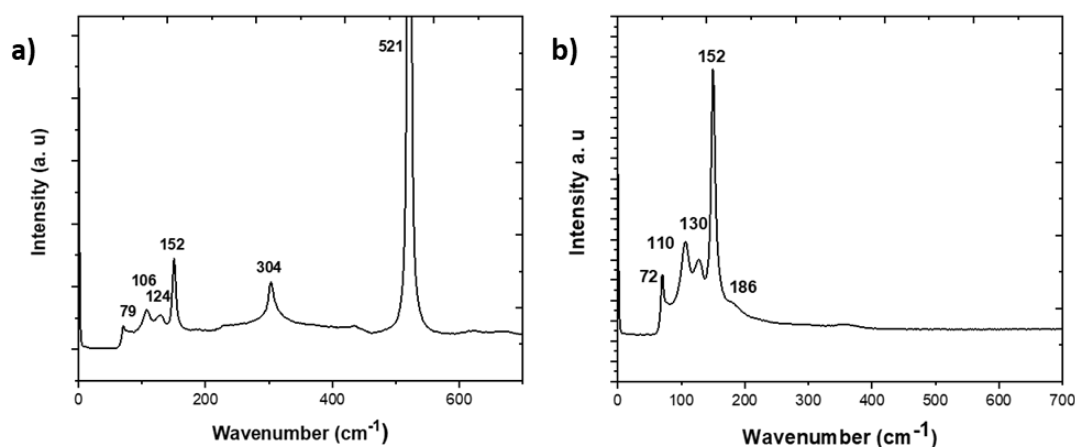


Figure 6-7: Raman spectra for an enhanced CVD film deposited from a) **[SnⁿBu₃(SeⁿBu)]** and b) **[SnEt₃(SeⁿBu)]**.

The successful depositions described here demonstrate the viability for use of further precursors within the SSP family described in Chapter 2, most likely incorporating ethyl substituents to achieve a suitable vapour pressure. The deposition process requires further optimisation, but shows very good potential for the versatility of the SSPs. The utilisation of the ethyl substituted precursor, **[SnEt₃(SeⁿBu)]**, to enhance the volatility significantly, demonstrates the simple manner with which the precursors can be adapted to use in different systems. In order to achieve greater and more even coverages several parameters could be exploited. For example, varying the precursor pulse and purge times, the substrate temperature, the carrier gas rates, the substrate material and, as **[SnEt₃(SeⁿBu)]** was successfully deposited without the need for the hydrogen plasma, different inlet configurations (e.g. shower head inlet). Unfortunately, it was not possible to carry out these experiments during this research project due to the travel restrictions. However, the work described here provides a very promising basis for the large scale deposition of uniform coatings and, if the thickness can be controlled carefully, also the deposition of exciting multi-layered metamaterials.

6.4.2 Towards the deposition of ternary group 14 chalcogenide thin films using mixed precursor systems

In order to explore the thermoelectric performance of solid solutions comprised of different group 14 chalcogenide materials, depositions using specific mixtures of precursors to form ternary

materials were carried out. Typically, the precursors should have some overlap in their deposition temperature regions.

Investigation into mixed ternary systems is of great interest for thermoelectric materials and semiconductor materials for electronic applications in general, as they enable a degree of control over the thermal and electronic properties of the deposits. Further details on why solid solutions are of interest for thermoelectric applications can be found in section **1.3.4**. The combinations selected here have been chosen for their increase in the sustainability of the materials (by reducing dependency on low abundant elements, especially Te and Ge) and/or to increase the electronic transport properties or the Seebeck coefficient of the films compared to their binary counterparts.

All depositions towards ternary materials were performed using the LPCVD procedure described previously. None have been explored using the Picosun R-200 Advanced ALD system at this time. Other ternary systems, besides those described below, were explored, but the XRD patterns obtained indicated multiple phases and so these were not investigated further.

Many examples of mixed phase systems where enhanced performances have been obtained have been reported in the literature, for example when nanoprecipitates are formed.¹⁶⁻¹⁹ However, as these improvements mostly focus on reducing the thermal conductivity,²⁰ which is not investigated in this work, these were of less immediate interest.

The ratio of 1:9 for the combination of different precursors was selected as a suitable starting point to investigate the potential for depositing solid solutions. This ratio was selected as it is closely tied to the composition found in many literature examples of solid solutions with enhanced performances compared to their binary components.^{7-10,21,22} This ratio does not reflect a certainty to the composition of the final deposited material but is selected a starting point to gauge future ratios likely to deposit solid solutions with compositions of interest.

6.4.2.1 Attempted growth of a germanium selenide telluride ternary thin film using LPCVD

To explore ternary $\text{GeSe}_{1-x}\text{Te}_x$ systems a 1 to 9 ratio mixture of **[GeⁿBu₃(TeⁿBu)]** and **[GeⁿBu₃(SeⁿBu)]** was used for all deposition attempts, typically using around 15-40 mg of the precursor mixture. The Se incorporated into the Te sites is expected to decrease the crystal symmetry, which has been shown to decrease the thermal conductivity - as discussed in Section **1.2.3.4**. GIXRD analysis was used to establish the nature of the crystalline deposits, and particularly to determine whether the deposited films were comprised of a mixture of the two individual phases (GeTe and GeSe) or a true solid solution containing the desired elements evenly distributed through a single phase. EDX analysis was used to confirm the presence of the three

elements expected and to determine the resulting ratio. As can be seen in Figure 6-8 below, the EDX analysis showed only Ge, Se and Te to be present, with Te being the minor constituent, as expected.

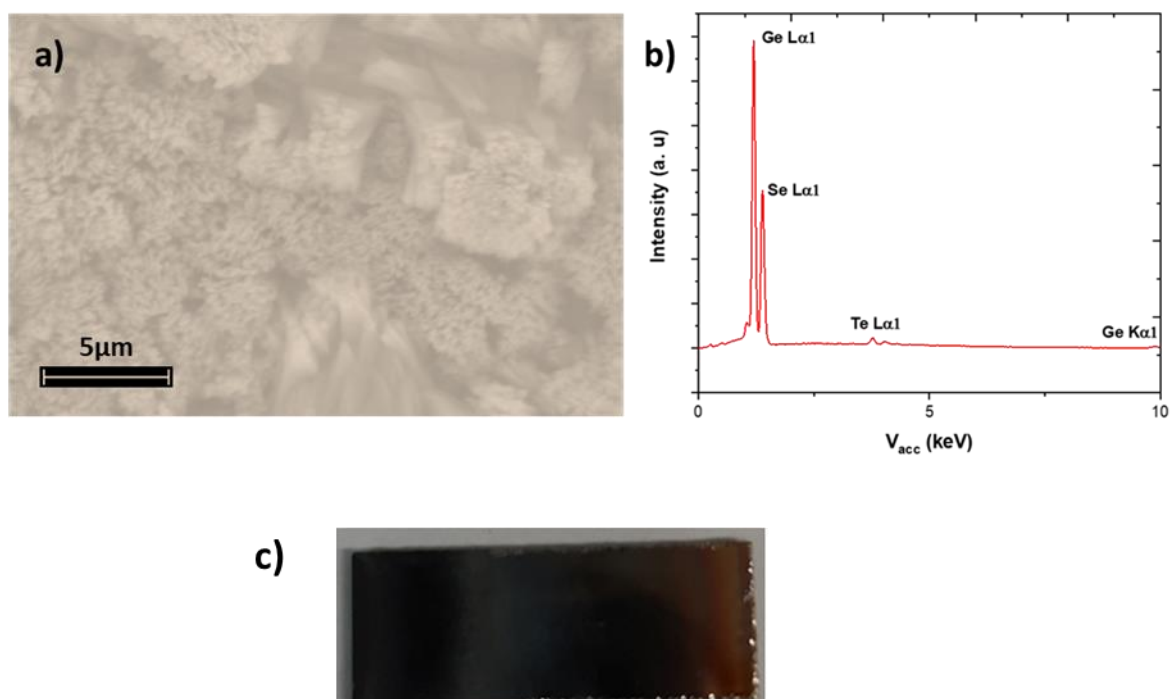


Figure 6-8: **a)** Top down SEM image of ternary GeSe_{1-x}Te_x deposition, **b)** the corresponding EDX spectrum and **c)** an image of the tile.

Sample	%C	%O	%Ge	%Se	%Te
GeSe _{1-x} Te _x deposit	12.4	1.3	44.9	38.8	2.6

Table 6-2: EDX analysis of a sample determined to be a solid solution of GeSe_{1-x}Te_x by GIXRD.

The GIXRD pattern from this film displayed in Figure 6-9, shows that the pattern strongly resembles that of GeSe, with no peaks that could be attributed to GeTe visible. This strongly implies that the deposited material is a solid solution containing Ge, Se and Te atom evenly distributed in the lattice. This is also a contribution to the broader peaks observed for the XRD pattern from the ternary film below, as compared to the two binary films in Figure 6-9.

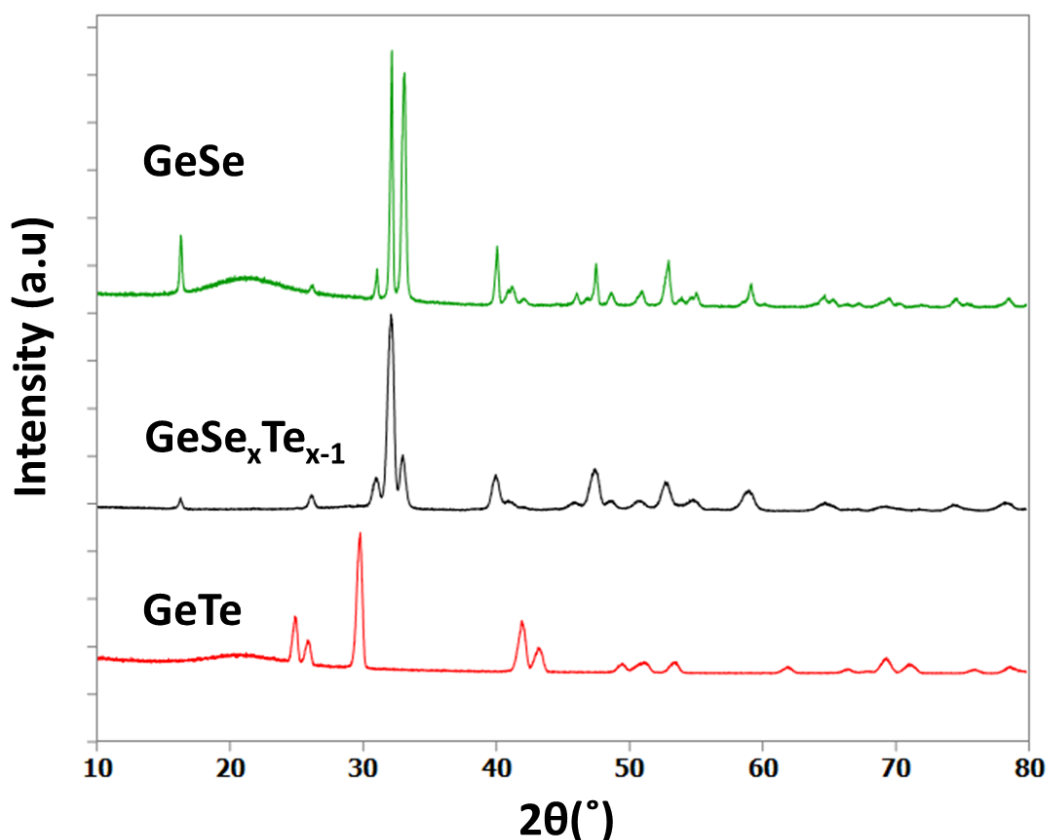


Figure 6-9: GIXRD pattern for GeSeTe ternary film in black as well as patterns for GeSe in green and GeTe in red.

Vegard's law states that the crystal structure of a ternary solid solution will resemble a weighted mean of the two binary constituent materials. The way that this manifests in the XRD data is a difference in the lattice parameters and therefore peak positions, in such a way that is in a midpoint between the two binary components proportionally to the contribution from each. Therefore, the slight increase in the lattice parameters moving from GeSe to $\text{GeSe}_{1-x}\text{Te}_x$, as shown in Table 6-3, is in agreement with a small degree of Te being incorporated in the structure. Previous investigations of $\text{GeSe}_{1-x}\text{Te}_x$ with low Te content indicate that the Pnma structure is maintained for Se rich solid solutions ($x \leq 0.05$).^{4,23} Thus, a slight increase in the lattice parameters is expected.

Material	Crystal system	a (Å)	b (Å)	c (Å)	Cell volume (V)/ Formula unit (Z) (Å ³)
GeSe	Orthorhombic	10.8089(7)	3.8222(2)	4.3679(3)	45.11
GeSeTe deposition	Orthorhombic	10.833(2)	3.8463(8)	4.3797(11)	45.62
GeTe	Hexagonal	4.1778(5)	4.1778(5)	10.6866(14)	62.17

Table 6-3: Comparison of the lattice parameters and cell volumes for both the binary materials, GeSe and GeTe, and the ternary deposition comprised of GeSe_{1-x}Te_x formed using a 9:1 ratio of **[GeⁿBu₃(SeⁿBu)]** and **[GeⁿBu₃(TeⁿBu)]**.

The Raman spectra collected for the binary materials and the ternary solid solution are displayed in Figure 6-10. Conversely to the findings shown in the GIXRD, the Raman spectrum collected for the GeSe_{1-x}Te_x deposit describe a material similar to that of GeTe. This is apparent from the two stretching modes at 80 and 108 cm⁻¹ for GeSe_{1-x}Te_x compared with the E stretching mode at 87 cm⁻¹ and the A_{1g} mode at 122 cm⁻¹ for GeTe. This finding could be reflective of the differing composition at different areas at different positions across the substrate, despite efforts made to ensure that approximately equivalent positions were analysed. Another explanation for the observation of the different composition implied by the GIXRD and Raman analysis could be that Raman is a surface technique and XRD is a bulk technique. Due to the different boiling points of **[GeⁿBu₃(SeⁿBu)]**, 454.15 K, and **[GeⁿBu₃(TeⁿBu)]**, 493 K, it is likely that the initial vapours to form deposited materials are that of the lower boiling point component. This could lead to a difference in the composition from the bottom of the deposition up and thus a surface composition closer to GeTe in nature and a bulk much closer to GeSe.

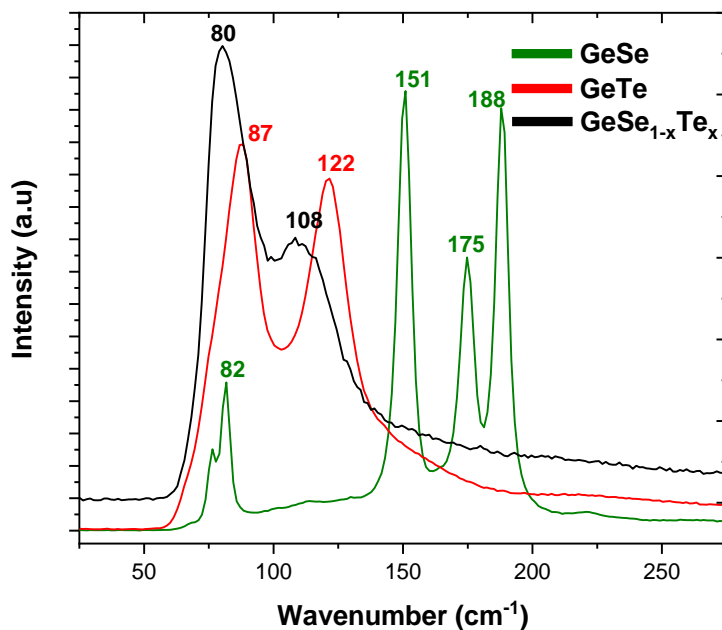


Figure 6-10: Raman spectra for GeSe_{1-x}Te_x in black, GeSe in green and GeTe in red.

6.4.2.2 Attempted deposition of a germanium tin telluride ternary thin film using LPCVD

The exploration of Ge_{1-x}Sn_xTe ternary films was performed using a 1:9 molar ratio of [GeⁿBu₃(TeⁿBu)] to [SnⁿBu₃(TeⁿBu)] selected as an interesting ratio as other solid solutions of different ternary materials with enhanced thermoelectric performances have contained from 1% to 20% of the minor component, as discussed in section 6.4.3. The interest in this ternary system stems from the incorporation of Ge into the Sn sites which will likely affect the occurrence of vacancies, helping to tune the thermoelectric properties, as well as reducing the crystal symmetry, which could lead to a reduction in thermal conductivity. One sample was produced that resembled a solid solution, deposited at 366 °C and 0.01 mmHg. This film was characterised using GIXRD, displayed in Figure 6-11, to show that the film was not simply a combination of GeTe and SnTe. The spikey appearance of the Ge_{x-1}Sn_xTe GIXRD pattern may be a result of a large crystallite size leading to poor averaging of the scattering.

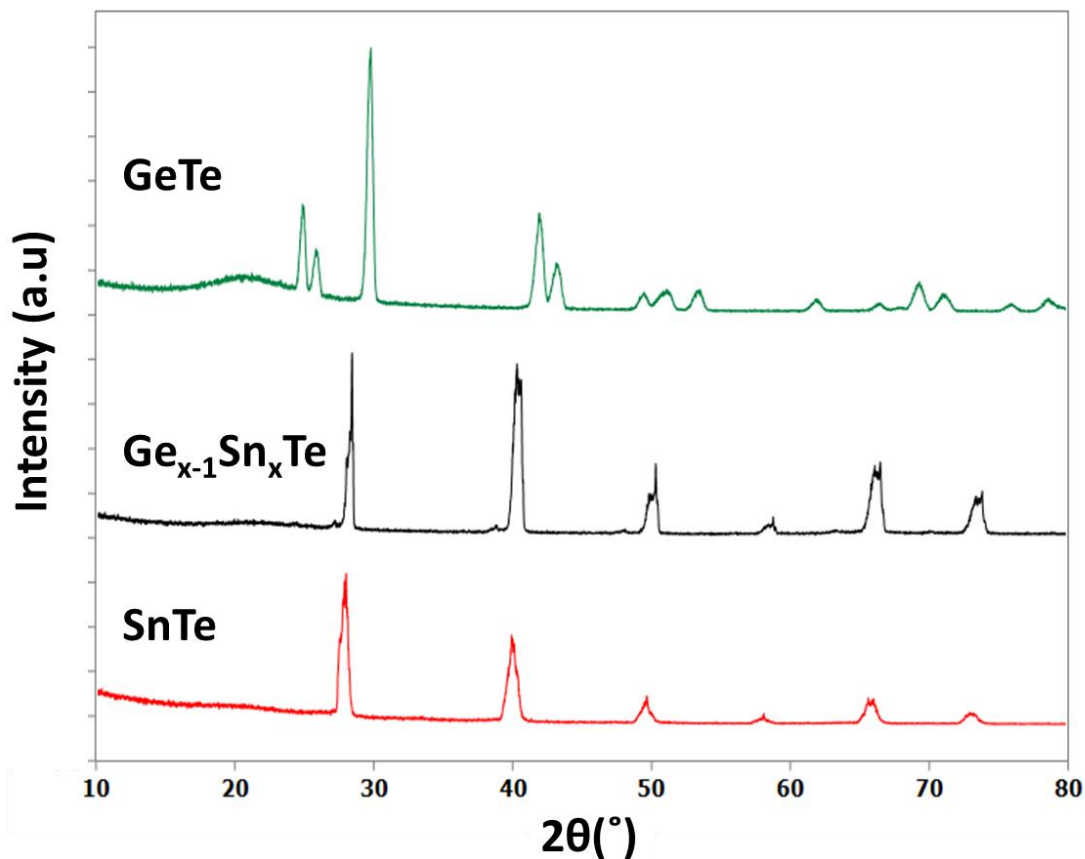


Figure 6-11: GIXRD pattern for $\text{Ge}_{1-x}\text{Sn}_x\text{Te}$ ternary film displayed in black as well as the patterns for GeTe in green and SnTe in red.

This can be further corroborated by inspection of the lattice parameters, displayed in Table 6-4 along with those of the binary materials for comparison. The deposition adopts the same cubic structure as SnTe. However, the deposit has a reduced unit cell/ formula unit ratio compared to the binary SnTe. This is good evidence for the deposition of a solid solution, as discussed in section 5.2.1.1, as this is in keeping with Vegard's Law. However, in order to further corroborate these findings further deposits with differing compositions would need to be produced and compared to show a linear correlation with respect to the lattice parameter change and composition.

Table 6-4: Comparison of the lattice parameters and cell volumes for both the binary materials, GeTe and SnTe, and the ternary deposition comprised of GeSnTe.

Material	Crystal system	a (Å)	b (Å)	c (Å)	Cell volume (V)/ Formula unit (Z) (Å ³)
GeTe ²⁴	Hexagonal	4.1778(5)	4.1778(5)	10.6866(14)	62.17
GeSnTe deposition	Cubic	6.3017(4)	6.3017(4)	6.3017(4)	62.56
SnTe	Cubic	6.3033(5)	6.3033(5)	6.3033(5)	62.61

EDX analysis was also deployed to probe the composition of the deposited film, as well as verify the absence of impurities. The EDX spectrum can be seen in Figure 6-12 and the quantification of the atom % is displayed in Table 6-5. The EDX analysis indicates a large quantity of O, however, as this peak overlaps with intensities from both Te and Sn, this is certainly exaggerated.

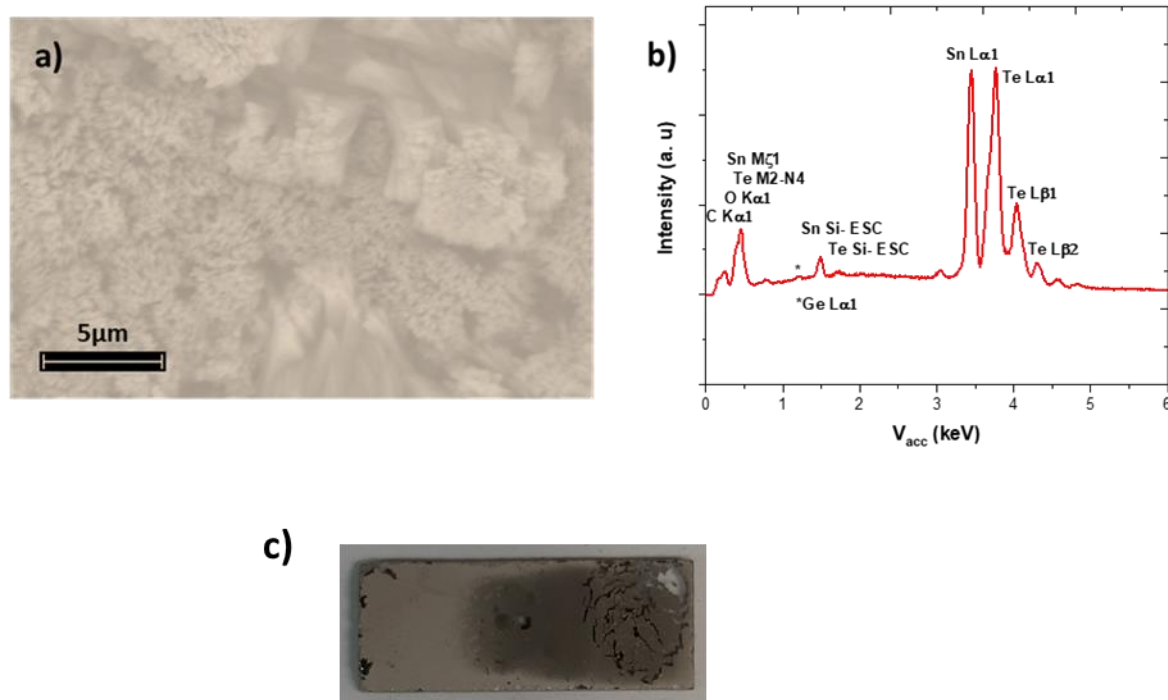


Figure 6-12: **a)** Top down SEM image of ternary GeSnTe thin film, **b)** the corresponding EDX spectrum and **c)** an image of the deposition tile in investigated.

Table 6-5: EDX analysis results for a solid solution thin film containing Ge, Sn and Te (on SiO₂).

Sample	%C	%O	%Si	%Ge	%Sn	%Te
GeSnTe Ternary	1.6	23.2	1.0	1.6	36.7	36.0

The film was further characterised by Raman spectroscopy, shown in Figure 6-13 showing a pattern similar to SnTe, with a very slight shift towards lower wavenumbers (peak at 140 cm⁻¹ compared to 142 cm⁻¹ and 121 cm⁻¹ compared to 123 cm⁻¹). There is also the emergence of a feature at 94 cm⁻¹, this is not present in the binary SnTe and resembles a stretching frequency observed in GeTe. This is further evidence for a well distributed solid solution being successfully deposited.

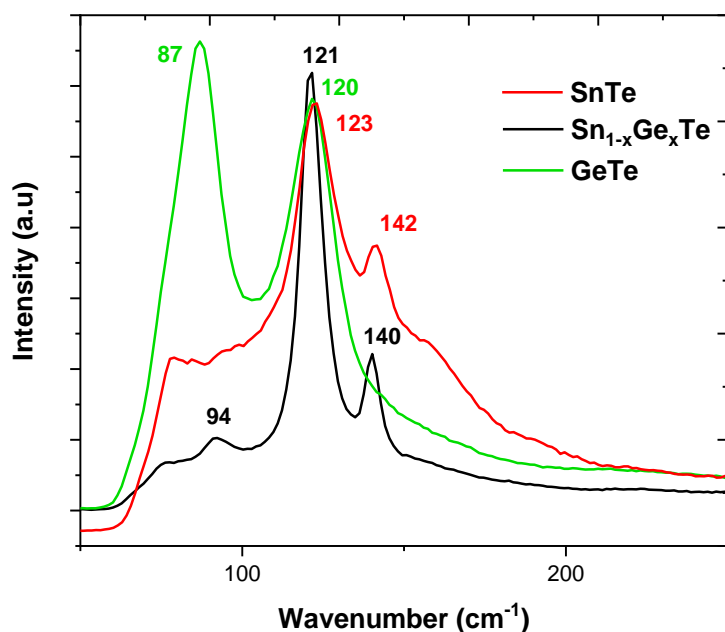


Figure 6-13: The Raman spectrum for the deposited solid solution containing Ge, Sn and Te.

6.4.2.3 Attempted growth of a tin selenide telluride ternary thin film using LPCVD

The SnSeTe ternary has previously been described as having improved thermoelectric performance as a result of improved mobility due to the improved crystal symmetry, as the orthorhombic SnSe structure moves closer to the cubic structure of SnTe with increasing Te concentration, as well as lower thermal conductivity and higher carrier concentration.²⁵ In the aforementioned work, by Qin *et al.*, ternary systems were investigated, SnSe_{1-x}Te_x such that x =

0 - 3%. The system explored in the present work was obtained from a precursor mixture of 9 parts $[\text{Sn}^n\text{Bu}_3(\text{Se}^n\text{Bu})]$ to 1 part $[\text{Sn}^n\text{Bu}_3(\text{Te}^n\text{Bu})]$.

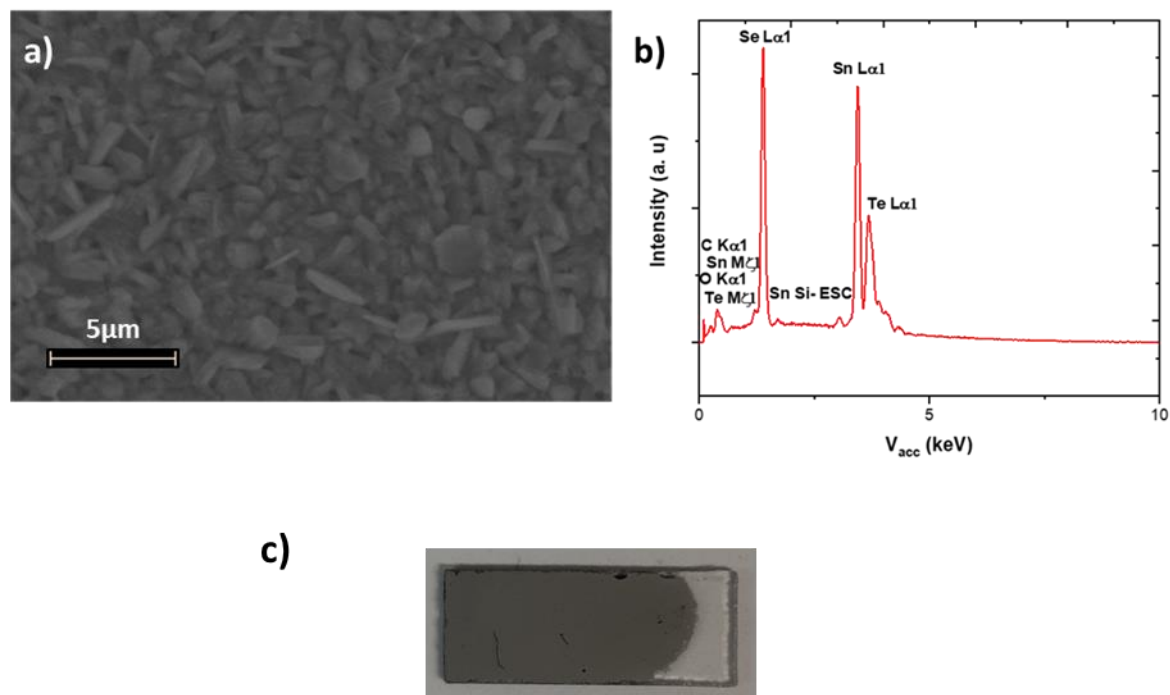


Figure 6-14: **a)** Top down SEM image of a deposition obtained using a precursor mixture of $[\text{Sn}^n\text{Bu}_3(\text{Se}^n\text{Bu})]$ and $[\text{Sn}^n\text{Bu}_3(\text{Te}^n\text{Bu})]$, **b)** the corresponding EDX spectrum collected for that same deposition and **c)** an image of the deposition tile investigated.

Table 6-6: EDX analysis results showing the atom percentages for all the elements present.

Deposition	%C	%O	%Si	%Se	%Sn	%Te
SnSeTe	5.1	9.2	1.0	32.4	43.1	9.3

The GIXRD pattern for this film is compared to patterns of SnSe and SnTe deposits, produced and reported in previous chapters, is displayed in Figure 6-15. The refined lattice parameters can be seen compared to the two binary materials in Table 6-7. As expected for a SnSe system with partial substitution of Se for Te, the unit cell/ formula unit ratio is increased compared to pure SnSe. This is good evidence for the deposition of a solid solution.

Table 6-7: Comparison of the lattice parameters and cell volumes for both the binary materials, SnSe and SnTe, and the ternary deposition comprised of SnSeTe.

Sample	a (Å)	b (Å)	c (Å)	Cell volume (V)/ Formula unit (Z) (Å ³)
SnSe	11.4844(18)	4.1555(7)	4.4289(10)	52.84
SnSeTe (FR222T3)	11.680(4)	4.2174(9)	4.4603(11)	54.93
SnTe	6.3033(5)	6.3033(5)	6.3033(5)	62.61

The GIXRD shown in Figure 6-15 shows very good evidence for a solid solution of SnSe_{1-x}Te_x. This is highlighted in the expanded section between the 2θ angles of 25-33° where a shift of the peak position from the binary SnSe to lower angle towards the major peak of SnTe is seen. This indicates the shift towards higher d-spacing (lower 2θ) with increasing Te content.

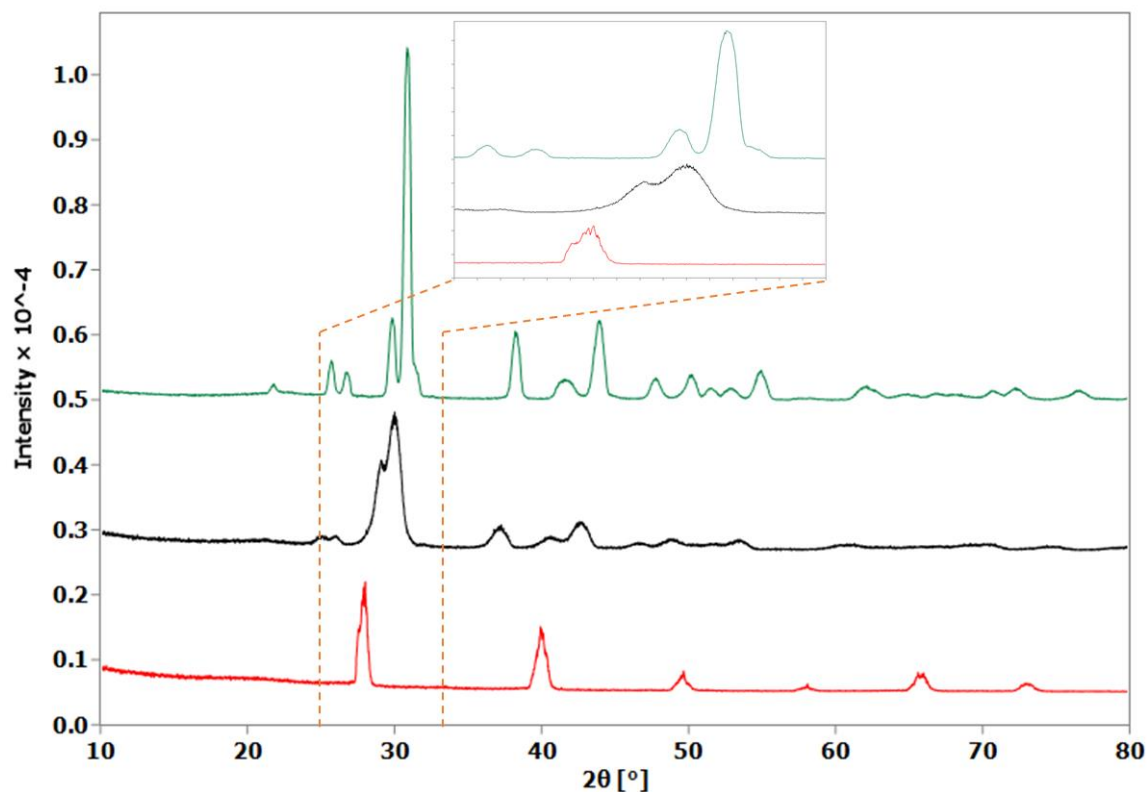


Figure 6-15: GIXRD pattern for the mixed precursor deposition from 9 parts [SnⁿBu₃(SeⁿBu)] to 1 part [SnⁿBu₃(TeⁿBu)], in green, and literature profiles for bulk SnSe¹² and SnTe,²⁴ in black and red respectively.

The Raman spectrum, displayed in Figure 6-15, of the ternary SnSe_{1-x}Te_x resembles neither binary SnSe or SnTe closely. The peak at the lowest wavenumber, 100 cm⁻¹, is shifted away from the SnSe

A_g mode, at 72 cm^{-1} , towards the A_1 mode observed in SnTe at 123 cm^{-1} . Similarly, the higher wavenumber stretching mode, at 148 cm^{-1} , is shifted away from the SnSe A_g mode at 152 cm^{-1} towards the SnTe E mode, at 140 cm^{-1} . This shifting of the stretching mode peaks is in keeping with that observed in solid solutions of other materials.^{5,6,26}

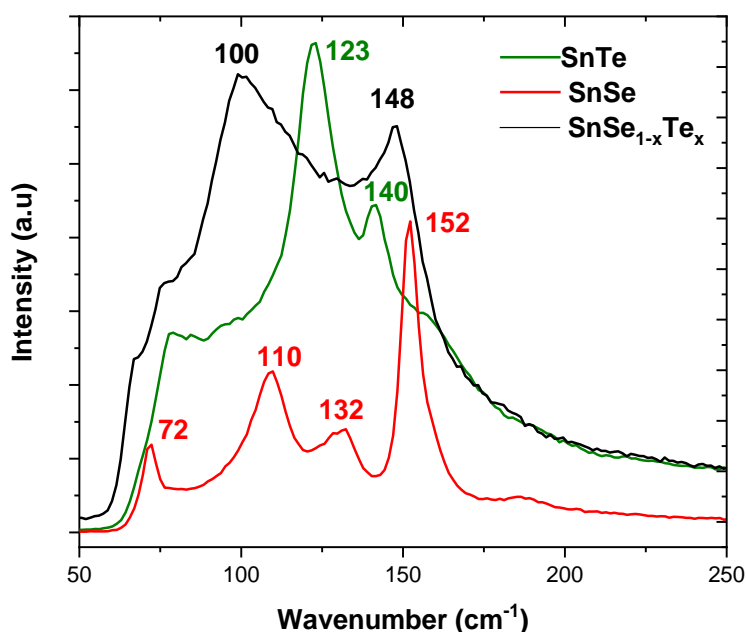


Figure 6-16: Raman spectra for ternary $\text{SnSe}_{1-x}\text{Te}_x$ in black, SnTe in green and SnSe in red.

6.5 Conclusions

The LPCVD of SnSe thin films was successfully translated to the enhanced CVD process using a Picosun R-200 Advanced ALD reactor. The depositions were achieved from both $[\text{Sn}^n\text{Bu}_3(\text{Se}^n\text{Bu})]$ with a hydrogen plasma and $[\text{SnEt}_3(\text{Se}^n\text{Bu})]$, and the films were characterised by GIXRD, SEM with EDX and Raman spectroscopy. The initial evidence for successful deposition came from ellipsometry measurements, and were then confirmed by both Raman spectroscopy and GIXRD analysis. In order to further establish this wafer scale procedure. Further experiments will be required with the higher vapour pressure SSP, $[\text{SnEt}_3(\text{Se}^n\text{Bu})]$, to explore the potential for uniform wafer scale depositions via careful control over the precursor concentration, flow rate, internal temperature and the precursor inlet design. This same procedure could then be translated to other similar SSPs for the deposition of various other materials and then, in principle, to create multi-layered stacks comprising combinations of different group 14 chalcogenide films. Evidence of C contamination was found in both of the deposits produced using the commercial set up described. However, as this could be a feature of the overlapping characteristic X-rays of Sn and

Se with C further work is required to validate these findings before attempts to mitigate this can be performed, this could be performed using WDS analysis.

Thin films of several different ternary solid solutions have been produced, including $\text{GeSe}_{1-x}\text{Te}_x$, $\text{Ge}_{1-x}\text{Sn}_x\text{Te}$ and $\text{SnSe}_{1-x}\text{Te}_x$. The resulting films were fully characterised using GIXRD, SEM with EDX and Raman spectroscopy. Other ternary systems were attempted, including $\text{SnS}_{1-x}\text{Te}_x$ and $\text{GeS}_{1-x}\text{Te}_x$ but were unsuccessful using the conditions selected. The ternaries successfully obtained provide insight into useful SSP mixture ratios. The $\text{GeSe}_{1-x}\text{Te}_x$ and $\text{Ge}_{1-x}\text{Sn}_x\text{Te}$ solid solutions contained low quantities of the minor element, between 1-4%, whereas $\text{SnSe}_{1-x}\text{Te}_x$ contained over 9% Te. Thus, the precursor mixtures chosen for future ternary depositions should reflect this to obtain samples with various stoichiometries. The exploration of further ternary samples within these families using different element ratios of their components would give a stronger basis for evidence of solid solutions being present, by testing the characterisation data for a series of solid solution samples with differing compositions. This would allow for a more robust investigation of Vegard's law. The successful deposition of these initial ternary phases shows a good precedent for the deposition of other ternary solid solutions using this SSP family. Further work on these materials would involve comparing their thermoelectric and electronic properties to those of the binary phases.

6.6 References

- 1 US Patent, 20130183444, 2014, 8753716.
- 2 X. Song, Y. Ke, X. Chen, J. Liu, Q. Hao, D. Wei and W. Zhang, *Nanoscale*, 2020, **12**, 11242.
- 3 L. Vegard, *Zeitschrift für Phys.*, 1921, **5**, 17.
- 4 M. G. Herrmann, R. P. Stoffel, M. Kupers, M. A. Haddouch, A. Eich, K. Glazyrin, A. Grzechnik, R. Dronskowski and K. Friese, *Acta Cryst.*, 2019, **B75**, 246.
- 5 A. Soni, Z. Yanyuan, Y. Ligen, M. K. K. Aik, M. S. Dresselhaus and Q. Xiong, *Nano Lett.*, 2012, **12**, 1203.
- 6 M. Hong, T. C. Chasapis, Z. G. Chen, L. Yang, M. G. Kanatzidis, G. J. Snyder and J. Zou, *ACS Nano*, 2016, **10**, 4719.
- 7 Y. M. Han, J. Zhao, M. Zhou, X. X. Jiang, H. Q. Leng and L. F. Li, *J. Mater. Chem. A*, 2015, **3**, 4555.
- 8 T. R. Wei, C. F. Wu, X. Zhang, Q. Tan, L. Sun, Y. Pan and J. F. Li, *Phys. Chem. Chem. Phys.*,

- 2015, **17**, 30102.
- 9 S. Perumal, S. Roychowdhury, D. S. Negi, R. Datta and K. Biswas, *Chem. Mater.*, 2015, **27**, 7171.
- 10 S. Perumal, S. Roychowdhury and K. Biswas, *Inorg. Chem. Front.*, 2016, **3**, 125.
- 11 Picosun, PICOSUN® R-200 Advanced, <https://www.picosun.com/product/r-200-advanced/>, (accessed 5 March 2021).
- 12 M. Sist, J. Zhang and B. B. Iversen, *Acta Cryst.*, 2016, **B72**, 310.
- 13 K. C. Ross, J. A. Petrus and A. M. McDonald, *Powder Diffr.*, 2014, **29**, 337.
- 14 D. M. Jang, H. Jung, N. D. Hoa, D. Kim, S. K. Hong and H. Kim, *J. Nanosci. Nanotechnol.*, 2012, **12**, 1425.
- 15 I. Y. Ahmet, M. S. Hill, P. R. Raithby and A. L. Johnson, *Dalton Trans.*, 2018, **47**, 5031.
- 16 Y. X. Chen, Z. H. Ge, M. Yin, D. Feng, X. Q. Huang, W. Zhao and J. He, *Adv. Funct. Mater.*, 2016, **26**, 6836.
- 17 S. Perumal, P. Bellare, U. S. Shenoy, U. V. Waghmare and K. Biswas, *Chem. Mater.*, 2017, **29**, 10426.
- 18 R. Moshwan, W. Di Liu, X. L. Shi, Y. P. Wang, J. Zou and Z. G. Chen, *Nano Energy*, 2019, **65**, 104056.
- 19 L. D. Zhao, V. P. Dravid and M. G. Kanatzidis, *Energy Environ. Sci.*, 2014, **7**, 251.
- 20 Y. M. Han, J. Zhao, M. Zhou, X. X. Jiang, H. Q. Leng and L. F. Li, *J. Mater. Chem. A*, 2015, **3**, 4555.
- 21 A. Banik, T. Ghosh, R. Arora, M. Dutta, J. Pandey, S. Acharya, A. Soni, U. V. Waghmare and K. Biswas, *Energy Environ. Sci.*, 2019, **12**, 589.
- 22 H. Wiedemeier and P. A. Siemers, *High Temp. Sci.*, 1984, **17**, 395.
- 23 P. Bauer Pereira, I. Sergueev, S. Gorsse, J. Dadda, E. Müller and R. P. Hermann, *Phys. status. Solidi B*, 2013, **250**, 1300.
- 24 B. Qin, D. Wang, W. He, Y. Zhang, H. Wu, S. J. Pennycook and L. D. Zhao, *J. Am. Chem. Soc.*, 2019, **141**, 1141.

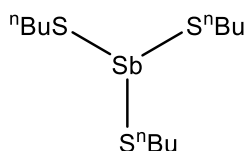
Chapter 6

- 25 S. L. Benjamin, C. H. de Groot, C. Gurnani, S. L. Hawken, A. L. Hector, R. Huang, M. Jura, W. Levason, E. Reid, G. Reid, S. P. Richards and G. B. G. Stenning, *J. Mater. Chem. C*, 2018, **6**, 7734.

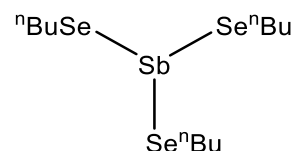
Chapter 7 Evaluation of Single Source Precursors for the Deposition of Bi_2E_3 and Sb_2E_3 (E = S, Se or Te) Thin Films

7.1 Single source precursors used in this work

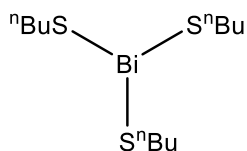
[Sb(SⁿBu)₃]: Antimony tris-n-butylthiolate



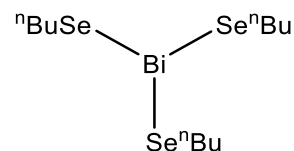
[Sb(SeⁿBu)₃]: Antimony tris-n-butylselenolate



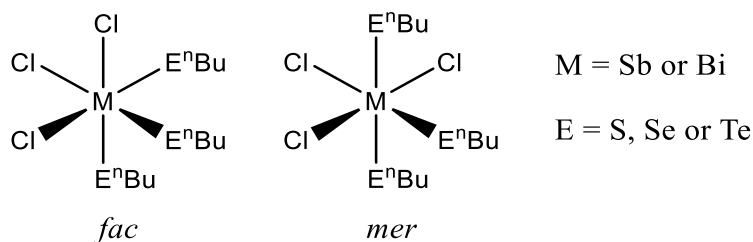
[Bi(SⁿBu)₃]: Bismuth tris-n-butylthiolate



[Bi(SeⁿBu)₃]: Bismuth tris-n-butylselenolate



[MCl₃(EⁿBu)₂]: Antimony/ bismuth trichloride tris-n-butylchalcogenoether (*fac/mer*)¹⁻³



7.2 Introduction

Antimony and bismuth chalcogenide materials have long been reported as important within the field of thermoelectrics for near room temperature applications.⁴⁻⁸ Lots of different methods of material synthesis and thin film deposition have been reported, including precursors and methods developed within the Reid group. In terms of thin films, these depositions used quite different precursors for the growth of Bi_2Te_3 , Sb_2Se_3 and Sb_2Te_3 , $[\text{MCl}_3(\text{E}^n\text{Bu})_2]$ (where M is Bi or Sb and E is Se or Te),^{1,2} $[\text{Sb}(\text{Se}^n\text{Bu})_3]$ and $[\text{SbMe}(\text{Te}^n\text{Bu})_2]$ ^{3,9} respectively. The different styles of precursor have not been shown to extend to the entire series of Bi and Sb chalcogenides, particularly the sulfides, thus may not translate well to the use of mixed precursor systems for solid solutions of some other ternary combinations. The development of a single unified precursor type that translates to all the materials would make the prediction of how these mixed systems might operate much simpler. As the type described previously for the deposition of Sb_2Se_3 , **[Sb(SeⁿBu)₃]**, resembles

closely the other precursors described within the work this thesis is concerned with, this was selected as the most suitable precursor form to adopt. The adoption of this SSP style also allows for a very simple synthesis route compared to that for $[\text{SbMe}(\text{Te}^n\text{Bu})_2]$, as MCl_3 is commercially available but MeMCl_2 requires a multistep synthesis.^{9,10}

7.2.1 The crystal structure of Sb_2E_3 and Bi_2E_3 ($\text{E} = \text{S}, \text{Se}$ or Te)

All of the Sb and Bi chalcogenide materials form 2D layered structures. The sulfides and Sb_2Se_3 adopt orthorhombic layered structures, whereas the Bi_2Se_3 and the tellurides form rhombohedral structures due to the destabilisation of the lone pair s^2 on the Sb or Bi in a similar fashion to that described for the Ge monochalcogenide structures. These crystal structures can be seen displayed in Figure 7-1.

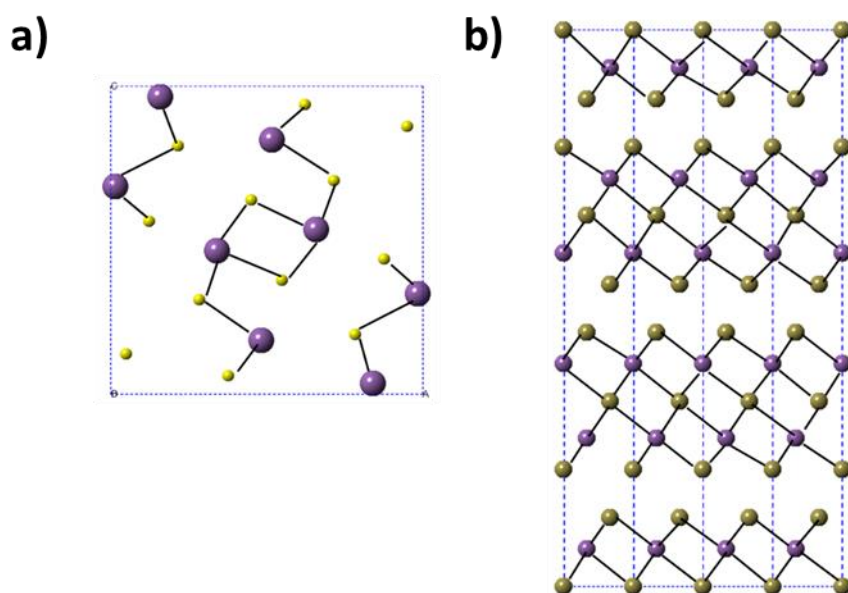


Figure 7-1: Crystal structures of **a)** Sb_2S_3 ,¹¹ Sb_2Se_3 ,¹² Bi_2S_3 ¹³ and **b)** Sb_2Te_3 ,¹⁴ Bi_2Se_3 ¹⁵ and Bi_2Te_3 .¹⁶

7.2.2 Thermoelectric properties of Sb_2E_3 and Bi_2E_3

The thermoelectric properties of the Sb and Bi chalcogenides are well established and have been investigated since the 1950s.^{6,8} They form a highly researched group of near room temperature thermoelectric materials. Bi_2Te_3 is typically an n-type thermoelectric material and Sb_2Te_3 is an p-type thermoelectric material, thus, they can be paired together to form a thermoelectric device,^{2,17-20} as described in Section 1.4. Many examples of such devices are available commercially.²¹ The layered orthorhombic structured Sb_2S_3 , Sb_2Se_3 and Bi_2S_3 display relatively poor

electrical conductivities and are therefore of less interest for thermoelectric applications when undoped, as can be seen in Table 7-1.

Table 7-1: Collection of some room temperature thermoelectric and electrical parameters for Bi_2E_3 and Sb_2E_3 including the electrical conductivity, Seebeck coefficient, thermal conductivity and the electronic bandgap. *Predicted value, no experimental value available due to the low electrical conductivity leading to instrumental difficulties.

Material	Electrical conductivity (S cm^{-1})	Seebeck coefficient ($\mu\text{V K}^{-1}$)	Thermal conductivity ($\text{W m}^{-1}\text{K}^{-1}$)	Bandgap (eV)
Sb_2S_3	$(1.6 \times 10^{-9})^{22}$	2888* ²³	<i>c.a.</i> 2.4 ²³	2.30 ²⁴
Bi_2S_3	$(3.6 \times 10^{-5})^{25}$	-325 ^{26,27}	<i>c.a.</i> 0.75 ²⁶	<i>c.a.</i> 1.6 ²⁵
Sb_2Se_3	$(10^{-6}-10^{-7})^{2,9,28}$	661 ²⁹	0.38-1.9 ²⁹	1.1 ³⁰
Bi_2Se_3	100-550 ³¹	-115 ³²	3.10 ³³	0.24 ³¹
Sb_2Te_3	104-1695 ^{9,34,35}	190 ³⁴	2.02 – 2.52 ³⁶	0.28 ^{2,5}
Bi_2Te_3	340-1780 ^{1,2,31,37,38}	<i>c.a.</i> -100 ³⁹	<i>c.a.</i> 1.6 ⁴⁰	0.16 ³¹

7.2.3 Optimised properties

The thermoelectric performance of Bi_2E_3 and Sb_2E_3 based materials have been shown to be greatly enhanced by a number of different approaches. These include: the combination of materials to ternary solid solutions,⁴¹ the formation of superlattices,⁴² nanostructuring^{43,44} and doping.⁴⁵⁻⁴⁷ The techniques have yielded state of the art ZT values of *ca.* 1 for materials for near room temperature regimes.^{48,49} A detailed description of the optimisation techniques can be found in Section 1.3.

7.2.4 Applications near room temperature

As discussed, the Bi_2E_3 and Sb_2E_3 materials operate best near room temperature. This means they are good candidates for power generation devices that operate within this common temperature range. These include wearable electronic devices, workplace or household sensing devices and outdoor ambient low energy devices. A more in depth description of the temperature ranges and the applications that occupy them can be found in Section 1.2.1.1.

7.2.5 Previous single source precursors and deposition

As discussed in section 2.1, the use of SSPs is highly advantageous for use in CVD. Larger molecules, with low volatility and or stability, can be used in AACVD. The SSPs shown in Figures 7-1 and 7-2 display some different SSPs reported for the deposition of Sb_2E_3 and Bi_2E_3 , where E is S, Se or Te. The lack of a precursor type or family that spans all of the materials, M_2E_3 , where M is Sb or Bi and E is S, Se or Te, makes the mixing of precursors to produce ternary solid solutions much more difficult. Employing a SSP family that can access all the materials would lead to comparable volatilities, stabilities and equivalent stoichiometry of the M:E within the mixtures.

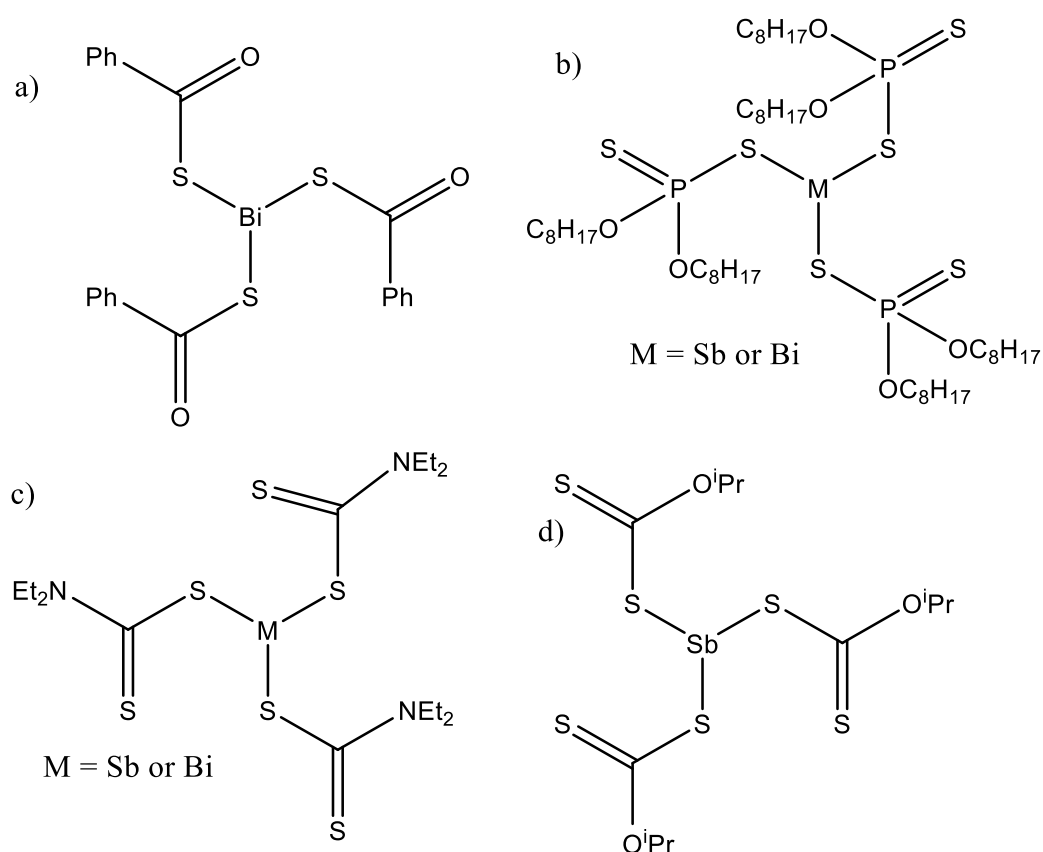


Figure 7-2: Some examples of single source precursors reported in the literature for the deposition of Sb_2S_3 and Bi_2S_3 , namely: a) $[\text{Bi}(\text{SCOPh})_3]$,⁵⁰ b) $(\text{M}[\text{S}_2\text{P}(\text{OC}_8\text{H}_{17})_2]_3)$,⁵¹ c) $(\text{M}[\text{S}_2\text{CNET}_2]_3)$ ⁵² and d) $[\text{Sb}(\text{S}_2\text{CO}^i\text{Pr})_3]$.⁵³

The difference in the chemistry of the precursors largely arises due to the different energy overlap or mismatch of the group 15 metal and chalcogen in question. The reaction of SbCl_3 or BiCl_3 with a chalcogenolate can lead to further reactions due to the free coordination site. For this reason, the SSPs displayed in Figure 7-2 all contain bidentate ligands which occupy all coordination sites. This yields more stable SSPs. However, by careful control over the reaction stoichiometry, SSPs containing only covalently bonded ligands are a viable option, as can be seen in Figure 7-3.

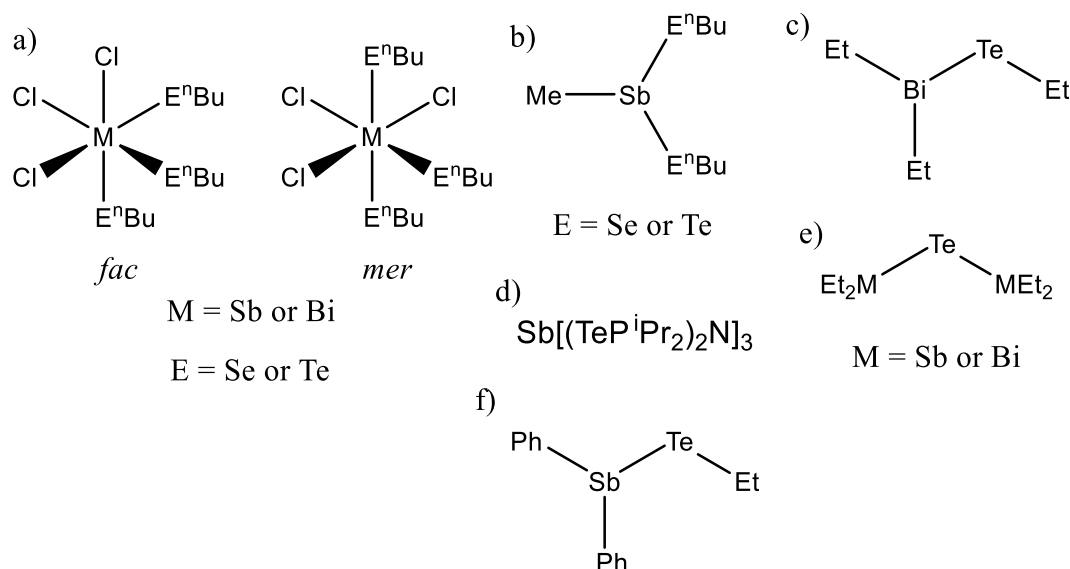


Figure 7-3: Single source precursors described in the literature for the deposition or synthesis of Sb_2Te_3 and Bi_2Te_3 , namely: a) $[\text{MCl}_3(\text{E}^n\text{Bu}_2)_3]$,^{1,2} b) $[\text{SbMe}(\text{Te}^n\text{Bu})_2]$,^{3,9} c) $[\text{BiEt}_2(\text{TeEt})]$,⁵⁴ d) $\text{Sb}[(\text{TeP}^i\text{Pr}_2)_2\text{N}]_3$,⁵⁵ e) $(\text{Et}_2\text{M})_2\text{Te}$ ^{54,56} and f) $[\text{SbPh}_2(\text{TeEt})]$.⁵⁷

The class of SSPs of the form $[\text{MCl}_3(\text{E}^n\text{Bu}_2)_3]$ were explored previously within the group for the depositions of $\text{Bi}_2(\text{Se}_{1-x}\text{Te}_x)_3$ and $(\text{Bi}_{1-\gamma}\text{Sb}_\gamma)\text{Te}_3$ solid solutions² and in the selective deposition of Bi_2Te_3 .¹ However, this work did not extend the group to the thioether complexes. Therefore, one aim was to explore $[\text{MCl}_3(\text{S}^n\text{Bu}_2)_3]$ precursors to test the versatility of this group and explore the possibility of mixed S and Se as well as S and Te based solid solutions, for more sustainable thermoelectric materials. Also of great interest is the exploration of compounds similar to those discussed in previous chapters, *i.e.* the group 14 chalcogenolate SSPs, of the form $[\text{M}(\text{E}^n\text{Bu})_3]$. Some precedent for SSP of this type has already been established with the successful depositions from $[\text{SbMe}(\text{Te}^n\text{Bu})_2]$ ^{3,9} and $[\text{Sb}(\text{Se}^n\text{Bu})_3]$.⁹ Once the SSPs have been successfully prepared and fully characterised, their potential for LPCVD would be explored via TGA. If appropriate, LPCVD experiments would then be carried out and any films produced would be characterised using GIXRD, Raman spectroscopy and SEM with EDX. If successful, this would enable the mixture of these precursors to investigate the potential for the deposition of solid solutions.

7.3 Experimental

7.3.1 Precursor preparation and characterisation

All reactions were performed under an inert atmosphere using Schlenk, vacuum line and glove box techniques under a dry nitrogen atmosphere. The solvents used (acetonitrile) were dried by distillation from sodium wire prior to use and NMR solvents were stored in a glovebox over molecular sieves. Ligands used (E^nBu_2 where E is S, Se or Te) were obtained using methods

described in the literature.^{58,59} BiCl₃ and SbCl₃ were obtained from Merck Life Science UK Ltd, stored in glovebox and used as received and the chalcogenoether ligands, ⁿBu₂E, where E is Se or Te, were prepared using literature methods^{58,60} and ⁿBu₂S was obtained from Sigma Aldrich and used as received. All ¹H, ¹³C{¹H}, ⁷⁷Se{¹H} (referenced against neat SeMe₂), ¹¹⁹Sn{¹H} (referenced against neat SnMe₄), ¹²⁵Te{¹H} (referenced against neat TeMe₂) and 2D HMQC NMR spectra were collected on a Bruker AV400 spectrometer in CDCl₃ at room temperature. Due to the rapid degradation of the precursors, despite storing at -18 °C, no microanalysis was possible. This degradation could clearly be seen in the decolouration of the brightly coloured yellow or orange precursors to brown or black as well as in their NMR spectra.

7.3.2 Precursor synthesis

[SbCl₃(SⁿBu₂)₃]: SbCl₃ (181.0 mg, 0.79 mmol) was dissolved in MeCN (10 mL) and the solution cooled to 0 °C. A solution of SⁿBu₂ (347.9 mg, 2.4 mmol) in MeCN (10 mL) was slowly added with no change in colour observed. The solution was allowed to warm to room temperature prior to stirring for 1 h. The volatile components were removed leaving a colourless oil that was dried in vacuo. Yield: 263 mg, 50 %. ¹H NMR (CDCl₃): δ = 2.58-2.55 (m, [12H], CH₂S), 1.63-1.55 (m, [12H], CH₂), 1.46-1.37 (m, [12H], CH₂), 0.93 (t, [18H], CH₃). ¹³C{¹H} NMR (CDCl₃): δ = 32.4 (CH₂S), 31.5 (CH₂), 22.1 (CH₂), 13.6 (CH₃). IR (Nujol, cm⁻¹): ν = 315 br (Sb-Cl).

[BiCl₃(SⁿBu₂)₃]: BiCl₃ (224.3 mg, 0.71 mmol) was dissolved in MeCN (10 mL) and the solution cooled to 0 °C. A solution of SⁿBu₂ (308.9 mg, 2.1 mmol) in MeCN (10 mL) was slowly added with no change in colour observed. The solution was allowed to warm to room temperature prior to stirring for 1 h. The volatile components were removed leaving a viscous yellow oil that was dried in vacuo. Yield: 120 mg, 22 %. ¹H NMR (CDCl₃): δ = 3.02 (t, [2H], CH₂S), 1.71-1.64 (m, [2H], CH₂), 1.51-1.42 (m, [2H], CH₂), 0.95 (t, [3H], CH₃). ¹³C{¹H} NMR (CDCl₃): δ = 33.7 (CH₂S), 31.8 (CH₂), 22.0 (CH₂), 13.7 (CH₂). IR (Nujol, cm⁻¹): ν = 283 (Bi-Cl).

[Sb(SⁿBu)₃]: Butane thiol (2.083 g, 2.31 × 10⁻² mol) was added to a solution of sodium metal (0.531 g, 2.31 × 10⁻² mol) dissolved in anhydrous ethanol (20 mL) and stirred vigorously over the course of 2 h. Removal of volatiles from this colourless solution gave a white powder. THF (20 mL) was then added, followed by a solution of SbCl₃ (1.759 g, 7.71 × 10⁻³ mol) in THF (20 mL), which was added dropwise over the course of 5 min., the solution turned to yellow immediately on addition and then to a cloudy white after some time. The reaction was stirred for 1 h before the THF was removed in vacuo and hexane was added. The cloudy solution was then filtered, producing a clear pale yellow solution. After the hexane had been removed under vacuum, the yellow liquid remaining was washed in anhydrous hexane (30 mL), filtered once more to remove

particulates and dried *in vacuo*. Yield: 2.427 g, 81 %. ^1H NMR (CDCl_3): $\delta/\text{ppm} = 0.92$ (t, $J = 8.00$ Hz, [9H], CH_3), 1.44 (tquart, [6H], CH_2), 1.66 (tt, [6H], CH_2), 2.91 (t, [6H], SCH_2). $^{13}\text{C}\{^1\text{H}\}$ NMR (CDCl_3): $\delta/\text{ppm} = 13.57$ (CH_3), 21.73 (CH_2), 30.16 (SCH_2), 35.69 (CH_2).

[Sb(SeⁿBu)₃]: Selenium shot (1.341 g, 1.70×10^{-2} mol) was ground into a fine powder under an inert atmosphere in a glovebox before being suspended in THF (30 mL). The suspension was then frozen in liquid nitrogen (77 K) before the dropwise addition of ⁿBuLi solution in hexanes (9.6 mL, 1.44×10^{-2} mol). After the mixture had thawed and been allowed to stir, a colour change from a black suspension to a yellow solution and then to a deep red solution was observed. Further ⁿBuLi solution (1 mL, 1.60×10^{-3} mol) was then added dropwise until a pale yellow colour persisted. A solution of SbCl_3 (1.291 g, 5.66×10^{-3} mol) in THF (30 mL) was then added dropwise to the cooled (273 K) solution of ⁿBuSeLi. Upon addition, the colour change to a bright yellow and then to a bright orange was observed. The reaction mixture was then stirred vigorously for half an hour. The reaction mixture was then concentrated under vacuum, hexane (30 mL) was added, at which point the solution turned cloudy with the precipitation of LiCl. The mixture was filtered by cannula filter, before concentrating under vacuum, washing with further hexane (30 mL), filtering once more and finally drying *in vacuo*, leaving a yellow/orange oil. Yield: 2.178 g, 73 %. ^1H NMR (CDCl_3): $\delta/\text{ppm} = 0.92$ (t, $J = 8.00$ Hz, [9H], CH_3), 1.44 (tquart, [6H], CH_2), 1.74 (tt, [6H], CH_2), 2.95 (t, [6H], SeCH_2). $^{13}\text{C}\{^1\text{H}\}$ NMR (CDCl_3): $\delta/\text{ppm} = 13.54$ (CH_3), 22.85 (CH_2), 25.24 ($^1J_{77\text{Se}13\text{C}} = 60$ Hz, SeCH_2), 35.44 (CH_2). $^{77}\text{Se}\{^1\text{H}\}$ NMR (CDCl_3): $\delta/\text{ppm} = 45.8$ (s).⁹

[Bi(SⁿBu)₃]: Butane thiol (1.703 g, 1.89×10^{-2} mol) was added to a solution of sodium metal (0.435 g, 1.89×10^{-2} mol) dissolved in anhydrous ethanol (20 mL) and stirred vigorously over the course of 2 h. Removal of volatiles from this colourless solution gave a white powder. THF (20 mL) was then added, followed by a solution of BiCl_3 (1.985 g, 6.30×10^{-3} mol) in THF (20 mL), which was added dropwise over the course of 5 min., during which the colour changed to yellow, then to light orange. The reaction mixture was then stirred for 1 h, at which point it was opaque and black, before then being filtered leaving a yellow solution. After the THF had been removed under vacuum, the yellow waxy solid remaining was washed in anhydrous hexane (30 mL), filtered to remove particulates and dried *in vacuo*. Yield: 2.018 g, 67%. ^1H NMR (CDCl_3): $\delta/\text{ppm} = 0.94$ (t, $J = 8.00$ Hz, [9H], CH_3), 1.45 (tquart, [6H], CH_2), 1.66 (tt, [6H], CH_2), 3.76 (t, [6H], SCH_2). $^{13}\text{C}\{^1\text{H}\}$ NMR (CDCl_3): $\delta/\text{ppm} = 13.73$ (CH_3), 21.77 (CH_2), 30.04 (SCH_2), 37.69 (CH_2).

7.3.3 Thin film growth by low pressure CVD onto fused silica substrates

The fused quartz substrates were first washed with deionized water then ethanol before being dried thoroughly in an oven before use. In a typical LPCVD experiment, the precursor (15-80mg)

and fused quartz substrates were loaded into a closed ended silica tube inside the glovebox. The precursor was loaded into the precursor bulb at the end of the sealed silica tube and the substrates were positioned end to end (0-4 cm away from the precursor bulb) down the silica tube. The tube was positioned horizontally in the furnace and held in place such that the precursor containing bulb was protruding from the end of the furnace. The tube was evacuated to 0.01- 0.4 mmHg. The furnace was heated to the necessary temperature for the experiment, as determined by TGA experiments and experimental observations, and allowed to stabilise. The tube was positioned so that the precursor was close enough to the furnace for volatilisation to be observed. The position was then maintained until all of the precursor had volatilised. This typically took 15-25 minutes. Once the deposition was complete, the tube was removed from the furnace area and allowed to cool naturally to room temperature before being transferred to the glovebox, where the substrates were removed and stored until they could be characterised. In all cases after the deposition had concluded, a small amount of solid material could be observed within the precursor bulb. This is likely some of the deposition material, as would be expected due to the large amounts of residual mass observed for the TGA experiments.

The depositions produced dark grey/ silver films with good coverages of between 1-2cm by 0.8 cm.

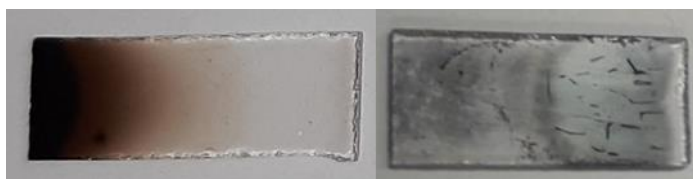


Figure 7-4: Examples of deposited material on tiles for Bi_2S_3 (left) and Sb_2S_3 (right).

The deposition of Sb_2Se_3 using $[\text{Sb}(\text{Se}^n\text{Bu})_3]$ is described in the work of Benjamin *et al.*⁹ However, similar spectroscopic analysis results were collected from depositions produced using $[\text{Sb}(\text{Se}^n\text{Bu})_3]$ in this work.

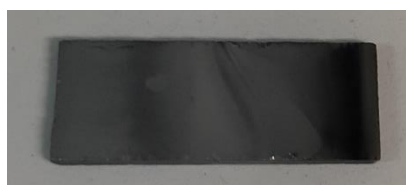
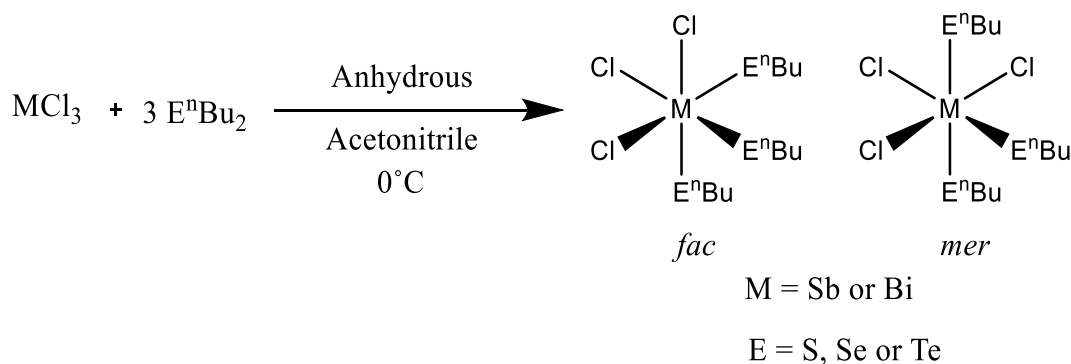


Figure 7-5: Sb_2Se_3 deposited onto a silica tile.

7.4 Results and discussion

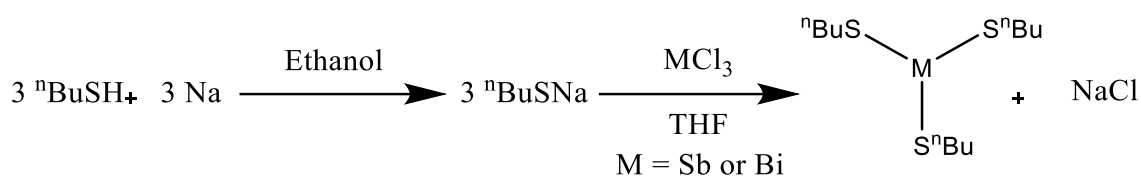
7.4.1 Single source precursor preparation and evaluation

SSPs of the form $[\text{MCl}_3(\text{E}^n\text{Bu}_2)_3]$ can be prepared by the simple combination of MCl_3 and a chalcogenoether, as displayed in Scheme 7-1. This synthesis was employed previously and these precursors have been deployed for the deposition of Bi_2Te_3 ¹ using $[\text{BiCl}_3(\text{Te}^n\text{Bu}_2)_3]$ as well as the use of $[\text{BiCl}_3(\text{Se}^n\text{Bu}_2)_3]$, $[\text{SbCl}_3(\text{Se}^n\text{Bu}_2)_3]$ and $[\text{SbCl}_3(\text{Te}^n\text{Bu}_2)_3]$ ² as well as $[\text{BiCl}_3(\text{Te}^n\text{Bu}_2)_3]$ in the exploration of the deposition of solid solutions of the form M_2E_3 , where M is Sb or Te and E is Se or Te. The extension of this class of SSP to also include the complexes $[\text{BiCl}_3(\text{S}^n\text{Bu}_2)_3]$ and $[\text{SbCl}_3(\text{S}^n\text{Bu}_2)_3]$, explored by project students (Hannah and Sana) under my supervision, would enable more cost effective and sustainable materials for thermoelectric applications. The products formed by the coordination of n-butylchalcogenoether ligands were then isolated by the removal of the acetonitrile under vacuum leaving yellow, orange or red oils. Particular care was taken to ensure that the precursor was not exposed to vacuum for long periods of time once the solvent had been removed, as this can lead to the loss of the chalcogenoether ligands, in particular this is an issue for the formation of $[\text{MCl}_3(\text{S}^n\text{Bu}_2)_3]$ due to the comparatively weak S-M interactions (*cf.* Se-M or Te-M interactions).



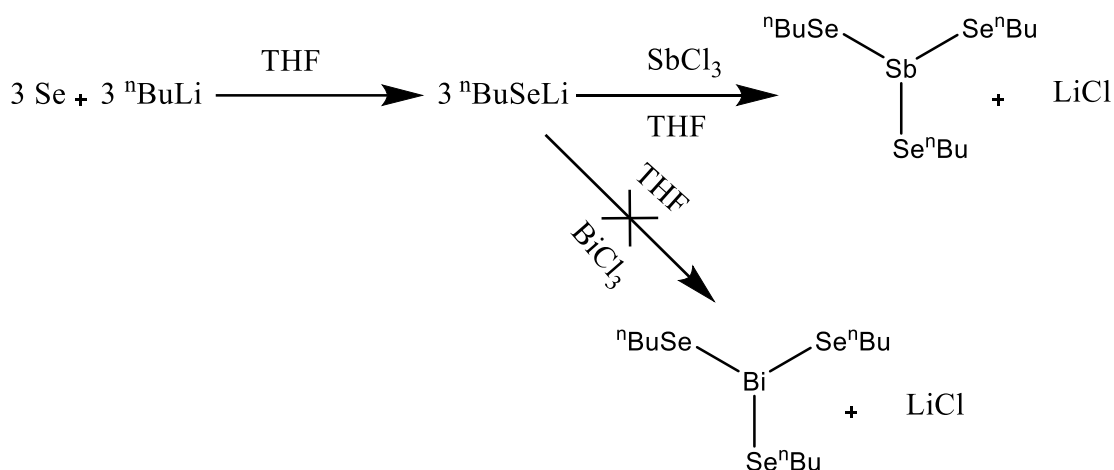
Scheme 7-1: Reaction schemes for the preparation of $[\text{MCl}_3(\text{E}^n\text{Bu}_2)_3]$.

The tris-thiolate precursors were obtained in good yields using the reaction outlined in Scheme 7-2. Care was taken to ensure that the stoichiometry was exactly balanced to ensure that no further coordination of thiolate groups to the metal centre, which was observed in reactions where an excess of $^n\text{BuSNa}$ was used. In such reactions a waxy solid was obtained, likely an anionic tetra-kis species, such as $[\text{Na}][\text{Sb}(\text{S}^n\text{Bu})_4]$.



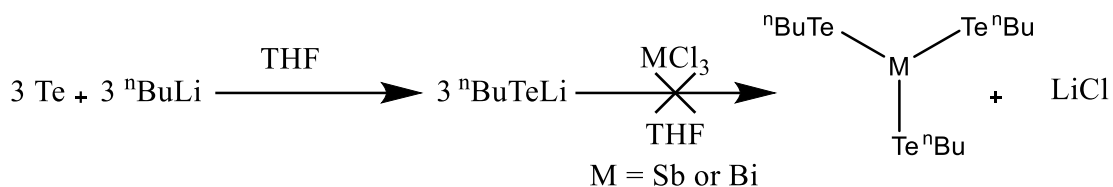
Scheme 7-2: Reaction scheme outlining the preparation of **[Sb(SⁿBu)₃]** and **[Bi(SⁿBu)₃]**.

The reaction of ⁿBuSeLi with SbCl₃, as described in Scheme 7-3, successfully produced **[Sb(SeⁿBu)₃]**, as described previously.⁹ However, the analogous reaction performed with BiCl₃ did not produce **[Bi(SeⁿBu)₃]** but rather lead to the formation of primarily ⁿBu₂Se₂. This was observed during the reaction with the immediate colour change to a deep red and could clearly be seen in the ⁷⁷Se {¹H} NMR spectra with a peak observed at 346 ppm.⁶¹



Scheme 7-3: Reaction scheme highlighting the successful preparation of **[Sb(SeⁿBu)₃]** and the unsuccessful preparation of **[Bi(SeⁿBu)₃]**.

All attempts to synthesise **[M(TeⁿBu)₃]**, where M is Sb or Bi, resulted in the formation of ⁿBu₂Te₂. This was observed during the reaction with the immediate colour change to a deep red and could clearly be seen in the ⁷⁷Se {¹H} NMR spectra with a peak observed at 112.9 ppm.⁶² Even when extreme care was taken to ensure the reaction was performed at -78 °C, the reaction produced only ⁿBu₂Te₂. This is likely to be a result of the weak interaction between the tellurium and the metal centres, due to the poor orbital overlap, allowing for easy cleavage and recombination with an adjacent tellurolate, with matching energy levels. This could occur via a disproportionation reaction, where by two molecules containing a M-Te bond react to form one species with a M-M bond and one with a Te-Te bond, ⁿBu₂Te₂. Another possibility is the elimination of ⁿBu₂Te₂ from a compound containing two or more tellurolate groups via a reductive elimination step.



Scheme 7-4: Reaction scheme of the attempted preparation of **[Sb(TeⁿBu)₃]** and **[Bi(TeⁿBu)₃]**.

The compatibility of these precursors successfully prepared for use in LPCVD was explored by means of TGA. Temperature ramp experiments from 30-600 °C were used to explore the purity, stability, volatility and possible temperature regime for the SSPs. These experiments can be seen in Figure 7-6.

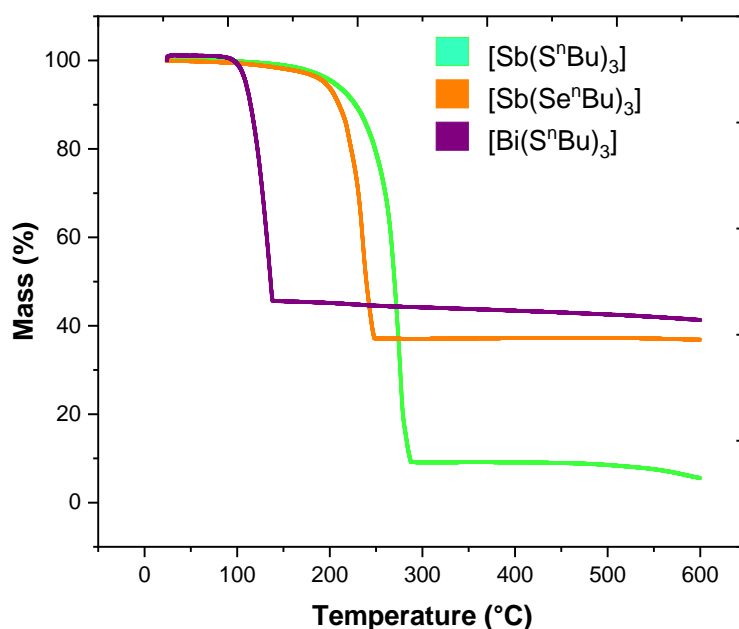
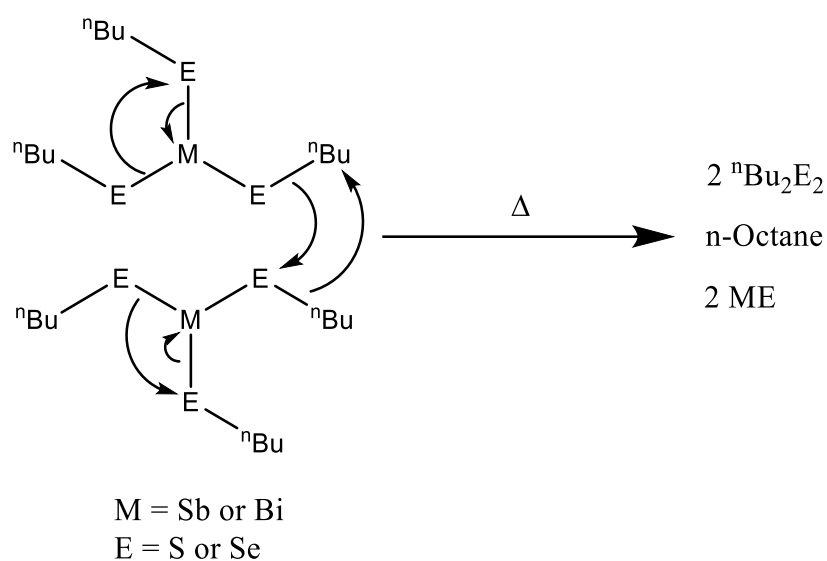


Figure 7-6: TGA experiments showing the change in mass with increasing temperature for **[Sb(SⁿBu)₃]**, **[Bi(SⁿBu)₃]** and **[Sb(SeⁿBu)₃]**.

As can be seen in Figure 7-6, the TGA temperature ramp experiments of **[Sb(SⁿBu)₃]**, **[Bi(SⁿBu)₃]** and **[Sb(SeⁿBu)₃]** all resulted in some residual mass remaining, *c.a.* 9 % down to 4 % at 600 °C, *c.a.* 44 % and 37 %, respectively. In the case of **[Sb(SⁿBu)₃]**, this residual mass does not account for any reasonable decomposition product and shows that the precursor mostly evaporates and only a small portion of the SSP is decomposed. However, **[Bi(SⁿBu)₃]** and **[Sb(SeⁿBu)₃]** both leave considerable residual masses. With respect to **[Bi(SⁿBu)₃]**, inspection of some reasonable decomposition products implies that a simultaneous loss of ⁿBu₂S₂, corresponding to a *ca.* 37 % mass loss, and the loss of ⁿBu corresponding to an *ca.* 12 % mass loss, leaving *ca.* 38 % residual

mass. With respect to **[Sb(SeⁿBu)₃]**, a loss of ⁿBu₂Se₂, corresponding to a *ca.* 52 % mass loss, and the loss of an ⁿBu corresponding to an *ca.* 11 % mass loss, would leave an *ca.* 37 % residual mass. Both of which are in good agreement with the TGA results. The formation of a dialkyl dichalcogenide volatile product has been reported previously in other chalcogenolate complex decompositions.^{64,65} It is important to note that this suggested decomposition has not been verified at this time and that the conditions in the TGA measurement differ greatly from those in the LPCVD experiments. During the LPCVD the lower pressure will lead to a much higher proportion of precursor to be evaporated. This proposed decomposition pathway is displayed in Scheme 7-5.



Scheme 7-5: Suggested thermal decomposition pathway for **[Bi(SⁿBu)₃]** and **[Sb(SeⁿBu)₃]**.

The residual material after TGA was analysed using powder XRD by Tom Crickmore. These experiments did show crystalline material in all cases. However, due to restrictions concerning room access during COVID, all of the samples were exposed to air for between 1 and 2 weeks. The powder XRD experiments performed on the TGA residue produced from **[Bi(SⁿBu)₃]** showed crystalline BiS and Bi₂S₃ the powder XRD, as shown in Figure 7-7.

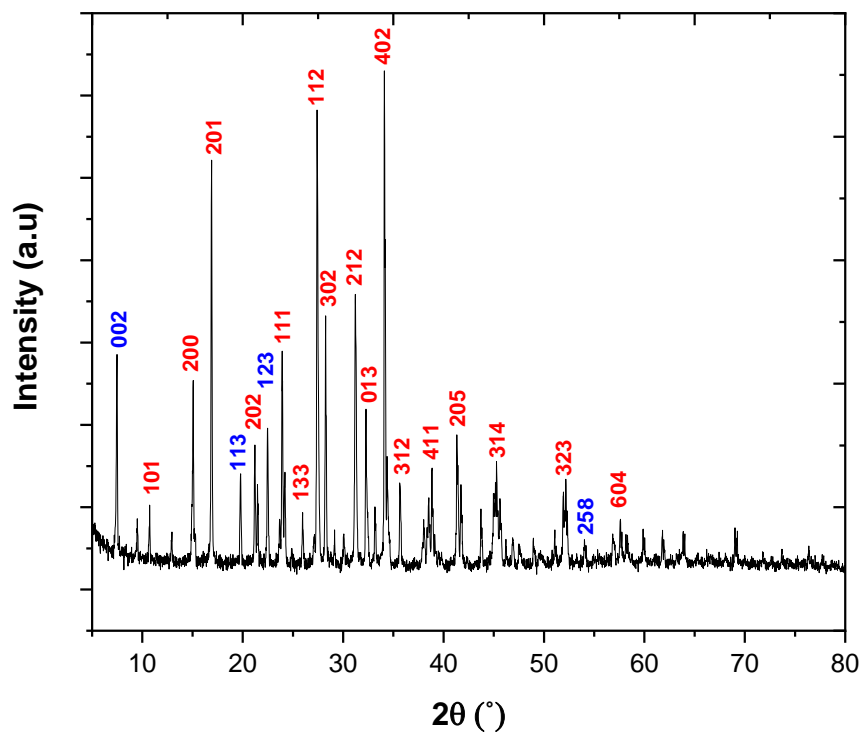


Figure 7-7: Powder XRD pattern of the residue from the TGA of $[\text{Bi}(\text{S}^n\text{Bu})_3]$, matched to a literature pattern for BiS ,⁶⁵ blue, and Bi_2S_3 ,¹³ red.

The powder XRD pattern for the residue produced in the TGA of $[\text{Sb}(\text{S}^n\text{Bu})_3]$ shows the presence of the oxide product Sb_2O_3 . This is likely a result of the highly fine nature of the powder and its exposure to air.

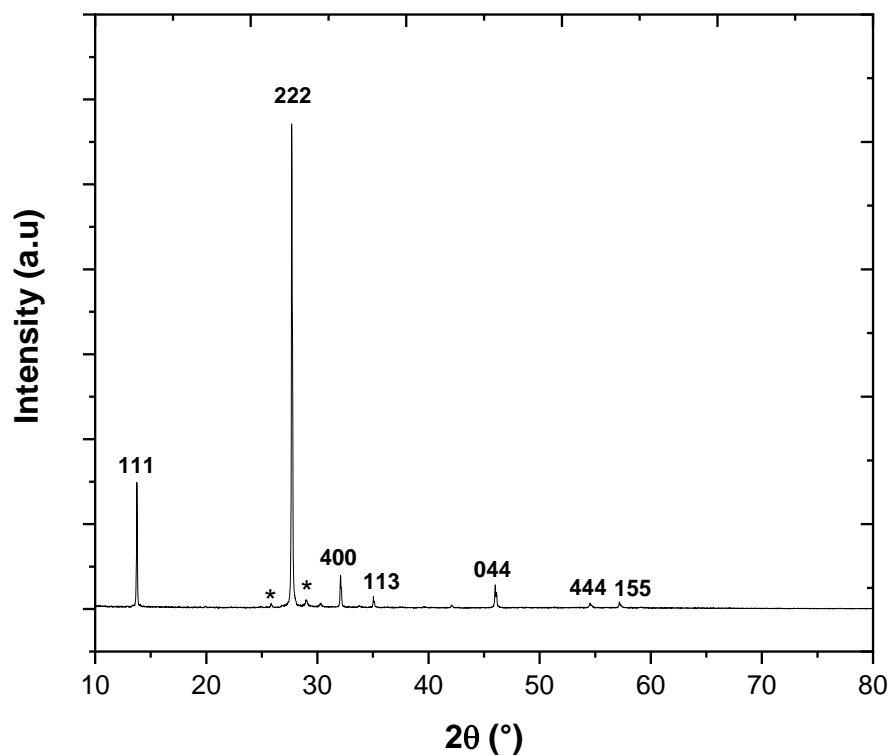


Figure 7-8: Powder XRD pattern of the decomposition product formed in the TGA of **[Sb(SⁿBu)₃]**, matched to literature patterns for Sb₂O₃.⁶⁶ The small peaks labelled with * correspond to elemental Sb.⁶⁵

The powder pattern for the residue produced in the TGA of **[Sb(SeⁿBu)₃]** shows Sb₂Se₃, as displayed in Figure 7-9.

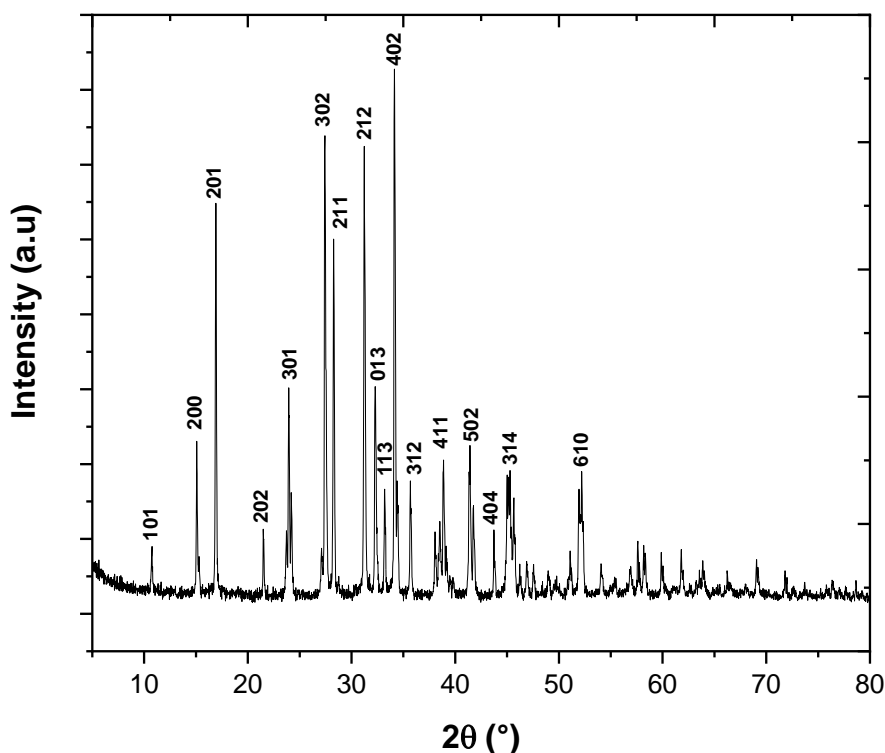


Figure 7-9: Powder XRD pattern of the decomposition product formed in the TGA of $[\text{Sb}(\text{Se}^n\text{Bu})_3]$, with some of the more intense peaks highlighted with the Miller index labels that coincide with literature bulk Sb_2Se_3 .⁶⁷

7.4.2 Low pressure chemical vapour deposition experiments

Precursor (15-60 mg) was loaded into the precursor bulb, taking care not to contaminate the walls of the CVD tube. This was achieved using a glass tube insert, to protect the walls of the CVD tube, and a long pipette. Fused silica substrates were positioned inside the tube end to end just outside the precursor well. The tube was positioned horizontally in a tube furnace and held in place such that the precursor containing bulb was protruding from the end of the furnace. The tube was evacuated to 0.01- 0.4 mmHg. The furnace was heated to the necessary temperature, 600 °C for $[\text{Bi}(\text{S}^n\text{Bu})_3]$ and $[\text{Sb}(\text{S}^n\text{Bu})_3]$ and 500 °C for $[\text{Sb}(\text{Se}^n\text{Bu})_3]$,⁹ for the reaction and allowed to stabilise. The tube was positioned so that the precursor was close enough to the furnace for sublimation to be observed. The position was then maintained until all of the precursor had sublimed. This typically took 10-40 minutes. Once the deposition was completed, the tube was removed from the furnace area and allowed to cool naturally to room temperature before being transferred to the glovebox, where the substrates were removed and stored until they could be characterised.

Depositions from the SSPs of the form $[\text{MCl}_3(\text{E}^n\text{Bu}_2)_3]$ proved suitable for the extension of the family of Bi_2E_3 films from this family of SSPs to include Bi_2S_3 . However, possibly due to the poorer

Lewis acidity of SbCl_3 (*cf.* Lewis acidity of BiCl_3), depositions from $[\text{SbCl}_3(\text{S}^n\text{Bu}_2)_3]$ did not produce Sb_2S_3 . This is likely due to the stronger S-C bond enthalpy (*cf.* Se-C and C-Te) due to the better orbital energy match and weaker dative covalent bond between S-Sb. The combination of these effects leads to a higher temperature needed for decomposition of the SSP and also a lower temperature required for the SSP prior to volatilisation, as this could otherwise cause cleavage of the dative covalent bond between the S-Sb. Breaking the dative covalent bond would be expected to lead to the distillation of S^nBu_2 through the CVD and the formation of SbCl_3 in the precursor bulb. This could be remedied either by the slower evaporation of $[\text{SbCl}_3(\text{S}^n\text{Bu}_2)_3]$, by positioning the precursor bulb further from the hot zone, or by the flash evaporation of the SSP, by using a hotter temperature and positioning the CVD tube closer to the hot zone. The precursor could also still be used in an AACVD or direct liquid injection CVD process.

7.4.3 Sb_2S_3 depositions

As mentioned above, depositions from $[\text{SbCl}_3(\text{S}^n\text{Bu}_2)_3]$ were unsuccessful, for depositions attempted between furnace temperatures of 600 and 650 °C, pressures of between 0.1 and 0.7 mmHg and precursor loads of between 15 and 42 mg. In these deposition attempts no films were produced for analysis and the precursor was observed decomposing to leave a light grey residue in the precursor bulb. For this reason the covalently bonded SSP $[\text{Sb}(\text{S}^n\text{Bu})_3]$ was developed to improve the thermal stability of the precursor to facilitate complete volatilisation prior to decomposition and film growth.

Depositions produced using $[\text{Sb}(\text{S}^n\text{Bu})_3]$ were characterised using GIXRD, SEM with EDX and Raman spectroscopy. The GIXRD pattern, shown in Figure 7-10, matches well to the literature pattern for bulk Sb_2S_3 . The refined lattice parameters of this deposition are: $a = 11.3549(10)$, $b = 3.8256(3)$ and $c = 11.2465(10)$ Å. Which are in good agreement with the literature data: $a = 11.311(1)$, $b = 3.8389(3)$, and $c = 11.223(1)$ Å.⁶⁸

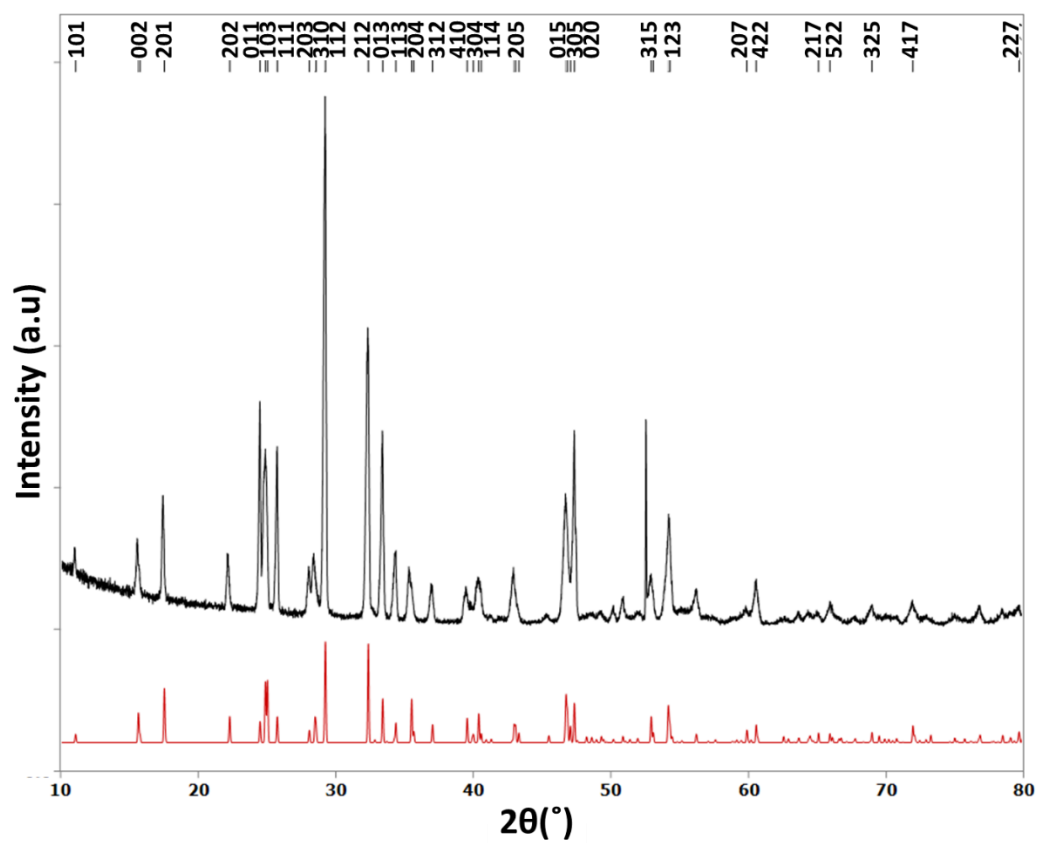


Figure 7-10: GIXRD pattern of an Sb_2S_3 , deposited using $[\text{Sb}(\text{S}^n\text{Bu})_3]$, in black matched to a literature pattern of Sb_2S_3 .⁶⁸

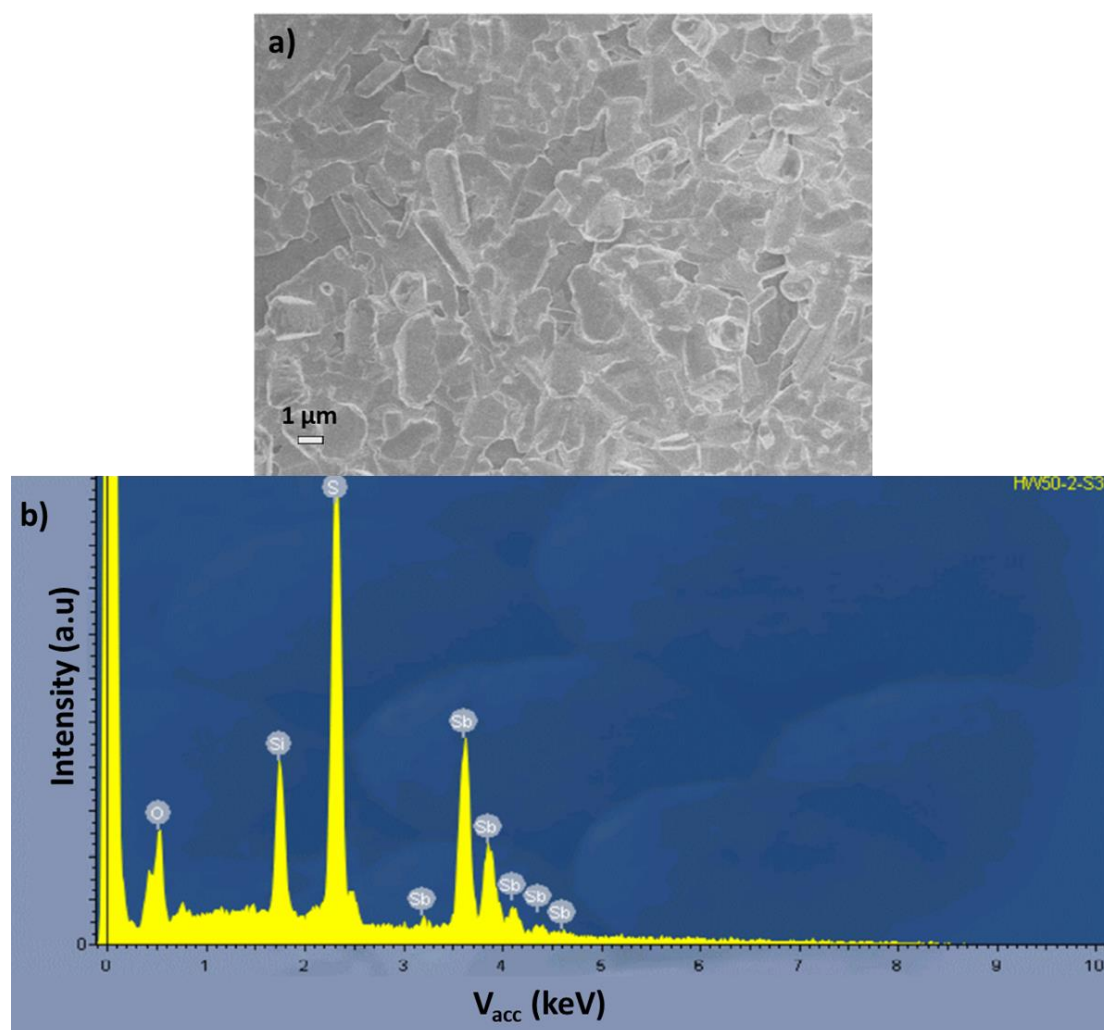


Figure 7-11: **a)** Top down SEM image of a deposit of Sb_2S_3 and **b)** the corresponding EDX spectrum for the same deposit.

The Raman spectrum displayed in Figure 7-12 shows peaks at 158, 191, and 282 cm^{-1} which can be attributed to A_g modes and peaks at 130, 239, and 312 cm^{-1} to B_{1g} modes. This is in good agreement with literature examples of Sb_2S_3 .⁶⁹

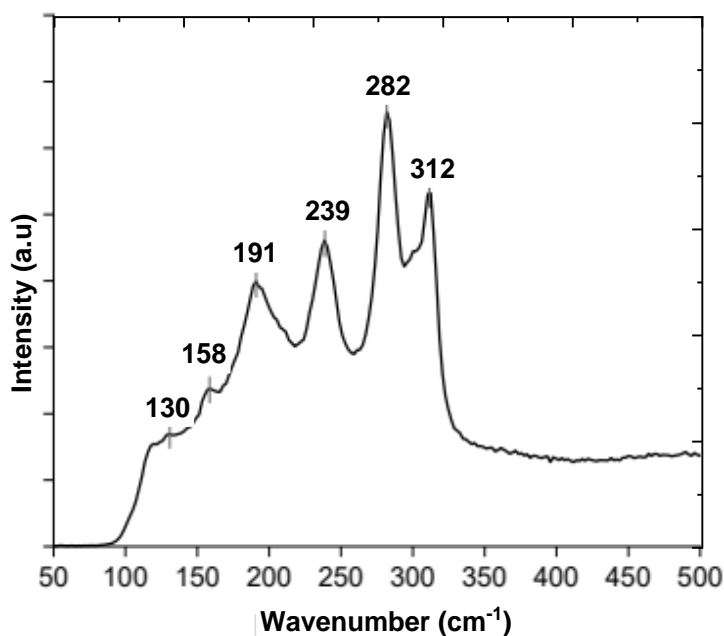


Figure 7-12: Raman spectrum collected from a sample of Sb_2S_3 deposited from $[\text{Sb}(\text{S}^n\text{Bu})_3]$. The peaks indicated at 158, 191, and 282 cm^{-1} correspond to the A_g modes and the peaks indicated at 130, 239, and 312 cm^{-1} correspond to B_{1g} modes.⁶⁹

7.4.4 Bi_2S_3 depositions

Depositions produced using $[\text{BiCl}_3(\text{S}^n\text{Bu}_2)_3]$ were initially explored by two UG project students under my guidance, Hannah Watson and Hamidah Sana, who found that this was a suitable SSP for the deposition of Bi_2S_3 .

Depositions produced using $[\text{Bi}(\text{S}^n\text{Bu})_3]$ were characterised using GIXRD, SEM with EDX and Raman spectroscopy. The GIXRD pattern, shown in Figure 7-13, matches well to the literature pattern for bulk Bi_2S_3 . The refined lattice parameters of this deposition are: $a = 11.263(6)$, $b = 3.987(2)$ and $11.120(5)\text{ \AA}$, which are in good agreement with the literature values of $a = 11.316(3)$, $b = 3.9709(2)$, and $c = 11.178(2)\text{ \AA}$.¹³

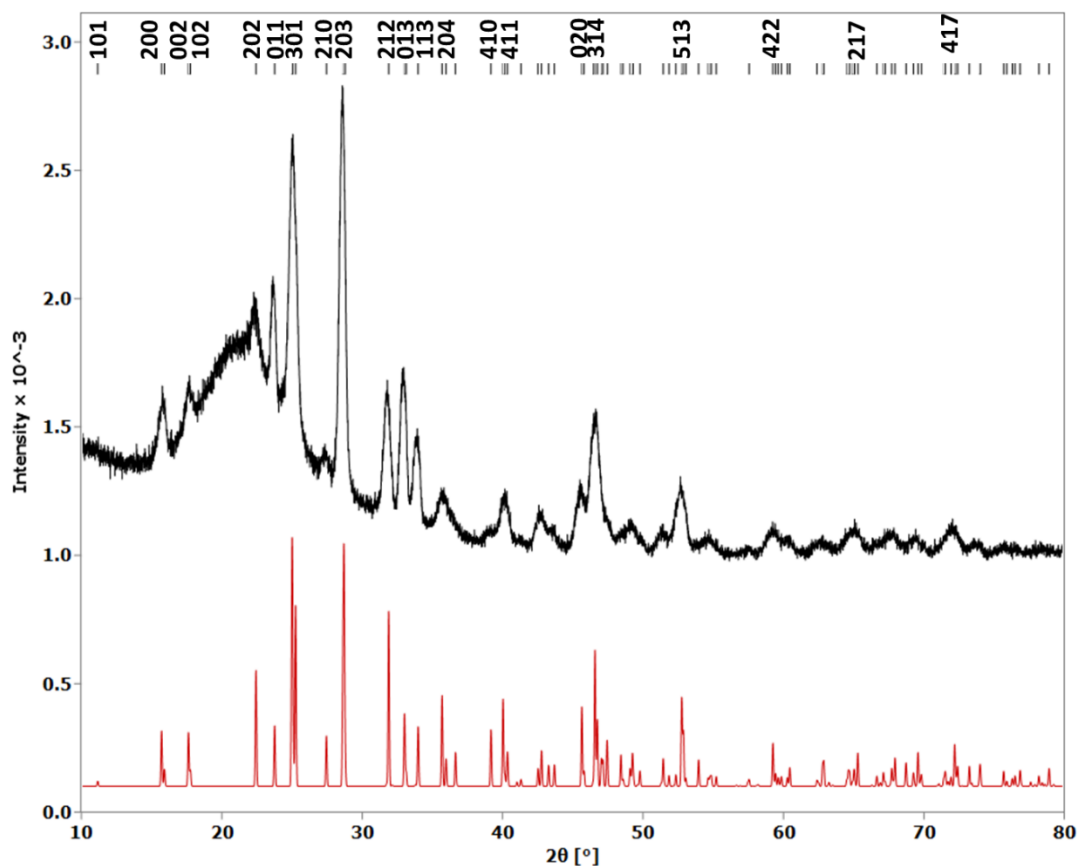


Figure 7-13: GIXRD pattern, in black, collected for a Bi_2S_3 thin film deposited using $[\text{Bi}(\text{S}^n\text{Bu})_3]$ matched to a literature pattern of Bi_2S_3 .¹³ The broad feature observed between *c.a.* 15 and 30 ° is caused by the underlying fused quartz substrate.

The Raman spectrum displayed in Figure 7-14 shows peaks at 100, 188, and 237 cm^{-1} which can be attributed to A_g modes and peaks at 166 and 263 cm^{-1} to B_{1g} modes. This is in good agreement with literature examples of Bi_2S_3 .⁷⁰

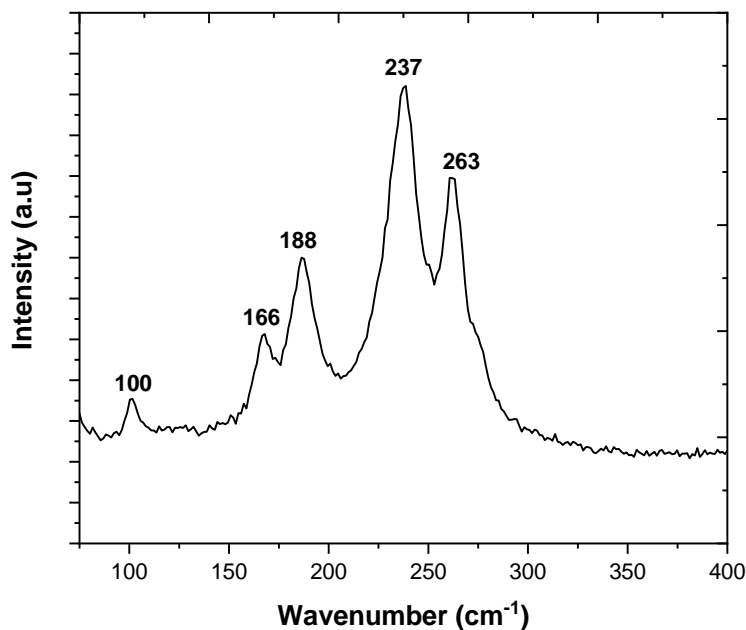


Figure 7-14: Raman spectrum of Bi_2Te_3 deposited using $[\text{Bi}(\text{S}^n\text{Bu})_3]$. The peaks indicated correspond to A_g , B_{1g} , A_g , A_g and B_{1g} modes, respectively.⁷⁰

7.5 Conclusions

Two separate classes of SSP for the deposition of Bi_2E_3 and Sb_2E_3 thin films, one containing anionic chalcogenolate ligands covalently bonded to the metal centre and the other neutral chalcogenoether ligands dative covalently bonded to the metal trichloride, have been prepared and characterised spectroscopically and via TGA. The chalcogenoether ligand containing SSPs, of the form $[\text{MCl}_3(\text{E}^n\text{Bu}_2)_3]$, were found to deposit Bi_2Te_3 , Sb_2Te_3 , Bi_2Se_3 , Sb_2Se_3 , as shown previously,¹⁻³ and in this work Bi_2S_3 . However, possibly due to the poor Lewis acidity of SbCl_3 and the modest Lewis basicity of $^n\text{Bu}_2\text{S}$, $[\text{SbCl}_3(\text{S}^n\text{Bu}_2)_3]$ was not shown to deposit Sb_2S_3 . The chalcogenolate style SSPs, of the form $[\text{M}(\text{E}^n\text{Bu})_3]$, were shown to deposit Sb_2Se_3 , as previously described,¹⁰ as well as Bi_2S_3 , Sb_2S_3 in the present work. However, likely due to the poor orbital overlap of Se with Bi as well as Te with Bi and Sb, $[\text{M}(\text{E}^n\text{Bu})_3]$, where M is Sb and E is Te or where M is Bi and E is Se or Te, could not be synthesised.

7.6 References

- 1 S. L. Benjamin, C. H. de Groot, C. Gurnani, A. L. Hector, R. Huang, E. Koukharenko, W. Levason and G. Reid, *J. Mater. Chem. A*, 2014, **2**, 4865.
- 2 S. L. Benjamin, C. H. de Groot, C. Gurnani, S. L. Hawken, A. L. Hector, R. Huang, M. Jura, W.

Chapter 7

- Levason, E. Reid, G. Reid, S. P. Richards and G. B. G. Stenning, *J. Mater. Chem. C*, 2018, **6**, 7734.
- 3 D. W. Newbrook, S. P. Richards, V. K. Greenacre, A. L. Hector, W. Levason, G. Reid, C. H. K. de Groot and R. Huang, *Appl. Energy Mater.*, 2020, **3**, 5840.
- 4 A. Polozine, S. Sirotinskaya and L. Schaeffer, *Mater. Res.*, 2014, **17**, 1260.
- 5 T. C. Harman, B. Paris, S. E. Miller and H. L. Goering, *J. Phys. Chem. Solids*, 1957, **2**, 181.
- 6 N. S. Rajagopalan and S. K. Ghosh, *Physica*, 1963, **29**, 234.
- 7 T. C. Harman, B. Paris, S. E. Miller and H. L. Goering, *J. Phys. Chem. Solids*, 1957, **2**, 181.
- 8 D. A. Wright, *Nature*, 1958, **181**, 834.
- 9 S. L. Benjamin, C. H. de Groot, A. L. Hector, R. Huang, E. Koukharenko, W. Levason and G. Reid, *J. Mater. Chem. C*, 2015, **3**, 423.
- 10 H. J. Breunig, I. Ghesner, M. E. Ghesner and E. Lork, *Inorg. Chem.*, 2003, **42**, 1751.
- 11 L. F. Lundegaard, R. Miletich, T. Balic-Zunic and E. Makovicky, *Phys. Chem. Miner.*, 2003, **30**, 463.
- 12 G. P. Voutsas, A. G. Papazoglou, P. J. Rentzeperis and D. Siapkias, *Zeitschrift fur Krist. - New Cryst. Struct.*, 1985, **171**, 261.
- 13 L. F. Lundegaard, E. Makovicky, T. Boffa-Ballaran and T. Balic-Zunic, *Phys. Chem. Miner.*, 2005, **32**, 578.
- 14 K. A. Kokh, V. V. Atuchin, T. A. Gavrilova, N. V. Kuratieva, N. V. Pervukhina and N. V. Surovtsev, *Solid State Commun.*, 2014, **177**, 16.
- 15 C. P. Vincente, J. L. Tirado, K. Adouby, J. C. Jumas, A. A. Toure and G. Kra, *Inorg. Chem.*, 1999, **38**, 2131.
- 16 Y. Feutelais, B. Legendre, N. Rodier and V. Agafonov, *Mater. Res. Bull.*, 1993, **28**, 591.
- 17 G. J. Snyder and E. S. Toberer, *Nat. Mater.*, 2008, **7**, 105.
- 18 L. E. Bell, *Science*, 2014, **321**, 1457.
- 19 V. A. Kutasov, L. N. Lukyanova and M. V. Vedernikov, in *Thermoelectrics Handbook: Macro to Nano*, ed. R. D. Michael, CRC Press, London, 2006.

- 20 C. J. Vineis, A. Shakouri, A. Majumdar and M. G. Kanatzidis, *Adv. Mater.*, 2010, **22**, 3970.
- 21 N. Jaziri, A. Boughamoura, J. Müller, B. Mezghani, F. Tounsi and M. Ismail, *Energy Reports*, 2020, **6**, 264.
- 22 M. Calixto-Rodriguez, H. Martínez, Y. Peña, O. Flores, H. E. Esparza-Ponce, A. Sanchez-Juarez, J. Campos-Alvarez and P. Reyes, *Appl. Surf. Sci.*, 2010, **256**, 2428.
- 23 Y. Kawamoto and H. Iwasaki, *J. Electron. Mater.*, 2014, **43**, 1475.
- 24 H. Maghraoui-Meherzi, T. Ben Nasr, N. Kamoun and M. Dachraoui, *Comptes Rendus Chim.*, 2011, **14**, 471.
- 25 H. Moreno-García, S. Messina, M. Calixto-Rodriguez and H. Martínez, *Appl. Surf. Sci.*, 2014, **311**, 729.
- 26 Y. Wu, Q. Lou, Y. Qiu, J. Guo, Z. Y. Mei, X. Xu, J. Feng, J. He and Z. H. Ge, *Inorg. Chem. Front.*, 2019, **6**, 1374.
- 27 B. Chen, C. Uher, L. Iordanidis and M. G. Kanatzidis, *Chem. Mater.*, 1997, **9**, 1655.
- 28 Y. Zhou, M. Leng, Z. Xia, J. Zhong, H. Song, X. Liu, B. Yang, J. Zhang, J. Chen, K. Zhou, J. Han, Y. Cheng and J. Tang, *Adv. Energy Mater.*, 2014, **4**, 1301846.
- 29 T. Y. Ko, M. Shellaiah and K. W. Sun, *Sci. Rep.*, 2016, **6**, 35086.
- 30 L. R. Gilbert, B. V. Pelt and C. Wood, *J. Phys. Chem. Solids*, 1974, **35**, 1629.
- 31 A. Akrap, A. Ubaldini, E. Giannini and L. Forró, *EPL*, 2014, **107**, 57008.
- 32 K. Kadel, L. Kumari, W. Z. Li, J. Y. Huang and P. P. Provencio, *Nanoscale Res. Lett.*, 2011, **6**, 57.
- 33 J. Navrátil, J. Horák, T. Plecháček, S. Kamba, P. Lošťák, J. S. Dyck, W. Chen and C. Uher, *J. Solid State Chem.*, 2004, **177**, 1704.
- 34 P. Fan, Z. H. Zheng, G. X. Liang, D. P. Zhang and X. M. Cai, *J. Alloys Compd.*, 2010, **505**, 278.
- 35 S. Zastrow, J. Gooth, T. Boehnert, S. Heiderich, W. Toellner, S. Heimann, S. Schulz and K. Nielsch, *Semicond. Sci. Technol.*, 2013, **28**, 035010.
- 36 N. W. Park, W. Y. Lee, J. E. Hong, T. H. Park, S. G. Yoon, H. Im, H. S. Kim and S. K. Lee, *Nanoscale Res. Lett.*, 2015, **10**, 20.

Chapter 7

- 37 M. M. Rashid, K. H. Cho and G. S. Chung, *Appl. Surf. Sci.*, 2013, **279**, 23.
- 38 N. Peranio, M. Winkler, Z. Aabdin, J. König, H. Böttner and O. Eibl, *Phys. Status Solidi Appl. Mater. Sci.*, 2012, **209**, 289.
- 39 D. W. Newbrook, S. P. Richards, V. K. Greenacre, A. L. Hector, W. Levason, G. Reid, C. H. (Kees. de Groot and R. Huang, *J. Alloys Compd.*, 2020, **848**, 156523.
- 40 M. K. Han, Y. Jin, D. H. Lee and S. J. Kim, *Materials (Basel)*, 2017, **10**, 1235.
- 41 X. Guo, X. Jia, K. Jie, H. Sun, Y. Zhang, B. Sun and H. Ma, *CrystEngComm*, 2013, **15**, 7236.
- 42 J. Gellman, J. M. Hare, C. J. Lowenstein, G. Gerstenblith, V. Coombs, P. Langenberg, J. A. Brinker and J. R. Resar, *Nature*, 2001, **413**, 597.
- 43 B. Poudel, Q. Hao, Y. Ma, Y. Lan, A. Minnich, B. Yu, X. Yan, D. Wang, A. Muto, D. Vashaee, X. Chen, J. Liu, Dresselhaus, G. Chen and Z. Ren, *Science*, 2008, **320**, 634.
- 44 J. R. Szczech, J. M. Higgins and S. Jin, *J. Mater. Chem.*, 2011, **21**, 4037.
- 45 R. J. Mehta, Y. Zhang, H. Zhu, D. S. Parker, M. Belley, D. J. Singh, R. Ramprasad, T. Borca-Tasciuc and G. Ramanath, *Nano Lett.*, 2012, **12**, 4523.
- 46 M. T. Pettes, J. Kim, W. Wu, K. C. Bustillo and L. Shi, *APL Mater.*, 2016, **4**, 104810.
- 47 S. Li, H. M. A. Soliman, J. Zhou, M. S. Toprak, M. Muhammed, D. Platzek, P. Ziolkowski and E. Müller, *Chem. Mater.*, 2008, **20**, 4403.
- 48 L. D. Zhao, B. P. Zhang, J. F. Li, M. Zhou, W. S. Liu and J. Liu, *J. Alloys Compd.*, 2008, **455**, 259.
- 49 F. Yu, J. Zhang, D. Yu, J. He, Z. Liu, B. Xu and Y. Tian, *J. Appl. Phys.*, 2009, **105**, 094303.
- 50 L. Tian, H. Y. Tan and J. J. Vittal, *Cryst. Growth Des.*, 2008, **8**, 734.
- 51 W. Lou, M. Chen, X. Wang and W. Liu, *Chem. Mater.*, 2007, **19**, 872.
- 52 S. Gao, *Growth (Lakeland)*, 2004, **4**, 513.
- 53 J. R. Castro, K. C. Molloy, Y. Liu, C. S. Lai, Z. Dong, T. J. White and E. R. T. Tiekink, *J. Mater. Chem.*, 2008, **18**, 5399.
- 54 G. Bendt, A. Weber, S. Heimann, W. Assenmacher, O. Prymak and S. Schulz, *Dalton Trans.*, 2015, **44**, 14272.

- 55 S. S. Garje, D. J. Eisler, J. S. Ritch, M. Afzaal, P. O'Brien and T. Chivers, *J. Am. Chem. Soc.*, 2006, **128**, 3120.
- 56 G. Bendt, S. Schulz, S. Zastrow and K. Nielsch, *Chem. Vap. Depos.*, 2013, **19**, 235.
- 57 G. Gupta and J. Kim, *Dalton Trans.*, 2013, **42**, 8209.
- 58 D. J. Gulliver, E. G. Hope, W. Levason, S. G. Murray, D. M. Potter and G. L. Marshall, *J. Chem. Soc., Perkin Trans. 2*, 1984, 429.
- 59 E. G. Hope, T. Kemmitt and W. Levason, *Organometallics*, 1988, **7**, 78.
- 60 D. J. Gulliver, E. G. Hope, W. Levason, S. G. Murray ' and D. M. Potter, *J. Chem. Soc. Dalt. Trans*, 1984, 429.
- 61 N. P. Luthra, A. M. Boccanfuso, R. B. Dunlap and J. D. Odom, *J. Organomet. Chem.*, 1988, **354**, 51.
- 62 S. L. Hawken, R. Huang, C. H. de Groot, A. L. Hector, M. Jura, W. Levason, G. Reid and G. B. G. Stenning, *Dalton Trans*, 2019, **48**, 117.
- 63 M. Bochmann and K. J. Webb, *J. Chem. Soc. Dalt. Trans.*, 1991, 2325.
- 64 K. Ramasamy, V. L. Kuznetsov, K. Gopal, M. A. Malik, J. Raftery, P. P. Edwards and P. O'Brien, *Chem. Mater.*, 2013, **25**, 266.
- 65 J. Q. Li, X. W. Feng, W. A. Sun, W. Q. Ao, F. S. Liu and Y. Du, *Mater. Chem. Phys.*, 2008, **112**, 57.
- 66 U. Dehlinger, *Zeitschrift für Krist.*, 1927, **66**, 108.
- 67 A. Kyono, A. Hayakawa and M. Horiki, *Phys. Chem. Miner.*, 2015, **42**, 475.
- 68 A. Kyono and M. Kimata, *Am. Mineral.*, 2004, **89**, 932.
- 69 S. Shaji, L. V. Garcia, S. L. Loredo, B. Krishnan, J. A. Aguilar Martinez, T. K. Das Roy and D. A. Avellaneda, *Appl. Surf. Sci.*, 2017, **393**, 369.
- 70 A. Harvey, J. B. Boland, Y. Guo, Q. Zhao, Z. Yao, K. Si, Y. Zhou and X. Xu, *Nanotechnology*, 2017, **28**, 335602.

Chapter 8 Summary and outlook

The work described in this thesis outlines the establishment and optimisation of the deposition of a number of materials of interest for a wide range of applications. This includes the description a single source precursor family, including the first example of a single source precursor for Si_2Te_3 , and their use in LPCVD. The work detailed also expands the reported thermoelectric performances of some of the materials and details some different techniques to control the enhanced thermoelectric performance some of these materials.

The successful synthesis of a number of different single source precursors for group 14 chalcogenide materials, including: Si_2Te_3 , GeS , GeSe , GeTe , SnS , SnSe and SnTe , and their characterisation using ^1H , $^{13}\text{C}\{^1\text{H}\}$, $^{29}\text{Si}\{^1\text{H}\}$, $^{77}\text{Se}\{^1\text{H}\}$ and $^{125}\text{Te}\{^1\text{H}\}$ NMR spectroscopy. The vapour pressure of all of these SSPs was also obtained using isothermal step TGA experiments and thermodynamic data was obtained from these results.

Successful depositions of the SnE , where $\text{E} = \text{S}, \text{Se}$ or Te materials, including the first example of selectively deposited SnTe , greatly expands the applications and diversity of SnE polycrystalline thin films. The SSPs developed for the production of SnS also lead to control over the quantity of sulfur within the deposit, which was determined to be a method of greatly enhancing the materials electrical conductivity. Thus, the performance of the SnS films described in this work can be controlled by SSP selection. The thermoelectric performance of SnSe and SnTe reported in this work are competitive with other polycrystalline depositions reported.

The deposition of GeE , where E is S, Se or Te , was highly successful and the first example of a single source precursor that spans the entire sulfide, selenide and telluride series. The depositions of GeTe was shown to have good thermoelectric performance, which was also affected by the deposition temperature. It was determined that higher deposition temperatures led to higher charge carrier concentrations, which lead to an enhanced power factor. This means that the deposition conditions yield some control over the performance of the GeTe deposited.

The deposition of SnSe was successfully shown to be transferable to a commercial set up by altering the vapour pressure of the SSP. This advancement opens up huge opportunities for all of the group 14 chalcogenide materials described in this work, both in terms of the larger scale of their deposition, higher control allowing for greater selective deposition potential, the possibility of depositing thinner films and the exciting prospect of producing multi-layered stacks.

Appendix A – General Experimental Techniques

A.1 Precursor Preparation and Characterisation

All reactions were performed under an inert atmosphere by utilisation of Schlenk, vacuum line and glove box techniques under a dry nitrogen atmosphere. The solvents used (THF and hexane) were all dried over sodium wire using a stiele prior to use and NMR solvents were stored in a glovebox over molecular sieves. The Et_3SnCl , ${}^n\text{Bu}_2\text{GeCl}_2$ and ${}^n\text{Bu}_2\text{SnCl}_2$ was acquired from Alfa Aesar, ${}^n\text{Bu}_3\text{SiCl}$, ${}^n\text{Bu}_3\text{SnCl}$ was acquired from Sigma Aldrich and ${}^n\text{Bu}_3\text{GeCl}$ was obtained from Alfa Chemistry. All of these were then stored in a glovebox and used as received. All ${}^1\text{H}$, ${}^{13}\text{C}\{{}^1\text{H}\}$, ${}^{29}\text{Si}\{{}^1\text{H}\}$ (referenced against neat SiMe_4), ${}^{77}\text{Se}\{{}^1\text{H}\}$ (referenced against neat SeMe_2), and ${}^{125}\text{Te}\{{}^1\text{H}\}$ (referenced against neat TeMe_2) NMR spectra were collected on a Bruker AV400 spectrometer in CDCl_3 . Elemental analysis results were measured at the London Metropolitan University elemental analysis service.

A.2 Thin film characterisation

Grazing incidence X-ray diffraction (XRD) patterns were collected using a Rigaku SmartLab system, using $\text{Cu-}\alpha$ X-rays, a 2θ scan range of $10 - 80^\circ$ and an ω -offset of 1° . The crystalline phase of the film was determined by comparison with a literature XRD pattern, accessed via the Inorganic Crystal Structure Database (ICSD),¹ and lattice parameters were obtained by further optimisation of the fit using PDXL.²

The SEM microscope used was a FEI XL30 ESEM (Environmental Scanning Electron Microscope) tungsten filament electron source with ThermoFisher UltraDry EDX, 10 mm^2 detector.

The Raman spectra were obtained using a Renishaw inVia confocal Raman microscope – 785 nm 500 mW laser.

A.3 Thermoelectric and electrical property measurements

Resistivity, carrier concentration, and carrier mobility were measured by Hall measurements (Nanometrics HL5500PC) from 125K to 450K in steps of 25K under a magnetic field of 0.5T. Care was taken to ensure linear contact between the probes and sample before each measurement and current was optimised to ensure normal ohmic conduction with maximum voltage signal. Seebeck and electrical resistivity were measured using the Joule Yacht MRS-3L from 300K to 600K

Definitions and Abbreviations

in steps of 25K. The Seebeck coefficient was measured using the differential method with a maximum temperature difference of 10K. The resistivity measured here was measured using a 4 point probe method and corrected for geometric error using the results from the Hall measurement system. These two measurement techniques are discussed in far greater detail in section 1.9.3.

A.4 Evaluation of LPCVD setup

As described, the LPCVD experiments were conducted using a quartz CVD tube positioned inside a tube furnace, the tube furnace is insulated at both openings. This leads to a difference in the temperature in the middle of the furnace as compared to the outer edges. The actual internal temperature were measured using a thermocouple and the results of these measurements are shown in Figure A.1.

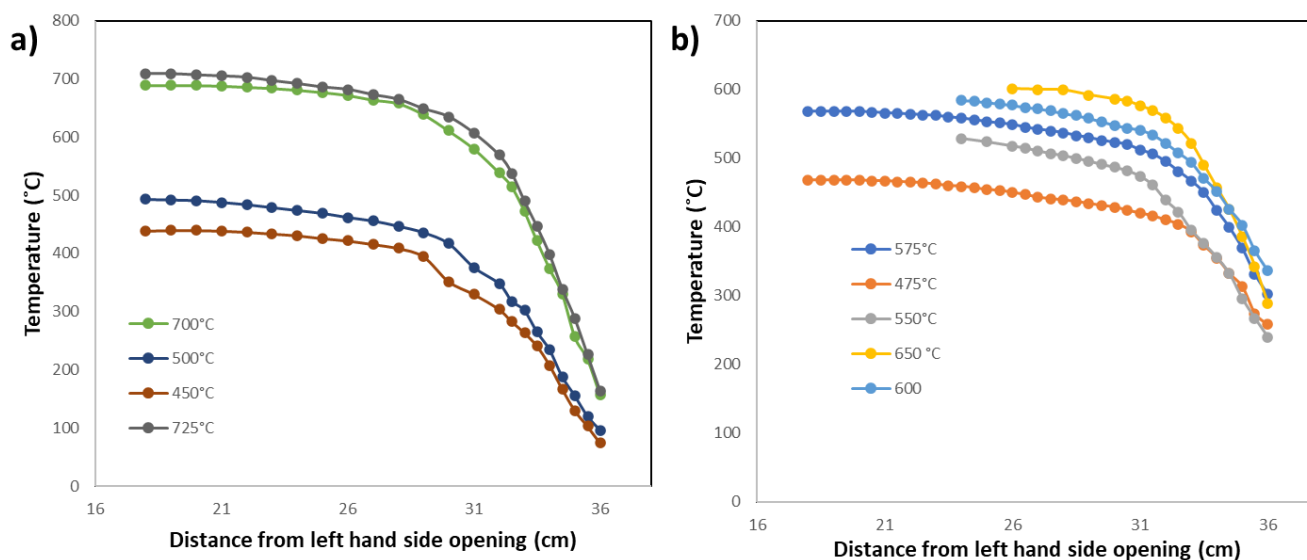


Figure A.1: Temperature profiles for a range of different furnace temperatures using **a)** fused silica wool (restek) and **b)** Superwool 607 Fiber, 4 μm (RS pro).

A.5 References

- 1 NIST Inorganic Crystal Structure Database, NIST Standard Reference Database Number 3, National Institute of Standards and Technology, Gaithersburg MD, 20899, DOI: <https://doi.org/10.18434/M32147>, (retrieved September 2019).
- 2 S. Graulis, D. Chateigner, R. T. Downs, A. F. T. Yokochi, M. Quirós, L. Lutterotti, E. Manakova, J. Butkus, P. Moeck and A. Le Bail, *J. Appl. Crystallogr.*, 2009, **42**, 726.